HIGH-RESOLUTION FACIES VARIABILITY AND CONNECTIONS TO COMPOSITIONAL AND MECHANICAL HETEROGENEITY IN THE UNION SPRINGS FORMATION OF CENTRAL NEW YORK

A Dissertation

Presented to the Faculty of the Graduate School

of Cornell University

In Partial Fulfillment of the Requirements for the Degree of

Doctor of Philosophy

by

John L Mason

January 2017

HIGH-RESOLUTION FACIES VARIABILITY AND CONNECTIONS TO COMPOSITIONAL AND MECHANICAL HETEROGENEITY IN THE UNION SPRINGS FORMATION OF CENTRAL NEW YORK

John L Mason, Ph. D.

Cornell University 2017

This work documents variability within the Union Springs Formation of the Marcellus subgroup across a variety of length scales along the northern margin of the Appalachian Basin. Visual, geochemical, and mechanical testing methods are utilized to describe rock properties spatially and to understand the drivers of change.

Three complete columns of Union Springs Formation in Seneca Falls, NY and Marcellus, NY are lithologically characterized, and placed into a microfacies framework. Based on hand sample analysis, thin section petrography, and scanning electron microscopy, rock properties variation is described both across and within facies. The distribution and arrangement of these facies are tracked across studied stratigraphic sections. Facies positions reveal variable depositional conditions across the distal rim of the basin, inclusive of bottom-water oxygenation, inconsistent sediment transport, and other features important to reconstructing the paleodepositional environment.

Geochemical data are used to indicate paleodepositional or diagenetic conditions, which can be important for evaluating resource potential or predicting geomechanical properties. With the goal of better understanding the depositional

environment, as well as modern inter-facies and intra-facies variability, this study measures chemical compositional variability of lithologically characterized samples via handheld x-ray fluorescence. Exploring the validity of associations of geochemical signals with depositional facies can clarify the predictive power of geochemical analysis in the Union Springs Formation.

Analysis of lithologic, chemical, and faunal characteristics informs analysis of the micro-mechanical behavior of these rocks. Procedures for accurately collecting grain-scale mechanical properties of mudrocks through nanoindentation and microindentation are developed. It is hoped that by creating a better understanding of the characteristic deformation behavior of individual constituents of mudstones within a rock matrix, the bulk deformation behavior can be more accurately modeled and predicted.

BIOGRAPHICAL SKETCH

Hailing from New Britain, CT, John Mason arrived at Cornell in 2011 after receiving a B.S. in Geological Sciences from Tufts University. Under the guidance of advisor Terry Jordan, John was immediately immersed in a multidisciplinary working environment as a member of the Earth-Energy Systems IGERT program, and started to undertake projects related to organic-rich shales and geothermal energy development. For its potential to provide a better understanding of variability in the Marcellus shale of New York State, John hopes his thesis research will be a valuable resource for sedimentary geologists, landowners, energy companies, and policymakers at multiple levels of government.

Within the academic community, John has been active as a Co-Founder of the Cornell Earth Energy club and a member of the Cornell team of finalists in the National Geothermal Student Competition. He has been honored to receive the AAPG Foundation David Worthington Family Research Grant as well as the Meyer and Stephen Bender Memorial Scholarship. While at Cornell, John has been heavily involved in the local music scene, and has had the privilege of performing in front of three Cornell presidents, the Board of Trustees, and diverse audiences of friends at numerous venues around Ithaca.

Thank You. Be your brother's keeper and keep your head to the sky.

ACKNOWLEDGMENTS

I leave Cornell University with extreme gratitude toward the many people who have made it possible to reach this point in my life.

Infinite thanks to my advisor Dr. Terry Jordan for her guidance and encouragement. Over the past 5 years, Terry has provided an optimistic and challenging work environment which has positively impacted my approach to science in a manner which is impossible to overstate. Thanks for everything from constructive feedback to a literal roof over my head. It has truly been a pleasure.

I'd like to thank my special committee members Jeff Tester and Jim Bisogni. Jeff has been a strong and constant source of support, leadership, and technical knowledge throughout my time at Cornell as a committee member, instructor, and leader of the Earth Energy IGERT Program. Jim has been a valuable source of knowledge, environmental engineering perspective, and positive outlook both in and out of the classroom.

Thanks to the non-committee professors at Cornell and elsewhere who helped me navigate the academic landscape, particularly Rick Allmendinger, Lou Derry, Alan Zehnder, and Shef Baker. This project would not be possible without Professor Mike McGlue, who has been a fantastic person to work with on mudstone stratigraphy and composition. Collaboration with Dick Lindemann was at once an informative and inspiring experience. Many thanks to the members of the Shale Mechanics Group, who provided an environment prime for innovation, cross-disciplinary collaboration, and open discussion. Thanks to Muawia Barazangi and George Hade for sharing their vast experience, sense of humor, and sustenance.

I thank the amazing professors from Tufts Earth and Ocean Sciences for giving me a top-notch geological foundation, and great experiences in the field. Thanks to my academic advisor Anne Gardulski for pushing me and always believing in my abilities.

This project would not have been possible without the support of many friends and colleagues. Many thanks to my labmates Erin Camp, Naomi Kirk-Lawlor, Joey Rosario, Ceren Karaça, Nico Cosentino, Katherine Herleman, and Casey Root for their brilliant minds and friendship. Similarly, without the thoughtful input and energetic discussion with my friends in the Earth-Energy IGERT program, my time at Cornell would not have been the same. Conversation and collaboration with those specializing in fields outside of my own was never anything short of a great experience; thanks to Joe Carloni, Brendan Anderson, Kyle Trostle, and Chris Siron. Many thanks to Katie, Michelle, and Kyle for taking me in off of the mean Ithaca streets so that I could finish my dissertation. Getting a start in applying research at the government and industry level in Idaho with the NGSC team of Sean Hillson, Koenraad Beckers, and Holly Taylor was both an incredible learning experience and a great time.

Thanks to the good people at the New York State Museum: Jim Leone devoted hours of time, access to Marcellus core, and help with total organic carbon measurements; and Chuck Ver Straeten provided crucial knowledge of Appalachian Basin stratigraphy and Marcellus outcrop sites. Many thanks to Seneca Stone Corporation and the Saunders quarry in Marcellus, NY for allowing us generous access to their Marcellus exposures. Thanks to John Hunt, Don Werder, Phil Carubia, and Jerry Drumheller for their expertise in the lab. Work by Anna-Katharina Von Krauland and Claire Behar provided substantial help in the early stages of

compositional analysis and fossil identification. Special thanks to Fairmount Industries for their support.

Acknowledgement and thanks to the National Science Foundation and the Cornell University Earth-Energy IGERT Program, as well as the donors of the American Chemical Society Petroleum Research Fund for their support. This work was supported in part by Cornell University's David R. Atkinson Center for a Sustainable Future (ACSF). Thanks to the AAPG Grants-in-Aid program and the David Worthington family for their generosity.

Many thanks to my friends doing great things all over the world. To all of those who have left us too soon, I thank you for the example you have left behind.

Thanks to my musical family at Cornell, in Boston, and in Connecticut – I appreciate the special moments we have shared that can only come through the creation of something special. I greatly appreciate the tutelage, understanding, and guidance of Alan Ettinger, Paul Merrill, Joel Larue-Smith, Scott Aruda, René McLean and the great people at the Artists Collective, and many others.

I am forever grateful to my family. I must acknowledge my brother for being someone I can truly look up to and talk to every day, and my parents, for showing me how to do things the right way and for working too hard to make sure we never went without. I appreciate my grandparents for unlimited love, inspiration, and canoe rides, and my extended family for consistently and unabashedly holding it down. Thanks to the Muzzulins for accepting me as part of the family. To Samantha, I thank you for being the best anyone could possibly ask for and I look forward to the rest of our lives together.

TABLE OF CONTENTS

PREFACE

Mudstones, commonly known as shales or mudrocks, represent approximately 50% of all sedimentary rocks (Boggs, 1995); however, most scientists would agree that the study of mudstone deposition is not the most glamorous branch of earth science. When combining the high degree of commonality with an average grain size which is invisible to the naked eye, it is not hard to see that the allure of mudstone research does not originate from the same place as the imposing ostentation of fiery eruptions or Earth-shaking tectonic perturbations. To appreciate mudstone research, one must appreciate the understated. While it is true that by definition the bulk of these rocks consists of incredibly small particles, and that the color palette of these rocks often does not deviate far from the grey scale, it is also true that what may seem like a slight change to one of these parameters may be a result of a drastic environmental shift in the paleodepositional system. In these rocks, very small packages of sediment may represent geologically extensive periods of time. Chemical changes in the water column which had catastrophic consequences for all life in the system may be manifested in hand sample by little more than a color change from dark grey to black. Neighboring individual grains which are indistinguishable to the naked eye may demonstrate disparate mechanical behaviors, and together they combine to form one material with its own distinct mechanical characteristics. Within mudstone research, the art of interpreting subtly expressed changes is crucial.

This work aims to document the extent to which these physical and chemical changes occur within one particular formation, across a variety of length scales within a similar basinal

setting. Rocks are placed into facies based upon physical properties (Chapter 1), the chemical signatures of these facies are studied in order to further characterize the paleodepositional system (Chapter 2), and the relationship between facies changes and constituent grain-scale mechanical properties is examined (Chapter 3). By analyzing multiple aspects of the mudstone system in detail within this formation, a clearer picture can be developed regarding often subtly-expressed changes in the depositional history, as well as the effects of geologic change on mechanical behavior in the present day.

A variety of visual, geochemical, and mechanical testing methods are utilized to describe this change spatially, to develop an understanding of the drivers of paleo-environmental change, and to explore how the modern Earth system is being affected as a result.

CHAPTER ONE

High-Resolution Facies Variability in the Union Springs Formation of Central New York

The Marcellus Subgroup (Ver Straeten & Brett, 2006) exists at the base of the Hamilton Group of the Appalachian Basin. It underlies seven states in the Eastern United States, with a thickness that ranges from 0 meters to roughly 580 meters within the basin (Ver Straeten et al., 1994). Within the past decade, the Marcellus has been utilized extensively as a hydrocarbon resource, and currently produces significant quantities of natural gas. With this production came a spike in geological research regarding the formation, building upon a sizable body of research conducted on the Marcellus for many decades. Recent studies such as Ver Straeten et al. (1994), Brett and Baird (1996), Werne et al. (2002), Sageman et al. (2003), Boyer et al. (2011), Brett et al. (2011), Ver Straeten et al. (2011b), Karaca (2012), Lash & Blood (2014), and others set a foundation for this project, which aims to document small-scale facies changes across length scales within the Union Springs Formation of the Marcellus Subgroup.

Facies analysis is a key tool for understanding paleodepositional change across time and space. Refining the facies characterization of the Union Springs Formation provides knowledge relevant to understanding variability in the depositional environments of the middle Devonian Appalachian Basin, in addition to knowledge of variability of properties relevant to the formation's success as a hydrocarbon resource, such as organic richness and mechanical properties information. This study describes the distribution and arrangement of facies in the

Union Springs Formation of the Marcellus shale within the northern portion of the Appalachian Basin.

A facies is a unit of rock which has a characteristic set of recognizable properties which are a result of its deposition in a particular environment (Boggs, 1995). In this analysis, rocks with similar primary depositional features are placed into categories called lithofacies groups and then further subdivided into more specific categories called microfacies, based on more subtle changes in lithologic properties. Facies definitions generally consider features which are interpreted to reflect the primary Union Springs depositional system, rather than changes which may have occurred post-deposition or post-lithification. These primary features include mineralogic distribution, organic carbon abundance, fossil appearance, and bedding characteristics.

By working toward a rigorous data set for the degree, scale, and frequency of variability in the Union Springs, a conceptual framework can be established in order to guide the modelling of physical and mechanical properties across the formation. Additionally, the comprehensive cross-scale description of facies variability based upon petrography is useful for testing of the validity of paleodepositional interpretations based upon geochemical data from mudstones. Chapter 2 of this study pairs the facies observations made here with geochemical characterization made at the same scale.

Stratigraphic and Geologic Setting

The Marcellus Subgroup forms the base of the Hamilton group, and is comprised of three formations in New York: the Union Springs, the Oatka Creek, and the Mount Marion. In

the study area, the Union Springs is present in its entirety, located above the Seneca member of the Onondaga Formation and below a partial section of the Oatka Creek Formation.

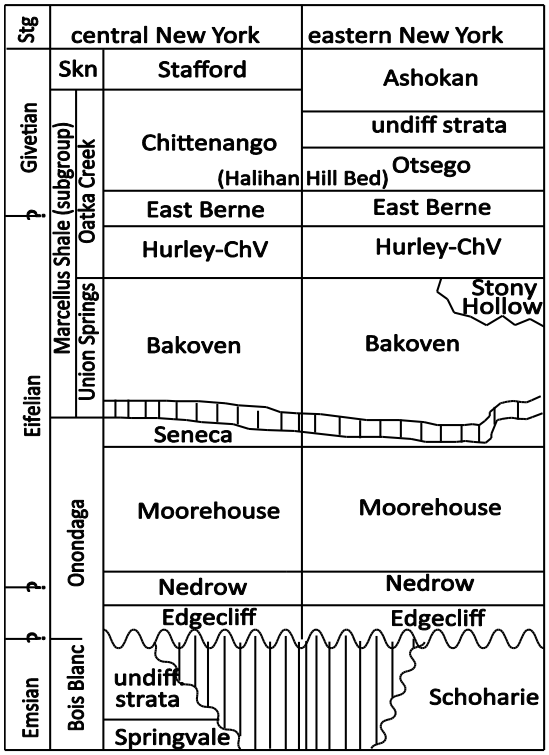

Figure 1: Regional middle Devonian stratigraphy, modified from Brett et al. (2011).

Deposition of the Union Springs occurred in the middle Devonian Acadian foreland basin at roughly 30˚S latitude (Scotese & McKerrow, 1990), as a new pulse of Acadian mountain building activity (Tectophase II of Ettensohn, 1985) led to renewed subsidence and terrigenous deposition within the basin (Ver Straeten, 2010). As the basin subsided and eustatic sea level rose (Brett et al. 2011), sediment was shed off of the Acadian Highlands and delivered to the basin via the Catskill delta complex to the southeast of the study area (Ettensohn, 1985).

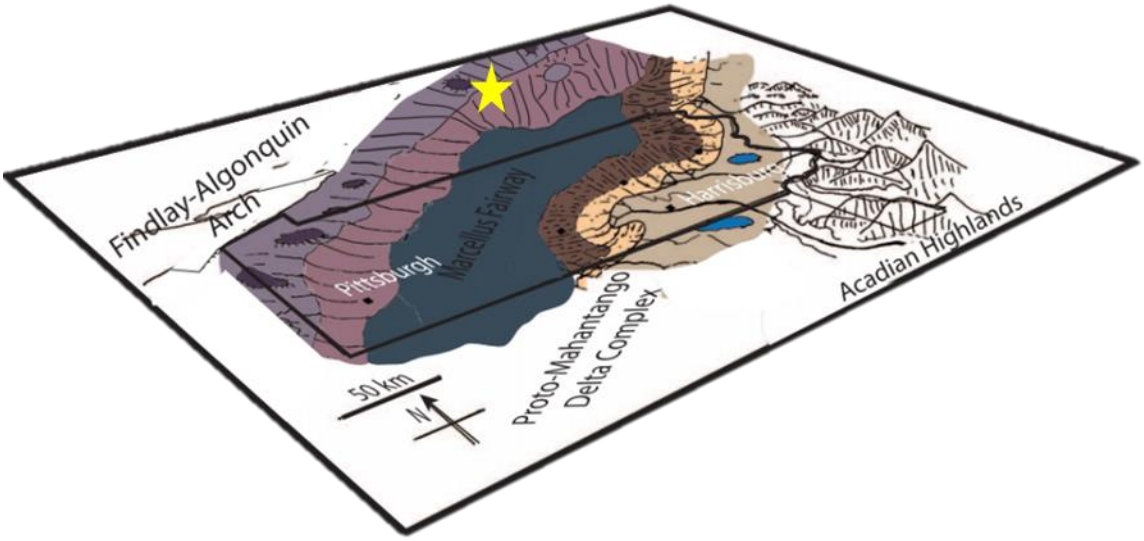

Figure 2: Paleogeographic reconstruction of the Eifelian Acadian foreland basin depositional system from Kohl (2014). Approximate location of study area indicated by yellow star.

The asymmetric distribution of accommodation space in the Acadian Basin, a result of crustal loading (Jordan, 1981), led to an uneven distribution of sediments during Union Springs time. Modern thicknesses of the Union Springs member are as high as 180 m in New York, and consist of black mudstones and calcareous mudstones and sandstones in the most proximal regions of the basin (Ver Straeten and Brett, 2006). The area examined in this study contains highly condensed strata within a distal setting (Figure 2). Thicknesses of Union Springs studied here range between 3.22 and 3.90 meters.

Method

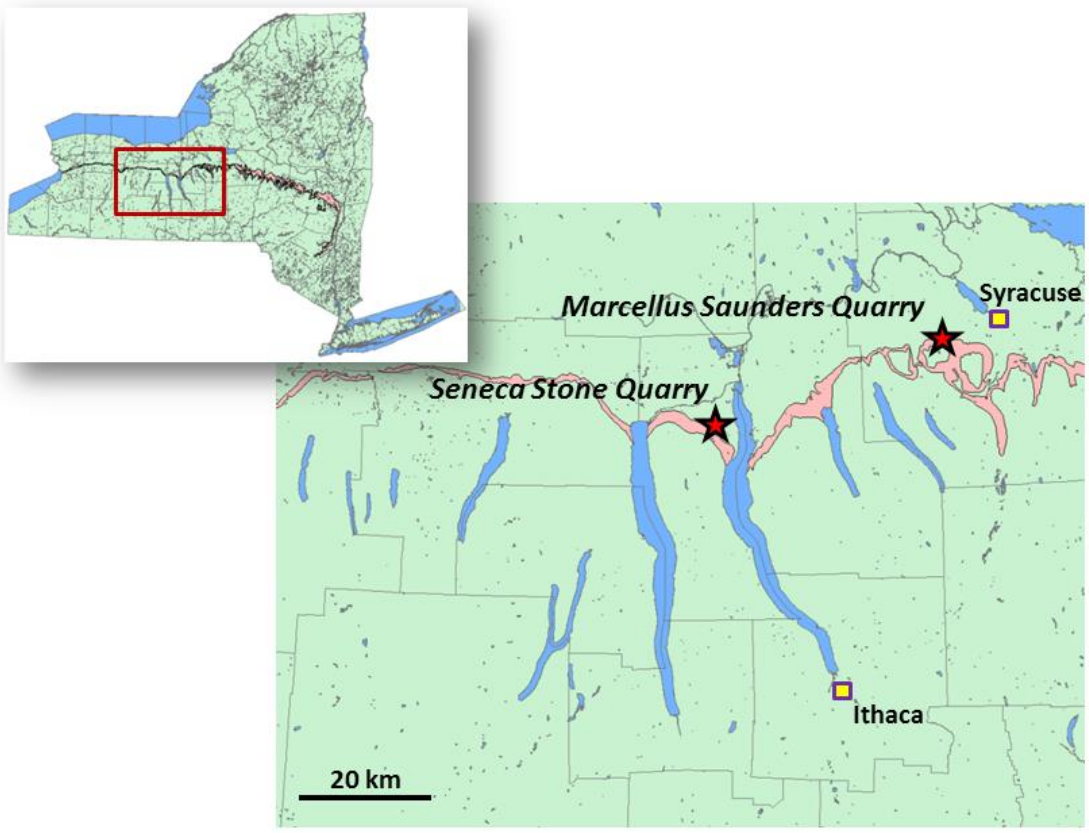

Figure 3: Study area in Finger Lakes region of central New York. Marcellus outcrop belt demarcated in red. Studied columns of Union Springs Formation are marked with red stars. Studied location with respect to New York State at top left

Complete stratigraphic sections of Union Springs Formation (Bakoven Member) were investigated at quarries in Seneca Falls, NY (Seneca Stone Corporation) and Marcellus, NY (Saunders Concrete). The field sites are active quarry operations which facilitated the preparation, measurement, description, and sampling of three sections of fresh quarry outcrop. Two sections located roughly 600 meters apart were described at the Seneca Falls field site. These sections, named *Seneca North* and *Seneca South,* were located along the northwestern and southern edges of the quarry, respectively. The *Seneca North* outcrop sits roughly 60

meters from the location described by Karaca (2012), which serves as a point of reference for this study. The Marcellus, NY outcrop is located 38.6 kilometers northeast of the *Seneca South* Section. *Seneca North* measured 3.87 m in thickness, while *Seneca South* measured 3.74 m. Across the Seneca Falls, NY field site, Union Springs thickness was found to be between 3.74 and 3.90 meters in thickness. The *Marcellus Saunders* section at the Marcellus, NY field site measures 3.22 meters in thickness.

Figure 4: Study site at the North Wall of the Seneca Stone Quarry near Seneca Falls, NY. Staff (center) sits at the Union Springs-Onondaga Formation contact and measures 1.5 meters long.

At each column location, sampling of the described sections was conducted to ensure that no more than 10 centimeters of stratigraphic thickness went unrepresented in the sample set, with additional sampling within stratigraphic ranges containing apparent sedimentological change. Outcrop samples were chosen to maximize the amount of material collected which extended several centimeters back from the exposed rock face, and areas with apparent weathering effects, such as along open fracture faces, were avoided. In collaboration with

researchers at the University of Oklahoma, a gamma ray profile was generated via measurements taken every ten centimeters along the face of the *Seneca North* section with a handheld gamma ray spectrometer.

Thin sections were prepared from the 106 samples collected across the study area, and petrographic analysis was conducted using Leitz Laborlux 12POL and Nikon Optiphot-Pol petrographic microscopes. Supplemental microscopy was obtained using a TESCAN Mira3 electron microscope. Based on observed physical properties, samples were classified into facies, representing groups of rocks with similar observed depositional properties. Broad lithofacies groups were identified within the study area. These facies groups were further divided into microfacies based upon higher-order visually identifiable differences in mineralogic content, bedding character, and fossil content.

Although numerous factors define each identified microfacies, the naming convention primarily refers to compositional features. Some microfacies names also include information to distinguish important textural features such as grain size or zonation within concretions. This naming convention, which utilizes concepts from Macquaker & Adams (2003) and Lazar et al. (2015), is used for all microfacies with the exception of those in the Limestone lithofacies group, which are named using the Dunham (1962) classification. Bioturbation was assessed using the Droser-Bottjer (1986) bioturbation index (Figure 5), assigning indices between 1 and 6 to each sample, with an index of 1 representing undisturbed bedding, and an index of 6 representing total bedding homogenization.

Within sequence stratigraphic analysis, the vertical succession of facies within a section was utilized as the primary means of identification of marine flooding surfaces and the differentiation of parasequences. In order to refine sequence stratigraphic interpretations, facies successions were examined alongside available gamma log data for the *Seneca North* outcrop.

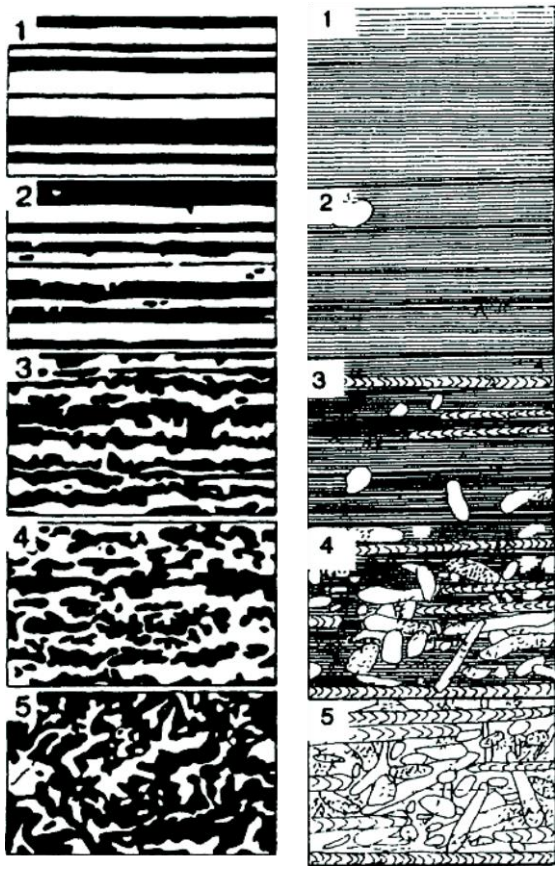

Figure 5: Bioturbation index illustrating ichnofabrics for shelf (left) and deep marine sediments. Adapted from Droser and Bottjer (1993).

Results

Lithofacies Overview

Of the three identified lithofacies groups, Carbonaceous Mudstones are most abundant at each location, with lesser amounts of the Limestone and Calcareous Concretion groups (Table 1). The Limestone lithofacies is comprised of four microfacies, and occurs near the base of the Union Springs Formation throughout the field area. This group of packstones and wackestones is rich in skeletal material and generally significantly bioturbated. At least two intervals bear abundant horizontal fodichnia as well as bone-debris. Limestone microfacies at each field site are generally consistent with regard to their fossil fauna constituents, however the faunal assemblages differ between quarries. Minor (>2 cm) interbeds dominated by clay and organic carbon occasionally interrupt these facies, and stand in contrast to the surrounding calcite-dominated rock. Overall, grain size within this lithofacies decreases upsection [in agreement with Karaca (2012)]; however, calcite remains the dominant mineral constituent.

The Carbonaceous Mudstone lithofacies is composed of nine microfacies. Clay-sized grains are most abundant within this lithofacies group, however its constituent microfacies encompass a range of compositions. This includes microfacies dominated by clay and organic matter as well as microfacies with abundant calcite silt. Compacted *Tasmanites* cysts contribute the bulk of the organic matter, and are variably distributed. Organic-rich veins make additional significant contributions to organic carbon content in some microfacies. Dacryoconarids are the most commonly-observed fauna; bivalves, ostracods, agglutinated foraminifera and several genera of brachiopods are volumetrically-minor.

The Concretionary Mudstone lithofacies is present in the upper half of the Union Springs Formation and is defined by bedding-displacive nodules comprised largely of calcite. This lithofacies, a result of bacterially-mediated sulfate reduction (Raiswell, 1971; Raiswell, 1976), often exists as a part of beds which pinch and swell, leading to variability in concretion position as one moves horizontally along the rock face. The lack of compaction across this lithofacies indicates that calcite cementation took place very early in diagenesis (Raiswell, 1971). Microfacies within this group are distinguished based upon their composition and their calcite cement texture.

Table 1: Relative abundances of lithofacies groups within the three studied Union Springs columns, given in percentage of total column thickness.

Column Location	Limestone	Carbonaceous Mudstone	Calcareous Concretion
Seneca Falls, NY North	14.8%	59.8%	25.4%
Seneca Falls, NY South	18.8	65.4	15.8
Marcellus, NY	13.7	74.2	12.1

Limestone Lithofacies

Microfacies I: Dacryoconarid Wackestone

Description

Microfacies I, the Dacryoconarid Wackestone, occurs near the base of the Union Springs within both stratigraphic sections studied in Seneca Falls, NY. This microfacies is mud-supported, and calcite is the dominant mineral constituent in the form of silt-sized allomicrite (allochthonous micrite; Flügel, 2010) (Figure 6). However, appreciable amounts of clay, organic matter and phosphatic skeletal material can be found, and occur in their highest abundance mostly in segregated interbeds. Silt-sized dolomite is common within burrow fills and dacryoconarid steinkerns. Partially compacted *Tasmanites* algal cysts are observed but not abundant, and appear replaced by calcite to varying degrees. *Tasmanites* may contain anything from a few 10-micron calcite crystals near the perimeter, to a fully replaced interior with only the organic cyst wall remaining.

Organisms of the order Dacryoconarida (Fisher, 1962) are the dominant fossil taxa. At least three types of dacryoconarids are observed in this microfacies, including members of the genera *Variatellina* and *Striatostyliolina.* Fossil shells of these organisms are present mostly as fragments, although some complete shells are present as well. Occasionally, the conical shells of dacryoconarids appear nested within one another in a telescoping fashion. Dacryoconarid shells appear in various states of recrystallization, from fully micritized to seemingly unaltered. Brachiopod shell debris and ostracod valves are less common.

This facies is moderately to highly bioturbated, and burrow traces are not uncommon. Bedding-parallel *Planolites* burrows are most frequently preserved, and can be identified based upon a change in matrix texture or mineralogy (e.g. pyrite content). One large (11 x 5 mm) highly pyritized burrow was found perpendicular to bedding.

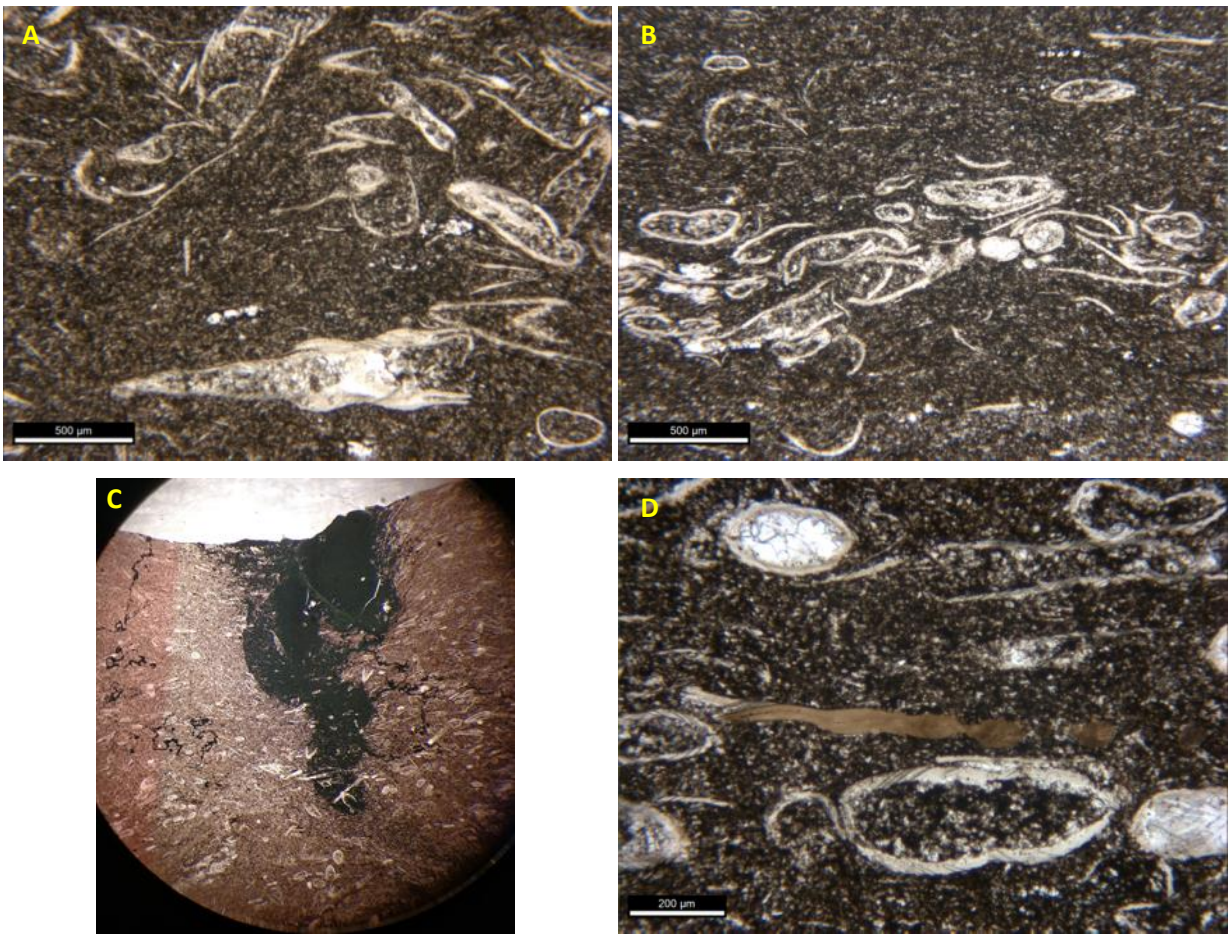

Figure 6: Dacryoconarid Wackestone. Images taken parallel to the original direction of bedding. A,B) Abundant dacryoconarids in transverse and longitudinal orientation. Bedding texture is highly bioturbated but not completely homogenized. 500 µm scale bar. PPL. C) Pyritized burrow crosscutting bedding. Stylolites (left, right) are abundant in this microfacies. 15X magnification. Reflected light. D) The concentration of phosphatic skeletal debris in this microfacies (brown, center) is indicative of a terrigenous-sediment-starved depositional environment. 200 µm scale bar. PPL.

Interpretation

This work agrees with the microfacies interpretations of the same rocks by Karaca (2012) although the naming terminology has been changed. Karaca (2012) designated as Styliolinid Wackestone what is here re-named Dacryoconarid Wackestone. The name change respects the fact that not all dacryoconarid taxa found within this facies belong to the genus *Styliolina*. The classification presented by Dunham (1962) is employed here and for all limestone microfacies.

This facies, comprised of a fine-grained mixture of biogenic and terrigenous sediment, is a result of hemipelagic deposition in a distal outer ramp setting (Flügel, 2004). Terrigenous sediment delivery was sporadic at this location, as indicated by low silt and clay content and the presence of minor bone-rich beds (Ver Straeten et al. 2011).

The highly burrowed and reworked sediment suggests at least partially oxygenated substrate, as does the highly localized concentration of pyrite within a single burrow (Schieber, 2003). Still, there is no evidence of a thriving benthic macrofaunal community within this facies. The observed arrangement of telescoping dacryoconarid shells (Hladil et al., 2014) and minor erosive surfaces at the bases of thin mud-rich interbeds indicates energetic tractive sediment transport processes. Although several types of dacryoconarids are observed, the temporal and depositional significance of the different taxa within this enigmatic planktonic order of organisms has not yet been established in the Union Springs Formation, and their paleoecology is poorly understood (Wittmer and Miller, 2011).

Microfacies II: Dacryoconarid Packstone

Description

Microfacies II, Dacryoconarid Packstone, is found in stratigraphic positions similar to Microfacies I, occupying horizons within the lower 80 cm above the Onondaga-Union Springs contact in Seneca Falls, NY. This facies, often in direct contact with the Dacryoconarid Wackestone, differs from its closely-related neighbor in that it is grain-supported, and calcite is an even more dominant mineral constituent in terms of abundance (Figure 7). Thin (<2 cm), finely laminated clay and organic matter-rich interbeds appear within this facies as well, sitting above scoured surfaces. Approximately 70 cm above the formation base at the Seneca Falls, NY study area, this facies hosts a horizon containing significant amounts of fish teeth and bone debris alongside recrystallized positive-relief bed-parallel burrows (Figure 8).

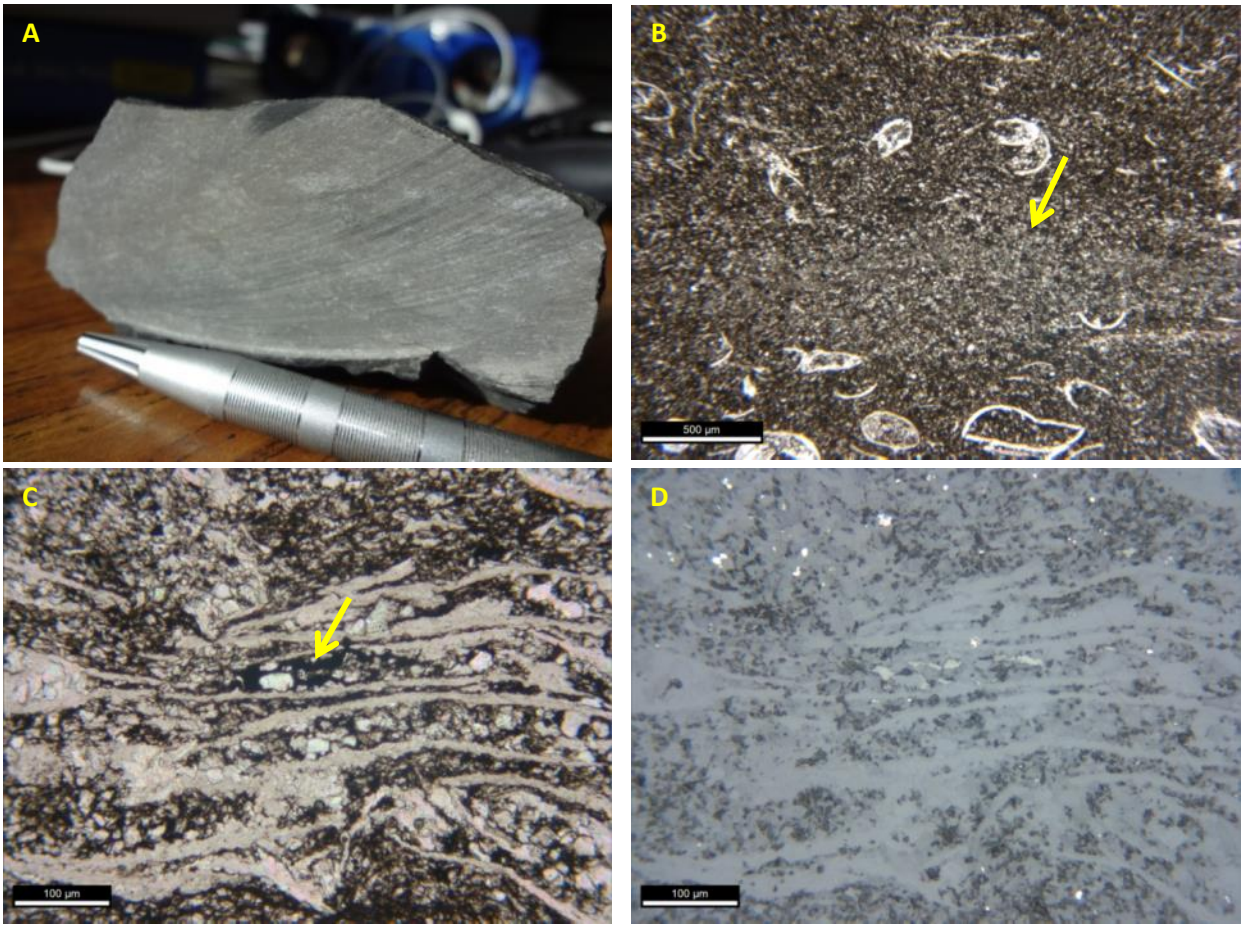

Figure 7 :Microfacies II. Dacryoconarid Packstone. Images taken parallel to the original direction of bedding. A) Hand sample showing mottled appearance and homogenized bedding (note saw striations, which partially obscure the mottling). B) Dacryoconarids are the dominant fauna within this microfacies. Calcite and dolomite-filled burrows such as the one shown here (center, arrow) have a slightly larger average grain size than the bulk rock. 500 µm scale bar. PPL. C) High magnification view of rock texture showing abundant dacryoconarids, silt-sized calcite, and a compacted agglutinated foram (arrow) with associated organic matter, quartz and dolomite. 100 µm scale bar. PPL. D) Reflected light view of [C]. Foram-associated organic matter exhibits moderate reflectance (center). Small subhedral pyrite grains are well-distributed throughout this microfacies (high reflectance). 100 µm scale bar. Reflected light.

Interpretation

The basinal setting for this microfacies is interpreted as similar to that of the Dacryoconarid Wackestone, with a significant change in texture from mud-supported (wackestone) to grain-supported (packstone). Silt-sized calcite and pelagic organisms dominate this facies as well, and the near-total absence of mud within this facies signals an even greater

degree of terrigenous sediment starvation. Surfaces such as the widely-observed bone bed indicate a lengthy time interval with no deposition of terrigenous or carbonate sediment, likely as a result of transgression (Brett, 1996). Apparent erosional surfaces at the base of thin, laminated black mudstone beds are inferred to mark the initiation of isolated sediment transport pulses that provided terrigenous sediment. These mudstone interbeds, which preserve significant amounts of organic carbon, represent the onset of severely oxygen-deprived depositional conditions. Variability in depositional relief or bottom-current activity may have resulted in variable sedimentation or differing amounts of bioturbation, which would lead to changes between wackestone and packstone textures.

Figure 8: *Onychodus* tooth from the most prominent of several bone-rich horizons within the lower Union Springs, approximately 75 centimeters above formation base. These horizons represent periods of depositional hiatus, and can be found across the study area, indicating widespread sediment starvation early in Union Springs depositional time.

Microfacies III: Benthic Wackestone

Description

The Benthic Wackestone facies is a mud-supported fossiliferous limestone with benthic macrofossil debris and trace fossils. This microfacies, found only at the Marcellus, NY study area, shares many traits with the wackestone microfacies in Seneca Falls, from which it is distinguished primarily by its fauna. Articulated brachiopod shells, brachiopod shell debris, echinoderm arm plates and stem fragments, and trilobite carapace fragments are very common (Figure 9). Among microfossils, ostracod valves are found to a lesser degree, while dacryoconarids and agglutinated foraminifera tests are rare. Bioturbation has homogenized the original depositional bedding, and burrows are common and can be recognized by a change in texture.

Calcite is once again the dominant constituent, accompanied by relatively minor amounts of quartz silt, phosphatic skeletal debris, pyrite, and clay minerals within the mud matrix. Little organic carbon occurs in this facies.

Diagenetic effects upon this facies vary slightly between individual samples, but alteration of shell material is generally low to moderate. Micritization is the most common form of bioclast alteration, but pyritization is observed as well. Pyrite is not especially common, but appears mostly as small (10's of microns) post-depositional euhedral crystals scattered throughout the facies, and in framboids and partial shell replacements to a lesser degree. Quartz is frequently seen as a replacement mineral, and appears within crinoid stems and as steinkerns inside brachiopod shells. This facies hosts the most significant observed occurrences

of diagenetic quartz across the studied columns. Stylolites are common within this facies, and evidence of post-depositional mass transfer is present in the form of truncated bioclasts.

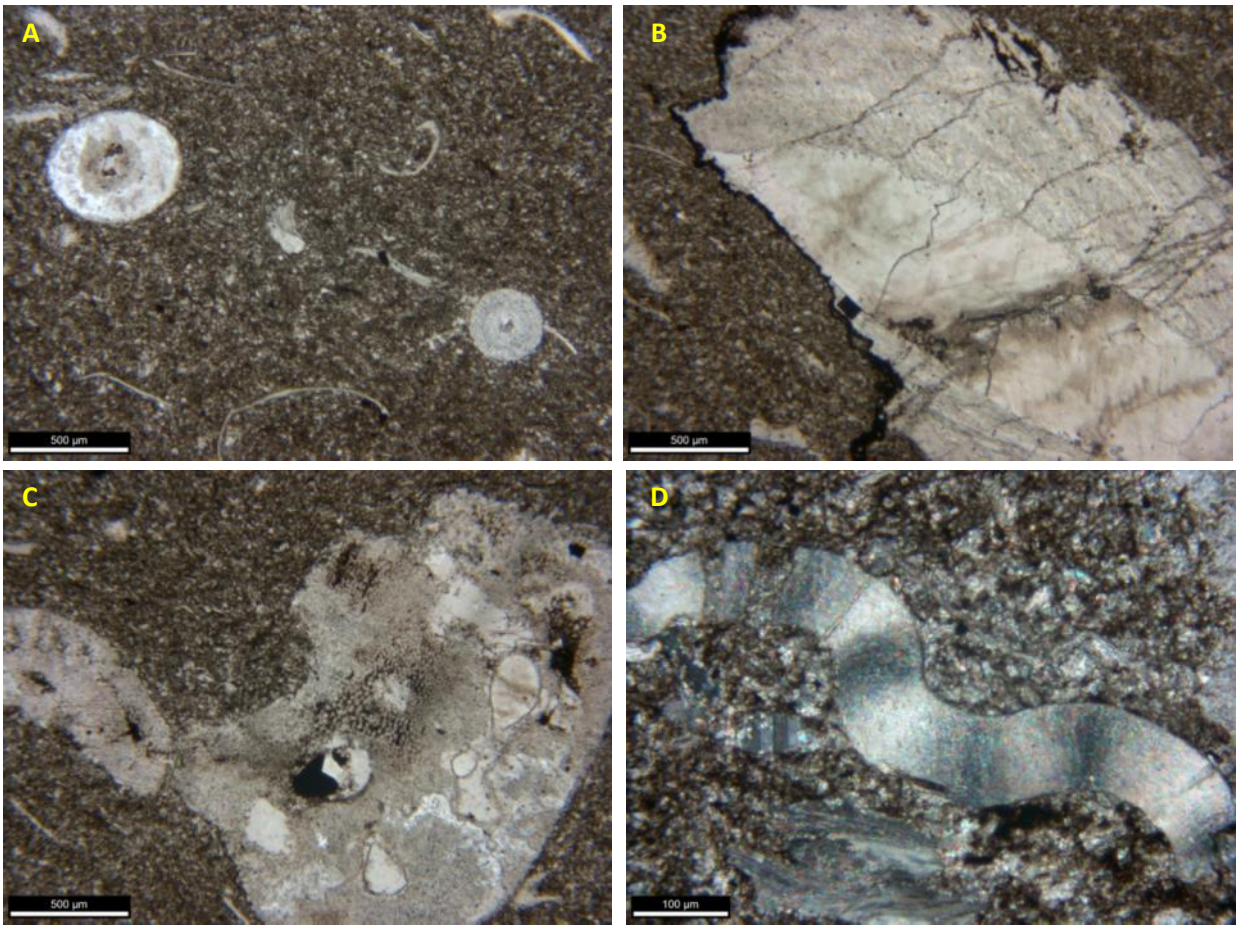

Figure 9: Microfacies III. Benthic Wackestone. Images taken parallel to the original direction of bedding. A) This microfacies is highly bioturbated and contains large amounts of silt size calcite along with fragmented crinoid stems, brachiopods, and bivalves. 500 µm scale bar. PPL. B) Articulated brachiopod shell with quartz steinkern which has been truncated by dissolution. 500 µm scale bar. PPL. C) Echinoderm debris with partial quartz and pyrite replacement. 500 µm scale bar. PPL. D) Disarticulated trilobites and brachiopods are common throughout this microfacies. 100 µm scale bar. XPL.

Interpretation

The Benthic Wackestone is texturally similar to Microfacies I, however the distinct faunal regime observed therein suggests a somewhat different environment. The benthic community at Marcellus, NY, which is not observed at the Seneca Falls field site, is suggestive of

an environment closer to that which existed in the underlying Onondaga Limestone (Brett & Ver Straeten, 1994). Although the tightly-bound nature of fossil material within the rock matrix prevented a positive identification of Onondaga fauna in this facies, the presence of less dysoxia-tolerant trilobites and crinoids along with articulated closed-valve brachiopods infilled with carbonate mud suggests a more oxygenated substrate (Boyer et al., 2009) and episodic in-situ burial (Brett and Baird, 1986; Speyer et al., 1988). The preservation of brachiopods in this state, along with the presence of bone-rich sediment starvation horizons similar to those found in Seneca Falls, NY, suggests infrequent, episodic terrigenous sediment delivery during this time (Brett and Baird, 1996).

Microfacies IV: Benthic Packstone

Description

The Benthic Packstone microfacies is a grain-supported fossil-rich limestone facies positioned just below the Benthic Wackestone (Microfacies III) at the Marcellus, NY field site. Silt-sized biomicrite dominates this facies (Figure 10) which possesses the same faunal assemblage as Microfacies III. Between this facies and Microfacies III, at least 3 species of brachiopods are observed. This facies contains the most intensely bioturbated texture observed in this study, with a complete loss of macroscopic bedding. Long, branching burrows contain a higher proportion of clay minerals and calcite silt with a slightly smaller average grain size, compared to the bulk rock adjacent to these burrows.

Calcite is even more dominant in this microfacies when compared to Microfacies III, and quartz is not seen as a replacement mineral in any capacity. Pyrite is disseminated as euhedral grains less than 50 µm in diameter. A horizon rich in fish teeth and bones is observed within this facies roughly 20 cm above the formation base. Despite the sharing with Dacryoconarid Packstone (Microfacies II) both burrows and skeletal material, the abundance of burrows and skeletal material is less than observed in the Dacryoconarid Packstone (Microfacies II) at the Seneca Falls, NY study location.

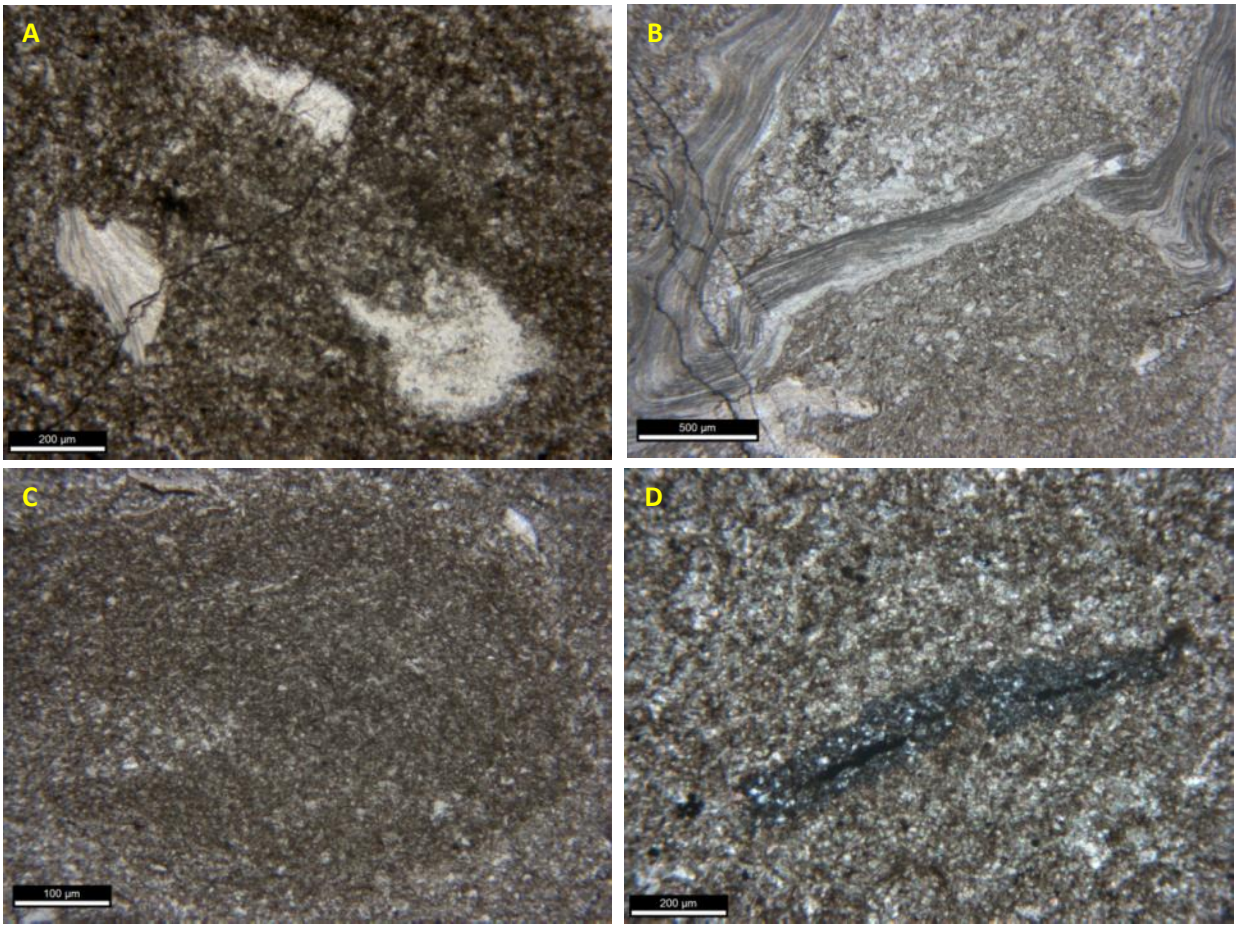

Figure 10: Microfacies IV. Benthic Packstone. Images taken parallel to the original direction of bedding. A) Small brachiopod shell (left) and micritized echinoderm fragments (right) surrounded by silt-sized calcite. Fossil material is prominent throughout this microfacies. 200 µm scale bar. PPL. B) The presence of fully articulated brachiopod shells is suggestive of minimal transport before burial. 500 µm scale bar. PPL. C) Burrows several hundred microns in diameter are especially common, and contain a smaller average grain size when compared to surrounding material. 100 µm scale bar. PPL. D) Photomicrograph showing a compacted agglutinated foraminifera, comprised of fine quartz silt and an organic interior. 200 µm scale bar. XPL.

Interpretation

The depositional environment for the Benthic Packstone is interpreted as similar to that of the Benthic Wackestone (Microfacies III), suited to relatively abundant marine life at or near the time of deposition, but in an even more sediment-starved environment. The carbonate matrix, presence of bone-rich beds, and high degree of bioturbation reflect a distal setting experiencing long gaps between pulses of terrigenous sediment from the paleo-delta complex.

The greatest degree of bioturbation and observed faunal diversity occurs within this facies, suggesting persistently oxygenated conditions in this part of the basin at the time of deposition.

Carbonaceous Mudstone Lithofacies

Microfacies V: Dolomite- and Quartz-Bearing Carbonaceous Mudstone

Description

Microfacies V, the "Dolomite- and Quartz-Bearing Carbonaceous Mudstone" microfacies, is found solely at the Seneca Falls field site, notably in the basal 14 cm above the contact with the underlying Onondaga Formation. This facies is comprised of largely continuous, subplanar beds of alternating composition. At a scale of 2-3 mm, beds alternate between clay-rich horizons, and calcite- and dolomite-bearing horizons. This microfacies (Figure 11) contains the greatest proportion of dolomite relative to the other identified microfacies. Individual laminae are typically hundreds of microns thick, although moderate "burrow-laminated" bioturbation (Schieber, 2003) has led to some degree of intra-bed homogenization. Bioturbation is also present in the form of compacted bedding-parallel burrows, generally filled with pyrite and chalcopyrite, but occasionally dolomite and quartz. Some laminae take on a lenticular morphology and contain relatively higher proportions of quartz silt and calcite which is more coarse than the surrounding material. At the Seneca Falls field site, this microfacies sits in direct contact with the Tioga F K-Bentonite (Ver Straeten, 2004) at the Onondaga Formation-Union Springs Formation contact.

Dacryoconarids are the most common fossil taxon, although scattered brachiopod valves are fairly common. Conodont elements and other phosphatic skeletal debris are relatively enriched within this facies, particularly in laminae two centimeters above the Onondaga-Union Springs contact across the Seneca Falls, NY quarry. Compacted *Tasmanites*

algal cysts are common, and account for the majority of the organic material in the facies. Agglutinated foraminifera occur as well, exhibiting an organic center with a rim comprised of calcite and fine sand-sized quartz.

Diagenesis within this facies is mostly evident in the form of veins. A large vein is observed at the Seneca Falls study area with abundant organic matter at its center and sand-sized calcite spar along the edges (Figure 11D). Additionally, diagenetic feldspar is common within this microfacies. Slickenlines found within this facies occur preferentially in a roughly North-South orientation, and occur just above the Tioga F K-Bentonite. Because the bentonite heavily weathers, it stains the exposed faces (5 to 11 cm thick) of this microfacies.

Interpretation

This Seneca Falls quarry facies, named by Karaca (2012), is differentiated from the other microfacies by both depositional processes and diagenetic conditions. Silty beds, along with lag horizons rich in quartz silt, indicate that at times winnowing and tractive transport mechanisms dominated. This winnowing, along with the presence of phosphatic skeletal material, is a common feature within Appalachian strata near limestone-black shale boundaries, and is associated with transgressions in condensed sections throughout the basin (Ver Straeten et al., 1994; Brett et al., 1996; Ver Straeten, 2007) .

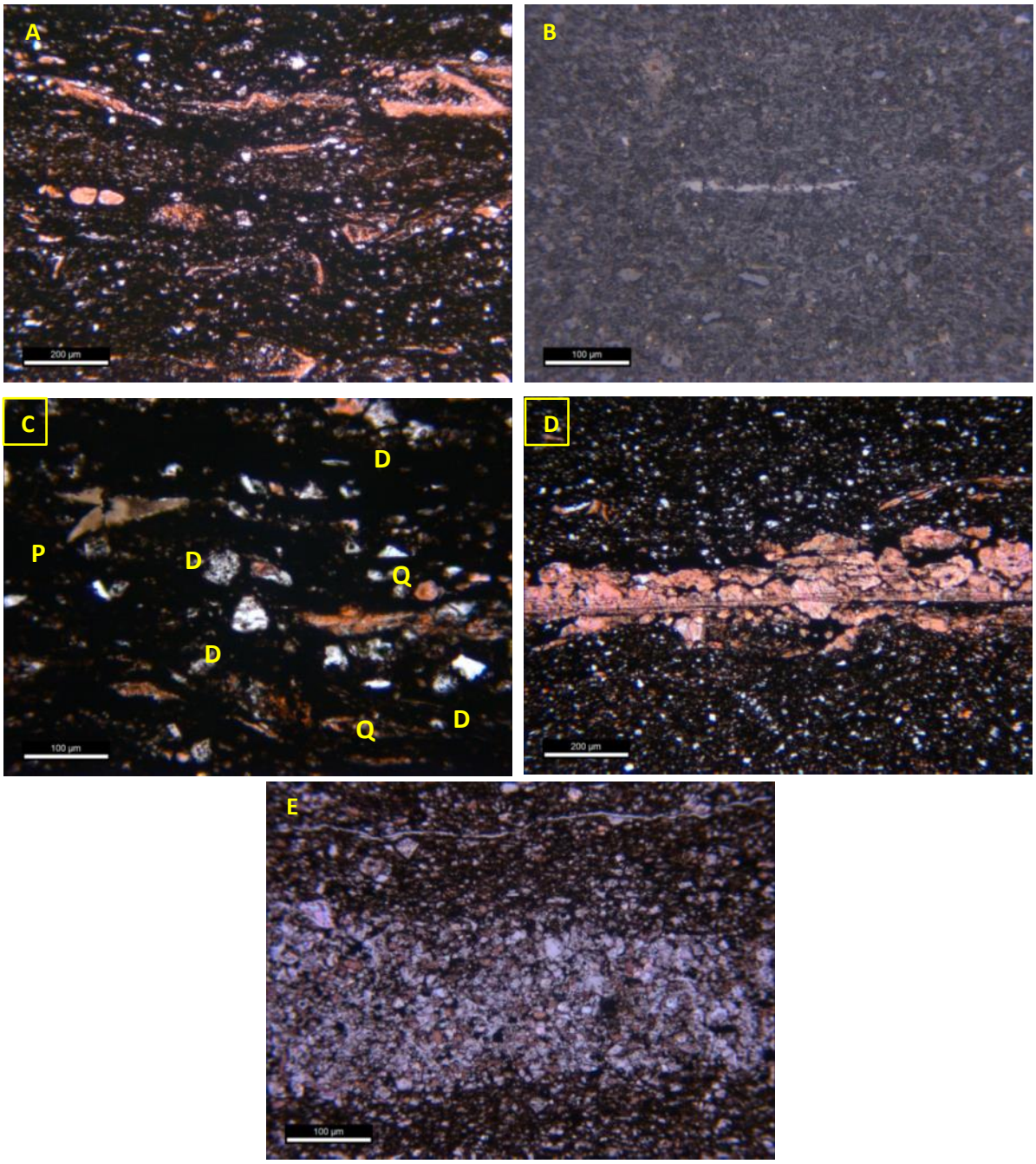

Figure 11: Microfacies V. Dolomite- and Quartz-Bearing Carbonaceous Mudstone. Images taken parallel to the original direction of bedding. A) Photomicrograph of a carbonate stained thin section showing moderately bioturbated texture, and diverse mineralogy of this facies. 500 µm scale bar. PPL. B) Compacted *Tasmanites* algal cysts (center, moderate reflectance) contribute the bulk of the organic enrichment within this facies. 100 µm scale bar. Reflected light. C) Photomicrograph showing high resolution intra-lamination texture including dolomite [D], phosphatic skeletal debris [P], calcite [stained red] and quartz silt [Q]. 100 µm scale bar. PPL. D) Calcite and organic matter filling a continuous vein running parallel to bedding. Although not observed in this photomicrograph, N-S trending slickenlines are observed within this facies near the Union Springs-Onondaga Formation contact, and secondary features such as this may represent horizons which have experienced bed-parallel slip. 200 µm scale bar. Carbonate stain. PPL. E) Bed-parallel burrow containing abundant dolomite, with minor amounts of quartz and calcite. 100 µm scale bar. Carbonate stain. PPL.

Large silt grains associated with organic matter represent the remains of agglutinated foraminifera, confirming that at least some of the quartz present is biologically associated. The preservation of moderate quantities of *Tasmanites* cysts and foraminifera-associated organic carbon within this facies indicate that the environment was at times inhospitable to most marine fauna. Nevertheless, bioturbation, including compacted burrows several millimeters in length throughout many muddier, clay-rich beds indicate that the environment was not persistently hostile.

The appearance of dolomite in this facies is likely associated with ions released during the smectite-illite transition during diagenesis. McHargue and Price (1982) point out that this mechanism of dolomite formation may be especially prominent in areas where clays and carbonates are closely associated. This is the largely the case across much of the Union Springs Formation within the study area, which is bounded by two extensive limestone formations, and routinely contains significant quantities of carbonate material.

Microfacies VI: Clay-Rich Carbonaceous Mudstone

Description

The Clay-Rich Carbonaceous Mudstone is a fine grained, black mudstone enriched in clay and organic matter. This microfacies is found only within the two Seneca Falls sections and is not observed at the Marcellus, NY site.

Clay is the dominant mineral constituent, and clay to medium silt-sized grains comprise the vast majority of this facies (Figure 12). Pyrite, fine quartz silt, organic carbon, and feldspars are less abundant, but common. Calcite, dolomite, and sphalerite are present only in very minor amounts. This is the only facies in the study area in which carbonates are not a significant constituent (~5% by volume); the carbonate which is present is generally of fossil origin in the form of sparse dacryoconarids. Organic matter is quite concentrated in this facies (~15 wt%) (Table 3), and generally appears as highly compacted, bedding-parallel *Tasmanites* algal cysts, and disseminated within the mud "matrix". These cysts are occasionally partially pyritized or filled with sphalerite, although their thin, organic-rich walls are preserved. Pyrite is most commonly found as small framboids, appearing alone and as multi-framboid aggregates. In addition to framboids, subhedral pyrite is present along with lesser amounts of chalcopyrite and sphalerite as burrow fill. Pyrite is commonly found concentrated within individual lamina, and as a replacement mineral within other grains.

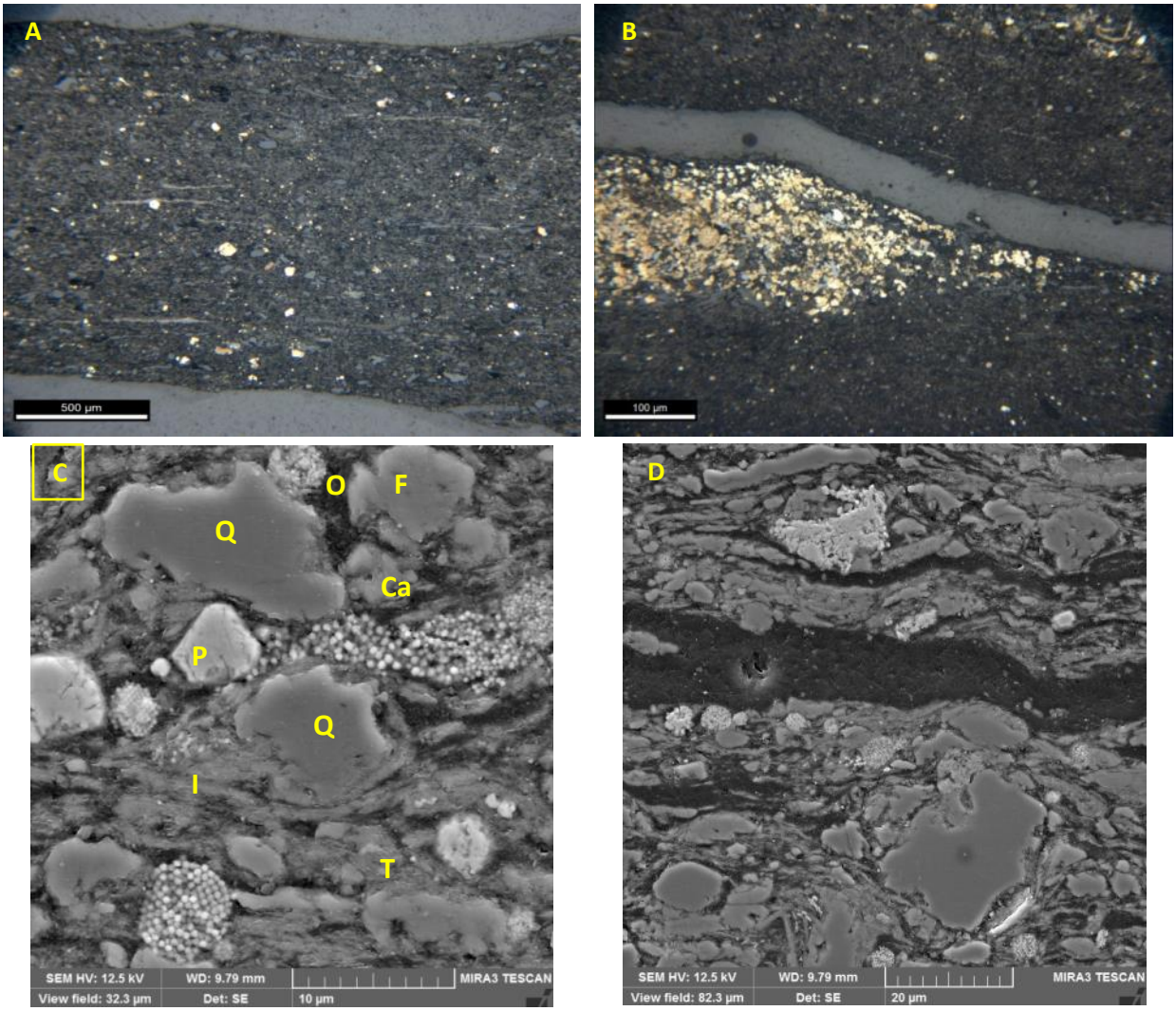

Figure 12: Microfacies VI. Clay-Rich Carbonaceous Mudstone. Images taken parallel to original direction of bedding. A) Reflected light photomicrograph showing planar lamination of mineral constituents. Pyrite (high reflectance) is particularly common within this facies as framboids and subhedral grains, while organic matter is abundant as thin (<10 µm) streaks thought to represent compacted *Tasmanites* cysts (medium reflectance). 500 µm scale bar. Reflected light. B) Pyritized compacted burrow, indicating that anoxia within this facies was not permanent. Here, a parting surface follows the upper contour of the burrow. 100 µm scale bar. Reflected light. C) Secondary electron image showing high resolution texture of Microfacies VI. Quartz (Q), feldspar (F), pyrite (P), titanium oxide (T), illite (I), calcite (Ca) and organic carbon (O) are indicated here. 10 µm scale bar. D) Compacted *Tasmanites* algal cysts (center) supply significant amounts of organic matter to this microfacies. 20 µm scale bar. Secondary electron image.

Bedding within this facies is laterally continuous and planar, with very fine lamination and fissile behavior in hand sample. “Sediment-swimming” bioturbation (Schieber, 2003) is minimal, and lamination is well-preserved, although several pyritized bedding-parallel collapsed burrows are present.

Interpretation

In the Clay-Rich Carbonaceous Mudstone the well-preserved lamination, the absence of "event beds" containing graded silt or the shells of pelagic organisms, and the high concentration of organic matter are indicative of a low energy, oxygen-limited environment at the time of deposition. Sedimentary features indicative of quiescent deposition of fine grained clastic sediment, low amounts of bioturbation, and a high concentration of compacted algal cysts suggests a depositional environment conducive to the preservation of organic matter (Sageman et al. 2003). The occasional presence of pyritized compacted burrows is a testament to the resilience of life, but there is no other sign of a benthic community throughout this facies. Indeed, even pelagic organisms are rarely found within this facies, possibly indicating oxygen-deficient conditions extending well above the sediment-water interface during the time of deposition. The occasional presence of imprints of dacryoconarid shells on bedding plane surfaces suggests that while dacryoconarids were present at least intermittently, pore waters undersaturated with respect to calcium carbonate led to the post-depositional dissolution of their thin calcite shells (Flügel, 2004). However, this opens the possibility that numerous dacryoconarid shells may have been dissolved post-mortem and pre-deposition as they made their way through the water column. This suggests that although anoxia at the sediment-water interface is a strong possibility during the deposition of this facies, a lack of dacryoconarid shell material does not necessitate total water column anoxia.

Both the description and interpretation of this facies match well with that which Karaca (2012) provides for the "*Clay and Organic Rich Laminated Algal Mudstone (MF6)*" in Seneca

Stone Quarry. The position that we document here for the appearance of our Clay-rich Carbonaceous Mudstone is contained within the more vertically-expansive "*MF6*" facies area described by Karaca in the lower half of the Union Springs section. In the Marcellus, NY study area, this facies does not appear. Because there is a significant amount of quartz silt throughout Union Springs depositional time at Marcellus, NY, no intervals fit the definition of Microfacies VI.

Microfacies VII: Clay-Rich Quartz Silt-Bearing Carbonaceous Mudstone

Description

The Clay-Rich Quartz Silt Bearing Carbonaceous Mudstone (Microfacies VII) is an organic matter enriched, finely laminated facies (Figure 13) which appears in all three study locations. The average grain size is somewhat larger in this facies as compared to Microfacies VI, as a result of increased silt content and preserved fossil debris. Clay is the most volumetrically significant constituent in this facies (45-70%), although disseminated fine silt-sized quartz and calcite may mislead one to overestimate clay mineral content in some samples. Quartz in this facies is generally present most commonly as fine to medium silt, although significant amounts of very fine silt/clay size quartz grains exist, as does a much lesser amount of coarse quartz silt. Calcite appears mostly as compacted shell material from dacryoconarids and brachiopods, and silt-sized calcite likely of biogenic origin. Pyrite exists mostly as framboids and subhedral grains generally 10-100 μm in diameter, and is occasionally found concentrated within individual laminations replacing biogenic calcite grains. Compacted *Tasmanites* are again the primary source of organic material, with more minor contributions from macerals inside of shells and between grains within shell-rich beds. Organic matter concentration varies from abundant to modest amounts between samples (~3%-15%) (Table 3). Titanium oxides and dolomite are present in modest amounts.

Bedding is planar to gently wavy, and generally continuous, with occasional discontinuous silt laminae. Within this facies, clay-rich beds occasionally alternate with siltier

beds every 2-4 millimeters. Also repeating as common interbeds are shell-rich beds that often include a higher content of silt-sized particles than average.

Bioturbation is generally low, although isolated bedsets are occasionally altered via "sediment-swimming" bioturbation (Schieber, 2003). Bioturbation indices of 1 or 2 have been assigned for the majority of samples. Fecal pellets appear regularly. Compacted bedding-parallel burrows are often pyritized in this facies. Dacryoconarids appear in continuous "event laminae" as well as scattered solitarily throughout the rock matrix. They generally appear crushed and filled with silt and clay. Thin shelled brachiopods are the next most common fauna and appear highly compacted or broken, usually within brachiopod-enriched laminae.

Diagenetic features include fills of calcite and rarely, pyrite steinkerns, within dacryoconarid shells. Shell condition varies from apparently unaltered, to largely intact with calcite overgrowths, to fully micritized.

Interpretation

Much like Microfacies VI, the high clay content, organic enrichment, low degree of bioturbation, and relatively planar bedding found in this facies are suggestive of deposition in a low-energy, oxygen-stressed environment. However, subtle changes distinguish Microfacies VII from its more clay-rich counterpart (VI). The presence of quartz silt and titanium oxides in addition to clay signals an increase in depositional energy at this point in the basin. The mineralogical profile of this microfacies comes closest to that which might be found comprising significant portions of the Union Springs in more proximal depositional settings (Laughrey et al., 2011). Furthermore, the occasional wavy and erosive laminae signal towards deposition

facilitated by bottom-currents, as opposed to sediment settling resulting from hypopycnal flows or aeolian sediment delivery (Schieber, 2016).

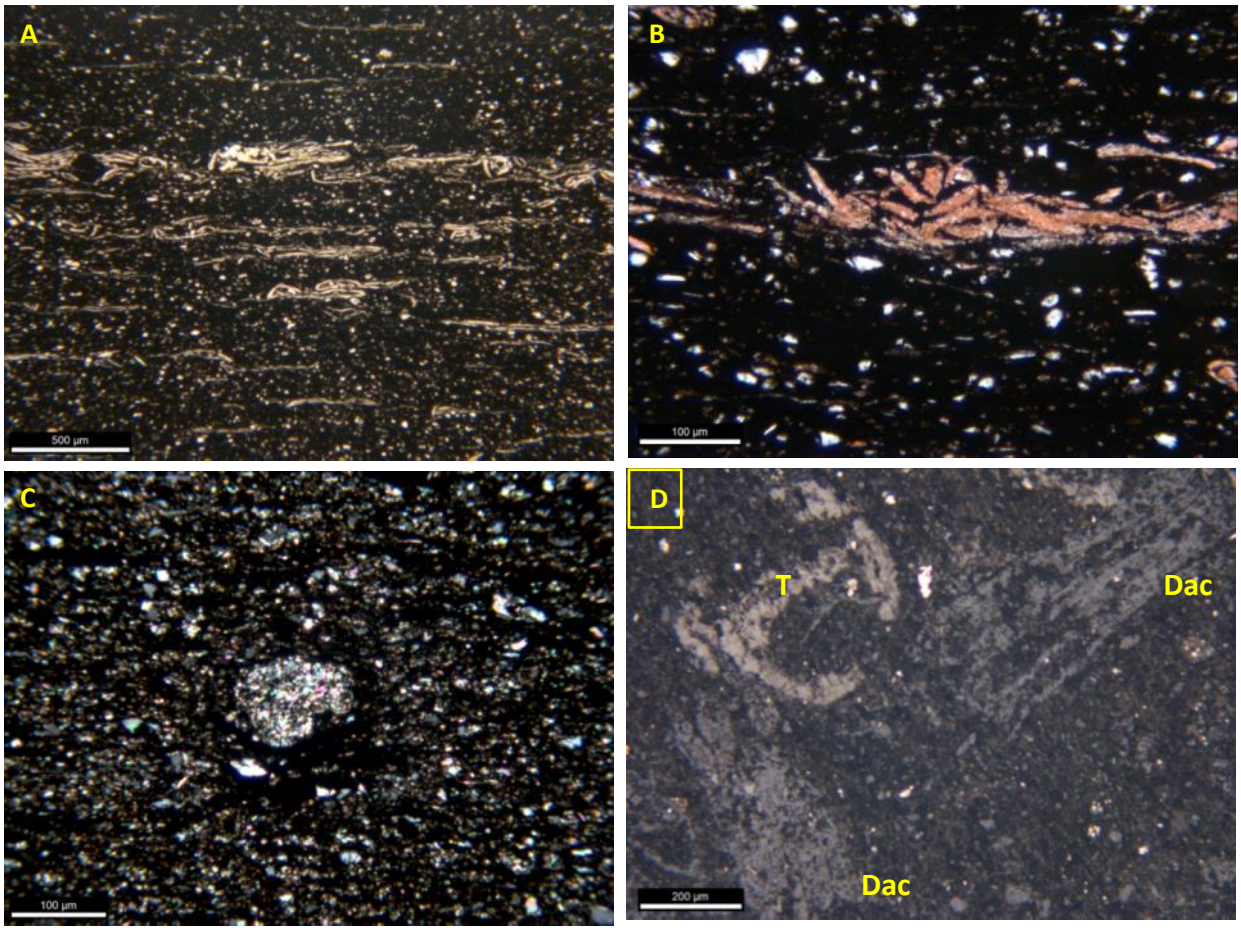

Figure 13: Microfacies VII. Clay-Rich Quartz Silt-Bearing Carbonaceous Mudstone. Images A-C taken parallel to the original direction of bedding. Image D taken perpendicular to the direction of bedding. A) Silt, clay and organic matter are the primary constituents of this facies, along with calcite, largely sourced from dacryoconarids shown here scattered within the rock matrix as well as within a single event lamination. 500 µm scale bar. PPL. B) High magnification view of dacryoconarid shell lamination, surrounded by clay and quartz silt. 100 µm scale bar. Carbonate stain. PPL. C) Fecal pellet (center) associated with organic matter (black, directly beneath pellet). 100 µm scale bar. XPL. D) Bedding plane-perpendicular view showing compacted dacryoconarid tests (Dac) and *Tasmanites* algal cysts (T). 200 µm scale bar. Reflected light.

The depositional environment of Microfacies VII reflects a more benign chemical environment that that of Microfacies VI. Biogenic calcite is significantly more abundant here, largely in the form of fine silt and pelagic fauna. The moderate bioturbation in certain horizons,

and the occasional appearance of small brachiopods and bivalves, indicate that the seafloor experienced some degree of oxygenation at least intermittently. Dacryoconarids in concentrated continuous laminae were likely deposited during single events. Additionally, they commonly appear along bedding planes only as compacted imprints, implying that original shell material has been selectively diagenetically dissolved and mobilized.

There remains uncertainty regarding the primary source of the quartz silt in this facies, and indeed throughout the studied stratigraphic sections in general. Schieber (2009) notes significant accumulations of silt sourced from agglutinated foraminifera in Upper Devonian Eastern North American mudstones. Additionally, Schieber (2000) utilizes scanning electron microscopy with cathodoluminescence (SEM-CL) techniques to show that large amounts of quartz silt within similar Upper Devonian rocks are diagenetic in origin, and outlines morphologic criteria for identifying quartz of this nature using microscopy methods, including embayments and pointed projections on silt grains. Karaca (2012) notes these criteria in samples from within the studied area, and proposes a likely diagenetic origin for the majority of observed quartz throughout the Union Springs Formation.

Although it is certainly possible that biogenic and diagenetic processes contribute significantly to the total abundance of quartz silt observed in this study, caution should be taken regarding these interpretations in the absence of pertinent detailed micropaleontologic and SEM-CL investigations. In the samples observed in this work, morphologically identifiable remains of benthic foraminifera were only rarely observed. Features such as pointed projections on quartz grains resulting from diagenetic overgrowths are certainly noted, but this

is not enough to declare the majority of observed quartz as diagenetic. If 50-100% of observed Union Springs quartz is non-terrigenous, as is the case with the Upper Devonian samples of Schieber (2000), the appearance of quartz silt would have dramatically reduced implications for sequence stratigraphic interpretations. However, throughout Microfacies VII and others, there is a subtle overall increase in quartz grain size moving upsection from the maximum flooding surface (located at 61, 59, and 30 cm above formation base for Seneca North, Seneca South, and Marcellus, NY). Additionally, if quartz silt contained little to no terrigenous signal, it should not possess its observed association with facies which contain other hallmarks of terrigenous input, such as clay-rich, titanium oxide bearing rocks.

It should be noted that the samples of Schieber (2000) were much more quartz-enriched (~40% by volume, as opposed to the 10-20% observed here), and that Schieber (2016) and Schieber and Winsch (2005) show significant accumulations of Appalachian Highlands-sourced metamorphic quartz in the Upper Devonian Illinois basin, many hundreds of kilometers from the source area. The areas analyzed in this study were significantly more source-proximal than the Upper Devonian Illinois Basin, implying that terrigenous quartz should have been able to reach relatively closer areas such as the New York Appalachian Basin locations in this study.

Microfacies VIII: Clay-Rich Calcite Silt-Bearing Carbonaceous Mudstone

Description

The Clay-rich Calcite Silt-Bearing Carbonaceous Mudstone is a mudstone facies found at all three studied columns, and is the most abundant microfacies at the Marcellus, NY location. Similarly to Microfacies VII, this finely laminated microfacies is defined by high amounts of clay minerals and silt-sized grains, although the Clay-rich Calcite Silt-Bearing Carbonaceous Mudstone is distinguished from Microfacies VII because silt-sized calcite is more abundant than quartz silt (Figure 14). Organic matter is relatively abundant and appears as compacted *Tasmanites* cysts, as amorphous macerals, and within shell beds. Pyrite is common in this facies, most commonly as framboids and disseminated euhedral grains roughly 50 μm in diameter, and to a lesser degree replacing shell material and within compacted burrows.

Dacryoconarids are the most common fossil taxa, and appear crushed within shell rich laminations and scattered solitarily throughout the matrix. Bivalve shell debris is rare. Fragmented conodont elements and fecal pellets are relatively common. Bioturbation is generally low throughout this facies.

Microfacies VIII has generally continuous, parallel bedding, which is largely planar, except when distorted by nearby concretionary facies. Compositional segregation is particularly common within this facies at the Marcellus, NY study area, where beds alternate between calcite silt-enriched beds and thinner beds with more abundant clay and quartz silt.

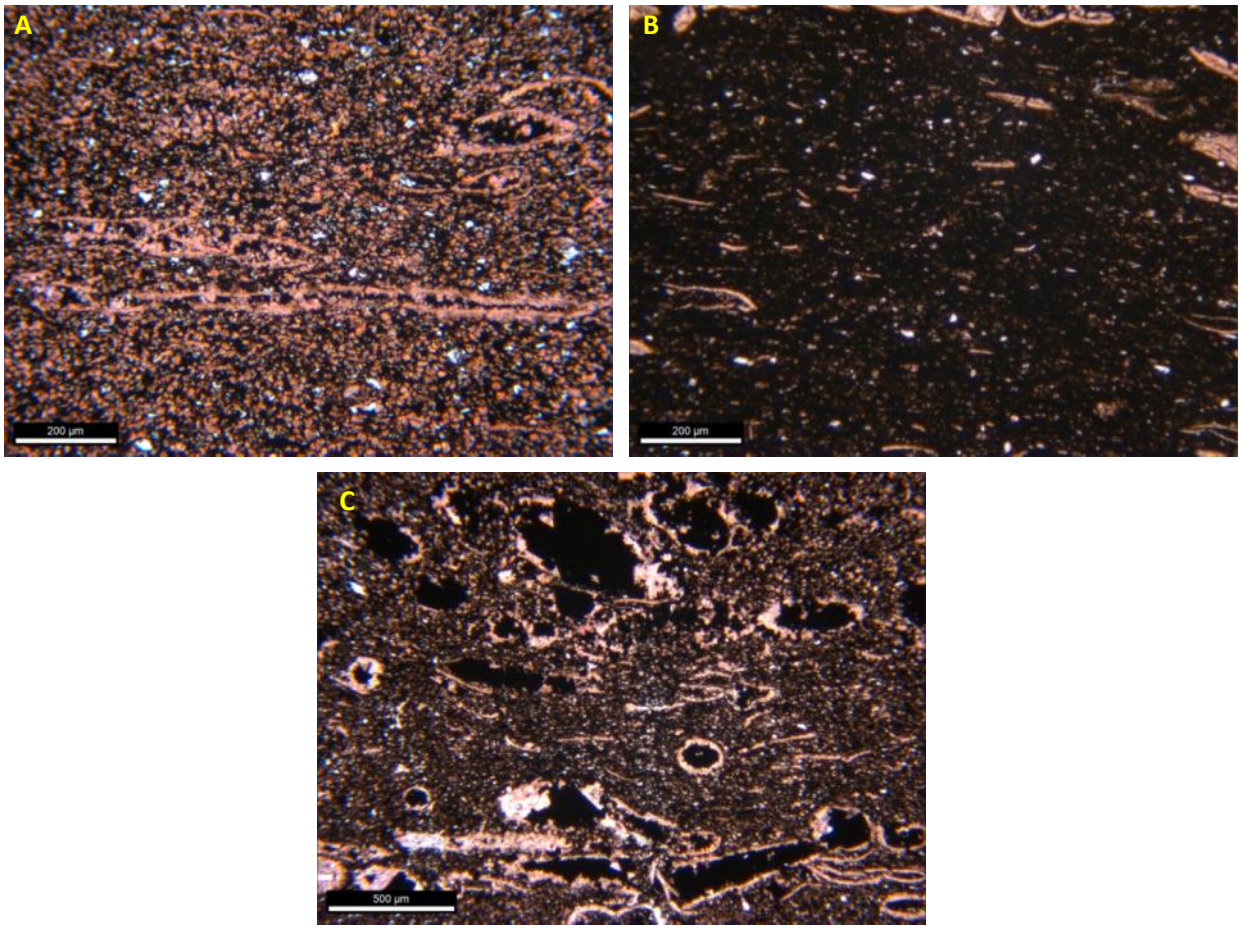

Figure 14: Microfacies VIII. Clay-Rich Calcite Silt-Bearing Carbonaceous Mudstone. Images taken parallel to the original direction of bedding. A) Photomicrograph of carbonate stained section showing abundant calcite as silt-sized grains and compacted dacryoconarids. Non-stained silt-sized grains include medium silt sized quartz and coarse silt sized dolomite. 200 µm scale bar. Carbonate stain. PPL. B) Photomicrograph showing more clay rich region of MF VIII than (A). Carbonate stain. 200 µm scale bar. PPL. C) Pyrite-bearing lamination showing the early infilling of partially compacted dacryoconarid shells. 500 µm scale bar. Carbonate stain. PPL.

Interpretation

The depositional environment of this microfacies is similar to that of Microfacies VII, however the fact that the majority of silt-sized grains are calcite rather than quartz is suggestive of an overall slower rate of terrigenous sedimentation. A higher concentration of fragmented conodont elements and fecal pellets may suggest this as well. The fact that the vast majority of

fossil material in this facies is crushed beyond the point of taxonomic identification points to higher degree of post-mortem tractive transport.

Morphologic evidence including shape and microstructure suggests that significant quantities of calcite silt found in this facies are biogenic in origin. For this reason, if one assumes a relatively constant pelagic faunal abundance throughout the depositional time captured between two adjacent beds within this microfacies, the shift from a clay- and quartz silt-rich composition to a more calcite silt-rich composition may signal a decrease in terrigenous sedimentation. Changes between calcite silt-rich and quartz silt-rich beds imply sedimentation during times (likely of unequal duration) of relatively low and high terrigenous sedimentation, respectively.

Sparse burrows exist throughout this facies, however nothing points to the existence of any particularly established benthic fauna at the time of deposition. This suggests an oxygen-stressed seafloor throughout the majority of Microfacies VIII deposition.

Microfacies IX: Fossil-Bearing Clay-Rich Carbonaceous Mudstone

Description

Microfacies IX is a mudstone facies found in the two studied Seneca Falls, NY columns, with a stratigraphic range in the upper half of the Union Springs. Similar to Microfacies VI, the Fossil-Bearing Clay-Rich Carbonaceous Mudstone is characterized by fine, continuous lamination of clay-rich sediment, low silt content, high organic carbon enrichment, and a general lack of bioturbation (Figure 15).

This facies is distinguished from Microfacies VI as a result of the common occurrence of fossil-rich laminations containing brachiopods and occasionally dacryoconarids and bivalves. Brachiopods tend to occur along bedding planes in densely covered, low-diversity assemblages, while dacryoconarids and bivalves tend to not occur in such high concentrations, and may occasionally be found within a brachiopod-rich horizon. Fossil-rich laminations occur every 0.5 — 3 mm, and are comprised of occasionally articulated brachiopod shell material. Dacryoconarids within shell-rich beds are generally compacted but intact. Pyrite is often found replacing shell material, and as framboids and subhedral grains between 5-30 µm in diameter. Silt is minor, composed more frequently of quartz than calcite.

The absence of this facies from the Marcellus, NY study site is consistent with expectations set by the other microfacies. In general at Marcellus facies are silt-rich, and quartz silt is a relatively more prominent constituent throughout the Marcellus, NY column than in the Seneca Falls, NY sections. Those attributes at Marcellus contrast sharply with Microfacies IX, which thus far has been found only at Seneca Falls quarry.

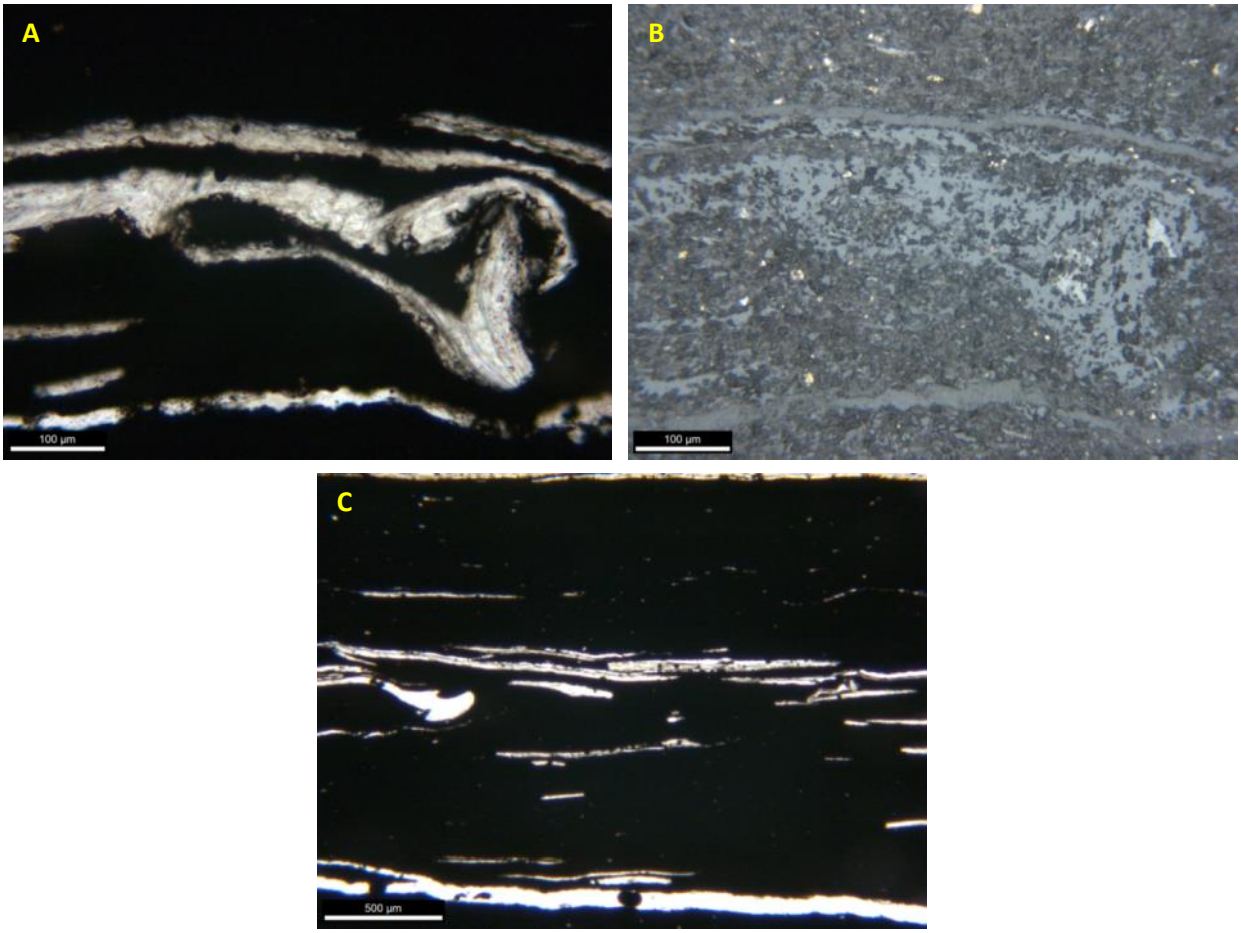

Figure 15: Microfacies IX. Fossil-Bearing Clay-Rich Carbonaceous Mudstone. Images taken parallel to the original direction of bedding. A) High magnification view of brachiopod shell within a shell-rich lamination. 100 µm scale bar. PPL. B) Reflected light view of (A), showing the preservation of organic matter within the shell (at right, medium reflectance). 100 µm scale bar. Reflected light. C) Much like Microfacies VI, clay and organic matter dominate this microfacies. However, this presence of planar laminations with abundant fossil coverage indicates ocean conditions were suitable at times for the establishment of opportunistic, low diversity faunal assemblages. 500 µm scale bar. PPL.

Interpretation

The planar, undisturbed lamination, high organic matter content, and minimal average bioturbation of the Fossil Bearing Clay-Rich Carbonaceous Mudstone indicates deposition within a relatively quiescent oxygen-deprived environment. However, anoxia at the sediment-water interface could not have been a permanent feature, as indicated by the presence of

intermittent horizons rich in benthic *Cherryvalleyrostrum* and *Eumetabolotoechia* brachiopods and *Pterochaenia* bivalves. The fact that these fauna are occasionally found in an articulated state suggests minimal or no transport prior to burial, and the presence and distribution of these low to moderate dysoxia-tolerant organisms is suggestive of modest periodic increases in bottom water oxygenation (Boyer and Droser, 2009). Shell-rich beds of both benthic and pelagic fauna are often found to be associated with elevated levels of intra- and intershell organic matter. In the case of the benthic fauna, this may mark a quick return to oxygen-starved conditions, effectively killing off the benthic community and allowing for the preservation of organic material. In the case of the pelagic fauna, organic matter may be preserved via efficient movement of organic matter within shells from the position in the water column where the organism lived down through the water column into conditions suitable for preservation, such as an anoxic epeiric sea floor (Arndt et al., 2013).

Microfacies X: Interbedded Dacryoconarid-Bearing Calcareous Mudstone

Description

The Interbedded Dacryoconarid-Bearing Calcareous Mudstone appears at each studied location. The stratigraphic range of this facies is narrow at both Seneca Falls field sites, concentrated within ~20 cm vertical range, and positioned above the Limestone facies group roughly one meter from the Union Springs-Onondaga contact. At the Marcellus study location this facies is more widely distributed, appearing near the Union Springs-Onondaga contact, above the Limestone facies group, and stratigraphically higher in the section roughly 2.4 m from the basal contact.

This facies is characterized largely by a distinctive bedding expression, which consists of clay-and silt-rich beds alternating with dacryoconarid shell beds; there is a strong compositional segregation between those two lithologies. Within these dacryoconarid-dominated beds, which make up between one third and one half of this facies by volume, dacryoconarids are joined by calcite cement and minor amounts of quartz silt and dolomite (Figure 16). Two dacryoconarid genera have been identified (*Variatellina; Striatostyliolina*), although fragmented shells are common and hinder taxonomic identification. Faunal diversity is somewhat augmented at the Marcellus, NY study location, where small pterochaenid bivalves and, rarely, crinoid arm plates are observed stratigraphically high in the section (roughly 2.5 meters above formation base). Dacryoconarid shells occur in telescoping “cone-in-cone” arrangements within shell beds.

Clay minerals and quartz silt dominate the muddy beds, which contain organic matter in thin (~20 μm), continuous bedding-parallel laminations. These siliciclastic-dominated beds are

more volumetrically significant at the Marcellus, NY study site, as compared to the Seneca Falls, NY site. Pyrite in these beds is present as framboids and small (<30 µm) subhedral grains.

Compared to the vast majority of other facies observed in this study, bedding thickness is highly variable, and ranges between 0.25 mm and 3.0 mm, with a median thickness of 0.75 mm. Shell laminations are commonly discontinuous, and often exhibit laterally-variable thickness. Wavy lamination is common, and shell beds occasionally scour underlying muddy laminae.

Calcite cementation of shell beds is common but not all-inclusive; some single beds are largely uncemented, while containing smaller, cemented shell intraclasts containing multiple shell fragments. Calcite and sphalerite commonly fill dacryoconarid shells, often simultaneously (Figure 16). Silt-sized rhombohedral dolomite appears occasionally, and pyrite within shell beds is largely euhedral and 10's to 100's of microns in diameter. A minor amount of chalcopyrite is present as well.

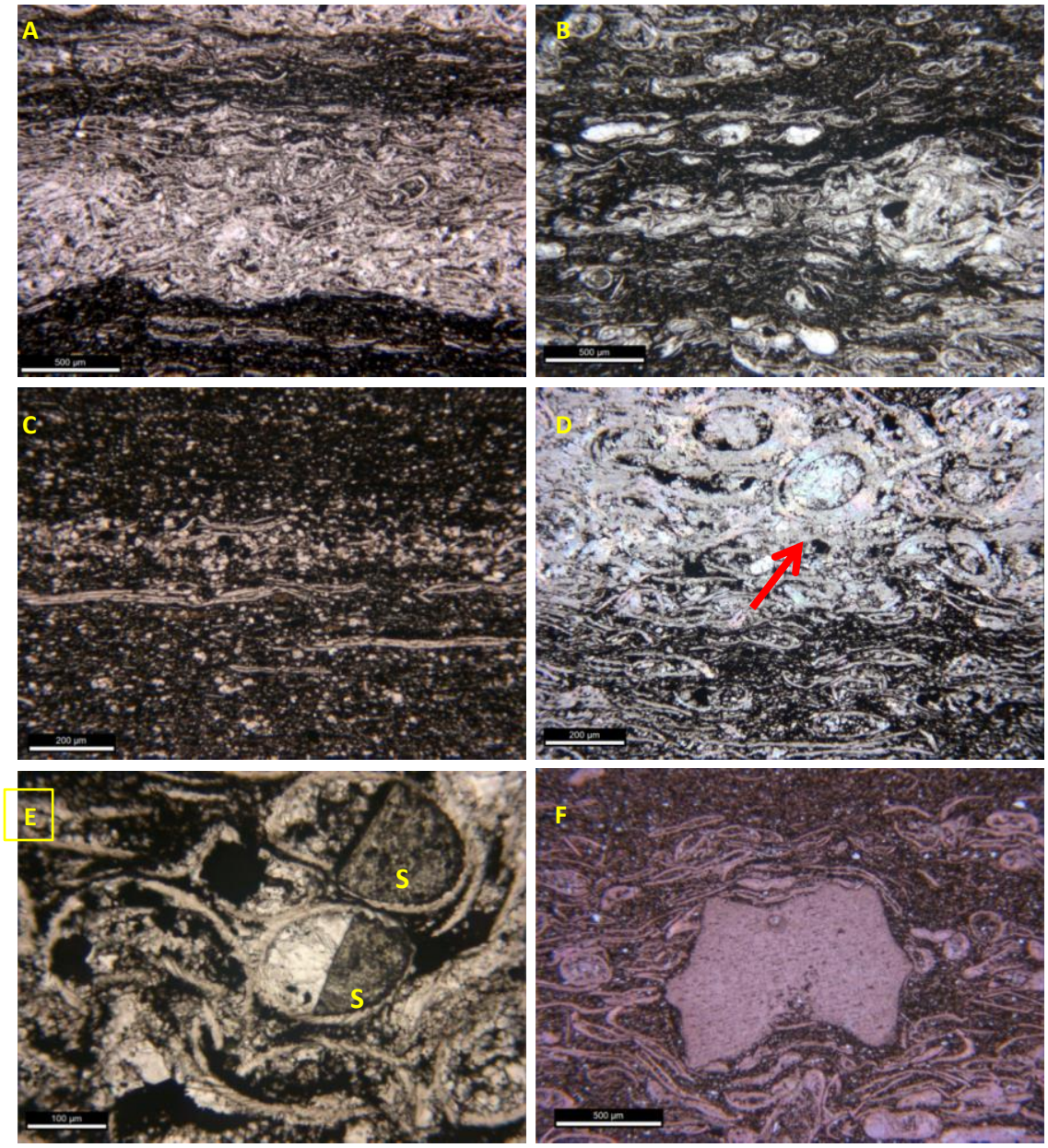

Figure 16: Microfacies X. Interbedded Dacryoconarid-Bearing Calcareous Mudstone. Images taken parallel to the original direction of bedding. A) Bedding size and composition is highly variable. Note the erosive contact at the lower bound of the shell rich bed indicative of storm-driven shell deposition. 500 µm scale bar. PPL. B) Wavy bedding with variable thickness and continuity is common. 200 µm scale bar. PPL. C) Lag deposits of quartz silt, phosphatic debris, and coarse sand sized dacryoconarid shell debris suggestive of current winnowing. 200 µm scale bar. PPL. D) Nested dacryoconarid shells (arrow, transverse view) within shell-dominated beds suggestive of turbulent deposition. 200 µm scale bar. PPL. E) Sphalerite [S] commonly fills dacryoconarid shells, often simultaneously with calcite. Sphalerite may have formed as a result of zinc released from organometallic complexes into sulfate-reducing conditions, or as a result of metals-enriched fluid flow through the shell beds comprised primarily of coarse sand sized allochems. 100 µm scale bar. PPL. F) Echinoderm fragment (center) found ~3/4 of the way upsection at the Marcellus, NY site. Although evidence suggests this allochem was transported from elsewhere in the basin, echinoderms such as this may suggest the onset of Stony Hollow bioevent within the Appalachian Basin. 500 µm scale bar. Carbonate stain. PPL.

Interpretation

This facies is representative of unsteady deposition in relatively energetic conditions. The dacryoconarid shell beds which are a hallmark of this facies are a result of the entrainment, tractive transport and redeposition of sand-sized dacryoconarid shell fragments and cemented shell intraclasts. The existence of high-energy conditions in these beds is supported by the existence of telescoping dacryoconarid shells (Hladil, 2014), rippled laminae, and the presence of crinoid fragments in a Marcellus, NY sample. Crinoids are abundant in the oxic Benthic Packstone and Benthic Wackestone facies (Microfacies III and IV), but are not observed in any other microfacies in the Carbonaceous Mudstone group, which are significantly less bioturbated and contain a limited benthic community. It is likely that these crinoid bioclasts were transported from a relatively basin-marginal, oxygen-enriched position by an energetic current. The presence of this taxon high within the Bakoven member of the Union Springs is atypical, and further study is required to determine if it represents the incursion of the extrabasinal Stony Hollow bioevent fauna (Desantis and Brett, 2011). Making this determination is dependent on both a more precise taxonomic identification, and the geographical origin of the bioclast, as it appears in a bed indicating relatively high-energy transport.

Current-driven deposition is not relegated solely to the shell beds in this facies. Grading within silt and clay-rich beds (as shown in Karaca, 2012) as well as silt lag laminations and erosive surfaces point to relatively high-energy conditions transporting and delivering sediment within the Microfacies X paleoenvironment. Both the muddy beds, as well as the shell-rich

beds, are interpreted as a result of turbulent current deposition. The bimodal composition, and compositional segregation of this facies, may indicate two sediment source areas. For example, the terrigenous mud may be derived from the delta at the proximal edge of the foreland basin, and the biogenic calcite may be derived from currents driven by strong storms carrying accumulated shell debris from the basin flank. Alternatively, if the sediment transport direction strictly carried material basinward from the proximal edge, the shell accumulations could represent geologically brief periods of sediment starvation in this distal basin location. Due to the occurrence of this facies well into the regressive sequence (Ver Straeten, 2007) at Marcellus, NY, during a time of increasing terrigenous sediment abundance and grain size, the former interpretation is preferred.

Laterally continuous, draping, kerogen-bearing laminations within this facies are interpreted as the remnants of benthic microbial mats, after Schieber (1986). These organisms require periods of low sediment input to survive, and imply that laminations in which they appear contrast with much of the remainder of this facies in that they represent quiescent conditions. The partial establishment of these microbial mats across a bedding surface, and the subsequent coverage by draping terrigenous mud layers, followed by the re-establishment of another microbial mat horizon leads to the appearance of “false cross-lamination”, as a result of the apparent bed-truncation which occurs at the confluence of microbial mat horizons (Schieber, 1986).

Microfacies XI: Interbedded Dacryoconarid-Rich Calcareous Mudstone

Description

Microfacies XI shares many similarities with Microfacies X (Interbedded Dacryoconarid-Bearing Calcareous Mudstone), however dacryoconarid shell beds comprise more than 50% of the bulk rock volume. Shell beds contain almost exclusively dacryoconarid shells, kerogen, and calcite cement, which is more pervasive in the shell beds of this facies (Figure 17) as compared to those of Microfacies X. Quartz silt is not abundant within this facies.

With the exception of one heavily pyritized clay-rich bed, pyrite comprises roughly 1% of this microfacies. Pyrite appears occasionally as framboids and more often as subhedral grains as large as 100 µm in diameter. Sphalerite is commonly found within shell beds, largely within the shells of dacryoconarids. Chalcopyrite is rare. Organic carbon is abundant within this facies, and is found within laminations at both ends of the compositional spectrum. A large percentage of observed organic carbon within this facies is found in veins, which are generally oriented oblique to bedding in shell-rich beds and sub-parallel to bedding in mud rich beds. Organic carbon also appears in grainstone beds between and within dacryoconarid shells.

This facies contains the most variable bedding thickness of any of the identified non-concretionary microfacies, with muddy beds ranging in thickness between 0.2 and 2 mm, and shell beds range in thickness between 1 and 5 mm. Bedding is largely wavy and continuous, although it is not uncommon to observe single shell laminations which are discontinuous or possess variable thickness.

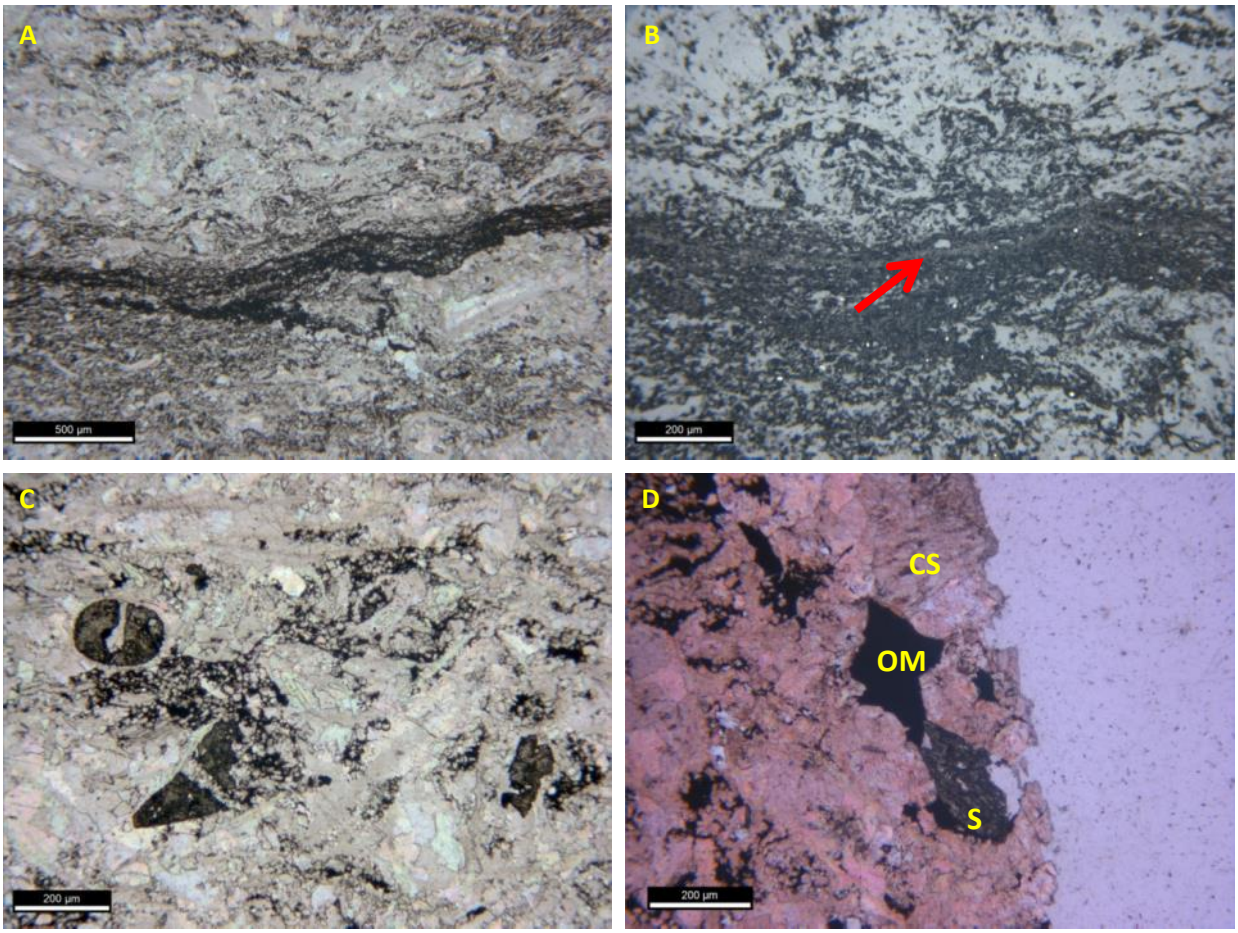

Figure 17: Microfacies XI. Interbedded Dacryoconarid-Rich Calcareous Mudstone. Images taken parallel to the original direction of bedding. A) Characteristically diverse bedding texture shows mostly cemented (top) and mostly uncemented (bottom) shell beds, separated by a clay- and organic-rich muddy bed. 500 µm scale bar. PPL. B) Reflected light view of A), showing wavy, continuous organic lamination within mud-rich bed. This is interpreted as the result of microbial mat formation during a period of low sedimentation rate. 500 µm scale bar. Reflected light. C) Calcite occasionally cross-cuts sphalerite within shells in cemented beds, indicating a later formation of calcite cement relative to the sphalerite steinkerns. 200 µm scale bar. PPL. D) Sphalerite [S] also appears within veins, co-occurring with calcite spar [CS] and organic matter [OM]. These veins crosscut bedding and indicate the emplacement of sphalerite [S] during burial diagenesis. 200 µm scale bar. Carbonate Stain. PPL.

Interpretation

The Interbedded Dacryoconarid-Rich Calcareous Mudstone was likely deposited through relatively energetic processes similar to those leading to Microfacies X, but during times of even less terrigenous input. The position of this facies within all studied columns, not far above the maximum flooding surface across the study area, is consistent with this interpretation. These

largely cemented dacryoconarid beds are likely the result of current redeposition within a sediment-poor environment, implying significant amounts of time-averaging within each bed. The similar positions of this facies in Marcellus, NY and Seneca Falls are likely a result of basin position and sediment source. Storms alternately supplied either terrigeous clay and silt or reworked pelagic organisms.

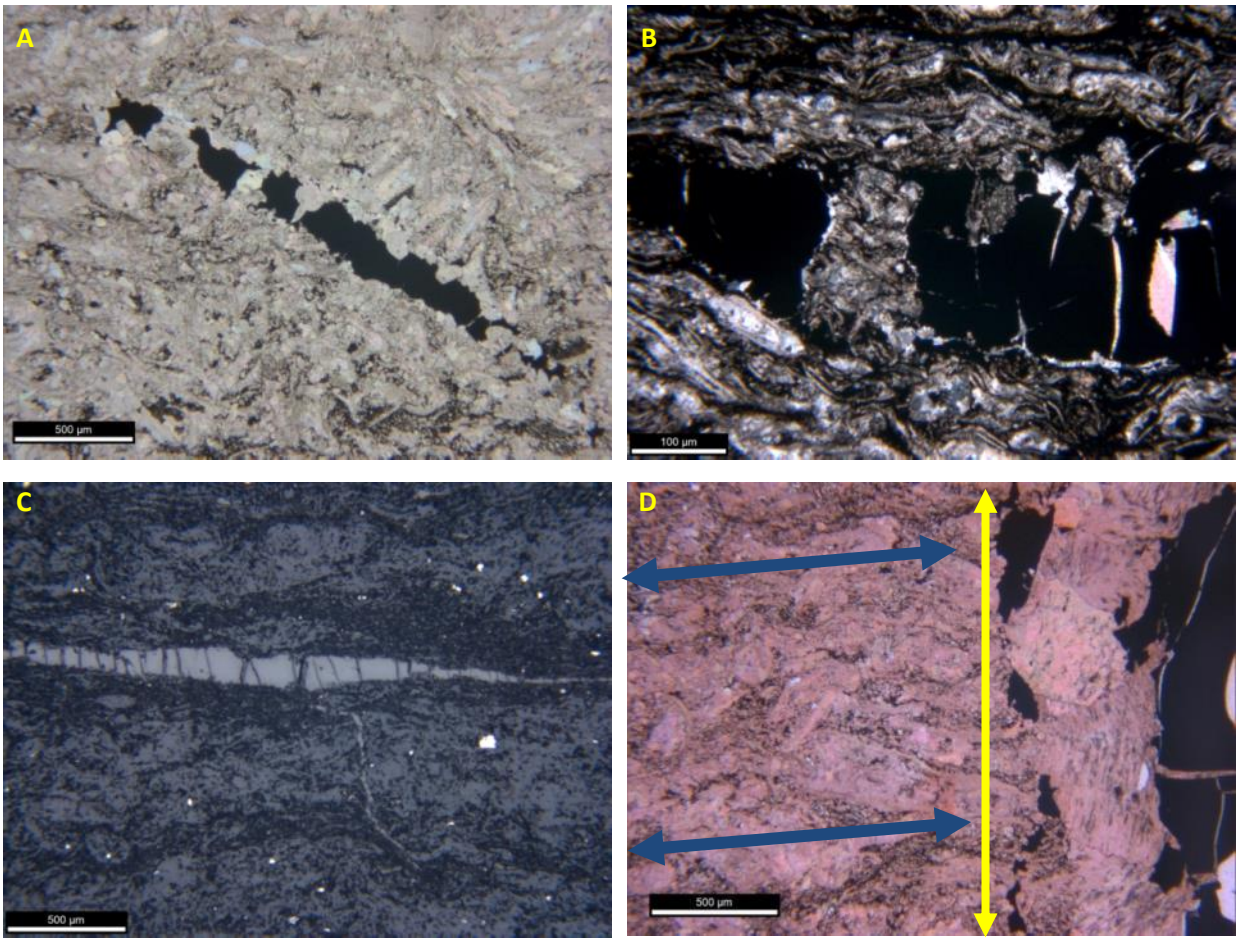

Figure 18: Despite the absence of significant amounts of biologically-identifiable organic matter (e.g. *Tasmanites*), MF XI is one of the microfacies most enriched in organic matter due to the prevalence of organic-rich veins. Veins crosscut cemented (A) and uncemented (B) shell beds, and are present in multiple orientations. (C) shows a thick organic-rich vein running parallel to bedding, with smaller veins branching off at an angle oblique to bedding. (D) shows a photomicrograph of a carbonate stained section with a calcite- and organic-rich vein (yellow arrows) oriented perpendicular to the bedding direction (blue arrows). Images taken parallel to the original direction of bedding.

Organic carbon abundance is high in this facies, due largely to veins of variable orientation, width, and concentration (Figure 18). Because sphalerite (ZnS) appears in this facies largely within these secondary veins, or filling shells in coarse-grained dacryoconarid beds, the sphalerite and significant portions of organic matter within this facies are interpreted as a product of diagenesis. Low-temperature hydrothermal brine migration may have led to the enrichment of sulfides within this microfacies which are not commonly found within facies outside of Microfacies X, XI, and horizons directly contacting these facies. Mississippi Valley-Type Zn-Pb enrichment via brine migration has occurred within the Appalachian Basin, although it has not been reported in New York (Kesler, 1996). With high intrabed porosity caused by an uncompacted dacryoconarid shell framework, metals-rich pore waters may have been able to move easily through the substrate during diagenesis relative to surrounding impermeable clay-rich layers, allowing for the concentrated precipitation of sulfide minerals.

Microfacies XII: Clay- and Calcareous Cement-Bearing Carbonaceous Mudstone

Description

The Clay and Calcite Cement-Bearing Carbonaceous Mudstone is one of the more texturally variable facies identified in this work. Medium to dark grey in hand sample, rocks of this facies generally do not part readily along bedding surfaces, although lamination is often visible. This facies commonly occurs adjacent to concretionary facies, although each studied column contains significant thicknesses of Microfacies XII which are not apparently associated with any concretionary horizon.

Lamination is sub-parallel to wavy, and largely continuous with the occasional erosive surface. Bioturbation is low to moderate, and organic matter is present in the form of partially compacted *Tasmanites*, amorphous pockets 10's of microns in length, and in thin veins running oblique to bedding (Figure 19). Fully compacted to partially compacted dacryoconarid shell fragments and small brachiopods are fairly abundant within this facies; ostracod valves are rare.

Calcite cement is widely disseminated throughout this facies, although the degree of cementation found across the study area varies significantly. Stylolites and veins bearing organic matter and small euhedral grains of pyrite and chalcopyrite commonly crosscut bedding in this facies.

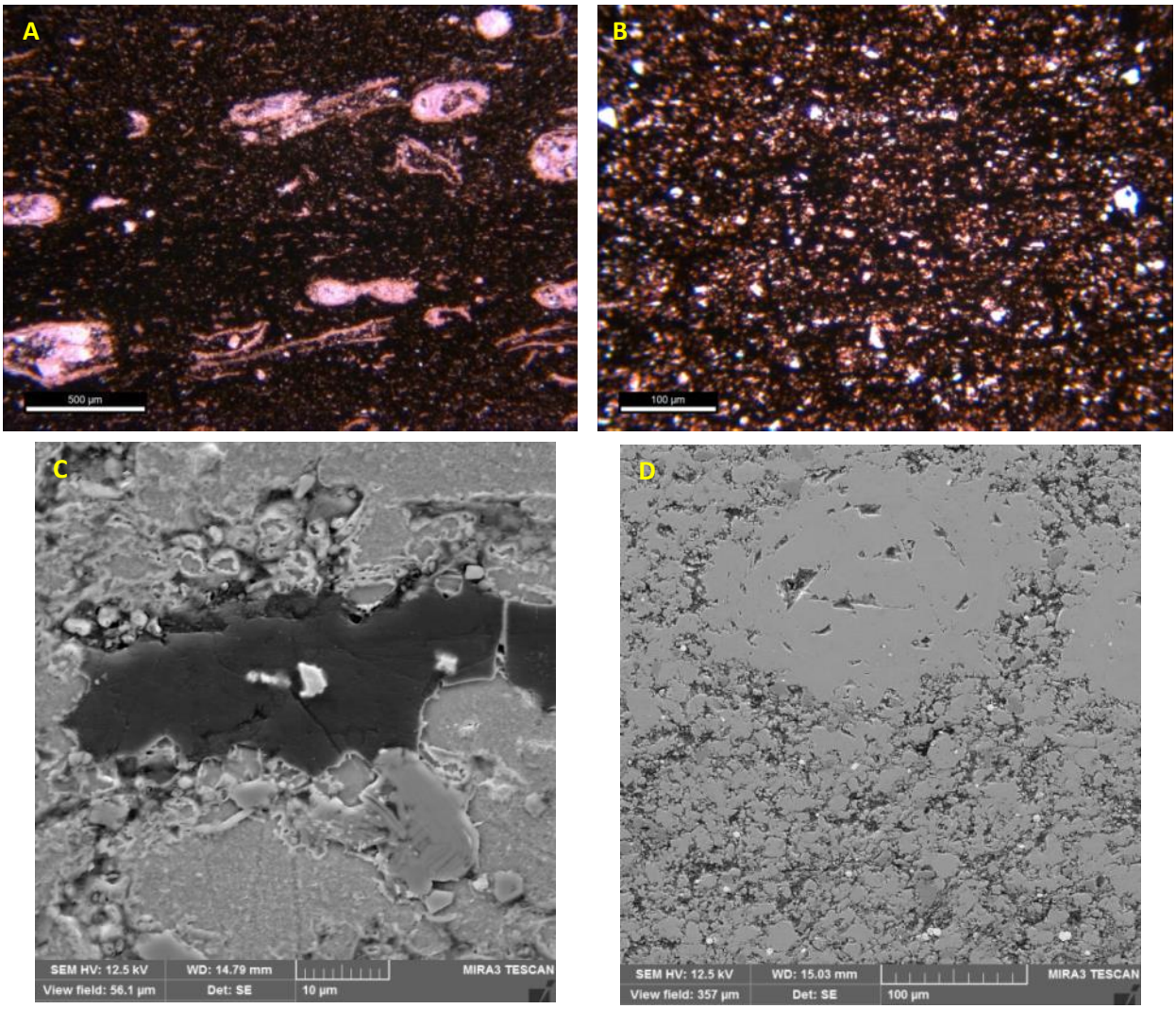

Figure 19: Microfacies XII. Clay and Calcareous Cement-Bearing Carbonaceous Mudstone. Images taken parallel to the original direction of bedding. A) Photomicrograph showing rock texture, partially-compacted dacryoconarids with calcite steinkerns, and compacted dacryoconarids. 500 µm scale bar. Carbonate stain. PPL. B) Silt texture shows interlocking silt-sized calcite grains are most abundant, followed by quartz silt and dolomite. 100 µm scale bar. Carbonate stain. PPL. C) Compacted *Tasmanites* algal cyst surrounded by calcite cement, with lesser amounts of illite, quartz, and pyrite. 10 µm scale bar. Secondary electron image. D) Secondary electron image showing facies texture, including an infilled, minimally-compacted dacryoconarid shell (top center). The bottom half of the image shows a matrix of calcite, quartz, clays, and pyrite, with minimal pore space. 100 µm scale bar.

Interpretation

The large amounts of calcite within this facies may make these rocks appear concretionary at a quick glance, and the inconsistent replacement of primary features with authigenic calcite can make the assessment of textural features difficult. Like concretions that

are treated in following sections, beds in this facies often contain a large amount of recrystallized material and create a mechanical contrast with stratigraphically adjacent rocks. This facies is distinguished from rocks in the Calcareous Concretion Lithofacies Group by the fact that it has undergone compaction, and exists largely as laterally continuous cemented horizons. To contrast, concretions are uncompacted, and often nodular and laterally discontinuous, and formed at very shallow depth prior to sediment compaction (e.g., Dix, 1987). Arguably, the microbial processes driving shallow concretionary growth might have occurred but to a lesser degree, and then the partially cemented sedimentary framework continued to compact. This phenomenon is most often observed directly adjacent to uncompacted concretions (Raiswell and Fisher, 2000).

Alternatively, the source of ions from which the calcite cement formed might have been the dissolution of shells of organisms in underlying laminations. Several other microfacies show imprints of pelagic and benthic organisms on bedding planes, which appear to preserve no original shell material, indicating that shell calcite was indeed dissolved. The compacted condition of dacryoconarid imprints indicates that dissolution took place post-compaction (Lindemann and Schuele, 1996). If fluid moving through the sediment and dissolving shell material became super-saturated with respect to calcite at a particular horizon, this could lead to the rapid precipitation of calcite within the pore space of that horizon. Additional work including a more complete assessment of Union Springs diagenetic variability may shed light on the causes of alteration such as this and allow for the prediction of its occurrence and intensity.

Concretionary Lithofacies

Microfacies XIII: Algae-Bearing Calcite Concretion

Description

The Algae-Bearing Calcareous Concretion (Karaca, 2012) is a calcareous facies occurring across the Seneca Falls, NY study area. This facies appears as bedding-displacive bodies with a nodular morphology which create a mechanical contrast with the beds which surround it. The thickness of beds of this facies, along with the other concretionary facies, pinches and swells significantly laterally.

Minimal primary sediment persists in this facies. Quartz silt and clay minerals are common, but are not volumetrically significant.

Tightly packed fine and medium silt-sized calcite spar dominate this facies, which commonly includes uncompacted *Tasmanites* cysts (Figure 20). These cysts generally have been replaced by calcite to some degree: *Tasmanites* may have a calcite interior, and retain their thin organic wall; or retain the bulk of their interior organic carbon, with silt- or sand-sized calcite growing into the cyst from the edge. Sphalerite is also occasionally observed replacing the interior of these cysts. Pyrite is widespread and occurs as subhedral to euhedral grains ranging in size from one micron to hundreds of microns.

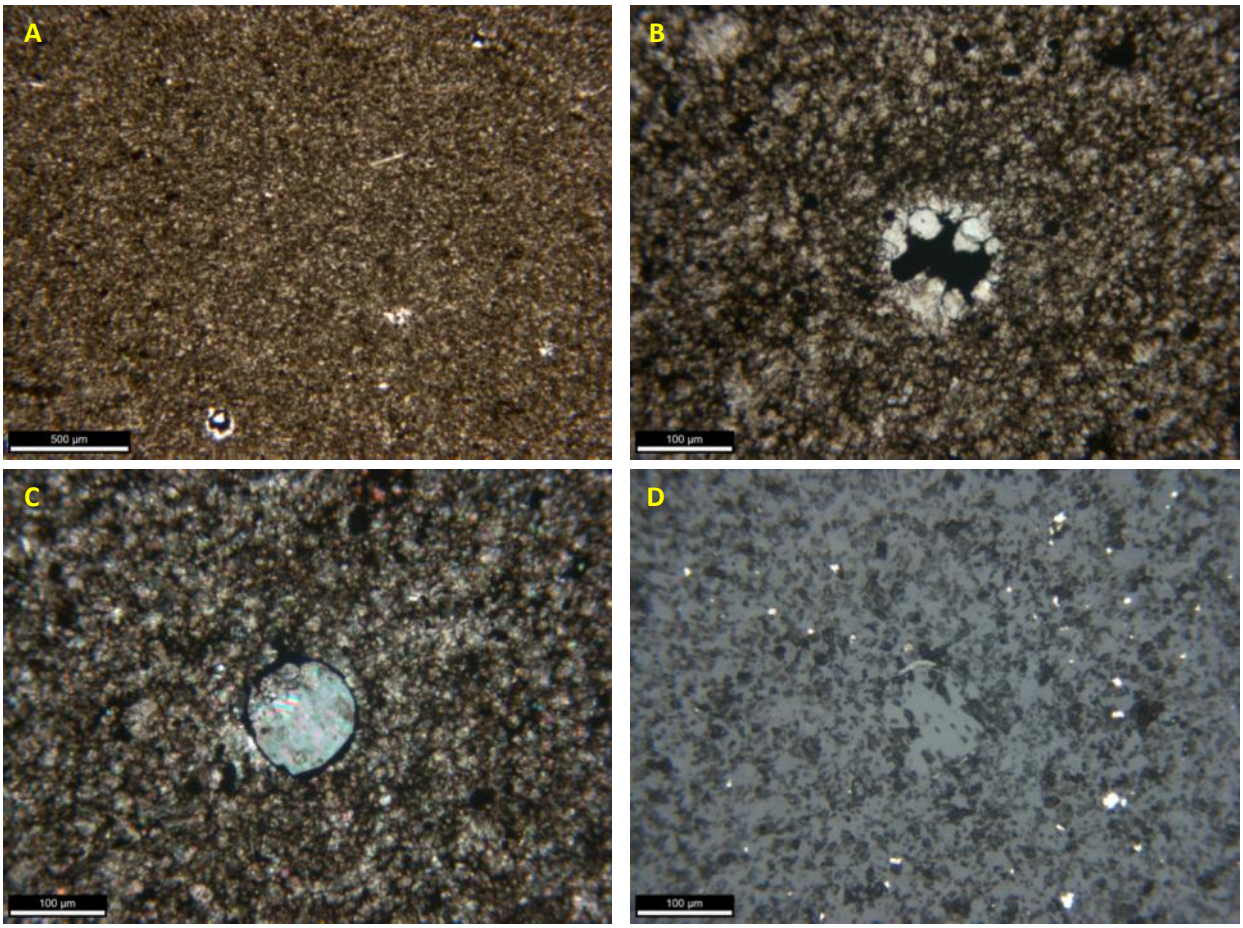

Figure 20: Microfacies XIII. Algae-Bearing Calcite Concretion. Images taken parallel to the original direction of bedding. A) Concretion texture. 500 µm scale bar. PPL. B) The preservation of spherical *Tasmanites* such as this demonstrates that concretions experienced minimal compaction during diagenesis. Here, organic carbon is preserved within the interior of the algal cyst, with calcite growing inward. 100 µm scale bar. PPL. C) Algal cyst with calcite growing outward from the center. 100 µm scale bar. XPL. D) Reflected light view of I, illustrating the preservation of the organic carbon at the rim of the algal cyst, as opposed to the organic carbon within the interior. Evenly disseminated small euhedral pyrite shown here is characteristic of this microfacies. 100 µm scale bar. Reflected light.

Interpretation

These concretions form as a result of microbial oxidation of organic material, and display a "concentric" carbonate growth pattern which displaces surrounding bedding textures [Raiswell, (1976); Raiswell and Fisher, 2000]. A lack of compaction features indicates that concretion growth took place during earliest diagenesis. Dix (1987) attributed the formation of concretions in the Union Springs Formation to be very early during diagenesis, and calculated

the depth at which they formed to be within one meter of the sediment-water interface. This interpretation is supported by the petrographic analysis of this work, as well as Karaca (2012) and Zapata (2014), all of which note uncompacted *Tasmanites* algal cysts, many of which have experienced some degree of calcite replacement texture. These concretions form only within environments with extremely slow sedimentation rates (Raiswell and Fisher, 2000), and largely preserve the sediment thickness that existed prior to compaction (Lindemann and Schuele, 1996). Low degrees of compaction amongst concretionary facies hamper compositional characterization of their components which are not calcite cement. However, the lack of observed trace and body fossils within this facies suggests an oxygen-starved environment at the sediment-water interface during the accumulation of Microfacies XIII sediments.

The pinching and swelling of these concretionary beds is thought to be a result of individual concretions coalescing into one continuous calcareous body of variable thickness during extended periods of slow sedimentation (Raiswell 1987). This variability may cause significant difference between the vertical positions of the prominent concretionary horizons in any two given sections of Union Springs strata which contains them. The presence of sphalerite filling pore space within this facies is noted in similar settings within Union Springs sections described by Karaca (2012) and Selleck (2014).

Microfacies XIV: Algae- and Dacryoconarid-Bearing Calcareous Concretion

Description

The *Algae- and Dacryoconarid-Bearing Calcareous Concretion* is a concretionary microfacies similar in texture and composition to Microfacies XIII. This microfacies differs in that dacryoconarids are a notable constituent (as much as 10% by volume) (Figure 21), with rare brachiopod shell debris. Dacryoconarids are filled with calcite-rich mud, or steinkerns of calcite, often with partial shell replacement by pyrite. At least 2 dacryoconarid taxa are present within this microfacies. *Tasmanites* are abundant, and generally exhibit some degree of calcite replacement. Uncompacted fecal pellets are present, although not common. This microfacies occurs within each of the studied stratigraphic sections.

Interpretation

The interpretation of this microfacies is similar to that of Microfacies XIII: slow sedimentation accompanied by the microbial decomposition of organic material facilitating concretionary growth. However, the appearance of dacryoconarids and fecal pellets in this microfacies may be indicative of some degree of environmental change relative to the non-dacryoconarid bearing concretions, such as elevated primary productivity leading to higher dacryoconarid abundance, or slower detrital sedimentation, allowing for a higher dacryoconarid density per unit of deposited sediment. Given that all concretionary calcite growth requires an exceedingly low sedimentation rate (Raiswell, 1987), the former explanation is preferred.

Like the degree of compaction of *Tasmanites* cysts, the degree of dacryoconarid compaction can also be used to quantify post-depositional compaction of the concretion itself (see Appendix, Lindemann and Schuele, 1996). Similarly to Microfacies XIII, the uncompacted nature of this microfacies implies concretion formation prior to significant burial.

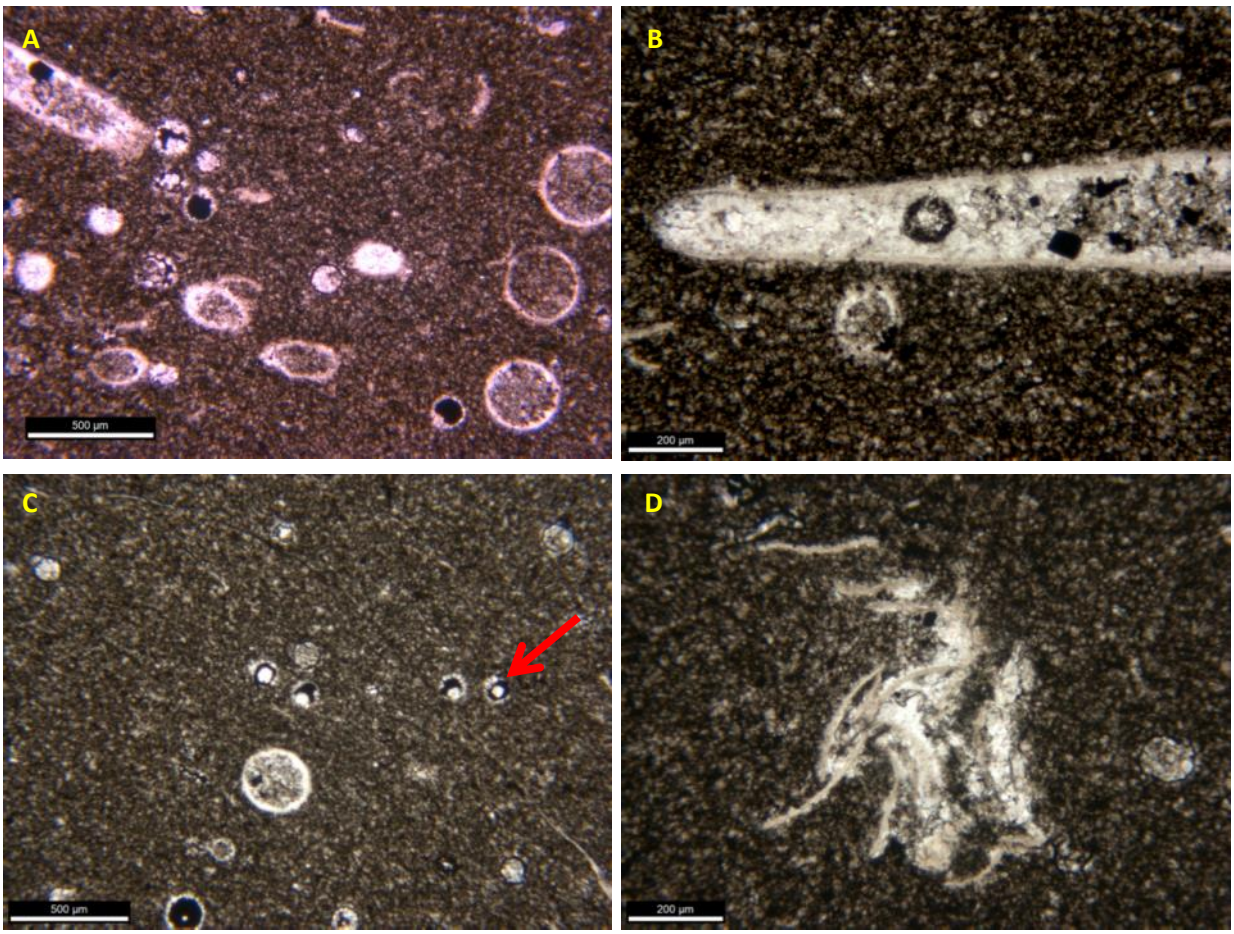

Figure 21: Microfacies XIV. Algae- and Dacryoconarid-Bearing Calcareous Concretion. Images taken parallel to the original direction of bedding. A) Carbonate-stained section showing concretion with uncompacted *Tasmanites* as well as abundant dacryoconarids in transverse and longitudinal view. 500 µm scale bar. Carbonate stain. PPL. B) Uncompacted dacryoconarid with calcite cement and pyrite infill. 200 µm scale bar. PPL. C) Thin, uncompacted fossil shell (arrow) encapsulating concretionary cement and algal cysts. 500 µm scale bar. PPL. D) Loosely associated crushed dacryoconarid shell debris, likely of fecal origin. 200 µm scale bar. PPL.

Microfacies XV: Algae- and Dacryoconarid-Bearing Zoned Calcareous Concretion

Description

Similarly to Microfacies XIII and XIV, the *Algae- and Dacryoconarid-Bearing Zoned Calcareous Concretion* is a concretionary microfacies primarily comprised of silt-sized calcite spar, along with lesser amounts of clay, pyrite, and organic matter (Figure 22). The distinguishing feature of this microfacies is a general decrease in calcite abundance and grain size moving outward from the center of a concretion.

Uncompacted *Tasmanites* and dacryoconarids are common, alongside occasional brachiopod shells. Calcite cement infilling dacryoconarids and brachiopod shells is widespread, along with calcite overgrowths around the shells. *Tasmanites* are largely replaced by calcite and occasionally sphalerite, while fossil shell material is heavily recrystallized or replaced by pyrite. Pyrite and occasionally chalcopyrite are found in euhedral grains as large as 100 µm. Fractures cross through this facies at numerous orientations, and many show evidence of mass transfer, containing variable combinations of calcite, organic matter, and pyrite.

Microfacies XV is found in continuous, relatively tabular beds, as well as along horizons which vary considerably in thickness. For example, at the *Seneca Falls North* section, the concretionary horizon at 270 cm above formation base is 13 cm thick. Traced along the quarry wall for several meters, this same horizon was observed to become as thin as 3 cm. Some concretionary horizons pinch out altogether and form isolated oblate ellipsoids.

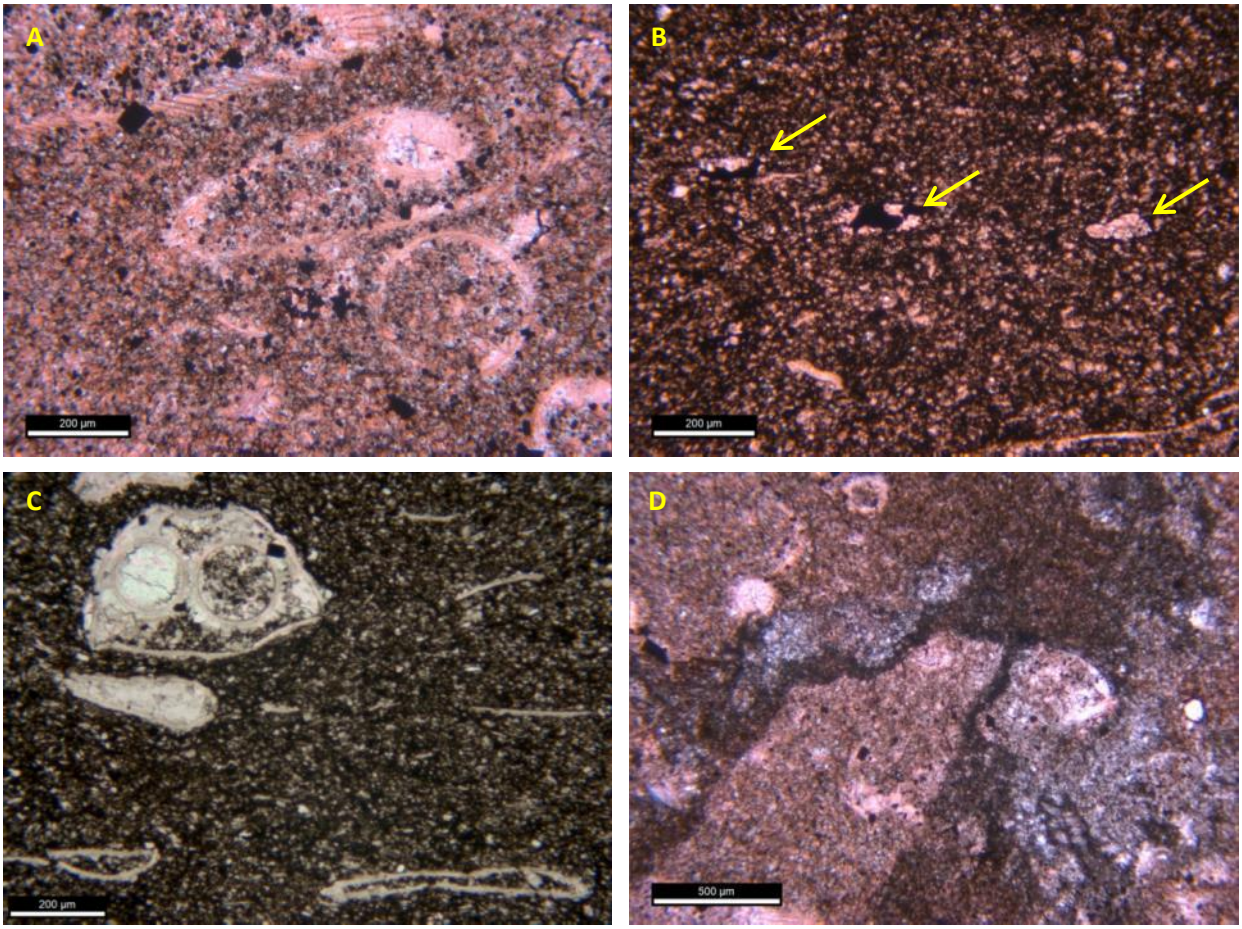

Figure 22: Microfacies XV. Algae- and Dacryoconarid-Bearing Zoned Calcareous Concretion. Images taken parallel to the original direction of bedding. A) Photomicrograph showing texture of the inner concretion zone. The inner concretionary zone is typically composed almost exclusively of calcite and euhedral pyrite. Uncompacted dacryoconarids show evidence of recrystallization. 200 µm scale bar. Carbonate stain. PPL. B) Texture of outer concretionary zone. Here, uncompacted *Tasmanites* algal cysts (arrows) are observed along with dacryoconarid shell debris. The outer concretionary zone is typically slightly more enriched in mud when compared to the inner zone. 200 µm scale bar. Carbonate stain. PPL. C) Outer concretionary zone showing uncompacted fossil shell encapsulating two dacryoconarids. Other shell debris within this photograph suggests some degree of compaction. 200 µm scale bar. D) Inner concretionary zone showing concretionary calcite (stained red) surrounded by an influx of clay and dolomite, likely a result of septarian cracking and infilling. Processes such as this can introduce heterogeneity into one of the more compositionally uniform horizons. 500 µm scale bar. Carbonate stain. PPL.

Interpretation

As is the case for the previous two microfacies, this concretionary microfacies formed primarily as a product of microbial oxidation of organic matter during times of slow

sedimentation (Raiswell, 1987; Raiswell and Fisher, 2000). The distinctive compositional and textural zonation outward to a less calcite-rich zone may be explained (Raiswell and Fisher, 2000) as a result of incomplete cementation followed by a plastic collapse and partial compaction during burial. In some cases, septarian cracking during shallow (<10 m depth) burial allowed for the infiltration of surrounding muddier sediment from the outer concretionary layer and created pore space allowing for the precipitation of dolomite cement (Figure 23).

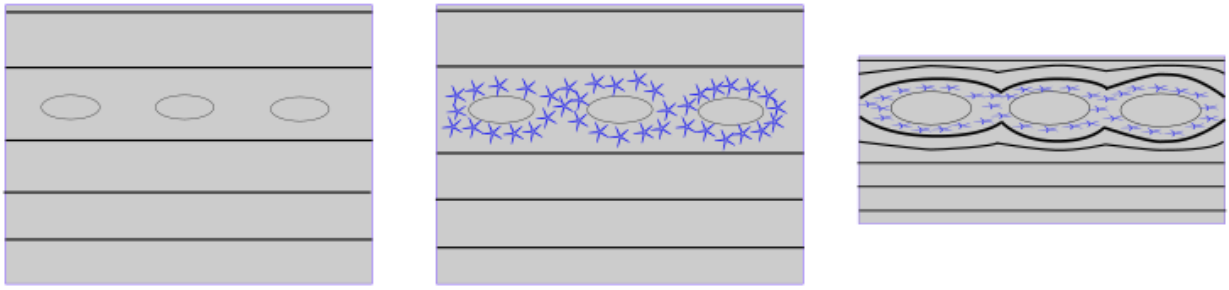

Figure 23: Cartoon illustrating outer-zone concretionary growth process described by Raiswell and Fisher (2000). A) Microbially-mediated reactions lead to concretion growth in the shallow subsurface. B) Concretion growth tapers off, leaving a halo of partially-cemented sediment directly surrounding the concretions. C) Compaction occurs, and weak unconsolidated laminations are distorted against the relatively hard calcite concretions. However, the partially cemented halo is not strong enough to resist compaction.

Facies Name	Facies Number	Lithofacies Group	% Abundance Seneca North	% Abundance Seneca South	% Abundance Marcellus, NY
Dacryoconarid Wackestone	**1**	Limestone	8.3	11.3	0.0
Dacryoconarid Packstone	**2**	Limestone	6.5	7.5	0.0
Benthic Wackestone	**3**	Limestone	0.0	0.0	4.3
Benthic Packstone	**4**	Limestone	0.0	0.0	9.3
Quartz and Dolomite- Bearing Carbonaceous Mudstone	**5**	Carbonaceous Mudstone	2.8	6.2	0.0
Clay-Rich Carbonaceous Mudstone	**6**	Carbonaceous Mudstone	4.4	5.6	0.0
Clay-Rich Quartz Silt-Bearing Carbonaceous Mudstone	**7**	Carbonaceous Mudstone	12.4	12.6	15.2
Clay-Rich Calcite-Silt Bearing Carbonaceous Mudstone	**8**	Carbonaceous Mudstone	11.4	10.5	**28.0**
Fossil-Bearing Clay-Rich Carbonaceous Mudstone	**9**	Carbonaceous Mudstone	8.3	4.0	0.0
Interbedded Dacryoconarid-Bearing Calcareous Mudstone	**10**	Carbonaceous Mudstone	5.2	5.1	18.3
Interbedded Dacryoconarid-Rich Calcareous Mudstone	**11**	Carbonaceous Mudstone	1.8	1.1	3.4
Clay and Calcareous Cement-Bearing Carbonaceous Mudstone	**12**	Carbonaceous Mudstone	**12.7**	**20.4**	9.3
Algae-Bearing Calcareous Concretion	**13**	Calcareous Concretion	7.5	6.4	0.0
Algae- and Dacryoconarid-Bearing Calcareous Concretion	**14**	Calcareous Concretion	9.6	7.0	7.1
Algae- and Dacryoconarid-Bearing Zoned Calcareous Concretion	**15**	Calcareous Concretion	8.3	2.4	5.0

Table 2: Microfacies distributions across the study area. Bold values indicate the most volumetrically abundant microfacies at each studied location.

Facies Number	Lamination Character	Pyrite Occurrence	Bioturbation (1-5)	Bioclast Type + Abundance	Organic Matter (OM) Morphology	Clay + OM %	Quartz %	Carbonate %
1	Irregular thickness, disturbed, often homogenized	Sparse framboids + euhedral grains; large burrow	3-5	Dacryoconarid, minor ostrocode, brachiopod + phosphatic debris	Sparse *Tasmanites* and thin veins	10-20	2-3	65-75
2	Homogenized	Sparse framboids + euhedral grains	2-4	Dac; brachiopod; bone beds with phosphatic debris + *Onychodus* teeth	sparse compacted *Tasmanites*	5-10	1-2	75-85
3	Generally Homogenized	Small (~10 µm) scattered euhedral grains; sparse framboids + shell replacement	5	Brachiopod; crinoid; trilobite; ostracod	Residual	10-20	2-3	65-75
4	Homogenized	Small (~10 µm) scattered euhedral grains, sparse framboids; rare shell replacement + frax fill	4-5	Large articulated Brachiopods; crinoid; trilobite; rare *Onychodus* teeth + conodont debris	Residual	5-10	1-2	75-85
5	Wavy, subparallel, discontinuous	Compressed burrows; subhedral grains; shell replacement	2-3	Dacryoconarid; phosphatic debris; rare brachiopod + bivalve	compacted *Tasmanites;* >1 mm bedding-parallel strands; subrounded macerals	40	5	40
6	Planar, parallel, continuous	Abundant framboids; some euhedral grains >75 µm	1	Dacryoconarid	compacted *Tasmanites*; intergranular within shell-rich beds	80	5-10	2-3

Facies Number	Lamination Character	Pyrite Occurrence	Bioturbation (1-5)	Bioclast Type + Abundance	Organic Matter (OM) Morphology	Clay + OM %	Quartz %	Carbonate %
7	planar to subplanar, parallel to sub-parallel, continuous to disturbed	Small framboids common; subhedral grains (10-100 µm); pyritized shells + detrital grains	1-3	Dac; bivalve; phosphatic debris; fecal pellets; graptolite	compacted *Tasmanites*; inter- and intragranular within shell-rich beds	50-70	10-20	10-20
8	Gently wavy, parallel, mostly continuous	Framboids; pyritized compacted burrows; scattered euhedral (~50 µm)	1-2	Dac; phosphatic debris; fecal pellets, rare bivalve	compacted *Tasmanites*; amorphous macerals; inter- and intragranular within shell-rich beds	30-50	5-10	20-50
9	Planar, parallel, mostly continuous	Scattered framboids + subhedral grains (<50µm)	1-2	Brachiopod; Dac; rare fecal pellets	compacted *Tasmanites*; intragranular within shell-rich beds	75	3-5	10-15
10	wavy, variable thickness, continuous to discontinuous	Scattered subhedral grains (<100 µm); sparse framboids and shell replacement	1-2	Dac dominated; rare brachiopod and crinoid	thin continuous bed-// bands; intragranular within shell beds; rare stylolites	40-50	3-5	40-50
11	wavy, variable thickness, continuous to discontinuous	Scattered framboids + subhedral grains (<100µm); rare shell replacement	1-2	Dacryoconarid	large branching vein; thin continuous bed-// bands; intragranular within shell beds	20-40	3-5	60-80

Facies Number	Lamination Character	Pyrite Occurrence	Bioturbation (1-5)	Bioclast Type + Abundance	Organic Matter (OM) Morphology	Clay + OM %	Quartz %	Carbonate %
12	planar to wavy, parallel to sub-parallel, continuous	Filling compacted burrows; scattered euhedral	1-4	Dacryoconarid; Brachiopod; Bivalve; rare phosphatic debris	variably compacted *Tasmanites;* amorphous macerals (< 120 µm); within branching veins	40-50	3	45-60
13	Not apparent	Subhedral euhedral grains (5-50 µm)	1	N/A	uncompacted *Tasmanites*	10-20	1-2	80-85
14	Not apparent	Subhedral euhedral grains (5-50 µm); Shell replacement and steinkerns	1	Dacryconarid; rare brachiopod + fecal pellet	uncompacted *Tasmanites;* vein fill	10-20	1-2	80-85
15	Not apparent to wavy, parallel	Subhedral grains (5-50 µm); rare shell replacement	1	Dacryoconarid; brachiopod	uncompacted *Tasmanites;* vein fill	10-35	1-5	65-85

Table 3: Summary of microfacies attributes described in full in text.

Discussion

Intra-quarry Facies Comparison

Performing microfacies analysis on two measured sections within one quarry provides knowledge at an important length scale. Measuring heterogeneity at the hundreds of meters scale allows for the general characterization of the near-field variability within the paleodepositional and diagenetic environments. Hundreds to thousands of meters are laterally probed by horizontal wellbores in shale gas operations, and accounting for variability in mineralogic and textural rock characteristics is important to the productivity of these operations (King, 2010). However, the data collection methods used in subsurface studies rarely permit facies analyses at the wellbore scale. The detailed characterization presented here documents the variations that are expected to occur but are not expressly treated in subsurface analyses.

Comparing the two columns analyzed in this study that are 600 m distant from one another within Seneca Stone Quarry in Seneca Falls, NY, several similarities regarding the arrangement of microfacies through the vertical columns are immediately apparent (Figure 24). The overall progression of lithofacies groups is similar: above a Tioga K-bentonite horizon, a thin interval of phosphate and dolomite-bearing Microfacies V is overlain by a package of highly-bioturbated limestones (Microfacies II and III) which contains thin interbeds that are enriched in organic matter.

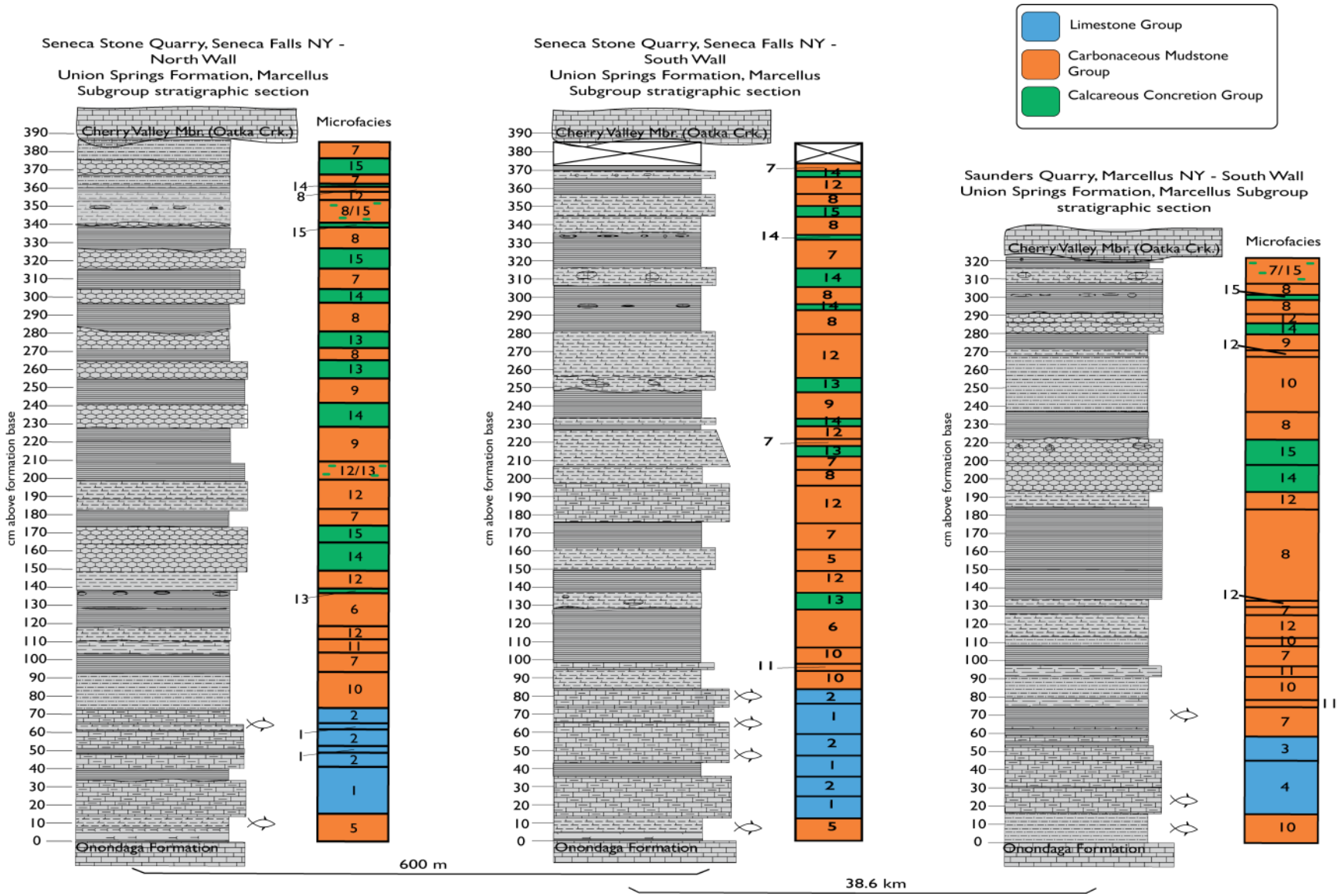

Figure 24: Complete stratigraphic sections of Union Springs Formation examined in this study. Microfacies classification based on lithologic description is indicated by "Microfacies #" column, with color indicating lithofacies group. Vertical Axis in cm.

These limestones contain the surface of maximum transgression, which is defined here based upon changes in limestone texture and the appearance of prominent starvation surfaces, including within Microfacies II the regionally-extensive bone bed (Conkin and Conkin, 1984; Baird and Brett, 1986, and others), found here roughly 70 cm above the base of the Union Springs in each location. These give way to shell-dominated facies rich in organic matter and sulfide minerals (Microfacies X and XI), and then are succeeded by a thin clay and organic matter dominated facies nearly devoid of calcite (Microfacies VI), a rarity in this particular depositional setting. This carbonate deficiency is geologically short-lived, and at each column the first significant concretionary horizon appears, followed by a calcite cemented horizon (Microfacies XIII and XII). From here upward, the columns begin to diverge somewhat, due to the uneven expression of concretionary horizons at opposite sides of the quarry (Figure 24, ~150 cm above formation base). Still, similarities remain. In both sections, concretions become more common in the upper half, a temporary increase in benthic faunal abundance occurs between ~2.1 and 2.5 meters above the formation base, and the average quartz silt abundance increases towards the top of the column within mudstone facies.

Concretionary Variability

The irregular expression of calcareous concretions is one of the largest contributors to near-field variability observed in this study. Take the *Seneca North* and *Seneca South* columns, within which concretionary horizons at the same stratigraphic position across the field site may possess the same properties (e.g. the horizon at 138 cm above formation base, Microfacies XIII, Figure 24). Alternatively, the properties of concretions at a given stratigraphic position may

change, such as the horizon at 368 cm above formation base (Fig. 24). This horizon is identified as Microfacies XV at *Seneca North* but as Microfacies XIV at *Seneca South*, as the *Seneca North* concretionary horizon at 368 cm has intraconcretionary textural zones, which do not exist in more homogeneous concretions at *Seneca South*. It is well-established within the study of sedimentary geology that across all types of depositional environments, a wide variety of spatially variable environmental properties, including migrating ripples, microbial mats, and pre-existing bathymetry, may lead to differences in sediment distribution, physical properties, and chemical properties across short length scales. This high-order variability is on display here in the distal foreland basin as well, where initial lateral environmental variations play roles during earliest diagenesis, and changes in pore water chemistry and sedimentation can create conditions favorable or unfavorable for concretionary growth (Raiswell, 1987). It stands to reason that variability of these parameters across short (100's of meters) distances may affect concretionary development within one bed.

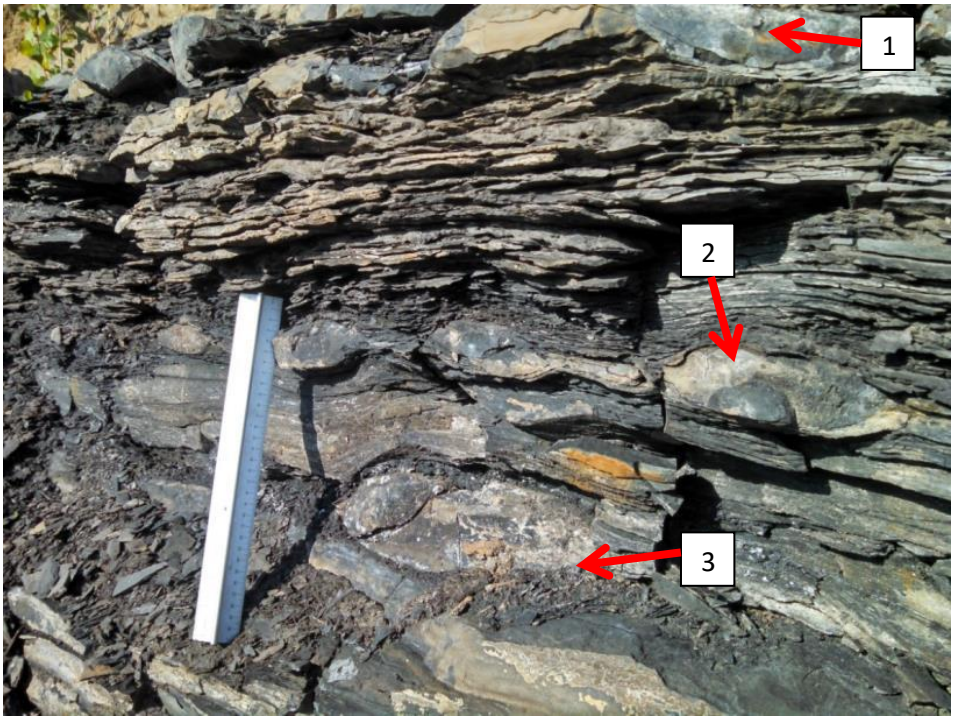

Figure 25: Field photo from Seneca Falls field site illustrating three modes of occurrence exhibited by calcareous concretions. 1) continuous tabular. 2) Continuous, variable thickness. 3) Discontinuous, nodular

Cemented Facies Variability

The distribution of calcite-cemented Microfacies XII is similarly complex. The degree of cementation of rocks within this facies is inconsistent. Some cemented horizons span the length of the quarry (~185 cm above formation base), whereas others do not (e.g., Seneca South at 270 cm). If these cements formed after substantial degrees of burial, possible cementation mechanisms include the dissolution and reprecipitation of concretionary or biogenic material, and the nucleation of cements around biogenic grains (Morad, 2009). If the formation mechanism for calcite cement involves partial cementation under 10's of centimeters of sediment followed by compaction (Raiswell and Fisher, 2000), one would expect to find this facies consistently flanking rocks of the Calcareous Concretion lithofacies group – the variability

of its distribution largely a function of the inherent variability associated with the Calcareous Concretion facies. This is not always the case. There is great potential for future work to shed light on the diagenetic history of the Marcellus in this area of the basin.

Comparing Seneca Falls and Marcellus, NY

Comparison of the two Seneca Falls, NY sections with the column analyzed at Marcellus, NY allows for examination of far-field variability (Figure 24). There exist several similarities between these columns which reflect a similar position in the Acadian foreland basin despite their ~39 kilometer separation. Each of the three studied columns in this study followed a similar progression at the lithofacies group level (Figure 24). Thin (<20 cm) bone-bearing mudstone horizons at the Onondaga-Union Springs contact are overlain by 50-80 cm of limestones. These limestones transition into dacryoconarid-dominated, organic rich interbedded mudstones (Microfacies X and XI) between 0-15 cm above the top of the last limestone horizon. As is the case at Seneca Falls, NY, concretions are frequent within the upper half of the stratigraphic section at Marcellus, NY, although their abundance is significantly less than that of the Seneca Falls sections (Tables 2 and 3).

Limestone Facies Variability

Several notable differences exist between the two sites, notably with respect to the faunal assemblages hosted by the limestone microfacies. Each of these microfacies is highly bioturbated and overlies a sharp contact with an organic-rich mudstone facies. The two limestone microfacies at the Seneca Falls site (Microfacies I and II) host a low diversity pelagic assemblage mostly consisting of dacryoconarids, with minor amounts of thin-shelled

brachiopod debris. At the Marcellus, NY site (Microfacies III and IV), a much more diverse assemblage is present. Disarticulated trilobite, crinoid, and brachiopod debris is very common. Several larger (>2 cm length) brachiopods are found in an articulated state. The limestone facies at each location contain prominent bone beds indicating significant regional sediment starvation (Ver Straeten et al, 1994; Brett and Baird, 1996). Within the *Marcellus* column, the limestone facies progresses upward from a packstone to a wackestone texture (Microfacies IV into Microfacies III), with slightly increasing silt and mud content. This contrasts with the *Seneca Falls* columns, which change between wackestone and packstone facies (Microfacies I and II) several times (Figure 24).

These changes may reflect differences in terrigenous mud sedimentation within the basin, possibly as a result of high-order changes in shoreline position, or they may result from local variations in sediment supply to this distal portion of the basin. At Marcellus, NY, the more gradual incorporation of terrigenous sediment into the limestone facies mirrors the observations of Karaca (2012) at Seneca Falls, NY. The shift from packstones to wackestones moving up-section is consistent with transgression and the basinal transition from the shallow carbonate platform facies of the Onondaga limestone to the siliciclastic-dominated deposition of the Union Springs within a tectonically-reactivated Acadian foreland basin (Ettensohn, 1985; Ver Straeten, 2007). Although there exists a slight increase in quartz silt content within the uppermost packstone bed at Seneca Falls, NY, a steady transition from carbonate to siliciclastic sedimentation is not obvious at this study site. The Seneca quarry textural fluctuations between wackestone and packstone may be a result of less steady terrigenous sediment delivery at

Seneca Falls when compared to Marcellus, NY, leading to the greater abundance of packstones at this location.

Relative Mudstone Abundances

One of the more obvious differences between the study areas at Marcellus, NY and Seneca Falls is the total thickness of each Union Springs stratigraphic section. Located nearly 39 kilometers from the 3.22 meter thick *Marcellus* column, the *Seneca North* column measures 3.87 ± .03 meters in thickness. In the case of highly condensed sections such as these, a small magnitude difference between sections may be a result of significant changes in sediment delivery, erosion, or length of non-depositional time (Posamentier et al., 1988). In this case, another possible explanation for this thickness difference is differential sediment compaction between locations during diagenesis.

It is well known that the composition, formation mechanism and grain size of sediments can affect their compaction behavior, and this is often reflected in sedimentary rocks (Raiswell, 1976; Allen and Allen, 2013). Tables 1 and 2 shows the relative abundances of each lithofacies group within each studied column, and reveal that the relative abundances of lithofacies groups are not equal in the *Seneca North* and *Marcellus* sections. The differential compaction of the varying lithofacies can bias perceptions of environmental conditions and sediment supply across the basin if current column thicknesses are used as criteria for interpreting the original contributions of sediment at each location. In order to make a rudimentary calculation of original sediment thickness at each location, a range of facies-specific Union Springs compaction values, based on observations by Lindemann and Schuele (1996), was used to

account for lithology-specific amounts of compaction within the limestones, calcite-cemented mudstones, and carbonaceous mudstones present.

The calculations illustrate the roles of lithologically controlled compaction in attaining the measured column thicknesses (Appendix). For all cases, the original sediment thickness was much greater than the measured thickness, ranging between approximately two times to eight times thicker. However, the fractional difference between the two locations was less than it is today. For example, for both the cases of minimal and intermediate values of compaction of the three lithofacies groups, the original thickness was about 55 cm greater at Seneca North than at Marcellus Saunders, corresponding to 6% of the Seneca North thickness for the minimal compaction case and 5% for the case of intermediate compaction values (Appendix). For the case of maximum compaction values, the initial thickness difference was a mere 33 cm, or 1% of the Seneca North original thickness. To compare, the present-day thickness difference between sections, 65 cm, represents 17% of the modern *Seneca North* rock column. This analysis reveals that the two study areas, situated roughly 39 km from one another, may not have had as severe a difference in sedimentation as the rock record may suggest.

Variable Silt Within Carbonaceous Mudstones

In addition to differing lithofacies distributions and differing degrees of compaction between the two studied locations, the composition and abundance of silt also differs between the Seneca and Marcellus regions. Following the same general pattern as those at Seneca Falls, rocks within the carbonaceous mudstone lithofacies group at Marcellus, NY display a slight increase in the size of quartz silt grains moving upwards from top of the Limestone facies group

towards the Union Springs-Cherry Valley member contact. However, the overall silt content of carbonaceous mudstones at Marcellus, NY is slightly higher when compared with Seneca Falls, NY. Although the Marcellus Saunders section is currently thinner than either of the Seneca Falls sections, it contains volumetrically greater amounts of carbonaceous mudstone facies (Table 2, Figure 24). At Marcellus, NY, the two Carbonaceous Mudstone microfacies largely defined by their silt (Microfacies VII and VIII) comprise nearly 45% of the total column value, as opposed to less than 25% at each of the Seneca Falls sections. Additionally, while each Seneca Falls section contains the clay-enriched carbonaceous mudstone microfacies (Microfacies VI), this is not the case at Marcellus, NY, and all clay-rich facies contain some significant silt fraction as well, which may point toward a slightly more energetic paleodepositional environment.

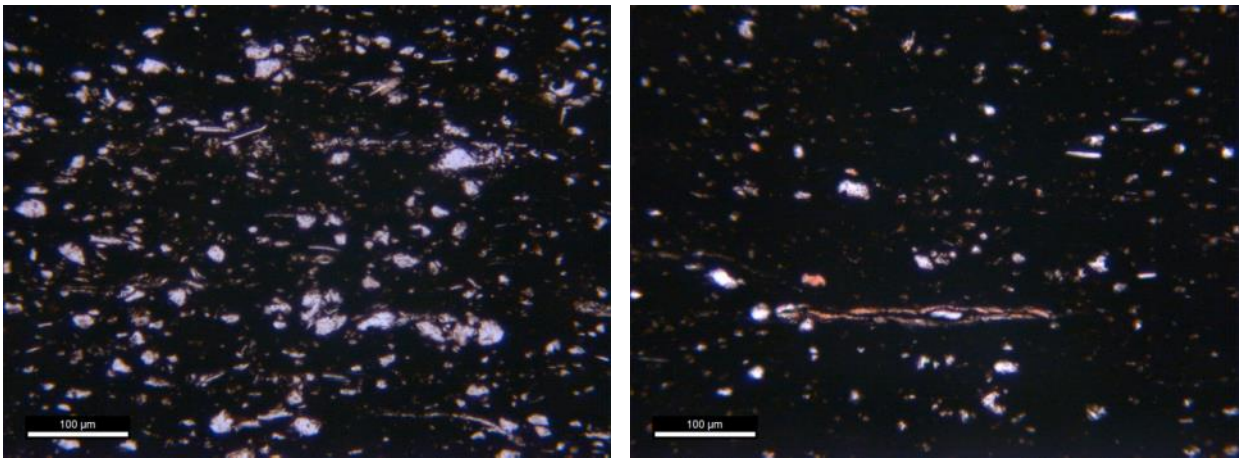

Figure 26: Examples of Clay Rich Quartz Silt Bearing Carbonaceous Mudstones from the Marcellus, NY (left) and Seneca Falls, NY (right) study areas. Note the higher silt fraction in the Marcellus, NY mudstone.

Depositional Variability Across the Appalachian Basin

Detailed comparison of the Union Springs Formation within the study area to Union Springs sections found in differing basinal positions facilitates comparison of depositional

variability across facies gradients at the hundreds of kilometers scale. As expected, the stratigraphic sections within the study area are more similar to one another than to rocks in the ultra-far field. For example, the Union Springs of Somerset County, PA, found within the Yoder-1 core of Kohl et al. (2014), rarely contains more than 10% calcite abundance. The rocks which comprise the bulk of the Union Springs within this core are much more clay-rich, are interpreted as dominantly anoxic (Kohl, 2012; Kohl et al., 2014), and appear most similar to Microfacies VI and IX described in this study. Similar to the Yoder-1 core, the Union Springs of the northern basin records substantial oxygen stress via a number of faunal, ichnological, and chemical indicators, although constant anoxia/euxinia is not interpreted for the rocks of this study (see also Chapter 2). The environments which created these two sections likely differed both in terrigenous sediment supply and depositional energy, as indicated by substantially less clay deposition within the distal study area as well as the presence of facies possibly indicating a position above storm wave base (Microfacies X, XI). As described by Bruner et al. (2015), much of the Union Springs found along the Marcellus outcrop belt in West Virginia appears to be more similar to the northern basin with regard to depositional energy, although the elevated percentage of siliciclastic material is indicative of a somewhat less terrigenous sediment-starved environment.

Connections to Sequence Stratigraphy

Sequence stratigraphy is a valuable tool for examining inter- and intra-formational stratal relationships to eustasy and time in a regional and global context. Placing characterized mudstone successions within a sequence stratigraphic framework allows for the analysis of

relationships between local mineralogical, chemical, and mechanical variability and major far-field eustatic and tectonic events. Sequences are defined as relatively conformable successions of genetically related strata, and each sequence is bounded at its top and base by unconformities or their correlative conformities (Mitchum et al. 1977). Sequences are classified by "order," based upon the amount of time represented within the package of rock in question. For example, *Eif*-2 (Ver Straeten, 2007) (roughly sequence *I-d* of Johnson (1985)), the sequence encompassing the Moorehouse Member of the Onondaga Formation through the top of the Union Springs Formation, is defined as a third-order sequence (Ver Straeten, 2007; Brett et al. 2011). Third-order sequences are commonly interpreted to represent depositional cycles lasting on the order of one million years (Vail et al., 1977).

Sequences, which are cyclical depositional manifestations of interactions between sea level, sediment supply, water depth, and tectonic activity, are divided into systems tracts based upon position in the relative sea level cycle (Posamentier, 1988). Here, the terminology of "Depositional Sequence IV" of Catuneanu (2002) and Catuneanu et al. (2009) is used to describe systems tracts. This convention classifies packages of rock representative of stratigraphic sequences comprised of lowstand, transgressive, highstand, and falling stage systems tracts, and is in agreement with a number of recent works regarding Union Springs sequence stratigraphy (Ver Straeten, 2007; Kohl, 2014; Zapata, 2014). Ver Straeten's (2007) regional study of the Marcellus subgroup sets the stage for this paper's detailed analysis by anticipating that transgressive and highstand systems tracts occur within the Bakoven Member of the Union Springs Formation. The sequence boundary is placed at the base of the Cherry Valley Member of the Oatka Creek Formation, which corresponds to the lowstand systems tract

of the overlying sequence. Regionally, a falling stage systems tract between the Bakoven and Cherry Valley members is expressed as the Stony Hollow Member, but its expression in the region of Seneca Falls NY to Marcellus NY is unclear.

Occurring during a period of eustatic transgression and regional orogenic reactivation (Johnson et al., 1985; Ettensohn, 1985), Union Springs depositional time began in the midst of the *Eif-2* transgressive systems tract (TST) (Ver Straeten, 2007) which began during the deposition of the Seneca Member of the Onondaga Formation (Ver Straeten, 2007). The facies that define the transgression continue through the lower Union Springs (Microfacies 1-5). Within those transgressive facies occur at least 3 bone-bearing horizons, including a prominent, regionally extensive bone bed (Figure 24). Prior workers have interpreted the position of the maximum flooding surface in the Union Springs using evidence of non-deposition (Ver Straeten, 2007), grain size trends (Karaca, 2012), gamma log response (Lash and Engelder, 2011; Kohl et al., 2014; Zapata, 2014), and total organic carbon content (Zapata, 2014), and the positions selected by those methods vary between a few centimeters above formation base (Zapata, 2014) to above the mid-point of the section (Karaca, 2012). In this work, the maximum flooding surface is placed between 30 cm (Marcellus, NY) and 65 cm (*Seneca South*) above formation base, based upon associations with the most prominent bone bed along with the limestone textures indicative of lowest depositional energy and maximum siliciclastic sediment starvation (Figure 27).

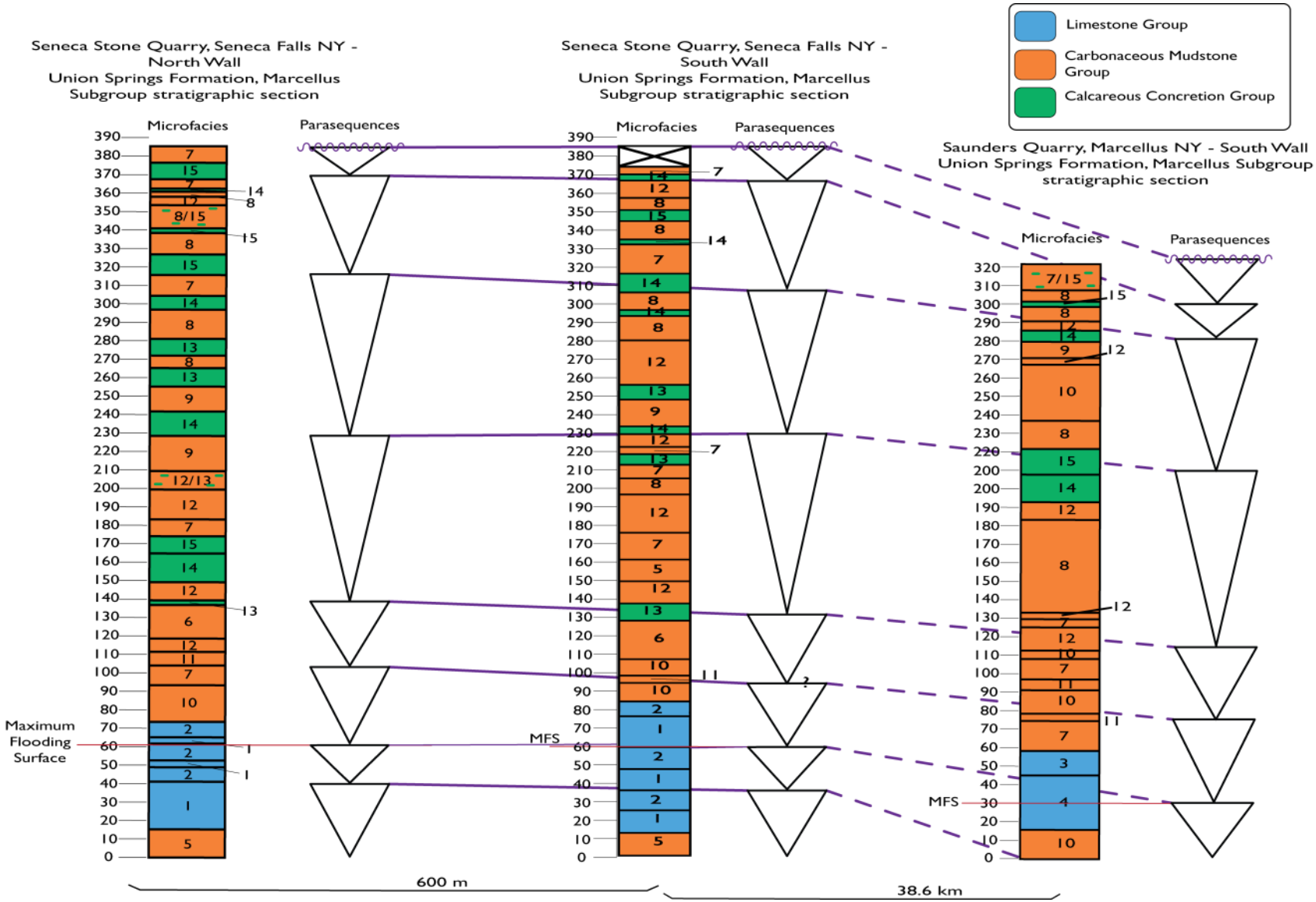

Figure 27: Microfacies classifications alongside identified parasequences at each location. Solid and dashed lines indicate perceived parasequence correlations. Maximum flooding surface indicated by solid red line. Undulating lines indicate the upper *Eif-2* sequence boundary. Vertical Axis in cm.

The division of the strata above the maximum flooding surface into a highstand systems tract and a falling stage systems tract is difficult within the highly condensed study area. In principle, the highstand systems tract would have been deposited during a period of a regressing shoreline despite rising sea level, and the falling stage systems tract would be the strata accumulated during a period of "forced regression" in which base level drops and facies distributions shift basinward regardless of sediment supply (Catuneanu, 2002). Directly above the maximum flooding surface, strata inferred to be within the highstand systems tract begin with a succession of carbonaceous mudstones highly enriched in organic matter (Microfacies VII). Some of the lowest highstand systems tract strata (Microfacies X and XI) are indicative of an increase in depositional energy relative to the underlying bone bed-bearing limestone microfacies within the study area. In more proximal areas of the basin, the sand-bearing Stony Hollow strata are representative of falling stage systems tract deposition under conditions of forced regression from base level drop (Ver Straeten, 2007). Although there does exist a subtle gradual increase in average silt grain size moving up-section from the study area's maximum flooding surface, neither a sedimentological nor faunal expression of the Stony Hollow Member is definitively observed within the study area, and no strong depositional signal for forced regression is identified. For the purposes of this study, the highstand and falling stage systems tract are combined into one regressive package of HST/FSST strata, encompassing all the Union Springs strata above the maximum flooding surface. Future work characterizing dacryoconarid populations may yield a new method for deciphering the sequence stratigraphy of this interval in distal locales.

Higher-order sequences within these rocks, called parasequences, are bound by marine flooding surfaces and their correlative conformities (Van Wagoner et al., 1988). Parasequence arrangements are used to recognize systems tract relationships within sedimentary successions (Van Wagoner et al., 1990; Catuneanu et al., 2009). Marine flooding surfaces mark a shift toward deeper-water conditions as a result of transgression, and may be accompanied by depositional hiatus or minor submarine erosion (Van Wagoner et al., 1990). In this study, the vertical facies succession and gamma log data reveal two parasequences within the transgressive systems tract and six within the HST/FSST.

With reference to the primary criteria, facies properties, parasequences in the Union Springs Formation of the study area occur within the context of an overall average grain size increase upward from maximum flooding surface toward the formation top during the highstand and falling stage systems tracts. Karaca (2012) identified parasequences with thicknesses of tens of centimeters. However, she found that the petrographic identification of coarsening and fining within parasequence-scale packages of rock in the distal Union Springs Formation is unwieldy, even while working at a relatively high resolution. Therefore, Karaca (2012) used concretionary horizons as markers for marine flooding surfaces, on the premise that they represented time intervals of sediment starvation at the sediment-water interface because of an increased distance from sediment sources to the Seneca Falls region, allowing for the formation of carbonate concretions. Thus, she used concretionary horizons to mark parasequence boundaries in the middle to upper Union Springs. While the work here supports this assertion, the use of concretions as parasequence boundaries should be employed cautiously. The Results section, along with Figure 24, demonstrates that concretions vary

laterally, in texture as well as in thickness, and may even pinch out completely. Concretions may appear as continuous pseudo-tabular horizons, in rows of pinching and swelling nodular concretions, or as isolated discontinuous nodules (Figure 25). Consequently, the blanket use of concretions to identify laterally extensive parasequence boundaries is problematic. Here we bound parasequences only using concretionary horizons which appear to be continuous at each outcrop face, in an effort to ensure that parasequence boundaries were being placed at horizons which truly reflected regional changes in sediment delivery. Additionally, bulk lithologic changes indicative of sedimentologic change, including grain size and sediment composition, were used to discriminate parasequences. For example, moving up-section, a change from the quartz-silt bearing Microfacies VII to the silt-poor clay-rich Microfacies IX, or a change from the mud-supported Microfacies I to the grain-supported Microfacies II, was used in some cases as evidence of a decrease in sediment flux as is expected at a parasequence level flooding surface. Parasequence divisions are shown in Figures 27, 28, 29, and 30.

Overall, 7 parasequences are identified within the studied section at Marcellus, NY, while 8 were identified within both Seneca Falls sections. Similar microfacies stacking patterns have led to similar parasequence stacking patterns between the two Seneca Falls columns, and solid lines are shown correlating the parasequences of these locales. Dashed lines are shown correlating the Seneca Falls and Marcellus, NY sections as a result of higher uncertainty tracking parasequences across the 39 km distance between the locations. While trends in bulk lithology, grain size, and concretionary positions all point to robust parasequence boundaries at Seneca Falls and Marcellus, NY individually, stacking patterns are sufficiently dissimilar at a microfacies level such that the correlations between these locations are made tentatively, particularly

within the upper half of the Union Springs. This issue could be further resolved with the discovery of additional time constraints within the Union Springs' regressive systems tracts which do not currently exist at these locations.

At both Seneca Falls study areas, two parasequences are identified within the transgressive systems tract, contrasting with the one parasequence identified at Marcellus, NY. The additional TST parasequence at Seneca Falls, NY is included as a result of higher degrees of textural variability amongst the Seneca Falls limestones (Figure 27). During this time, the region experienced a near total loss of terrigenous sedimentation during a time of renewed uplift and erosion into the basin foredeep (Brett & Baird, 1996), while the local Seneca Falls area developed prominent sediment starvation surfaces, and oscillations in limestone texture between wackestone and packstone. The reasons for this more frequent textural oscillation only being manifested within the *Seneca* columns is not completely understood, but it could be due in part to a difference in paleo-oxygenation levels. Based upon the benthic faunal assemblage and consistently high bioturbation (Table 3), the Marcellus, NY section appears to have contained well-oxygenated bottom waters throughout the period of limestone deposition. Within the limestones of the *Seneca* sections, benthic macrofauna are not present, and bioturbation fluctuates between high and moderate levels (Table 3). This suggests that the pelagic limestones of the Seneca sections were more marginal in their ability to support life and that they may have been more susceptible to preserving in lithologies visible results of higher-order paleoenvironmental change.

Microfacies analysis broadly supports similar sequence stratigraphic interpretations at each study site. Transgression, which began high in the Seneca Member of the Onondaga Formation, continues in the lower Union Springs, and carbonate deposition is dominant. The maximum flooding surface, located within packstone microfacies across the three studied locations (Microfacies II and IV), separates the transgressive systems tract from the overlying highstand/falling stage systems tracts (Figure 27). Moving upsection above the maximum flooding surface, microfacies oscillations are still important for identifying parasequences. For example, in the third *Seneca North* parasequence above the base (Figure 28), the strata transition from limestones (Microfacies II) to shell-rich mudstones (Microfacies X) to organic rich mudstones (Microfacies VII) as a result of an approaching shoreline during a basin-wide transition to siliciclastic deposition (Ver Straeten, 2007). This parasequence is capped by a flooding surface represented by a return to clastic-starved high-energy shell deposition (Microfacies XI). Grain size trends are similarly important for parasequence identification. Take the third *Marcellus, NY* parasequence, which begins with shell-rich strata (Microfacies XI), grades up-section through X and XI interbeds, and progresses into a quartz silt-bearing carbonaceous mudstone with a roughly 20% quartz silt abundance (Microfacies VII). There is then a transition back into shell-rich facies followed by a bioturbated, calcite-cemented mudstone horizon (Microfacies X and XII, respectively). Above this sits another package of quartz silt-bearing mudstone, and within this strata the silt abundance is noticeably less (~10%) than the preceding package of Microfacies VII. This justifies the identification of a flooding surface within the preceding calcite-cemented horizon (Figure 27, 115 cm above *Marcellus, NY* formation base).

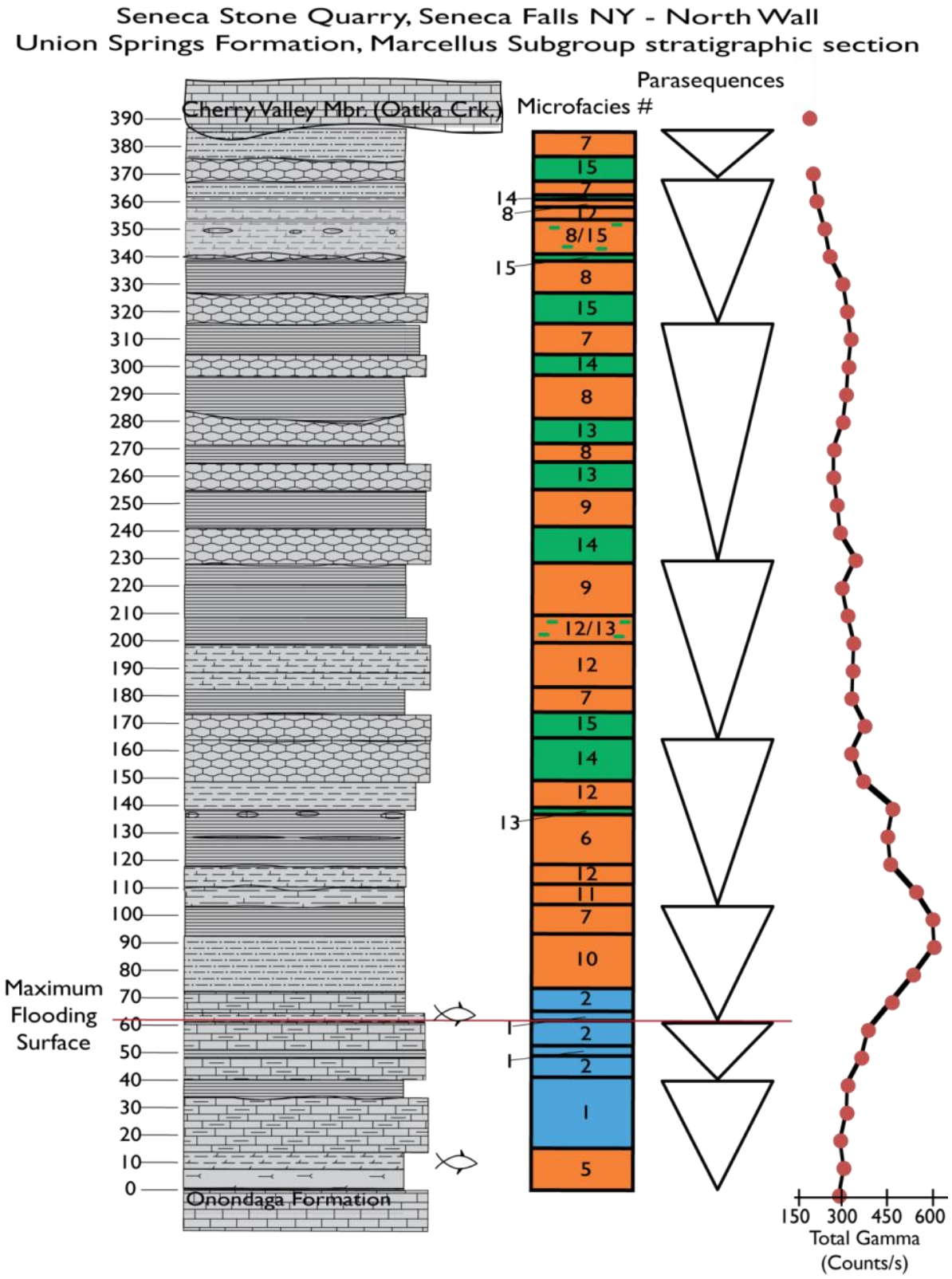

Figure 28: Stratigraphic section described at the north wall of the Seneca Stone Quarry in Seneca Falls, NY, including identified microfacies, parasequences, and gamma ray log. Fish symbols indicate bone-rich horizons.

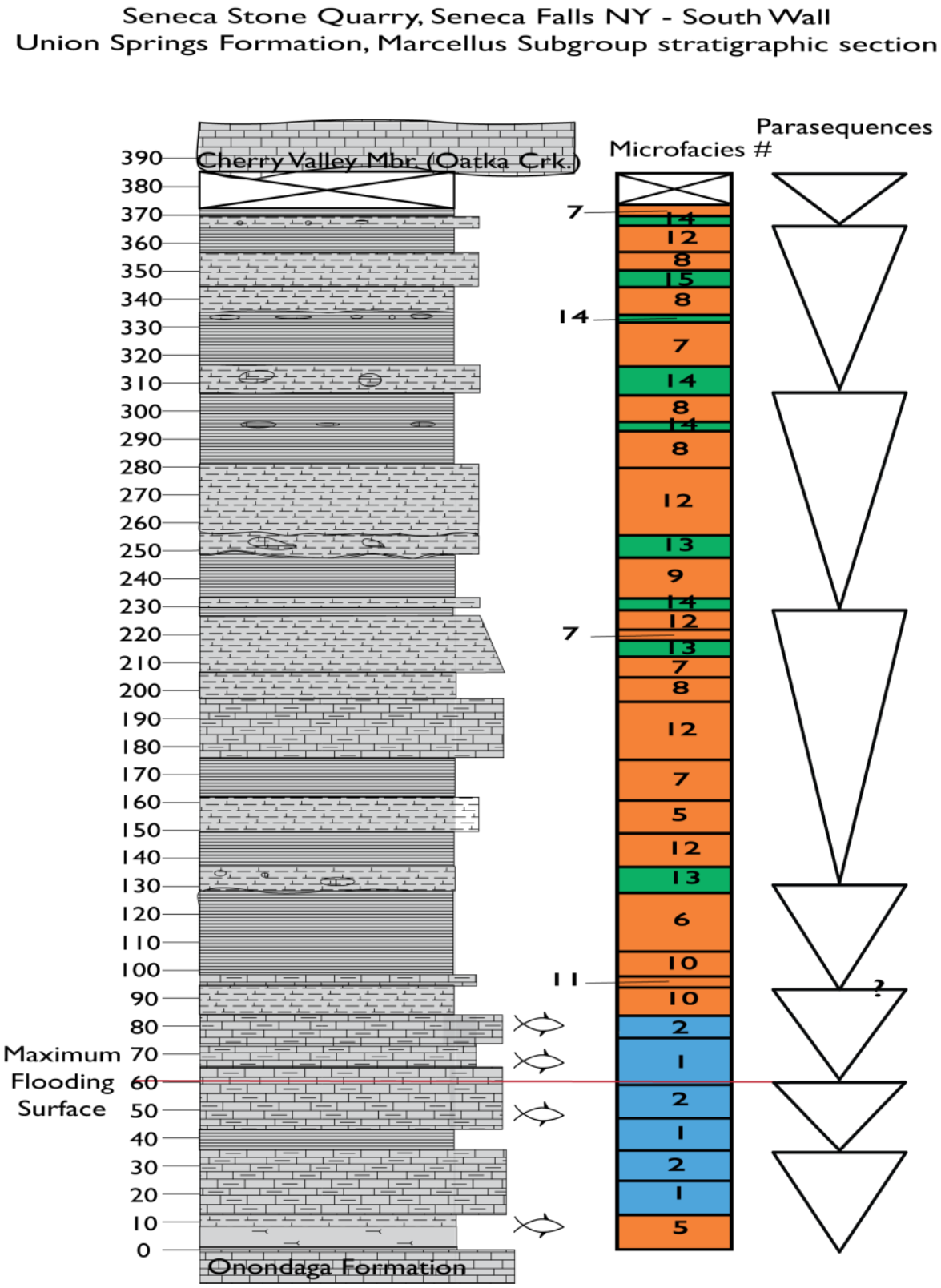

Figure 29: Stratigraphic section described at the south wall of the Seneca Stone Quarry in Seneca Falls, NY, including identified microfacies and parasequences. Fish symbols indicate bone-rich horizons.

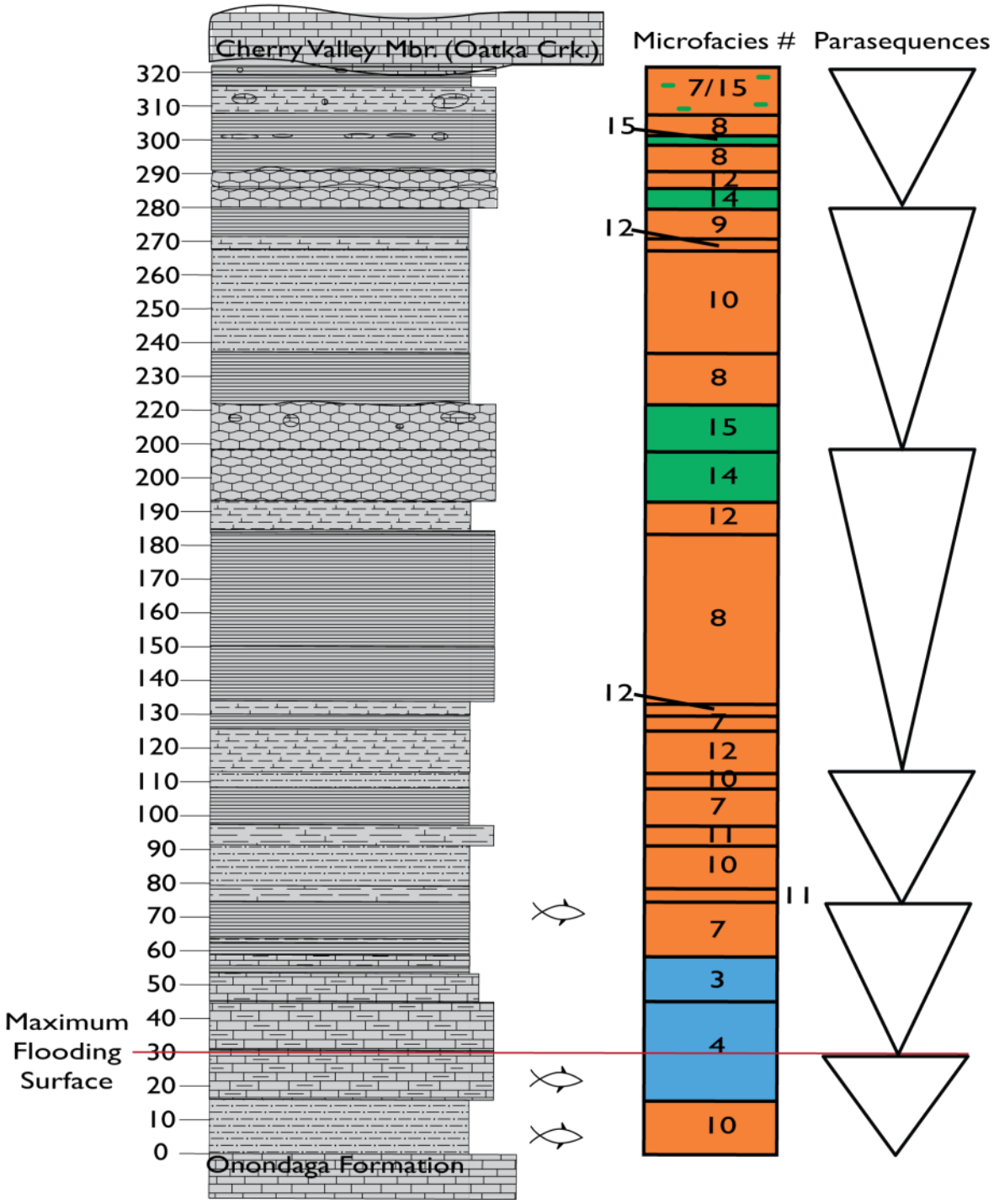

Figure 30: Stratigraphic section described at the south wall of the Saunders quarry in Marcellus, NY, including identified microfacies and parasequences. Fish pictures indicate bone-rich horizons.

Gamma Ray Profile Interpretation

Gamma ray logs, tools which measure naturally-emitted radiation from rocks, can be used to examine changes of lithology among sedimentary beds in drillcore, in boreholes, or in outcrop. Extensive experience with this method has led to its wide deployment as a tool for the identification of parasequences, on the premise the emitted gamma radiation is high in clay-rich mudstone facies and in organic matter, and lower in either clay-lean siliciclastics or in shallow water limestones (Van Wagoner et al. 1990; Bohacs, 1998). In log analysis, parasequences are identified by gradually-decreasing emitted gamma radiation moving upward in a section, representing a shoaling-upwards facies progression, followed above by a parasequence-bounding spike to high values of gamma radiation, representative of a flooding surface (Van Wagoner et al., 1990). This interpretation technique is built upon the premise that clay and organic-rich facies are most abundant near parasequence-bounding flooding surfaces.

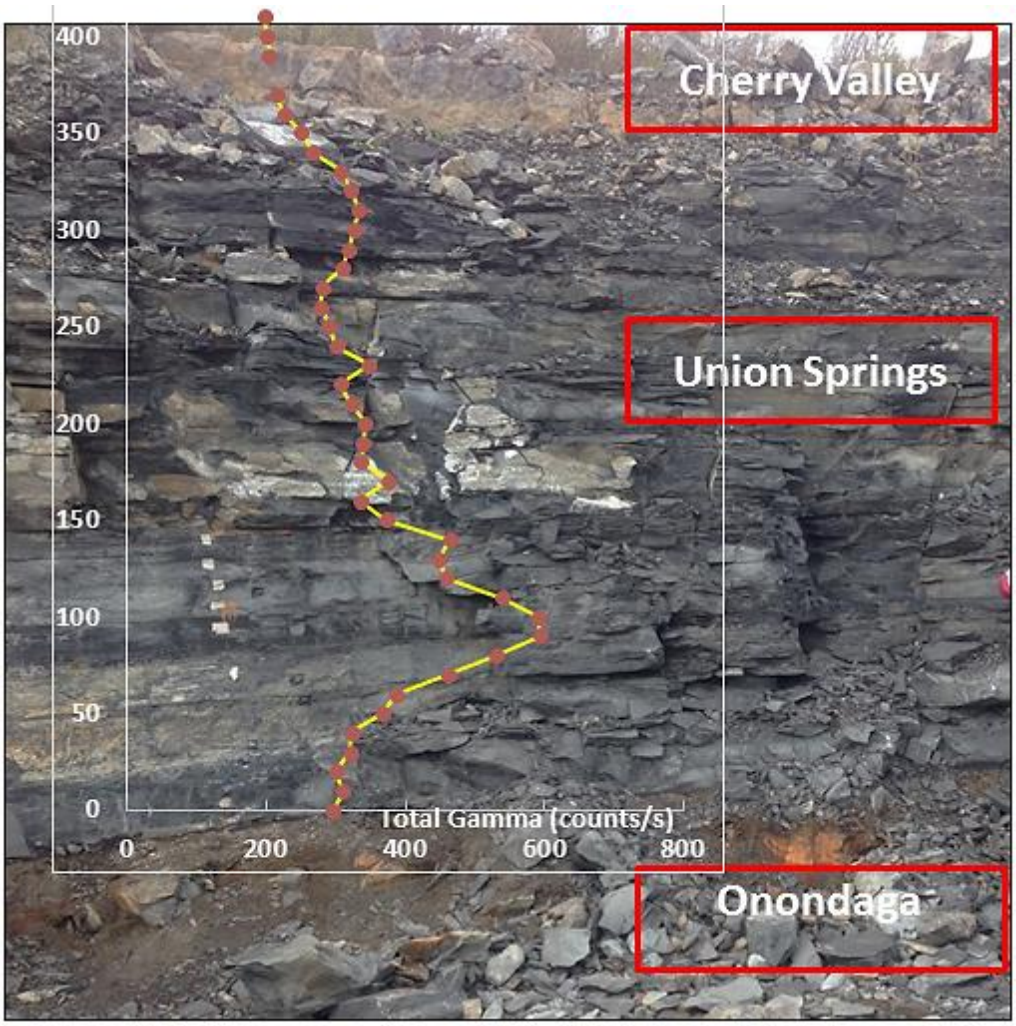

Figure 31: Gamma ray profile taken along the North wall of Seneca Stone Quarry (Seneca North site). Modified from from Joe Comisky, Son Dang, John Mason (unpublished field work).

Gamma ray measurements, spaced at 10 cm intervals along the *Seneca North* column, show a rising gamma signal moving upward from the limestones of the Onondaga Formation to roughly 100 cm above formation base (Figure 31). Although gamma ray maxima are commonly indicative of flooding surfaces (Van Wagoner et al., 1990; Bohacs, 1998), the maximum here exists nearly 40 cm higher in the section than the identified maximum flooding surface. This displacement at *Seneca North* is explained by considering that, at the time of maximum transgression, distal portions of the basin such as the study area were starved of siliciclastic

sediment and not receiving significant volumes of clay or silt. Rather, reworked pelagic carbonates with thin organic-rich interbeds and bone beds accumulated here during the time of maximum transgression. The organic-rich interbeds are expected to have a significantly high gamma ray signal, and organic rich beds from nearby stratigraphic positions contain amongst the highest organic carbon contents observed in the study area (~13%) (see Chapter 2). However, because the gamma ray detector has a vertical resolution on the order of 30 cm, the scale of these organic-rich horizons (< 3 cm) means that their high gamma-ray signature is only very weakly recorded, and measurements are significantly influenced by the surrounding strata of limestones, which produce very low levels of gamma radiation. During the deposition of the highest-gamma strata (at 90-100 cm above formation base), a geologically-brief regressional period had already begun and the study area was experiencing more prominent clay and silt sedimentation (Microfacies VI and VII at Seneca Falls and Marcellus, NY, respectively). In addition, the gamma-ray maximum is likely influenced by the high organic carbon content of adjacent strata which contain a shell-rich microfacies (Microfacies X) with significant secondary organic enrichment as a result of veins bearing organic matter, calcite and sulfide minerals

Within the highstand and falling stage systems tracts, a gradual drop in gamma ray signal reflects coarsening-up lithology. Peaks in the gamma ray signal such as those at 230 cm or 310 cm above formation base are useful for affirming the presence of parasequence boundaries (Figure 28). It should be noted that the gamma ray signal is lowered by the presence of concretions, and is affected whether these concretions are laterally continuous across 2 meters or 200 meters of outcrop. The gamma signal is useful here for discerning variations in grain size trends which are otherwise difficult to characterize, however,

petrography and outcrop description are better suited for parasequence characterization in concretion-rich areas of this highly condensed section.

Regional Parasequence Correlation

As detailed above, changes in rock properties identified within this work are used to inform a Union Springs sequence stratigraphic interpretation which broadly agrees with the framework outlined by Ver Straeten (2007). In the case of higher-order sequences, the interpretation presented here recognizes seven and eight parasequences at Seneca Falls and Marcellus, NY, respectively. This is similar to Kohl et al. (2014), who correlate seven parasequences that occur completely or partially during the deposition of the Union Springs. Kohl et al. (2014) acknowledge the substantial degree of interpretation involved in correlating at the parasequence level in mudstone successions utilizing gamma logs, particularly within the uppermost parasequences within the formation in question. Uncertainty undoubtedly exists regarding parasequence correlations between this work and Kohl et al. (2014), however important similarities exist. The maximum flooding surface in this study is placed in an analogous position stratigraphically low in the formation, and the *Seneca North* gamma ray signature is similar to that of Kohl et al. (2014) wells from central New York and western Pennsylvania (e.g. *Duddleston*, *J.P. Burke* wells) (Figure 28; Figure 31). This suggests that regional differences in sedimentation, chemical conditions, and basin topography do not completely obfuscate the correlation of high-order sequence stratigraphic divisions across the basin, particularly between sections which occupy a similar basinal position.

Mechanical Stratigraphy

In order to begin to characterize the connection between mechanical rock properties and the facies identified in this study, exploratory mechanical characterization work was conducted on rocks exhibiting a wide range of sedimentologic properties. Micro-hardness measurements sampled regions hundreds of microns in diameter within three compositionally and texturally distinct samples found 60 meters from the *Seneca North* study site (Chapter 3; Karaca, 2012). Tests carried out on limestone (MFII — Dacryoconarid Wackestone) and carbonaceous mudstone (MF VII – Clay-Rich Quartz Silt-Bearing Carbonaceous Mudstone) found significant hardness variations across facies groups, with Vickers hardness values averaging 110 HV for the Limestone sample and 45 HV for the Carbonaceous Mudstone (Chapter 3). Mechanical heterogeneity even within one microfacies is sizable; in fact hardness varies considerably within a single bed. Makee & Goulas (2016) test numerous samples of Microfacies XII (*Clay and Calcareous Cement-Bearing Carbonaceous Mudstone*) and demonstrate that regions of one bed may exhibit hardnesses which vary by as much as 27% from the mean bed hardness. In the same study, fracture toughness measurements within one calcite cemented bed exhibited significant variability, although mean values agreed with previously reported results for Union Springs rocks with similar lithologic characteristics (Engelder, 2012; Makee & Goulas, 2016).

This inter- and intra-facies variability points to the abundance of calcite as a strong control on mechanical behavior in the northern Appalachian Basin. As the abundance of calcite increases, the studied rocks tend to become harder and more stiff (Chapter 3; Makee & Goulas,

2016). It should be noted that this trend is not universally true; however, it holds true for the depositional scenario studied here, in which calcite abundance is negatively correlated with the abundances of clay and organic carbon (see also Chapter 2; Chapter 3). Additional high-resolution mechanical testing across a wider compositional and textural range will further characterize the relationship between facies and mechanical properties.

Hardness and modulus measurements made at the micron scale within the same microfacies via nanoindentation demonstrated that even at the individual grain scale, the effects of surrounding materials influence materials properties measurements (Chapter 3). Surrounding materials may have variable effects on individual grain measurements, given the rock texture and mineralogy within an examined area, particularly when modulus contrasts are significant (Chapter 3, Carloni & Baker, 2017). Much work remains to be done in the realm of high-resolution mechanical characterization of mudstones, but work within the Union Springs Formation has demonstrated significant variability at every length scale, although facies characterization can help predict trends within data sets. The nanoscale characterization of mudstones is more closely examined in Chapter 3 utilizing a range of Union Springs samples.

Biotic Turnover

Fossils observed within the two limestone facies found at Marcellus, NY (Microfacies III and IV) contrast significantly with those found throughout the other identified facies. The fauna within this interval is deserving of further study, and could shed light on the dynamics of faunal turnover in the Devonian Appalachian Basin. The benthic faunal assemblage ascribed to the Bakoven Member of the Union Springs (studied here) is largely distinct from that of the

underlying Onondaga Formation as well as from the overlying Stony Hollow fauna of the Stony Hollow bioevent occurring late in Union Springs depositional time (Brett et al., 2009; DeSantis and Brett, 2011). The fauna found in the Marcellus, NY limestone facies, including trilobites, crinoids, and a diverse community of brachiopods, is distinct from the typical Bakoven fauna described in literature (Brett et al. 2009; Desantis and Brett 2011, Ver Straeten et al., 2011). This assemblage may represent holdover fauna from Onondaga depositional time, a time of widespread shallow-water carbonate deposition in the Appalachian Basin, which hosted an ecological-evolutionary subunit defined by a diverse assemblage which includes numerous brachiopods, corals, trilobites, gastropods, and crinoids (Brett et al., 2009). Alternatively, the Marcellus, NY assemblage, which occurs between 15 and 60 cm above the Onondaga-Union Springs contact, could represent the earliest incursion of "Old World Realm" Stony Hollow fauna, which is defined by a warm-water low-diversity assemblage of brachiopods, the crinoid *Haplocrinites clio*, and the trilobite *Dechenella haldemani* (Ver Straeten and Griffing, 1991; Brett et al. 2009, Desantis and Brett, 2011). It should be noted that order-level identifications of fauna in these rocks were generally not made in this study, because fossil specimens are tightly bound within the rocks in which they occur and thus can be best appreciated in thin sections. In the case of crinoids and trilobites, the fossils are almost universally disarticulated or fragmented.

Conclusion

By expanding upon high-resolution microfacies characterizations, describing their arrangement across length scales, refining their paleoenvironmental interpretations, and

describing their characteristic variability, this study greatly increases understanding of the paleoceanographic conditions during deposition of the Union Springs Formation, and makes use of microfacies information more applicable to exploration, development, and regulation of unconventional gas and oil activity. Three lithofacies groups comprised of fifteen microfacies reflecting primarily high-order environmental variability were identified within the stratigraphic sections at Seneca Falls, NY and Marcellus, NY. Based upon high-resolution facies interpretations of these sections, systems tract and parasequence divisions were established. All three studied sections were deposited in a distal mixed carbonate-siliciclastic system during a time of significant clastic sedimentation closer to the proximal basin margin to the southeast.

Basin-scale changes related to eustasy and tectonic subsidence were major controls on broad facies trends, but much more variability exists at a regional and local scale. Within one column, carbonaceous mudstones show variation with respect to primary silt composition, bedding character, pyrite abundance, cementation, organic matter morphology and enrichment, and fossil type and abundance. In the near field (hundreds of meters scale), microfacies patterns are laterally similar. Variability is introduced through concretion position and texture, secondary organic enrichment, and bioturbation. Furthermore, cementation after partial compaction is also laterally discontinuous and inconsistent in its intensity. Far field heterogeneity is somewhat more significant, and is typified by differences in the depositional environment, including ecological factors expressed by fossil assemblages, energy of tractive currents expressed by shell accumulations, silt abundance and composition, and bacterial activity just below the sediment-water interface expressed by concretions. There was also far field heterogeneity induced by significant variation in the magnitude of compaction

experienced by deposited sediment. The environmental differences arose from factors including water column oxygenation (and possibly water depth) during deposition of the Limestone lithofacies group, and a slightly higher-energy depositional environment during carbonaceous mudstone deposition at Marcellus, NY. Overall, whereas short distance variations are most readily ascribed to biological activity, the variations at scales of tens of kilometers reflect a combination of physical environmental processes as well as spatially diverse biological systems.

The further understanding of heterogeneity in the Union Springs Formation at the outcrop (m), lateral wellbore (100's of m), and far-field (10's of km) scale is relevant to research geologists, policymakers, energy companies, and landowners. Physical lithologic variability is relevant to modern properties of interest including rock mechanical behavior and resource potential. Better understanding of this variability enhances the ability to predict how and why physical rock properties change vertically and laterally across distances, and the multiple interacting length scales over which heterogeneity exists.

Appendix: Original Thicknesses of Deposited Sediment at Studied Locations

$$Thickness_0 = (Thickness_{present})/(1-f_{compaction})$$

where $f_{compaction}$ is equal to fractional compaction value. $0 \leq f_{compaction} \leq 1$

Case 1: Low Compaction (Lindemann and Schuele, 1996)

Assume Mudstone Compaction = 65%
Limestone Compaction = 20%
Concretion Compaction = 0%

Column	Facies Group	Present Thickness (cm)	$f_{compaction}$	Original Thickness (cm)
Seneca North	Limestone	57	.20	71
Seneca North	Carbonaceous Mudstone	232	.65	663
Seneca North	Concretion	98	0	98
Seneca North	Total	387		832
Marcellus Saunders	Limestone	44	.20	55
Marcellus Saunders	Carbonaceous Mudstone	239	.65	683
Marcellus Saunders	Concretion	39	0	39
Marcellus Saunders	Total	322		777

Case 2: Mean Compaction Values (Lindemann and Schuele, 1996)

Assume Mudstone Compaction = 75%

Limestone Compaction = 30%

Concretion Compaction = 10%

Column	Facies Group	Present Thickness (cm)	$f_{compaction}$	Original Thickness (cm)
Seneca North	Limestone	57	.30	81
Seneca North	Carbonaceous Mudstone	232	.75	928
Seneca North	Concretion	98	.10	109
Seneca North	Total	387		1118
Marcellus Saunders	Limestone	44	.30	63
Marcellus Saunders	Carbonaceous Mudstone	239	.75	956
Marcellus Saunders	Concretion	39	.10	43
Marcellus Saunders	Total	322		1062

Case 3: High Compaction (Lindemann and Schuele, 1996)

Assuming Limestone Compaction = 55 %

Mudstone Compaction = 90 %

Concretion Compaction = 20 %

Column	Facies Group	Present Thickness (cm)	$f_{compaction}$	Original Thickness (cm)
Seneca North	Limestone	57	.55	127
Seneca North	Carbonaceous Mudstone	232	.90	2320
Seneca North	Concretion	98	.20	123
Seneca North	Total	387		2570
Marcellus Saunders	Limestone	44	.55	98
Marcellus Saunders	Carbonaceous Mudstone	239	.90	2390
Marcellus Saunders	Concretion	39	.20	49
Marcellus Saunders	Total	322		2537

References

Allen, P. A., & Allen, J. R. (2013). *Basin analysis: Principles and application to petroleum play assessment*. John Wiley & Sons.

Arndt, S., Jørgensen, B. B., LaRowe, D. E., Middelburg, J. J., Pancost, R. D., & Regnier, P. (2013). Quantifying the degradation of organic matter in marine sediments: A review and synthesis. *Earth-science reviews*, *123*, 53-86.

Baird, G. C., & Brett, C. E. (1986). Submarine erosion on the dysaerobic seafloor: Middle Devonian corrasional disconformities in the Cayuga Valley region. In *58th Annual Meeting Guidebook, New York State Geological Association* (pp. 23-80).

Bohacs, K. M. (1998). "*Contrasting expressions of depositional sequences in mudrocks from marine to non-marine environs*.": in Schieber, J., Zimmerle, W., and Sethi, P.S., eds., *Shales and Mudstones*: Schweizerbart'sche Verlagsbuchhandlung, Stuttgart, 33-78.

Boggs, S. (1995). *Principles of sedimentology and stratigraphy* (Vol. 3). New Jersey: Prentice Hall.

Boyer, D. L., & Droser, M. L. (2009). Palaeoecological patterns within the dysaerobic biofacies: Examples from Devonian black shales of New York state. *Palaeogeography, Palaeoclimatology, Palaeoecology*, *276*(1), 206-216.

Boyer, D. L., Owens, J. D., Lyons, T. W., & Droser, M. L. (2011). Joining forces: Combined biological and geochemical proxies reveal a complex but refined high-resolution palaeo-oxygen history in Devonian epeiric seas. *Palaeogeography, Palaeoclimatology, Palaeoecology*, *306*(3), 134-146.

Brett, C. E., & Baird, G. C.. (1986). Comparative Taphonomy: A Key to Paleoenvironmental Interpretation Based on Fossil Preservation. *PALAIOS*,*1*(3), 207–227.

Brett, C. E., & Ver Straeten, C. A. (1994). Stratigraphy and facies relationships of the Eifelian Onondaga Limestone (Middle Devonian) in western and west central New York State. In *66th Annual Meeting Guidebook: New York State Geological Association* (pp. 221-269).

Brett, C. E., & Baird, G. C. (1996). Middle Devonian sedimentary cycles and sequences in the northern Appalachian Basin. *SPECIAL PAPERS-GEOLOGICAL SOCIETY OF AMERICA*, 213-242.

Brett, C. E., Ivany, L. C., Bartholomew, A. J., DeSantis, M. K., & Baird, G. C. (2009). Devonian ecological-evolutionary subunits in the Appalachian Basin: a revision and a test of persistence and discreteness. Geological Society, London, Special Publications, 314(1), 7-36.

Brett, C. E., Baird, G. C., Bartholomew, A. J., DeSantis, M. K., & Ver Straeten, C. A. (2011). Sequence stratigraphy and a revised sea-level curve for the Middle Devonian of eastern North America. *Palaeogeography, Palaeoclimatology, Palaeoecology*, *304*(1), 21-53.

Bruner, K. R., Walker-Milani, M., & Smosna, R. (2015). Lithofacies of the Devonian Marcellus Shale In the Eastern Appalachian Basin, USA. *Journal of Sedimentary Research*, *85*(8), 937-954.

Carloni, J., Baker, S. P., (2017, in preparation). Measuring the elastic modulus and hardness of particles within a dissimilar matrix using instrumented indentation.

Catuneanu, O. (2002). Sequence stratigraphy of clastic systems: concepts, merits, and pitfalls. *Journal of African Earth Sciences*, *35*(1), 1-43.

Catuneanu, O., Abreu, V., Bhattacharya, J. P., Blum, M. D., Dalrymple, R. W., Eriksson, P. G., ... & Winker, C. (2009). Towards the standardization of sequence stratigraphy. *Earth-Science Reviews*, *92*(1), 1-33.

Conkin, J. E., & Conkin, B. M. (1984). Paleozoic Metabentonites of North America: Devonian Metabentonites in the Eastern United States and Southern Ontario: Their Identities, Stratigraphic Positions and Correlation. University of Louisville.

DeSantis, M. K., & Brett, C. E. (2011). Late Eifelian (Middle Devonian) biocrises: timing and signature of the pre-Kačák Bakoven and Stony Hollow events in eastern North America. *Palaeogeography, Palaeoclimatology, Palaeoecology*, *304*(1), 113-135.

Dix, G. R., & Mullins, H. T. (1987). Shallow, subsurface growth and burial alteration of Middle Devonian calcite concretions. *Journal of Sedimentary Research*, *57*(1).

Droser, M. L., & Bottjer, D. J. (1986). A semiquantitative field classification of ichnofabric: Research method paper. *Journal of Sedimentary Research*, *56*(4).

Dunham, R. J., & American Association of Petroleum Geologists. (1962). *Classification of carbonate rocks according to depositional texture*. Tulsa, Okla.: American Association of Petroleum Geologists.

Engelder, T., (2012). A Geomechanical Model for Gas Shales Based on the Integration of Stress Measurements and Petrophysical Data from the greater Marcellus Gas System. RPSEA. Annual Report.

Ettensohn, F. R. (1985). The Catskill delta complex and the Acadian orogeny: A model. *Geological Society of America Special Papers*, *201*, 39-50.

Fisher, D.W. 1962. Small conoidal shells of uncertain affinities. In: R.C. Moore (ed.), Treatise on Invertebrate Paleontology, Part W, Miscellanea, 98–143. The Geological Society of America and University of Kansas Press, Lawrence, Kansas

Flügel, E. (2004). Microfacies of Carbonate Rocks: Analysis, Interpretation and Application: Springer.

Griffing, D. H., & Ver Straeten, C. A. (1991). Stratigraphy and depositional environments of the lower part of the Marcellus Formation (Middle Devonian) in eastern New York State. In New York State Geological Association 63rd Annual Meeting, SUNY Oneonta (pp. 205-234).

Johnson, J. G., Klapper, G., & Sandberg, C. A. (1985). Devonian eustatic fluctuations in Euramerica. Geological Society of America Bulletin, 96(5), 567-587.

Jordan, T. E. (1981). Thrust loads and foreland basin evolution, Cretaceous, western United States. AAPG bulletin, 65(12), 2506-2520.

Karaca, C. (2012). Characterization of the Union Springs Formation, Finger Lakes Region, NY: An Integrated High Resolution Facies, Geochemical And Sequence Stratigraphical Approach. Cornell University. Thesis.

Kesler, S. E. (1996). Appalachian Mississippi Valley-type deposits: Paleoaquifers and brine provinces. Society of Economic Geologists Special Publication, 4, 29-57.

King, G. E. (2010, January). Thirty years of gas shale fracturing: What have we learned?. In *SPE Annual Technical Conference and Exhibition*. Society of Petroleum Engineers.

Kohl, D. R. (2012). Sequence Stratigraphy and Depositional Environments of the Shamokin (Union Springs) Mbr., Marcellus Fm. And Associated Strata in the Middle Appalachian Basin. Pennsylvania State University. Thesis.

Kohl, D., Slingerland, R., Arthur, M., Bracht, R., & Engelder, T. (2014). Sequence stratigraphy and depositional environments of the Shamokin (Union Springs) Member, Marcellus Formation, and associated strata in the middle Appalachian Basin. *AAPG bulletin*, *98*(3), 483-513.

Lash, G. G., & Blood, D. R. (2014). Organic matter accumulation, redox, and diagenetic history of the Marcellus Formation, southwestern Pennsylvania, Appalachian basin. *Marine and Petroleum Geology*, *57*, 244-263.

Lash, G. G., & Engelder, T. (2011). Thickness trends and sequence stratigraphy of the Middle Devonian Marcellus Formation, Appalachian Basin: Implications for Acadian foreland basin evolution. *AAPG bulletin*, *95*(1), 61-103.

Laughrey, C. D., Ruble, T. E., Lemmens, H., Kostelnik, J., Butcher, A. R., Walker, G., & Knowles, W. (2011). AV Black Shale Diagenesis: Insights from Integrated High-Definition Analyses of Post-Mature Marcellus Formation Rocks, Northeastern Pennsylvania. *AAPG Search and Discovery.* Article 110150.

Lazar, O. R., Bohacs, K. M., Macquaker, J. H., Schieber, J., & Demko, T. M. (2015). Capturing key attributes of fine-grained sedimentary rocks in outcrops, cores, and thin sections: nomenclature and description guidelines. *Journal of Sedimentary Research*, *85*(3), 230-246.

Lindemann, R.H. & Schuele, F.R. 1996. Mechanical compaction in Middle Devonian limestones of the Onondaga and Marcellus Formations at Cherry Valley, New York. Northeastern Geology and Environmental Sciences, 15, 219–229.

Macquaker, J. H., & Adams, A. E. (2003). Maximizing information from fine-grained sedimentary rocks: an inclusive nomenclature for mudstones. *Journal of Sedimentary Research*, *73*(5), 735-744.

Makee, D., Goulas, J., (2016). Micromechanical Characterization of Marcellus Shale. Cornell University. Master of Engineering Project Report.

McHargue, T. R., & Price, R. C. (1982). Dolomite from clay in argillaceous or shale-associated marine carbonates. *Journal of Sedimentary Research*, *52*(3).

Mitchum Jr, R. M., Vail, P. R., & Thompson III, S. (1977). Seismic stratigraphy and global changes of sea level: Part 2. The depositional sequence as a basic unit for stratigraphic analysis: Section 2. Application of seismic reflection configuration to stratigraphic interpretation.

Morad, S. (Ed.). (2009). *Carbonate Cementation in Sandstones: Distribution Patterns and Geochemical Evolution (Special Publication 26 of the IAS)* (Vol. 72). John Wiley & Sons.

Posamentier, H.W., Jervey, M.T., Vail, P.R. (1988), Eustatic Controls On Clastic Deposition. I. Conceptual Framework. In: Wilgus, C.K., Hastings, B.S., Kendall, C.G.St.C., Posamentier, H.W., Ross, C.A., Van Wagoner, J.C. (Eds.), Sea Level Changes—An Integrated Approach, vol. 42. SEPM Special Publication, pp. 110– 124.

Raiswell, R. (1971). The growth of Cambrian and Liassic concretions.*Sedimentology*, *17*(3-4), 147-171.

Raiswell, R. (1976). The microbiological formation of carbonate concretions in the Upper Lias of NE England. *Chemical Geology*, *18*(3), 227-244.

Raiswell, R. (1987). Non-steady state microbiological diagenesis and the origin of concretions and nodular limestones. *Geological Society, London, Special Publications*, *36*(1), 41-54.

Raiswell, R., & Fisher, Q. J. (2000). Mudrock-hosted carbonate concretions: a review of growth mechanisms and their influence on chemical and isotopic composition. *Journal of the Geological Society*, *157*(1), 239-251.

Sageman, B. B., Murphy, A. E., Werne, J. P., Ver Straeten, C. A., Hollander, D. J., & Lyons, T. W. (2003). A tale of shales: the relative roles of production, decomposition, and dilution in the accumulation of organic-rich strata, Middle–Upper Devonian, Appalachian basin. *Chemical Geology*, *195*(1), 229-273.

Schieber, J. (1986). The possible role of benthic microbial mats during the formation of carbonaceous shales in shallow Mid-Proterozoic basins. *Sedimentology*, *33*(4), 521-536.

Schieber, J. (2003). Simple gifts and buried treasures—implications of finding bioturbation and erosion surfaces in black shales. *The Sedimentary Record*, *1*(2), 4-8.

Schieber, J. (2009). Discovery of agglutinated benthic foraminifera in Devonian black shales and their relevance for the redox state of ancient seas. *Palaeogeography, Palaeoclimatology, Palaeoecology*, *271*(3), 292-300.

Schieber, J. (2016). Mud re-distribution in epicontinental basins—Exploring likely processes. *Marine and Petroleum Geology*, *71*, 119-133.

Schieber, J., Wintsch, R.P., 2005. Scanned Colour Cathodoluminescence Establishes a Slate Belt Provenance for Detrital Quartz in Devonian Black Shales of the Appalachian Basin. 15th Annual Goldschmidt Conference. Geoch. Cosmoch. Acta 10 (Suppl. 1), A592.

Scotese, C. R., & McKerrow, W. S. (1990). Revised world maps and introduction. Geological Society, London, Memoirs, 12(1), 1-21.

Selleck, B. (2014). GEOCHEMISTRY AND SULFIDE MINERAL PARAGENESIS IN MARCELLUS SUBGROUP AND UTICA FORMATION GAS SHALE INTERVALS. In *Geological Society of America Abstracts with Programs* (Vol. 46, No. 2, p. 98). Presentation.

Speyer, S. E., & Brett, C. E. (1988). Taphofacies models for epeiric sea environments: Middle Paleozoic examples. *Palaeogeography, Palaeoclimatology, Palaeoecology*, *63*(1-3), 225-262.

Tribovillard, N., Algeo, T. J., Lyons, T., & Riboulleau, A. (2006). Trace metals as paleoredox and paleoproductivity proxies: an update. *Chemical geology*, *232*(1), 12-32.

Vail, P. R., Mitchum Jr, R. M., & Thompson III, S. (1977). Seismic Stratigraphy and Global Changes of Sea Level: Part 4. Global Cycles of Relative Changes of Sea Level: Section 2. Application of Seismic Reflection Configuration to Stratigraphic Interpretation. *American Association of Petroleum Geologists Memoir*, *26*, 83-97.

Van Wagoner, J. C., Posamentier, H., Mitchum, R., Vail, P., Sarg, J., Loutit, T., & Hardenbol, J. (1988). An overview of the fundamentals of sequence stratigraphy and key definitions.

Van Wagoner, J. C., Mitchum, R. M., Campion, K. M., & Rahmanian, V. D. (1990). Siliciclastic sequence stratigraphy in well logs, cores, and outcrops: concepts for high-resolution correlation of time and facies. *AAPG Methods in Exploration, No. 7.*

Ver Straeten, C. A. (2004). K-bentonites, volcanic ash preservation, and implications for Early to Middle Devonian volcanism in the Acadian Orogen, eastern North America. *Geological Society of America Bulletin*, *116*(3-4), 474-489.

Ver Straeten, C. A. (2007). Basinwide stratigraphic synthesis and sequence stratigraphy, upper Pragian, Emsian and Eifelian stages (Lower to Middle Devonian), Appalachian Basin. *Geological Society, London, Special Publications*, *278*(1), 39-81.

Ver Straeten, C. A. (2010). Lessons from the foreland basin: Northern Appalachian basin perspectives on the Acadian orogeny, *in* Tollo, R.P., Bartholomew, M.J., Hibbard, J.P., and Karabinos, P.M., eds., From Rodinia to Pangea: The Lithotectonic Record of the Appalachian Region: Geological Society of America Memoir 206, p. 251–282.

Ver Straeten, C. A., Griffing, D. H., & Brett, C. E. (1994). The lower part of the Middle Devonian Marcellus "Shale," central to western New York State; stratigraphy and depositional history. *Guidebook—New York State Geological Association*, *66*(1994), 271-323.

Ver Straeten, C. A., & Brett, C. E. (2006). Pragian to Eifelian strata (middle Lower to lower Middle Devonian), northern Appalachian Basin-stratigraphic nomenclatural changes. *Northeastern Geology and Environmental Sciences*, *28*(1), 80.

Ver Straeten, C.E., BAIRD, G., BRETT, C., LASH, G., OVER, J., KARACA, C., JORDAN, T. and BLOOD, R. (2011). The Marcellus subgroup in its type area, Finger Lakes area of New York, and beyond. *Guidebook—New York State Geological Association, 83(2011), 1-64*.

Ver Straeten, C. A., Brett, C. E., & Sageman, B. B. (2011b). Mudrock sequence stratigraphy: a multi-proxy (sedimentological, paleobiological and geochemical) approach, Devonian Appalachian Basin. *Palaeogeography, Palaeoclimatology, Palaeoecology*, *304*(1), 54-73.

Wilson, D. D., & Brett, C. E. (2013). Concretions as sources of exceptional preservation, and decay as a source of concretions: Examples from the Middle Devonian of New York. *Palaios*, *28*(5), 305-316.

Wittmer, J. M., & Miller, A. I. (2011). Dissecting the global diversity trajectory of an enigmatic group: The paleogeographic history of tentaculitoids. *Palaeogeography, Palaeoclimatology, Palaeoecology*. *312*(1), 54-65.

Zapata, A. (2014). Geological Characterization of the Union Springs Formation, Lower Marcellus Shale in the Appalachian Basin, Central New York. Brooklyn College. Thesis.

CHAPTER TWO

Compositional Investigation of the Union Springs Formation of Central New York: Geochemical Analysis from a Sedimentologic Perspective

Introduction

Similar to most natural and manmade materials, sedimentary rocks can be defined in part by the things which comprise them. Other factors, including the arrangement, condition, and age of constituent materials are certainly important, but knowledge of composition is vital for a deep understanding of the conditions under which the rock was formed as well as of modern physical and mechanical properties relevant to resource characterization. As rock characterization technology has developed and proliferated, new methods to collect compositional data quickly, accurately and at high spatial resolution have become more commonplace. This study uses compositional signals (i.e. chemical composition) to form conclusions regarding modern rock properties and the geologic past, and compares geochemical evidence against broader physically-observed characteristics in an effort to assess the efficacy of commonly-employed compositional analysis techniques.

The Marcellus Subgroup (Ver Straeten and Brett, 2006) has been the focus of numerous recent compositional investigations (Werne et al., 2002; Sageman et al. 2003; Ver Straeten et al., 2011; Karaca, 2012; Lash and Blood, 2014; Zapata, 2014; Wendt et al. 2015). This study focuses on the Union Springs Formation, the basal formation within the Marcellus, and provides a high-resolution chemical analysis of condensed Union Springs strata across a range of length

scales in the northern Appalachian Basin. Major element, trace element, and total organic carbon abundances of rocks whose depositional categories have been determined through independent physical methods are measured. Data are subsequently examined inter-formationally within a sedimentologic and sequence stratigraphic context.

Geologic Context

The Union Springs Formation was deposited in the Acadian foreland basin during the Eifelian (Middle Devonian) at roughly 30˚S latitude (Scotese and McKerrow, 1990). At this time, a pulse of orogenic activity at the eastern basin margin led to reactivation of tectonic subsidence which, combined with rising eustatic sea level, led to the drowning of the relatively shallow-water carbonates of the underlying Onondaga Formation (Ettensohn, 1985; Brett and Baird, 1996; Brett et al. 2011). This orogenic uplift also led to a resurgence of siliciclastic-dominated deposition (Ver Straeten, 2010), represented by the 180 meter thick package of Union Springs Formation present in the proximal regions of the basin (Ver Straeten and Brett, 2006). The Union Springs thins moving north and west toward the study areas in central New York (Ver Straeten et al., 1994), where present-day thicknesses measure less than four meters.

Within this study area, three complete sections of the Union Springs Formation were sampled and described in detail (Chapter 1). Studied sections include two locations at Seneca Stone Quarry in Seneca Falls, NY separated by 600 m (*Seneca North and Seneca South*), and one section roughly 38.6 km away at the Saunders Quarry in Marcellus, NY (*Marcellus, NY*) (Figure 1). The sections are irregularly-spaced and oriented roughly along strike in order to examine variability within and between stratigraphic columns located within similar depositional

settings. Rocks were classified into facies categories based upon observed physical properties relevant to their depositional origin. Chapter 1 of this work sheds light on the physical characteristics of the studied sections and their relationships to depositional processes and to the sequence stratigraphy of the Devonian Acadian Basin.

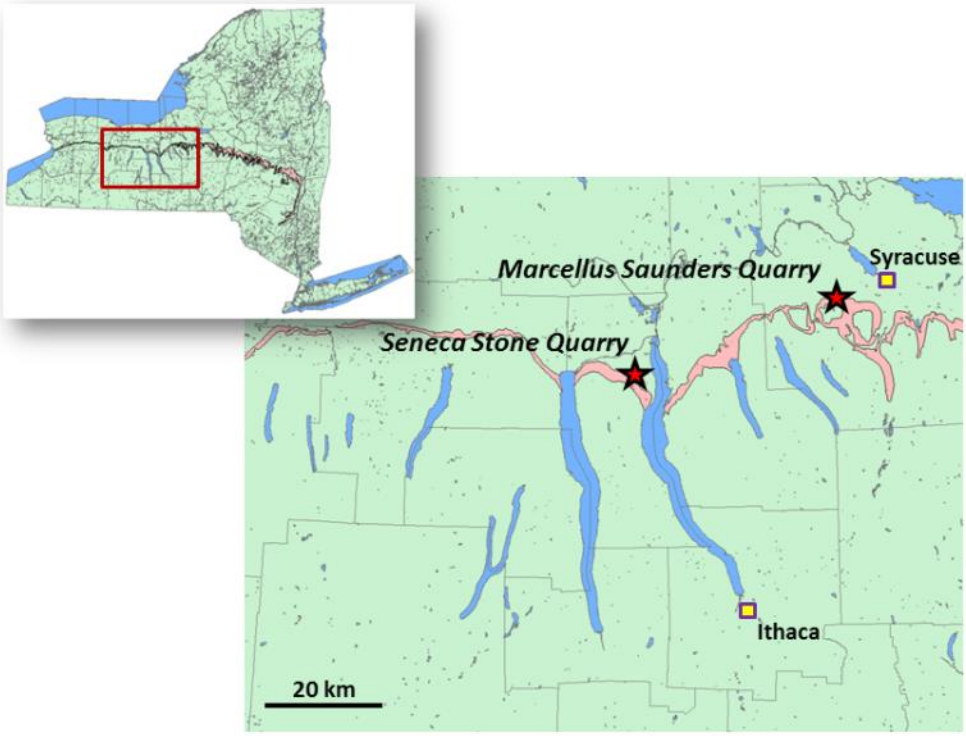

Figure 1: Study area in Finger Lakes region of central New York. Studied columns of Union Springs Formation are marked with red stars.

Figure 2 gives an example of the results of the high-resolution facies analysis executed in Chapter 1. Physical rock properties define three broad lithofacies groups: Limestone, Carbonaceous Mudstone, and Calcareous Concretion. These three lithofacies groups were further divided into 15 higher-order microfacies based upon properties such as mineralogy, bedding character, and fossil assemblage (Appendix A). Vertical successions of microfacies

reveal patterns used to identify parasequences within the column. By placing the Union Springs Formation in the study area within a sequence stratigraphic framework, stratigraphic relationships to regional tectonics and faunal variations can be established (Ver Straeten, 2007; Brett et al., 2011). High-resolution regional correlation of units and surfaces is important for both paleoenvironmental reconstruction and the characterization of petrophysical properties and potential fluid flow pathways (Cross et al. 1993).

This work incorporates geochemical analysis into the previously assembled data in order to strengthen physical interpretation and provide additional knowledge of paleo-oceanographic conditions during the Middle Devonian. The Union Springs is studied towards the distal basin margin, which facilitates the study of primary organic productivity in the Devonian oceans as well as the redox conditions near the paleodepositional substrate, with diminished interference from tectonically-controlled fluctuations in terrigenous input, which can dilute organic carbon concentrations (Sageman et al., 2003). Additionally, this work describes the relationships between compositional properties of the Union Springs, and depositional and diagenetic features such as bioturbation and cementation.

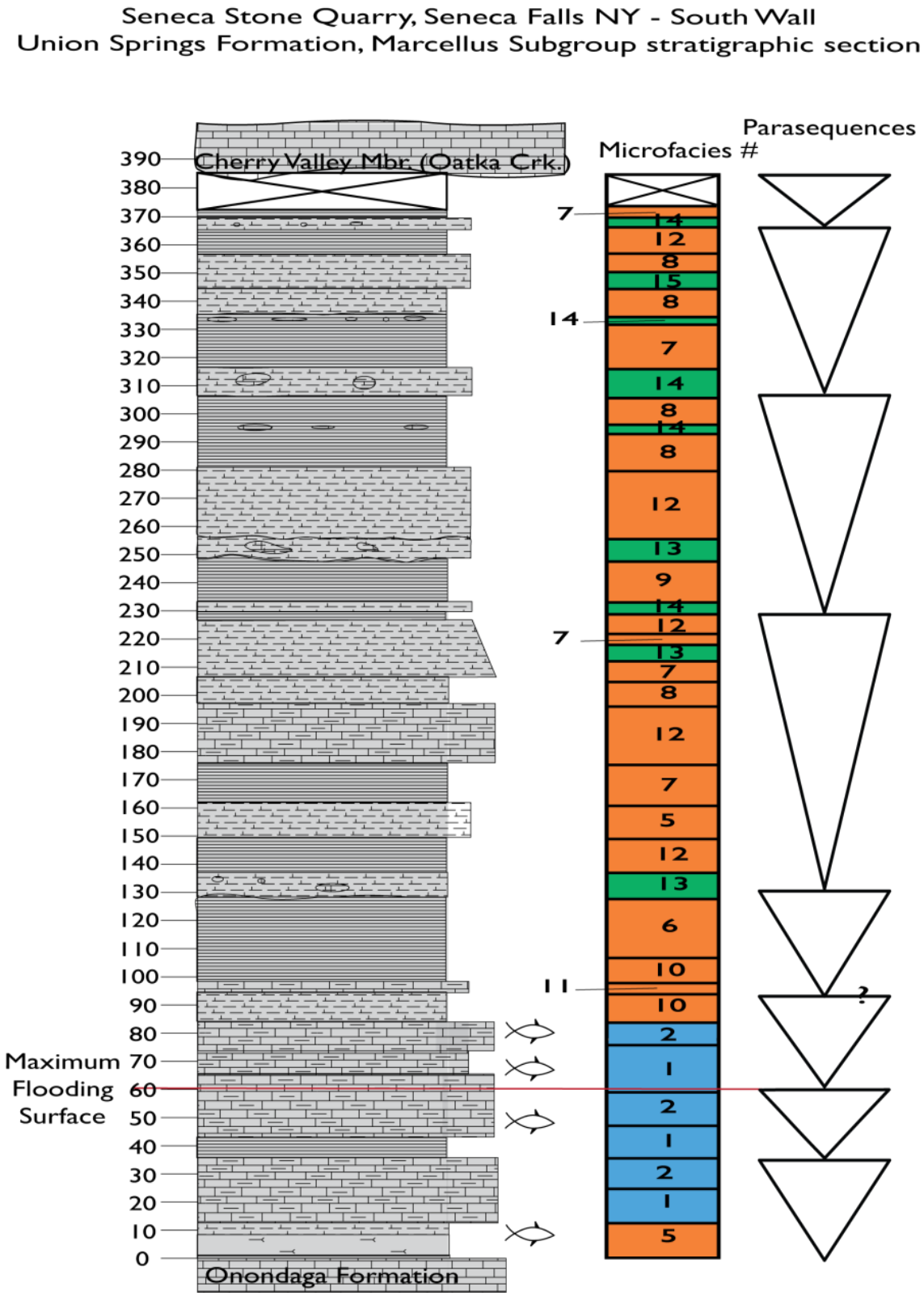

Figure 2: Sedimentological analysis for the South Wall of Seneca Stone Quarry in Seneca Falls, NY (Chapter 1). Microfacies numbers can be found in Appendix A. Vertical axis in cm above formation base. See Appendix A for microfacies identification.

Characterization Methods

Laboratory Analyses

Elemental abundance data was collected for samples of fresh, largely unweathered quarry outcrop; the same samples had been characterized previously by petrographic and scanning electron microscopy. X-ray fluorescence scans were taken from representative areas of each sample; samples that were heterogeneous were scanned in multiple sub-areas deemed to be representative of the variability. The elemental data were obtained using a Bruker Tracer IV handheld x-ray spectrometer at the University of Kentucky Stratigraphy Laboratory. Data for major rock-forming elements was collected using 15 keV and a 35µA current under a ~9 torr vacuum, to remove the possible influence of environmental factors. For trace elements, 40 keV and 15µA current was used. Scans were run for 90 seconds in both tests on clean, flat surfaces. Instrument calibration utilized Bruker proprietary software (S1CALPROCESS with TR2.cfz and MA1.cfz) and the reference catalog of mudrock chemistry described by Rowe et al. (2012). Internal consistency of the XRF was verified by routine scanning of the SARM41 shale standard (Ring, 1989). The sampling spot size is 3 mm in diameter, therefore features smaller than this size cannot be completely isolated, although they may still influence the signal of the data. X-ray count data was converted to weight percent data using the Bruker mudstone calibration, based on a wide variety of mudstone reference standards. This calibration is designed to deliver accurate data for a wide range of mudstone compositions. Total organic carbon content was measured via LECO carbon analysis and a UIC carbonate coulometer. Carbon measurements were conducted using powders (grain size < 125µm) which sampled roughly 0.25 cm^3 of each

rock being tested. Measurement precision, based on analysis of internal standards, was typically better than $\pm$ 0.15%.

Principal component analysis was performed on the data set in order to better understand variability and relationships between tested compositional characteristics of the sample suite. Analysis included 24 elements measured via XRF, total organic and inorganic carbon content, and bioturbation (Appendix B). The compositional data set was closed and transformed using additive log-ratio transformation after Aitchison (1986), in order to negate spurious correlations which can arise through multivariate statistical treatments of compositional data sets. The non-compositional parameter of bioturbation was then added into the compositional data set to run the analysis. Data transformation and principal components analysis were carried out using CoDaPack and PAST software, respectively (Comas-Cufí & Thió-Henestrosa, 2011; Hammer et al., 2001).

Utilizing Compositional Data for Paleoenvironmental Interpretation

Compositional data are used to decode paleoenvironmental conditions and the roles of detrital, biogenic, and authigenic fluxes to the depositional substrate (Sageman & Lyons, 2004). Aluminum, as a largely conservative and immobile element ubiquitous in clay minerals, is a particularly useful elemental proxy for detrital flux in mudstones (Arthur et al., 1985; Dean and Arthur, 1998; Young and Nesbitt, 1998), in which clay-sized grains comprise a significant volumetric percentage by definition. Abundances of titanium and silicon, typically measured against aluminum content, can be used to track the deposition of titanium oxides and quartz silt, respectively (Sageman and Lyons, 2004). These elements can serve as a proxy for fluvial or

aeolian terrigenous input into the basin. By comparing Ti and Si fluctuations in silt-sized grains versus clay grains, the depositional energy of the ancient environment can be interpreted (Murphy et al., 2000; Sageman and Lyons, 2004; Calvert and Pederson, 2007). The utility of silicon as a detrital proxy can be muddied by the presence of biogenic or diagenetic silica (Schieber et al., 2000; Werne et al., 2002; Sageman & Lyons, 2004), and for this reason the simultaneous examination of multiple terrigenous proxy elements is wise.

Trace metal concentrations in mudstones are commonly employed as indicators of redox conditions of depositional bottom waters during the time of deposition. One commonly utilized trace element, uranium, reduces from U(VI) to U(IV) in anoxic conditions, and can become enriched in sediment through complexing with organic matter or diffusing across the sediment-water interface and precipitating as an oxide (Klinkhammer & Palmer, 1991; Zheng et al., 2002; Algeo & Maynard, 2004; Tribovillard et al., 2006). Vanadium, present as V(V) in oxygenated marine settings, is reduced under anoxic conditions to V(IV), allowing for the formation of organometallic ligands (Tribovillard et al., 2006, and references therein). Under euxinic conditions (H_2S within the water column), it is possible for vanadium to be further reduced to V(III), facilitating the formation of vanadium oxides and hydroxides, and the substitution of vanadium for aluminum within clay minerals (Breit & Wanty, 1991; Tribovillard et al., 2006). Similarly, molybdenum may become immobilized in sediments under reducing conditions (Tribovillard et al., 2005). In marine systems with euxinic bottom-waters, molybdate ions present in seawater are converted to thiomolybdates, which can adsorb onto organic matter or iron and manganese oxyhydroxides at the sediment-water interface (Tribovillard et al., 2006; Algeo & Tribovillard, 2009). Because of the dependence of molybdenum enrichment

on the presence of hydrogen sulfide, U may become more enriched relative to Mo in sediments experiencing oxygen-limited conditions short of permanent anoxia and euxinia (Algeo & Tribovillard, 2009).

Organic carbon enrichment within rocks of marine origin is a result of complex interaction between primary productivity, dilution by non-organic sediments, and the preservation or destruction of organic matter in the water column or following deposition on the sea floor (Bohacs et al., 2005). High productivity depends upon high concentrations of nutrients and planktonic organisms in the water column, which are transported downward to the depositional substrate post-mortem (Murphy et al., 2000). Dilution of organic matter is a function of the flux of ocean-borne skeletal and terrigenous sediment to the substrate (Sageman et al., 2003; Bohacs et al., 2005). High dilution leads to a low concentration of organic carbon per unit sediment, whereas extremely low dilution leads to a sedimentation rate so low that the odds of organic carbon degradation increase (Bohacs et al., 2005). Organic carbon preservation requires that the chemical oxidation or biological uptake of organic carbon is slowed sufficiently to allow for accumulation within the substrate, and the rate of oxidation is slowed by the oxygen-limited conditions or the presence of free hydrogen sulfide in bottom waters. An alternative means to achieve the same result of preservation of organic carbon is a rate of mineral sedimentation which minimizes the exposure of organic carbon to potential physical, chemical, or biological destructors (Huc, 1980; Bohacs et al., 2005).

The extent to which organisms churn unconsolidated sediment on the seafloor is a measure of the water chemistry immediately above the sediment and within the sediment, and

thus is somewhat analogous to the elemental data obtained from lithified mudstones. Bioturbation indices can be used as a metric for establishing paleo-oxygenation levels in ancient environments (Savrda & Bottjer, 1986; Savrda & Bottjer, 1991; Droser & Bottjer, 1993; Boyer & Droser, 2009). These works associate increased bioturbation of sediment with increased bottom water oxygenation. Drops in benthic oxygen levels correspond with drops in sediment mixing, along with the diversity of species and of life habits of resident organisms (Wignall & Myers, 1988; Boyer & Droser, 2009). Combining bioturbation indices with trace element abundances leads to more refined paleoenvironmental interpretations (Boyer et al., 2011; Ver Straeten et al., 2011; Karaca, 2012).

Results

Lithofacies Groups

Selected element abundances for the identified lithofacies groups are presented in Table 1, alongside corresponding abundances for the average cratonic Phanerozoic shale from Condie (1993). Clear compositional differences between facies within the study area are highlighted. Elemental abundances for silicon and aluminum, elements found within clay minerals and other silicates, are elevated significantly within the Carbonaceous Mudstone lithofacies group. Within the Limestone and Calcareous Concretion lithofacies group, calcium is present at an average weight fraction approximately double that of the Carbonaceous Mudstone group. Compared to the average cratonic Phanerozoic shale (hereafter “average shale”), the major element concentration of these Union Springs samples is quite far from average. All three lithofacies groups, including the clay-rich Carbonaceous Mudstone group, contain significantly elevated abundances of calcium, which compensates for substantially

below-average amounts of silicon and aluminum. Silicon, aluminum, and titanium abundances of the Union Springs samples are far below those of the average shale (Table 1). Redox-sensitive trace elements uranium and molybdenum are quite enriched in the Carbonaceous Mudstone lithofacies group. For the Carbonaceous Mudstone lithofacies group, the enrichment factors of the studied samples against the average shale ($EF = \frac{X_{sample}/Al_{sample}}{X_{average}/Al_{average}}$) are 16.6 and 76.3 for uranium and molybdenum, respectively.

Table 1: Average elemental abundances for major elements (wt%) and trace elements (ppm) for identified lithofacies groups of Union Springs Formation. Standard deviations for each parameter given in parentheses. Composition for the Average Cratonic Phanerozoic Shale (Condie 1993) is given as a point of comparison.* TOC values measure total wt% carbon from organic solids; average value from Leeder (1982).

Element	Limestone (N = 15)	All Carbonaceous Mudstones (N = 59)	Calcareous Concretion (N = 27)	Average Cratonic Phanerozoic Shale (Condie 1993)
Al (wt%)	0.38 (.28)	2.98 (1.62)	0.58 (.58)	9.67
Si	3.96 (.63)	9.87 (4.40)	3.39 (1.46)	30.53
K	.38 (.13)	1.50 (.84)	.32 (.24)	3.94
Ca	35.50 (1.48)	22.52 (8.70)	35.61 (2.55)	0.95
Ti	0.04 (.01)	0.15 (.07)	0.05 (.02)	0.50
V (ppm)	53.69 (6.34)	218.41 (209.70)	54.50 (7.84)	117
U	6.13 (4.09)	16.09 (11.40)	2.75 (2.66)	2.9
Mo	0.22 (.40)	73.20 (81.47)	1.17 (2.34)	3.7
TOC (wt %)	2.02 (1.15)	7.94 (3.53)	2.80 (1.52)	2.1*
Bioturbation (1-6)	4.2	1.85	1	N/A

Intrafacies Variability

Significant compositional diversity with respect to major and trace elemental abundances exists within these facies groups, particularly the Carbonaceous Mudstone lithofacies group which consistently displays widest compositional range (Figure 3; Table 1). This is exemplified by Al, for which the Carbonaceous Mudstone ranges between values that are less than 5% to over 60% of the average shale values, while the two other lithofacies groups are consistently extremely depleted with respect to aluminum (Figure 3a). The Limestone group, despite the lower average clay content as suggested by aluminum abundances, contains several samples which approach five times the uranium enrichment of the average shale (Figure 3b; Table 2).

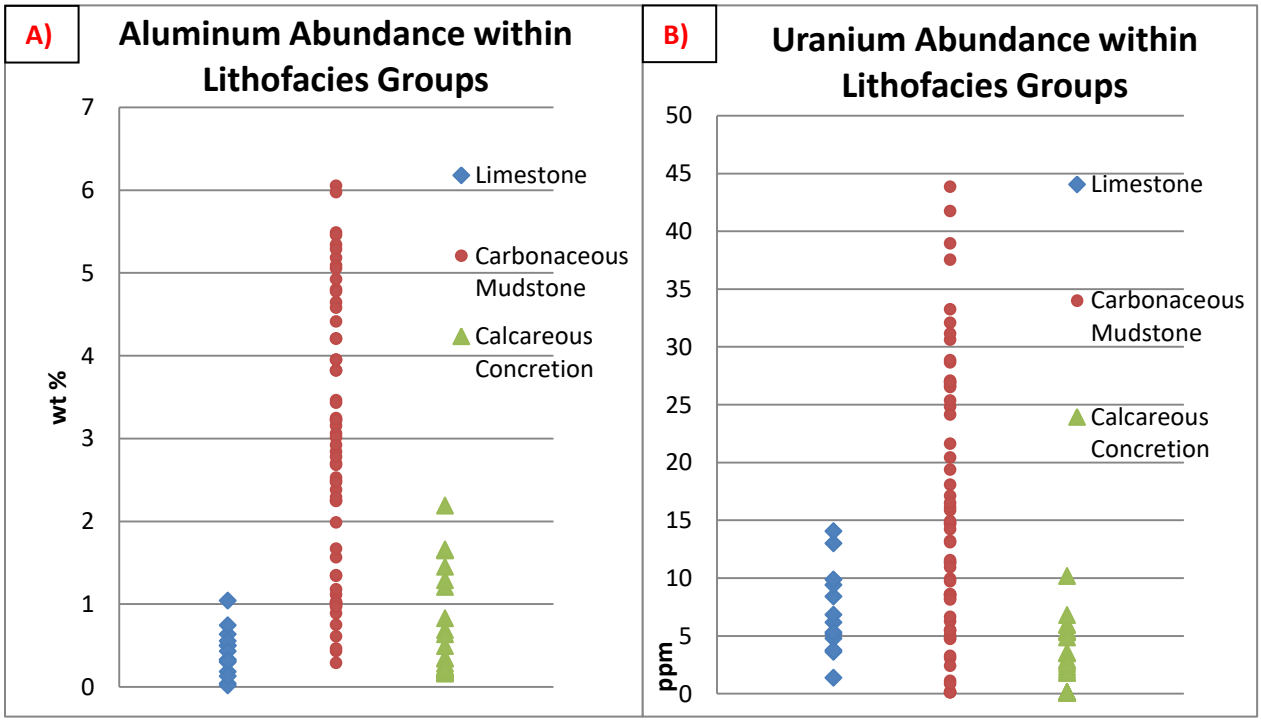

Figure 3: Aluminum (A) and Uranium (B) abundances organized by lithofacies group. Median aluminum values for [limestone, carbonaceous mudstone, and calcareous concretion] groups are [.33, 2.92, .24] measured in weight percent, while median uranium values are [5.32, 14.22, 2.30] measured in parts per million.

The next, most basic level of variability, where individual sample data can best be evaluated within a geologic context, is at the microfacies level. Table 2 shows the average abundances of selected elements within each of the fifteen identified microfacies (Appendix A), and illustrates the compositional diversity of the Carbonaceous Mudstone lithofacies group relative to the two other groups. Whereas Limestone and Calcareous Concretion microfacies rarely differ from one another by more than 1% for major elements or several parts per million for trace elements, Carbonaceous Mudstone microfacies may average as little as 12.81% (by weight) calcium, or as much as 31.86%. Molybdenum abundances in this group may resemble those found in the average shale (4.64 ppm), or may possess enrichment factors over 200 with respect to the average shale (Table 2).

Table 2: Average elemental abundances for microfacies identified across three sections of Union Springs Formation. See Appendix A and Chapter 1 of this work for further descriptive and sedimentologic information on each category. Standard deviations for each parameter given in parentheses. BI = Bioturbation index of Droser & Bottjer (1986).

Element	MF I (N=5)	MF II (N=6)	MF III (N=2)	MF IV (N=2)	MF V (N=2)	MF VI (N=3)	MF VII (N=12)	MF VIII (N=6)	MF IX (N=3)	MF X (N=13)	MF XI (N=2)	MF XII (N=18)	MF XIII (N=5)	MF XIV (N=7)	MF XV (N=15)
Al (wt %)	0.54 (0.15)	0.43 (0.32)	0.16 (0.15)	0.07 (0.06)	4.35 (1.13)	5.24 (0.77)	4.78 (0.76)	3.79 (0.45)	3.26 (0.52)	1.98 (0.97)	0.36 (0.07)	2.02 (1.16)	0.41 (0.4)	0.46 (0.4)	0.68 (0.68)
Si	4.49 (0.65)	3.81 (0.43)	3.62 (0.25)	3.4 (0.34)	12.83 (1.71)	15.48 (1.85)	15.28 (2.84)	11.52 (1.32)	10.28 (1.31)	7.26 (2.72)	3.25 (0.07)	7.15 (2.7)	2.99 (0.86)	3.13 (0.95)	3.65 (1.74)
K	0.44 (0.06)	0.41 (0.15)	0.3 (0.05)	0.23 (0.02)	2.7 (1.18)	2.78 (0.36)	2.33 (0.4)	1.87 (0.42)	1.58 (0.31)	1.03 (0.53)	0.23 (0.01)	0.98 (0.47)	0.26 (0.12)	0.3 (0.17)	0.35 (0.28)
Ca	34.41 (1.06)	35.79 (0.15)	35.36 (2.26)	37.55 (0.2)	19.39 (2.19)	12.41 (2.93)	12.05 (4.8)	19.99 (3.08)	19.59 (4.57)	25.75 (6.27)	31.86 (4.61)	29.62 (5.55)	36.78 (1.02)	36.88 (1.48)	34.63 (2.86)
Ti	0.05 (0)	0.04 (0.01)	0.03 (0.01)	0.03 (0)	0.17 (0.01)	0.25 (0.03)	0.23 (0.04)	0.19 (0.04)	0.17 (0.04)	0.11 (0.05)	0.03 (0.01)	0.11 (0.05)	0.04 (0.01)	0.04 (0.02)	0.05 (0.03)
Fe	0.47 (0.19)	0.4 (0.04)	0.42 (0.05)	0.46 (0.18)	1.81 (0.37)	3.6 (0.7)	3.5 (1.45)	2.26 (0.24)	2.93 (1.1)	1.54 (0.79)	1.13 (0.76)	1.26 (0.67)	0.75 (0.19)	0.71 (0.26)	1.16 (0.71)
V (ppm)	52.73 (5.33)	53.34 (7.12)	57.82 (5.6)	53.07 (5.25)	89.19 (47.42)	631.79 (212.7)	408.17 (243.19)	176.07 (166.14)	230.24 (41.14)	207.53 (112.32)	74.17 (8.86)	81.44 (43.45)	59.47 (3.36)	57.43 (5.48)	51.48 (8.46)
U	5.09 (3.73)	8.76 (3.89)	5.06 (0.26)	1.92 (1.82)	12.21 (3.66)	27.57 (8.94)	18.92 (11.21)	11.56 (8.5)	12.12 (2.84)	27.35 (8.73)	10.43 (5.71)	7.74 (6.26)	1.97 (2.41)	3.38 (2.57)	2.72 (2.72)
Mo	0.13 (0.06)	0.1 (0)	0.91 (0.81)	0.1 (0)	45.55 (37.1)	162.73 (67.44)	162.47 (98.82)	42.35 (23.32)	75.78 (2.72)	73.71 (63.8)	4.64 (0.69)	19.66 (27.39)	0.54 (0.88)	1.94 (3.05)	1.03 (2.2)
TOC (wt %)	1.44 (0.23)	2.73 (1.38)	2.5 (0)	1.06 (0.05)	8.8 (3.97)	11.67 (0.76)	10.95 (2.8)	7.9 (3.42)	8.33 (1.73)	8.00 (3.4)	5.82 (1.03)	4.62 (1.29)	2.91 (1.63)	3.27 (1.54)	2.42 (1.34)
BI	4.00	3.33	5.00	5.00	2.50	1.00	1.50	1.50	1.50	1.75	1.50	2.45	1.00	1.00	1.00

By examining the spread of elemental abundances within microfacies with respect to different elements, such as those shown in Figure 4, patterns emerge with respect to how compositionally constrained individual microfacies are. Compared to the bulk of the sample set, rocks belonging to Microfacies VII (*Clay-Rich Quartz Silt-Bearing Carbonaceous Mudstone)* exhibit low calcium abundances. The maximum calcium abundances within the entire data set approach 40%, however within Microfacies VII, values vary between roughly 5 and 20%, with an average abundance of 12.05% (Figure 4a, Table 2). This relatively small range does not apply for all elements, however, and this microfacies possesses the widest range of uranium abundances observed (Figure 4). For many microfacies, high levels of variability with respect to major element abundances correspond with trace element variability, but this pattern is not universal. Limestone and Calcareous Concretion samples are generally more compositionally constrained within microfacies, although some Limestone samples, particularly those from the Seneca Falls, NY field site (Microfacies I and II), exhibit moderate enrichments of redox-sensitive trace elements such as uranium (Figure 4).

Vertical trends in compositional data (Figure 5 and 6) are suited for cross-length-scale comparisons of the Union Springs Formation across the three columns within the study area, for the comparison of elemental abundances against sequence stratigraphic interpretations, and the temporal correspondence of physical and chemical attributes within one section. Figure 5 shows the microfacies categories and parasequences identified in Chapter 1 alongside abundance data for organic carbon, bioturbation, silicon and aluminum, and calcium at the *Seneca South* field site.

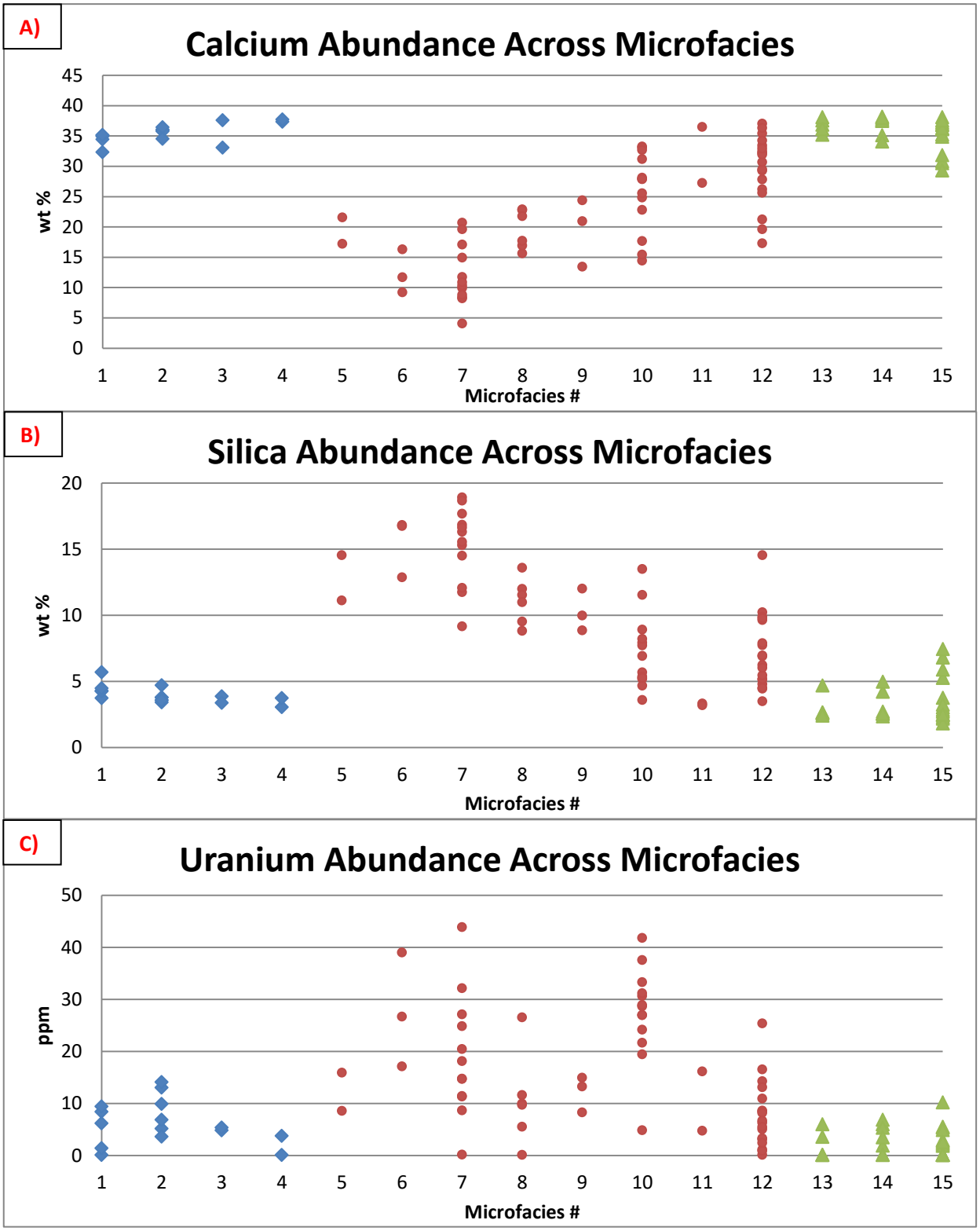

Figure 4: Variability in abundances of calcium (A), silica (B), and uranium (C) across each microfacies. Each data point represents one scanned sample. Average Shale enrichments of calcium, silica and uranium are .95%, 30.53%, and 2.9 ppm respectively (Condie, 1993).

Total organic carbon abundance is low (>2%) throughout the Limestone samples near the base, and significantly higher in overlying Carbonaceous Mudstones (Figure 5). Calcareous Concretions generally display TOC values similar to Limestone values, although some samples host thin carbon-rich veins acquired during diagenesis which boost the value into the 4% range. TOC abundances are highest in unbioturbated samples (index of 1 or 2) with high proportions of aluminum and silica, and lowest in the packstones near the maximum flooding surface (Figure 5). Bioturbation is prevalent moving upward from the underlying Onondaga Formation through the top of the Limestone lithofacies group, and then quickly diminishes; Carbonaceous Mudstones above this point generally exhibit bioturbation indices of 1-2. Aluminum and silica abundances are strongly correlated throughout the section (Figure 5). Calcium abundance, which is strongly tied to the amount of calcite observed in thin section, reaches nearly 40% in some concretionary and limestone horizons (Figure 5) and is present in distinct biogenic, micritic, and authigenic forms (see Discussion).

The abundances of the redox-sensitive trace elements uranium, molybdenum, and vanadium are shown for the *Seneca South* section in Figure 6. At the base of the section, Microfacies V (Quartz and Dolomite- Bearing Carbonaceous Mudstone), exhibits moderate uranium enrichment while molybdenum and vanadium abundances are largely flat moving upward from formation base to the top of the Limestone lithofacies group (Figure 6). Redox-sensitive trace elemental abundances within Microfacies V samples are not expected to be significantly impacted by the presence of dolomite precipitated during burial diagenesis (Chapter 1).

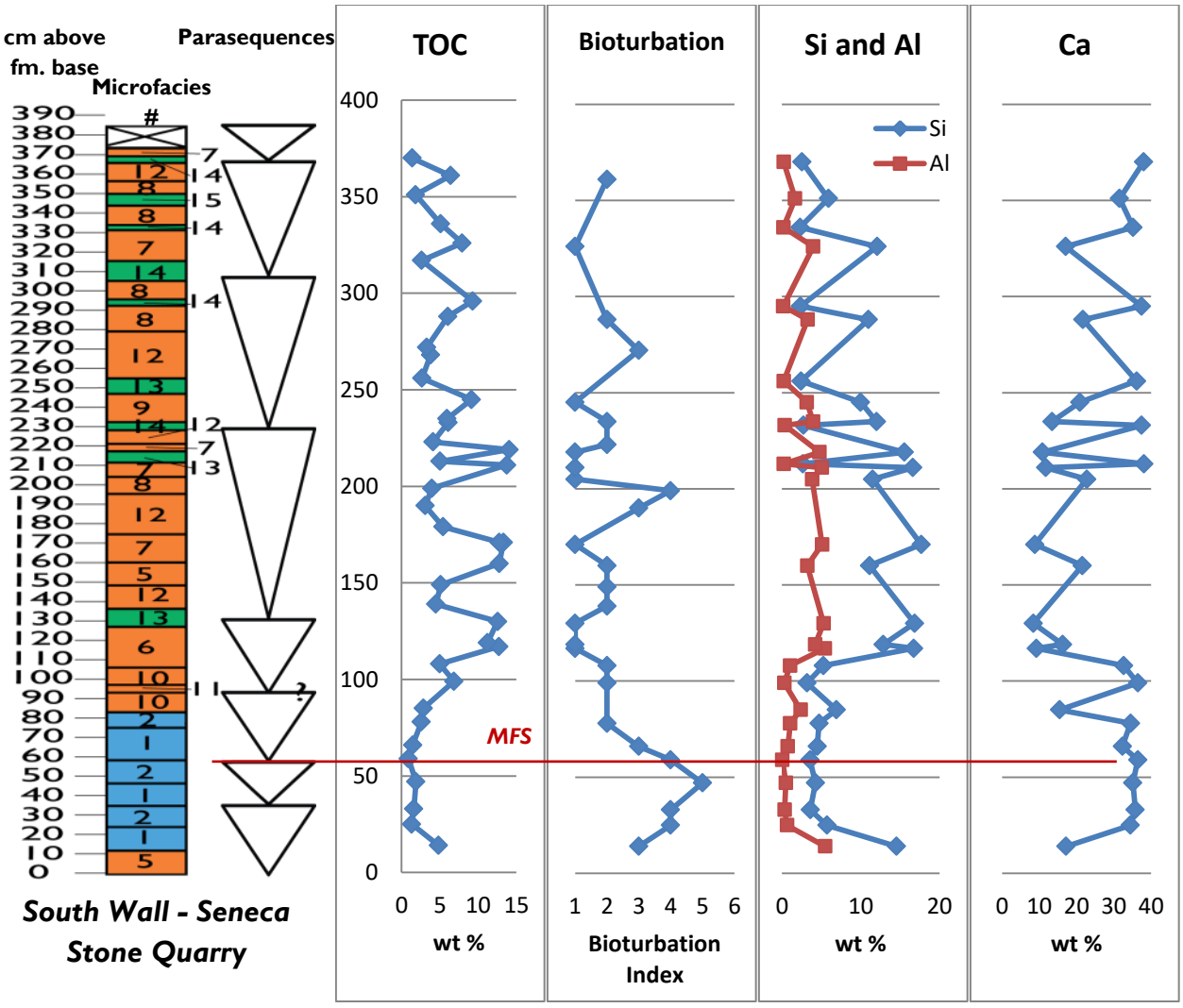

Figure 5: Microfacies positions at the South wall of study area at Seneca Stone Quarry (Seneca Falls, NY) alongside identified parasequence divisions, bioturbation and major elemental abundances. See Appendix A for microfacies identifications. Vertical axes in centimeters above base of Union Springs Formation.

Just above the Limestone lithofacies group, a significant uranium peak occurs in Microfacies X (Interbedded Dacryoconarid-Bearing Calcareous Mudstone), with only very modest gains in molybdenum and vanadium at the same horizon. All three trace elements reach their maximum value in Microfacies VI (Clay Rich Carbonaceous Mudstone), at 117 cm above formation base (Figure 6). This peak corresponds with uncommonly high values of TOC, silica, and aluminum within the section, as well as low levels of bioturbation and calcium content (Figure 5).

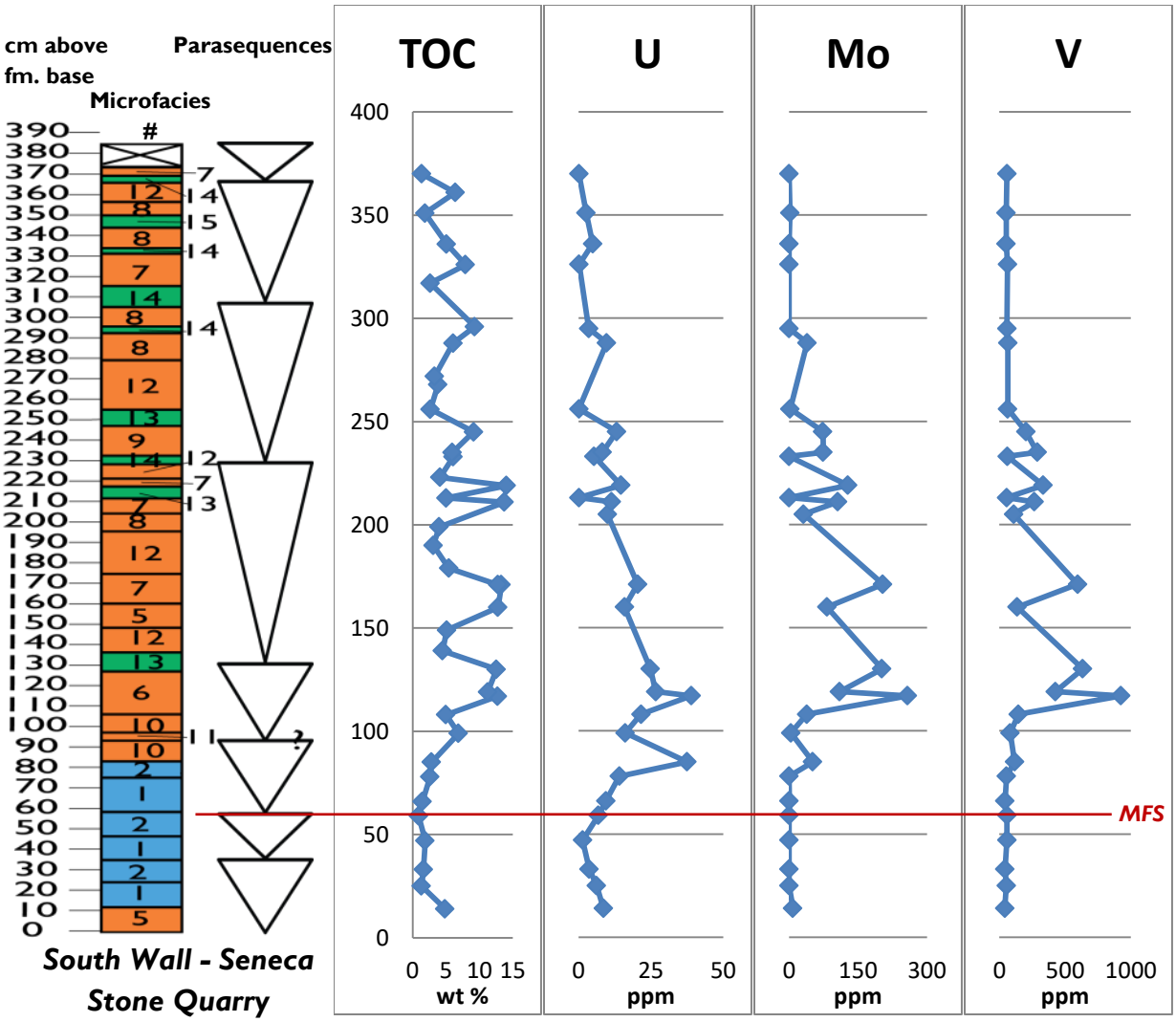

Figure 6: Microfacies positions at the South wall of study area at Seneca Stone Quarry (Seneca Falls, NY) alongside identified parasequences, total organic carbon content, and redox-sensitive trace element abundances. Vertical axes in centimeters above base of Union Springs Formation.

At 171 cm above formation base (Microfacies VII: Clay-Rich Quartz Silt-Bearing Carbonaceous Mudstone), molybdenum and vanadium peak sharply, while uranium exhibits only a modest gain (Figure 6). In some instances, such as within concretionary lithofacies sometimes interpreted as parasequence boundaries, abundances of all three elements do not change relative to underlying and overlying strata. The abundances of these trace elements somewhat mimic the TOC abundance curve. However, deviations occur; such as at 14 cm and 326 cm

above formation base, where TOC briefly jumps to nearly 8% while all three trace elements remain depleted relative to Average Cratonic Phanerozoic Shale values (Figure 6; Table 1; Condie, 1993).

Principal Components Analysis

Principal components analysis yielded two components which account for 73.5% of the variation within the data set. The first three components account for 79.33% of sample set variability (Figure 7).

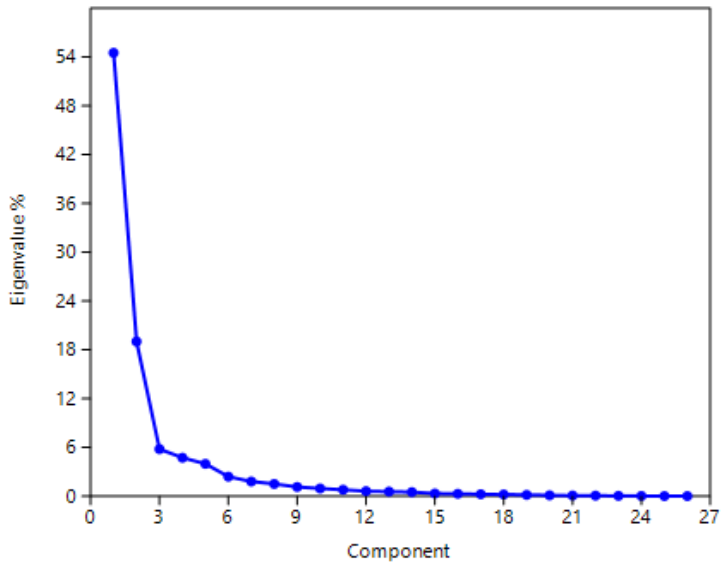

Figure 7: Scree Plot, showing each principal component and the percentage of data set variability accounted for by each component (Eigenvalue %). Principal components analysis considered 27 compositional parameters (see text).

The first component shows negative coefficients for bioturbation, inorganic carbon, Mg, Ca, Sr, and Y. Ca, inorganic C, and Mn are the strongest negative coefficients (Figure 8). All other variables possess positive coefficients for this component, with the strongest positive coefficients for elements tied to terrigenous sediment input: Ti, Si, K, Al, Zr, Rb; and the redox indicator trace elements Ni and Mo. This component, which explains the majority of variability

across the data set (Figure 7), implies that a significant portion of sample variability exists along a spectrum between carbonates and carbonate-associated elements, and terrigenous sediment-associated elements (along with redox state, to a lesser degree). This aligns well with the clustering of the Union Springs samples into three facies groups defined by their position along a spectrum from organic-rich mudstone to limestone.

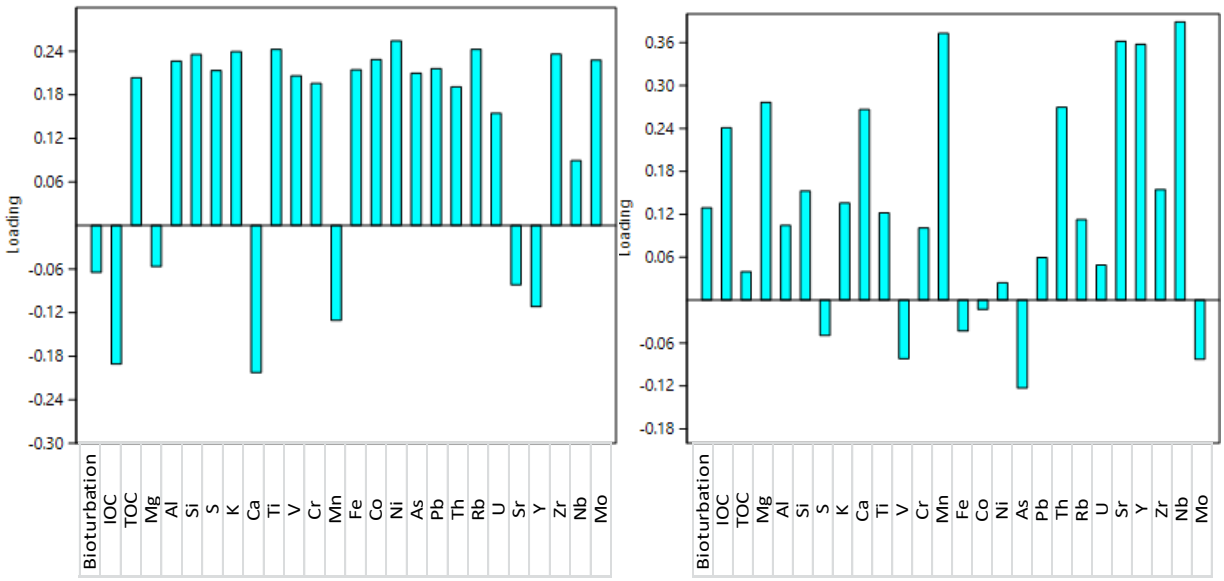

Figure 8: Loading plot indicating contributions made by individual tested constituents for the first (left) and second (right) principal components. Analyzed parameters include total organic carbon, total inorganic carbon, bioturbation, Mg, Al, Si, S, K, Ca, Ti, V, Cr, Mn, Fe, Co, Ni, As, Pb, Th, Rb, U, Sr, Y, Zr, Nb, Sb, and Mo.

The second principal component yields negative coefficients for As, Mo, V, Fe, S, and weakly, Co. All other variables yield positive coefficients, including a strong positive Mn coefficient (Figure 8). The correlation of the negative coefficients suggests sulfide-forming elements exert a primary control on this component, and thus, sample set variability. Given that in a marine depositional system, Mo, V and As can only incorporate into sulfides under strongly reducing conditions (in the presence of H_2S), this principal component contains strong influence of anoxia/euxinia.

Additional principal component analyses were carried out isolating the data specific to each location: samples from Seneca Falls and Marcellus, NY were analyzed separately to examine the potential for different controls on rock property variability across their nearly 39 km separation. Results of the single-location analyses were similar both at each location and to the combined group analysis described above (Appendix B). One exception occurs in the second component of the Marcellus, NY data. Although this component still contains significant euxinic influence, it also contains a significant negative TOC coefficient and a stronger coefficient for molybdenum. This further facilitates the examination of covariation trends between organic carbon and Mo enrichment and suggests a stronger degree of control on variability by TOC and Mo at Marcellus, NY as opposed to the Seneca Falls study site (Figure 8, Appendix B).

This analysis visualizes the paleo-oceanographic controls on compositional variability across the distal foreland basin. First-order variability results from the presence or absence of terrigenous sediment supply. Whether or not the distal basin received clay, quartz silt, and other detritus eroded from the Acadian Highlands determined broad compositional parameters: Terrigenous supply resulted in silt- and clay-rich rocks (e.g. Microfacies VII – Chapter 1; Appendix A), while sediment starvation resulted in pelagic fossil-dominated packstones and calcareous concretions (e.g. Microfacies II & XIII, respectively – Chapter 1; Appendix A). The next most important control on compositional properties was the paleoredox state at the sediment-water interface during deposition (Figure 8). Particularly at the Marcellus, NY study site, this second component contains strong negative components indicative of an anoxic or euxinic seafloor (Figure 8; Appendix B). The fact that the presence or absence of oxygen on the seafloor has a strong effect on organic carbon preservation, the appearance of

fossil material, and bedding texture will be demonstrated in the Discussion through the incorporation of petrographic data.

Discussion

Joint Interpretation of Chemical Proxies and Petrographic Data

Petrographic data act as a check on the paleodepositional interpretations which are commonly drawn from chemical abundance data. Further insight on correct interpretation of the compositional deviations from the "average" exhibited by the samples is extracted from knowledge of the general basin setting.

One of the most striking features within the data set is the high calcium content across all lithofacies groups (Figure 9). The samples analyzed in this study were collected from highly condensed sections, far from the terrigenous sediment source of the Catskill delta complex to the southeast (Ettensohn, 2008). The complete Union Springs thicknesses at the studied sections in Seneca Falls, NY and Marcellus, NY each measure less than 2% of the Union Springs thickness in more proximal locations of the Appalachian Basin (Ver Straeten and Brett, 2006). At the time of deposition, the slow accumulation of terrigenous sediment at the study site allowed for the accumulation of pelagic fossils, the development of starvation surfaces (Haq et al., 1987; Brett and Baird, 1986), and the precipitation of bacterially-mediated calcite concretions (Raiswell and Fisher, 2000).

This significant distance from the sediment source may in fact serve as a benefit of working in a significantly condensed section such as this. In more proximal basin areas, significant quantities of terrigenous sediment can dilute concentrations of organic matter

(Sageman et al., 2003). Because the terrigenous compositional signal is weak in this study, the relative importance of primary production and preservation are elevated in these rocks with respect to organic matter enrichment. This allows for more focused study on paleo-oceanographic factors affecting chemical bottom-water conditions and organic flux, as opposed to continental and tectonic factors, which are more important in more proximal basinal regions.

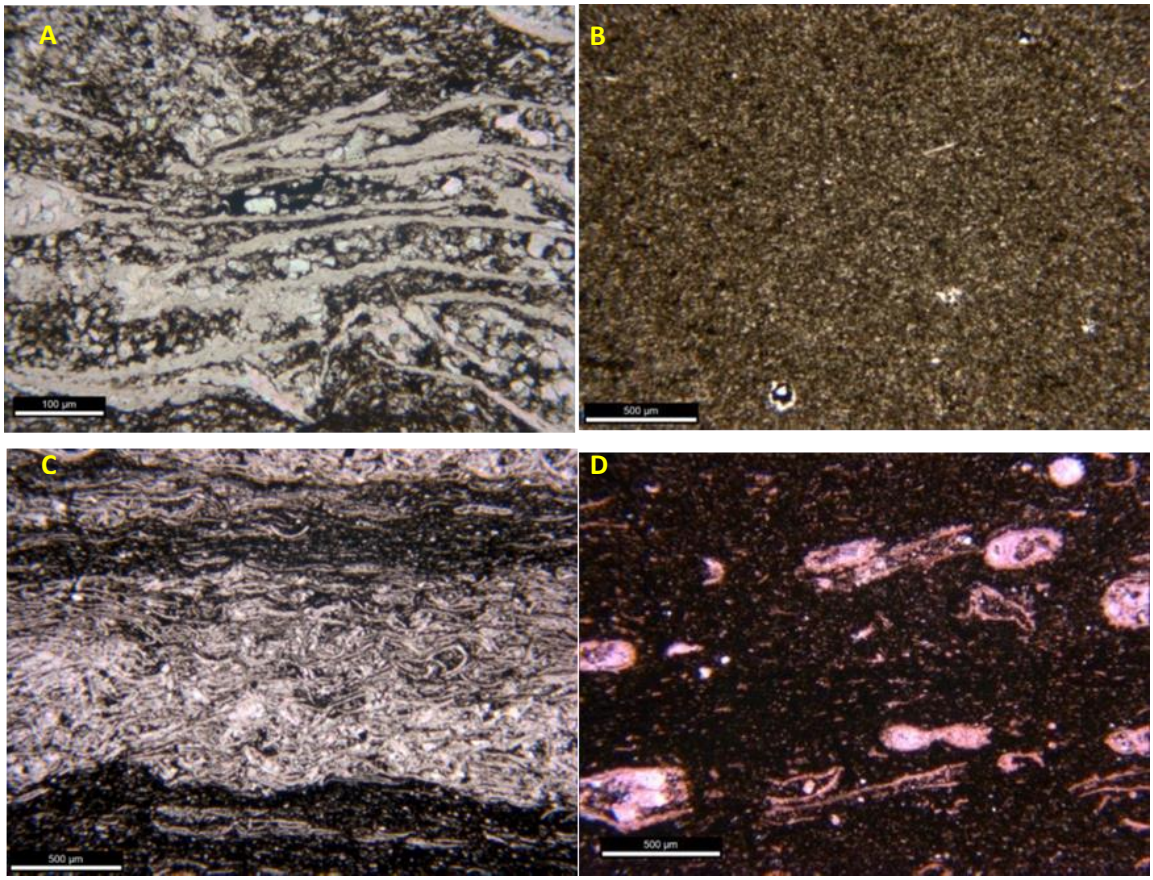

Figure 9: Images showing abundant biogenic calcite within the Limestone (A) and Carbonaceous mudstone (C, D) facies groups. The Calcareous Concretion lithofacies group (B) is comprised primarily of calcite precipitated as a result of bacterial processes just below the sediment-water interface shortly after deposition. (D) shows an example of a sample from the Carbonaceous Mudstone facies group which has undergone post-compaction diagenetic cementation. Images taken parallel to the original direction of bedding.

Given the diversity of the calcite types (Chapter 1), high calcium abundance does not point to one specific depositional scenario, and that authigenic calcite has the potential to alter depositional interpretations based on chemical abundances. From a purely compositional

standpoint microfacies within the Calcareous Concretion lithofacies group may somewhat resemble those within the Limestone group, but the biogenic processes in the water column and at the seafloor which created the limestones are quite distinct from the bacterial processes which lead to concretionary calcite growth during earliest diagenesis (Raiswell & Fisher, 2000). As a result of their differing paleodepositional conditions, calcite displays distinctive bedding characteristics and textures in these two lithofacies (Chapter 1). The use of elemental redox proxies as a basis for interpreting the primary depositional environment of rocks which belong to microfacies in the Calcareous Concretion group is unwise due to the authigenic origin of the bulk of constituent minerals within the facies. The interpretation of detrital indicators such as Al abundance should be conducted with this possibility in mind. Furthermore, an interpretation which places importance on the thickness of chemical indicators would be further compromised by the fact that this lithofacies group has undergone significantly less compaction than the other facies groups from the study area (Chapter 1 — Appendix A).

Other authigenic features deserve similar attention. Microfacies XII, Clay- and Calcareous Cement-Bearing Carbonaceous Mudstone, contains significant amounts of calcite cement (Figure 9D). Compaction of fossil constituents suggests a post-burial origin for cementation (Chapter 1), and the inconsistent abundance of cement and degree of compaction across samples in this facies lead to highly variable compositions (Figure 4). Additionally, it is uncertain whether the calcite cement is comprised of elements sourced from dissolved and re-precipitated components from within the same stratigraphic horizon (a largely closed system), or if calcium and carbonate ions originated from other stratigraphic positions within the proto-Union Springs sediments or from another formation altogether (an open system) (Chapter 1).

For this reason, paleoenvironmental interpretations tied to samples within this microfacies must recognize that a significant portion of its compositional variability is tied to authigenic, non-depositional causes. Table 3 illustrates the compositional averages at the lithofacies group level as does Table 1, but with Microfacies XII separated from the rest of the Carbonaceous Mudstone group, which contains less compositional diagenetic influence.

Table 3: Average elemental abundances of each lithofacies group, compared to the average cratonic Phanerozoic shale (Condie, 1993). Here, data for the Carbonaceous Mudstone lithofacies group is presented, alongside segregated data for Microfacies XII. Microfacies XII, Clay and Calcareous-Cement Bearing Carbonaceous Mudstone, is removed from the remainder of the Carbonaceous Mudstone lithofacies group due to its inconsistent alteration by post-compaction diagenetic cementation. *Average TOC value from Leeder (1982).

Element	Limestone (N = 15)	All Carbonaceous Mudstones (N=59)	Carbonaceous Mudstones (No MF XII) (N = 41)	Clay and Calcite Cement Bearing Carbonaceous Mudstone [MF XII] (N = 18)	Calcareous Concretion (N = 27)	Average Cratonic Phanerozoic Shale (Condie 1993)
Al (wt%)	0.38 (.28)	2.98 (1.62)	3.41 (1.57)	2.02 (1.16)	0.58 (.58)	9.67
Si	3.96 (.63)	9.87 (4.40)	11.06 (4.50)	7.15 (2.70)	3.39 (1.46)	30.53
K	.38 (.13)	1.50 (.84)	1.73 (.79)	.98 (.47)	.32 (.24)	3.94
Ca	35.50 (1.48)	22.52 (8.70)	19.40 (8.18)	29.62 (5.55)	35.61 (2.55)	0.95
Ti	0.04 (.01)	0.15 (.07)	0.17 (.08)	.11 (.05)	0.05 (.02)	0.50
V (ppm)	53.69 (6.34)	218.41 (209.7)	278.54 (225.26)	81.44 (43.45)	54.50 (7.84)	117
U	6.13 (4.09)	16.09 (11.40)	19.76 (11.47)	7.74 (6.26)	2.75 (2.66)	2.9
Mo	0.22 (.40)	73.20 (81.47)	96.71 (88.13)	19.66 (27.39)	1.17 (2.34)	3.7
TOC (wt %)	2.02 (1.15)	7.94 (3.53)	9.18 (3.28)	4.62 (1.29)	2.80 (1.52)	2.1*
Bioturbation (1-6)	4.2	1.85	1.62	2.45	1	-

The high-energy Microfacies XI, along with Microfacies X, is particularly likely within the study area to experience a rather unusual enrichment of zinc, with a maximum measured concentration (0.4 wt%; 4000 ppm) which is 77 times enriched relative to average upper crust

(Wedepohl, 1995). The enrichment of zinc occurs in the form of sphalerite, which is present as replacement steinkerns within dacryoconarid shells and within veins, appearing alongside calcite spar, organic matter, pyrite and rare chalcopyrite (Chapter 1). Primary organic matter appeared in bedding-parallel laminations (interpreted as preserved microbial mats) and compacted *Tasmanites* algal cysts, but the quantity of primary organic matter is often less than that found within secondary veins in these facies. Although galena was not identified within the study area, it has been reported by Selleck (2014) in the Union Springs of New York. One possible explanation for the suite of sulfides is low-temperature hydrothermal enrichment, similar to Mississippi Valley Type ore enrichment. Zn-Pb enrichment of this type via brine migration is known to have occurred within the Appalachian Basin, although no significant accumulations have been described within the New York promontory (Kesler, 1996). This process may have been facilitated by the higher average grain size in Microfacies X and XI, resulting from dacryoconarid grainstone beds.

Elemental Abundance Relationships

Within the samples studied, Si and Al are strongly correlated (Figures 5, 15). This suggests that Si, like Al, has a strongly terrigenous origin in these rocks. The intervals of weakest correlation still display strong covariation, and tend to occur at sediment starved horizons in the Limestone lithofacies group. Here, near the maximum flooding surface, the small amount of quartz present is likely biologically-transported, as indicated by the identification of agglutinated foraminifera tests (Chapter 1). Other less-correlated horizons arise within

Microfacies XI, which represents a high-energy depositional environment where winnowing of clay sediments would decrease the proportion of clay minerals to quartz silt (Chapter 1).

For the Union Springs of Seneca Falls and Marcellus, NY, terrigenous input proxies (Al and Si) are generally higher in microfacies which exhibit the highest organic carbon contents (Table 2), opposite to what is anticipated by other studies of the Union Springs (e.g., Lash and Blood, 2011). The reason for this discrepancy likely originates from the basin position occupied by the rocks in this study, along with the carbonate-rich nature of the totality of samples within the columns. Assuming relatively unchanged primary productivity throughout Union Springs depositional time, the fact that Al levels are so low throughout the entire section, including during times of extremely high TOC, indicates that even when the depositional environment was receiving its most abundant terrigenous sediment flux, it was not enough to effectively "dilute" the organic matter (Table 3).

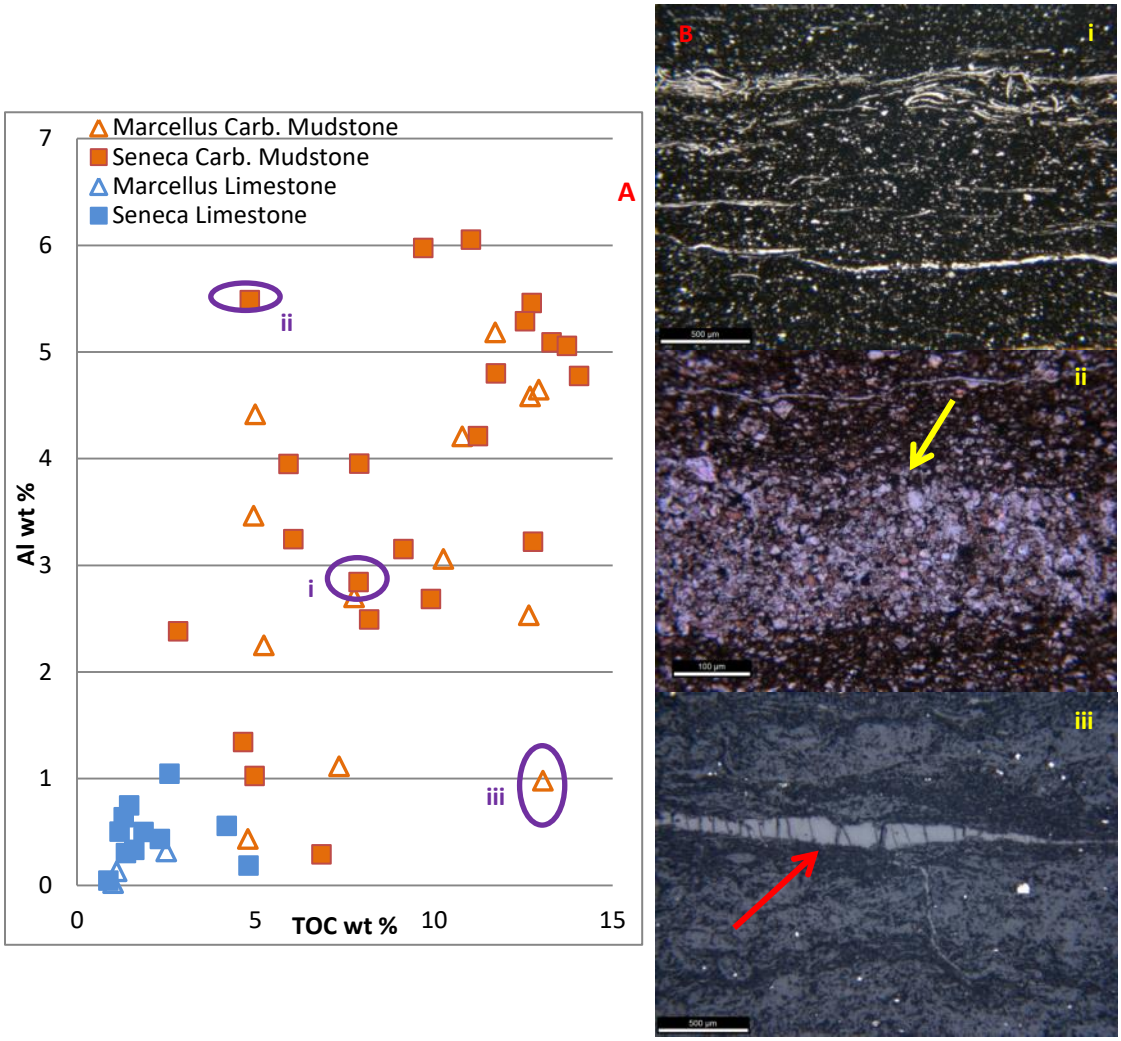

Figure 10: The relations between Al and Total Organic Carbon abundances can be deduced through knowledge of the environmental attributes revealed in thin sections of the corresponding samples. Images taken parallel to the original direction of bedding. A) Aluminum abundance and total organic carbon content for the Limestone and Carbonaceous Mudstone (sans Microfacies XII) lithofacies groups. B) i. Microfacies VII, Clay-Rich Quartz Silt-Bearing Carbonaceous Mudstone, contains significant amounts of clay and organic matter. ii. Microfacies V, Quartz and Dolomite-Bearing Carbonaceous Mudstone, is characterized by a high clay content and is moderately bioturbated. Biogenic action within this sample may have limited the preservation of organic matter (see text). Dolomitized burrow indicated by yellow arrow. Iii. Microfacies X, Interbedded Dacryoconarid-Bearing Calcareous Mudstone, is characterized by alternating beds of silty, organic enriched beds and dacryoconarid shell beds. Winnowing of clay minerals via current energy and networks of secondary organic veins (red arrow) affect the Al/TOC relationship within this sample.

Figure 10 explores alternate controls on organic enrichment by examining the variability in the Al vs TOC relationship. Within the middle of the Al-TOC distribution, point "i" is representative of the typical trend with respect to this relationship (Figure 10), containing roughly 7.9% organic carbon and 2.8% aluminum. This sample belongs to Microfacies VII (Clay-Rich Quartz Silt-Bearing Carbonaceous Mudstone), and is characterized by abundant clay and quartz silt, dacryoconarids and small brachiopod shell debris, and organic matter primarily in the form of compacted *Tasmanites* algal cysts (Figure 10A, Bi). Bioturbation is minimal within this facies (see Chapter 1).

Point "ii" is a sample with one of the highest aluminum contents, and one of the more moderate organic carbon percentages within the Carbonaceous Mudstone lithofacies group (Figure 10A, Bii). This sample belongs to Microfacies V (Quartz and Dolomite-Bearing Carbonaceous Mudstone) and occurs 14 centimeters above the top of the Onondaga Formation in the Union Springs. A possible explanation for the paired high Al and low TOC values can be found in the rock fabric. This microfacies is moderately bioturbated, and contains a high-concentration of dolomitized compacted burrows oblique to bedding. Biologic activity is known to cause chemical changes in sediment particles, create or alter transport pathways within sediment, and can lead to an alteration of local pH and solute distribution, leading to direct effects on organic decomposition reactions during earliest diagenesis (Aller, 1982). Although increased bioturbation may be a sign of enhanced productivity in the depositional system, in this case, biological sediment mixing appears to have decreased the overall preservation potential of organic carbon (Bohacs et al., 2005). Within this dolomite-bearing Microfacies V sample, which sits atop the Tioga F K-Bentonite (Ver Straeten, 2004), dolomitization as a result

of clay-derived fluids (McHargue & Price, 1982) is not believed to have significantly altered the Al-TOC relationship; the introduction of fluids enriched in Si, Ca, Fe, Mg, and K during diagenesis would have impacted relative abundances of aluminum and organic carbon to a similar degree.

To contrast, point 'iii' contains significantly elevated quantities of organic carbon (~13%), and just under 1% aluminum (Figure 10). This data point represents a sample of Microfacies X (Interbedded Dacryoconarid-Bearing Calcareous Mudstone) from the Marcellus, NY study location. This microfacies is characterized by alternating organic-rich horizons and dacryoconarid event beds (Figure 10B.iii) deposited under turbulent conditions (Chapter 1). The organic-rich horizons are characterized by relicts of microbial mats, but in addition this microfacies occasionally hosts networks of branching organic carbon-bearing veins generally oriented parallel and perpendicular to bedding (Figure 10) of diagenetic origin. These diagenetic features create a high degree of spatially variable organic carbon contents (Chapter 1). Additionally, the low aluminum percentage in this sample may result from an energetic depositional environment. Microfacies X and XI include silt lags, telescoping dacryoconarid shells, and truncated laminations indicative of relatively high-energy conditions which decreased deposition of clay minerals (Chapter 1). As a result, high-energy beds are almost completely devoid of clay minerals, containing almost exclusively biogenic calcite, with minor amounts of quartz silt, dolomite, and phosphatic debris. For this sample, depositional winnowing of clay minerals combined with secondary organic enrichment places it at the low-Al, high-TOC extreme of the spectrum.

Trace elements can elucidate relationships between deposition of petrographically-identified microfacies and seafloor oxygenation. Previously, anoxic or euxinic conditions were deduced (Chapter 1) from a lack of bioturbation, low fossil abundance and diversity, and high levels of organic matter preservation. Algeo & Maynard (2004) suggest redox sensitive trace elements will be well correlated with TOC in anoxic, noneuxinic conditions. Rocks deposited in euxinic conditions tend to show higher enrichments of trace elements, with a weaker element-TOC correlation. In contrast, sediments deposited under dysoxia will tend towards lower organic carbon and no correlation between trace elements and TOC (Algeo & Maynard, 2004). Figure 11 shows the variation of molybdenum and vanadium against total organic carbon abundances for Limestone (Microfacies I-IV) and Carbonaceous Mudstone (Microfacies V-X) microfacies. Microfacies XII and the Concretionary facies group are excluded in order to focus strictly on depositional conditions. Samples are divided into three categories: Limestone, which contains the four limestone microfacies from across the study area, Euxinic, which contains Microfacies VI and VII, and Non-Euxinic, which contains all other Carbonaceous Mudstone microfacies. Visual examination suggested that Microfacies VI and VII were the facies most likely to have experienced sustained anoxia or euxinia, based upon high organic carbon content (observed via microscopy), scant bioturbation, and substantial quantities of small framboidal pyrite (~5 μm) (Chapter 1; Table 2). Whereas the “non-euxinic” mudstone microfacies exhibit oxygen-stressed conditions, petrographic properties suggest they were less likely to have sustained persistent euxinia.

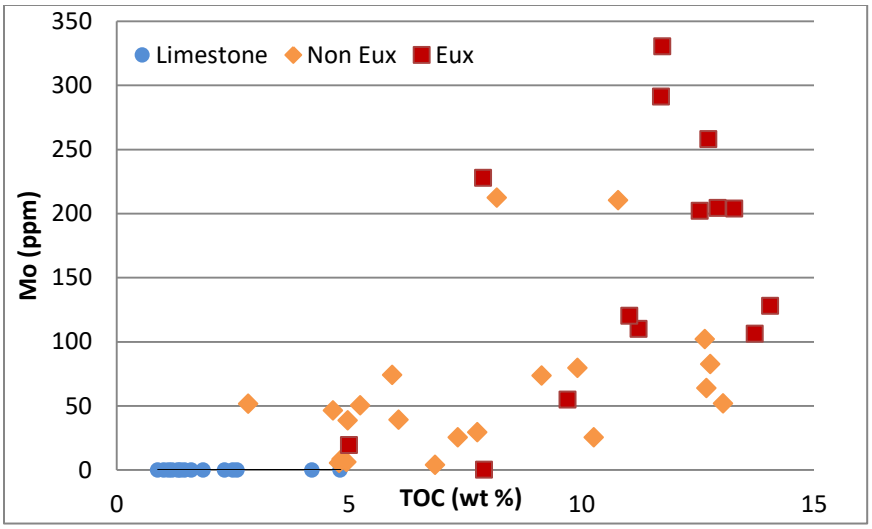

Figure 11: Trace element vs. TOC abundance for molybdenum, an element which demonstrates "strong euxinic affinity" (Algeo & Maynard, 2004). Selected samples are from each studied location.

Limestone samples, while they contain modest percentages of organic matter, exhibit no chemical euxinia signal, with no Mo enrichment across the range of organic carbon abundance (Figure 11). This observation agrees with petrographic characterization, as bioturbation remains high throughout the Limestone sample set and, in samples from Marcellus, NY, there is evidence of a relatively diverse benthic community, especially when compared to typical Union Springs fauna (DeSantis & Brett, 2010).

The Non-Euxinic sample set exhibited moderate to high organic carbon enrichment and Mo concentrations generally <100 ppm. Two samples from the Non Euxinic microfacies exhibit significantly elevated Mo abundances (>200 ppm). The samples in question belong to Microfacies X, and indicate that although sedimentological indicators are not suggestive of persistent euxinia (Chapter 1), this microfacies was at least occasionally euxinic. When these outliers are removed, Mo-TOC correlation in Non Euxinic microfacies is moderate (Pearson *r* = .41).

Samples from the Euxinic microfacies (“Eux”) exhibit a different pattern, exhibiting strong molybdenum enrichment nearing 350 ppm (Figure 11; Table 2), and Mo values which become more wide-ranging above 10% TOC (Figure 11). This is especially significant given the low abundance of aluminum throughout the data set when compared to the average shale (Table 3). This implies a volumetrically small detrital fraction amongst even the most clay-rich facies in the study, and signals significant trace element enrichment via organometallic complexation and sulfide formation (Tribovillard et al. 2006).

Superimposing stratigraphic context atop these data is helpful for illustrating fluctuating redox conditions, and shows that bottom waters transition from oxic-dysoxic during Limestone deposition to strongly anoxic-euxinic higher in the section (Figure 12). Just over halfway through the studied sections, falling molybdenum abundances contemporaneous with gently rising TOC values indicate anoxia rather than euxinia, given the significant enhancement effect euxinia has on molybdenum uptake in sediments (Algeo & Lyons, 2006). Progression farther upward in the section to the top of the Union Springs Formation is marked by drops in both parameters (Figure 12), likely indicating slight increases in oxygenation during the late regressive systems tract (Figure 6).

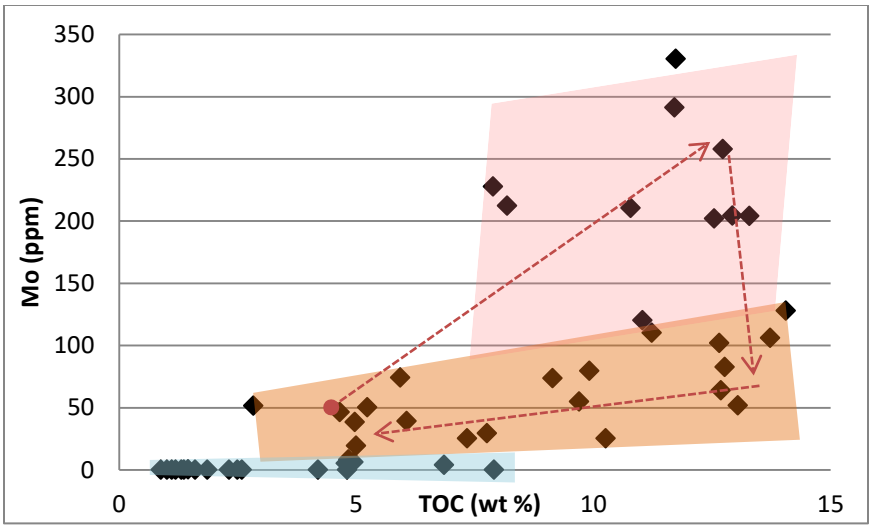

Figure 12: Molybdenum vs TOC abundance for Microfacies I-XI. Arrows roughly indicate data trends moving stratigraphically upsection, beginning from the red circle. Blue, orange, and red shaded regions indicate areas implying dysoxia, anoxia, and euxinia, respectively.

Chemical Composition, Bioturbation and Fossil Abundance

Looking across all microfacies, there exists a gradient of bioturbation indices which reflects the range of oxygenation conditions. The Limestone lithofacies group is significantly bioturbated, with numerous intervals experiencing near-complete bedding homogenization, and occasional macroscopic burrows oblique or parallel to bedding (Figure 13c, Figure 13d). Within the Carbonaceous Mudstone facies, bioturbation is more restricted, and numerous intervals contain unaltered lamination (Figure 13a). Also common are samples which contain both beds with unbioturbated laminae and occasional bioturbated beds (1-5 mm-scale thickness) which often contain one or more shell-rich laminations (Figure 13b). It is not uncommon for these shell-rich laminations, and bedding planes containing casts of small brachiopods or bivalves, to occur within samples which display strongly elevated trace element and TOC enrichment (e.g. 219 cm above formation base- Figure 5). These small benthic fauna occur largely concentrated in segregated horizons every several millimeters, and their presence

within horizons which return chemical signals suggestive of total oxygen deprivation implies at least periodic oxygenation, if only for geologically fleeting durations during the deposition of mostly-anoxic facies (Wignall & Myers, 1988).

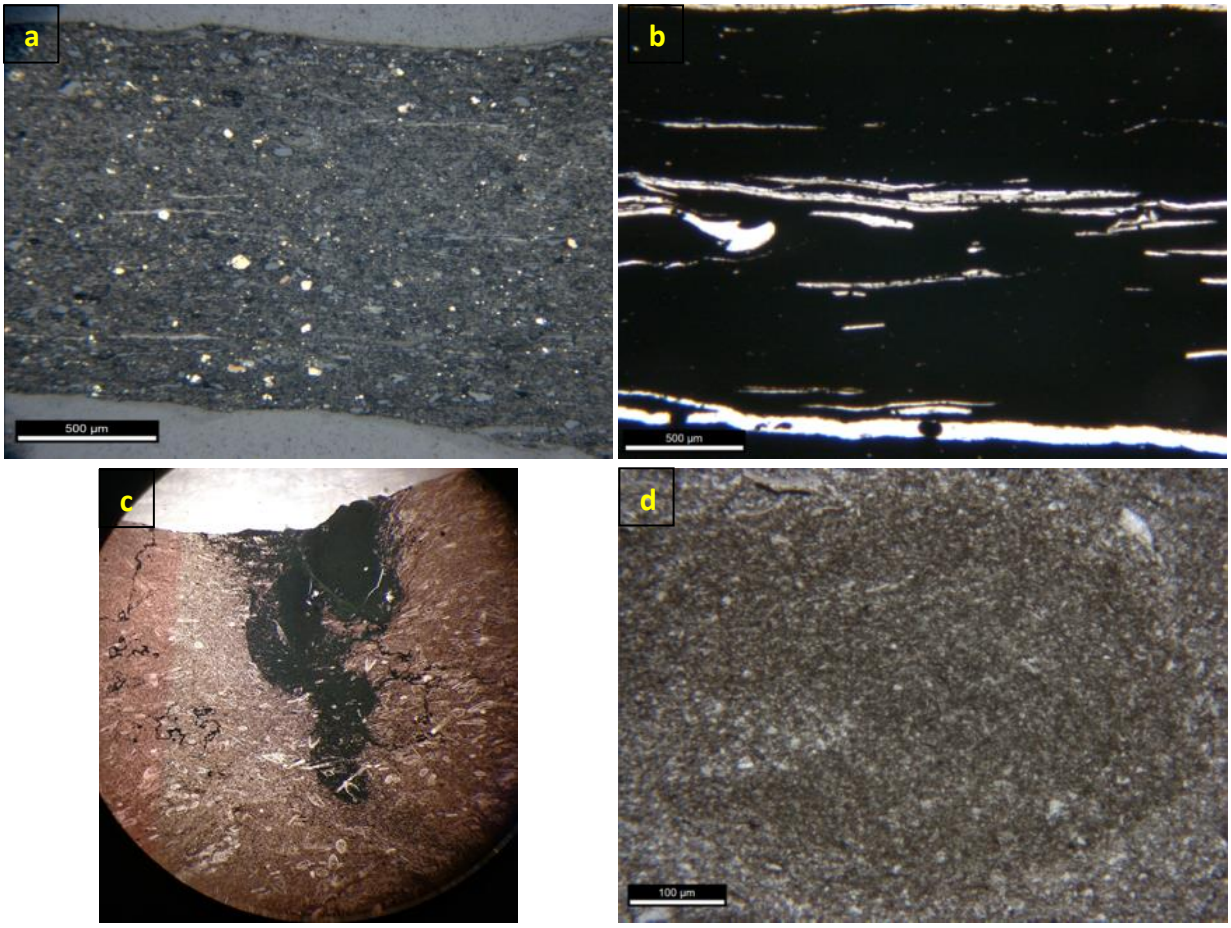

Figure 13: Samples across the study area range from unbioturbated with minimal identifiable fossil content (a), to occasionally bioturbated with occasional fossil-rich laminae (b), to heavily bioturbated with densely packed bioclasts. (c) shows a large (11 mm length) burrow within a muddy pelagic limestone which has been completely pyritized, whereas the cross-sectional burrow trace in a packstone microfacies (d) reveals a relatively constant composition despite a more fine average grain size. Images taken parallel to the original direction of bedding.

Bioturbation indices reveal several interesting patterns with respect to elemental abundances. Enrichments of uranium, molybdenum, and total organic carbon drop steeply as bioturbation increases (Figure 14). No sample with an index higher than 2 records an organic

carbon enrichment higher than 5%, and similarly, trace metal abundances drop steeply where this bioturbation threshold is passed (Figure 14). All of these relationships point to an agreement between paleoredox proxies and bioturbation indices regarding seafloor paleo-oxygenation. The relationship between aluminum and bioturbation is less clear. Whereas the most bioturbated samples (BI≥4) tend to be the most clay-lean, amongst the rest of the samples with lower bioturbation indices Al is more or less equally abundant (Figure B). This shows that amongst the Carbonaceous Mudstone facies group, comprised of samples which largely have a bioturbation index ≤3, clay content is a poor predictor of bioturbation.

Bioturbation is at a maximum in the mudstones, wackestones, and packstones in the 70 cm above the Onondaga Formation (Figures 6 and 16) where redox proxies, showing slight uranium enrichment and no enrichment of molybdenum or vanadium, indicate likely dysoxic conditions. Macroscopic burrows reach their maximum concentration within this range across the study area and bedding is largely homogenized within limestone microfacies. Both locations are extremely sediment-starved, and Limestone microfacies host the maximum flooding surface in each studied section, along with several bone-bearing starvation surfaces (Figures 5, 15; Chapter 1). Limestones at the Seneca Falls quarry are dominated by a diverse assemblage of dacryoconarids, but lack significant benthic macrofaunal diversity, containing small, crushed fragments of thin-shelled brachiopods. In contrast, the limestones from the Marcellus, NY quarry preserve evidence of a more diverse benthic community and contain abundant horizontal to oblique burrow traces, small crinoids, trilobite debris, and several types of brachiopods, occasionally preserved upright in a fully articulated position (see Chapter 1). Relative to Seneca Falls, not only do these Marcellus, NY limestones have a higher average

bioturbation index but also lower abundances of redox sensitive trace elements and the terrigenous sediment-associated elements aluminum, silica, and titanium (Table 4).

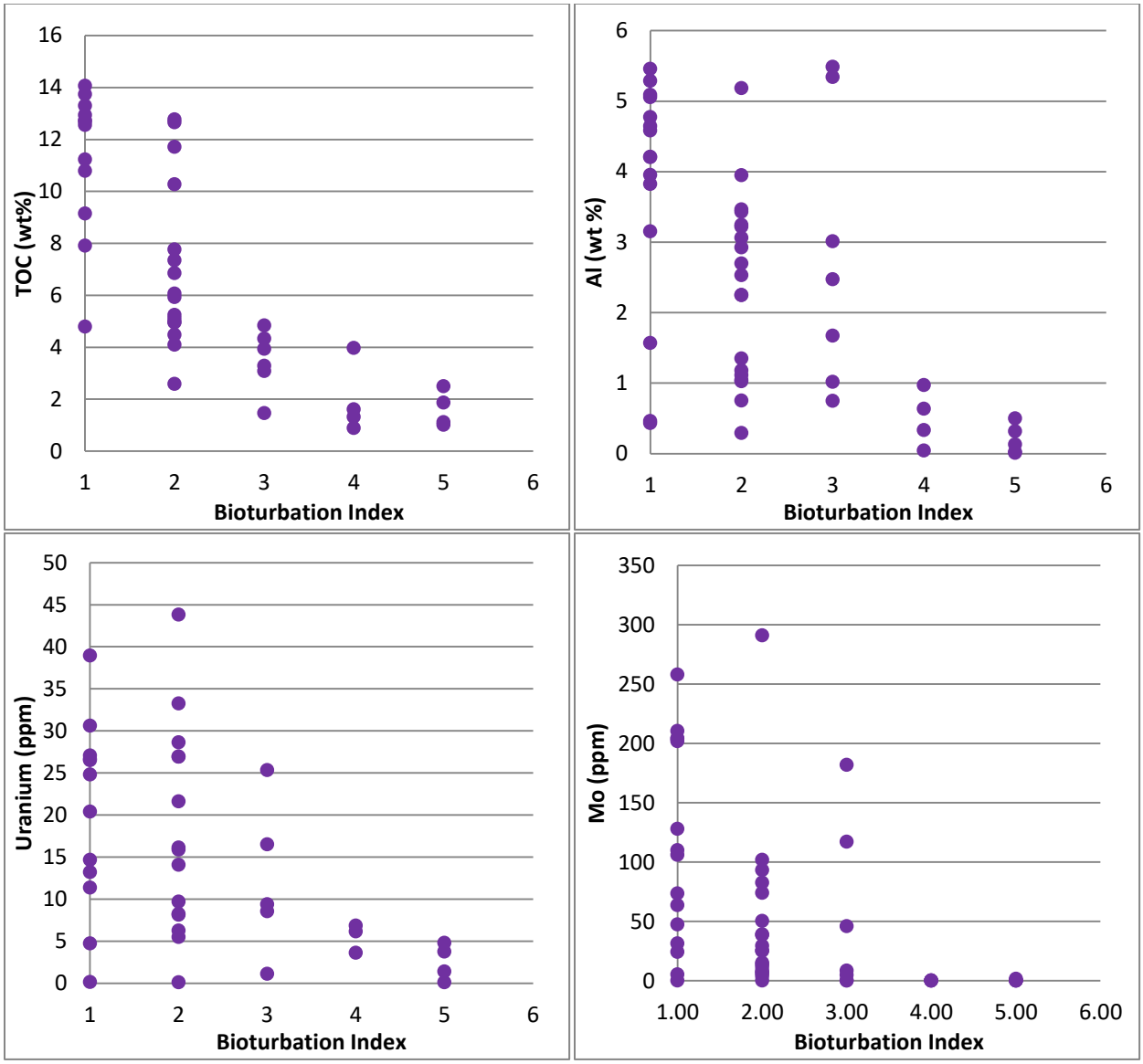

Figure 14: Examination of the relationship between bioturbation index (1-6) and (clockwise, from top left) TOC, aluminum, molybdenum, and uranium abundance. Bioturbation index from Droser & Bottjer (1986).

All of these signs point toward a relatively oxygenated depositional substrate at Marcellus, NY contemporaneous with some degree of oxygen stress at Seneca Falls during

deposition of the Limestone lithofacies group. The deposition of these facies represents a transition from the limestone deposition of the Onondaga Formation to significant organic-rich mudstone deposition within the Marcellus, which has a distinct and less diverse faunal assemblage when compared to the Onondaga (Brett et al., 2009; DeSantis & Brett, 2011). This environmental transition occurred as the basin deepened as a result of eustatic rise as well as orogenic loading at the proximal basin margin (Ettensohn, 1985; Brett & Baird, 1996; Ver Straeten, 2007; Brett et al., 2011). The combination of changed bathymetric form at the scale of the basin and increased terrigenous sediment flux ceased limestone deposition in both locations (Figures 5, 15; Chapter 1). The regionally increased water depth alone would explain a change in the benthic population but not an elimination of a diverse benthic community as recorded at Seneca Falls. Thus, I infer that the water oxygenation changes in the Marcellus seaway were initiated contemporaneously with basin deepening and limestone deposition in the study area, although dysoxic conditions were not yet widespread.

Table 4: Compositional profiles of Limestone microfacies from Seneca Falls, NY and Marcellus, NY

Element	Seneca Falls Limestones	Marcellus, NY Limestones
Al (wt%)	0.48	0.15
Si	4.12	3.56
K	0.42	0.27
Ca	35.16	37.57
Ti	0.04	0.03
V (ppm)	53.06	56.52
U	7.09	2.88
Mo	0.11	0.10
TOC (wt %)	2.15	1.54
TIC	9.66	7.74
Bioturbation (1-6)	3.67	5

Chemical Trends, Sedimentological Analysis and Sequence Stratigraphy

Seven parasequences at Marcellus, NY and eight parasequences at Seneca Falls, NY that are identified based on physical rock properties (Chapter 1) are packages of strata deposited in gradually shallowing environmental conditions, and are bounded by marine flooding surfaces and their correlative unconformities. These parasequences represent high-order base level changes within the major (third-order) “Eif-2” sequence, which began during the deposition of the Moorehouse member of the Onondaga Formation (Van Wagoner et al., 1988; Van Wagoner et al., 1990; Ver Straeten, 2007). The maximum flooding surface, placed across the horizon representing deposition at the time of maximum shoreline transgression within a third-order sequence (Catuneanu et al., 2009), is identified here based upon sedimentologic criteria

(Figures 5, 6, 15, 16). Although compositional analysis yields a clear signal for this location, the signal may not be intuitive.

Maximum transgression occurs during a time of limestone deposition within the study area, specifically within packstone facies (Microfacies II and IV at Seneca Falls and Marcellus, NY, respectively). These facies are highly bioturbated and calcite dominated, with low total organic carbon content, along with low amounts of Al, Si, and redox sensitive trace elements (Figure 5, Figure 15, Table 2). Gamma measurements described in Chapter 1 at the Seneca Falls field site, much like TOC presented here, indicate a low and relatively flat gamma response in the interval of strata corresponding to the maximum flooding surface. Gamma ray response is a measure of radiation associated with the decay of isotopes of potassium, thorium, and uranium, three elements largely associated with clays and organic matter in marine depositional systems (Fabricius et al., 2003). This low gamma, low TOC signal differs from observations made in less condensed regions of the basin, including Kohl et al. (2014) and Lash and Blood (2014), who place maximum flooding surfaces at maxima for gamma ray signal and TOC, respectively. Two explanations of the difference in properties of the geochemical and gamma radiation signals of the Pennsylvania sites reported by Kohl et al. (2014) and Lash and Blood (2014) and those of the northern Finger Lakes region in New York state (this study) are plausible.

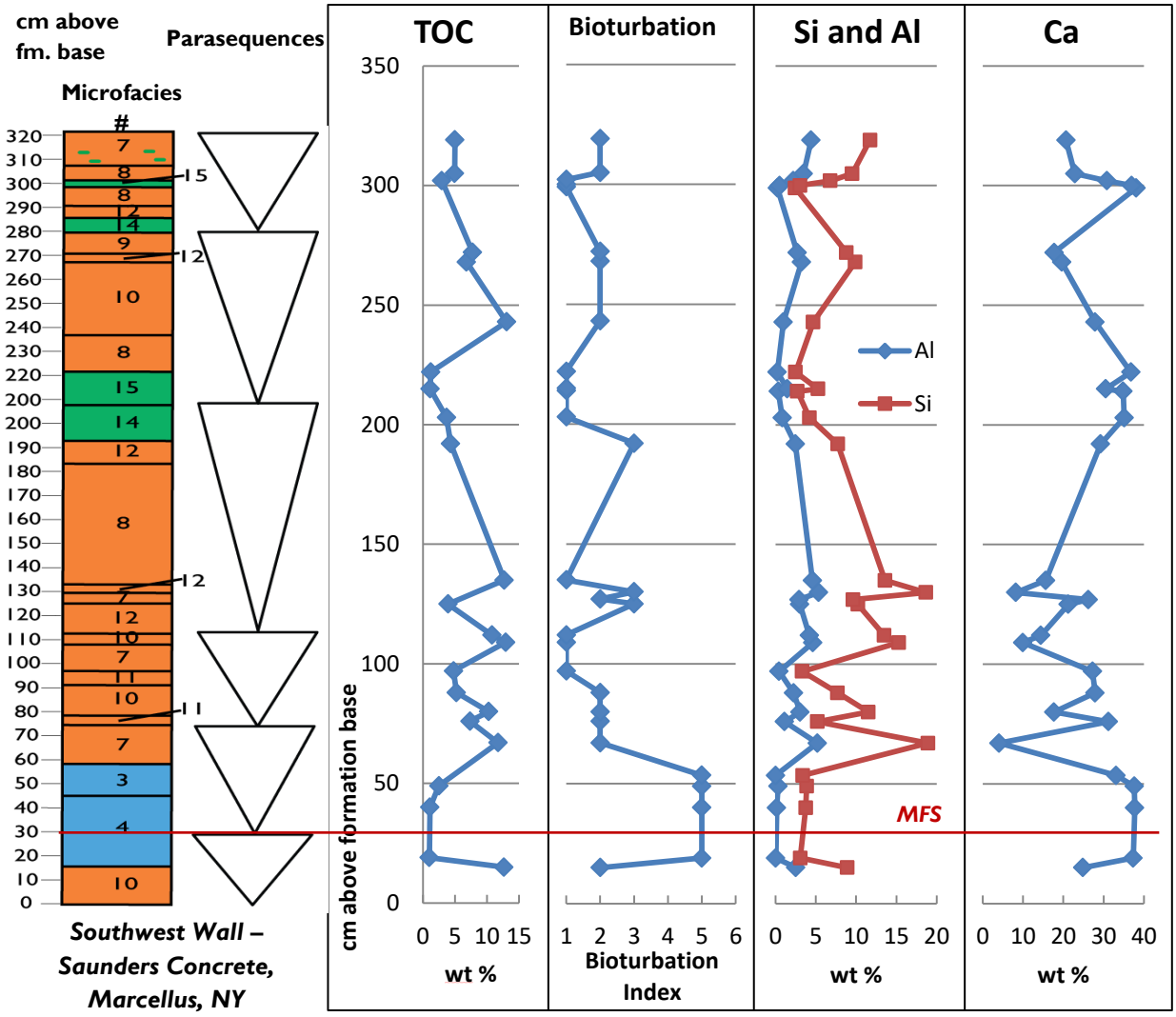

Figure 15: Measured Union Springs stratigraphic section at Saunders Concrete in Marcellus, NY, with parasequences and microfacies identifications (see Appendix A and Chapter 1). Within microfacies column, blue corresponds to Limestone, orange to Carbonaceous Mudstone, and green to Calcareous Concretion. Oriented abundances are given for total organic carbon, calcium, and silica and aluminum, along with bioturbation index.

One explanation is that the sedimentological criteria for identification of the maximum flooding surface reported here (chapter 1) are inappropriate. The criteria used is the simultaneous occurrence of fish bone-bearing sediment starvation surfaces, an upward disappearance of large brachiopods at the Marcellus, NY study area, and a slight decrease in bioturbation at Seneca Falls that indicates increased dysoxia (Savrda & Bottjer, 1991) (see Chapter 1).

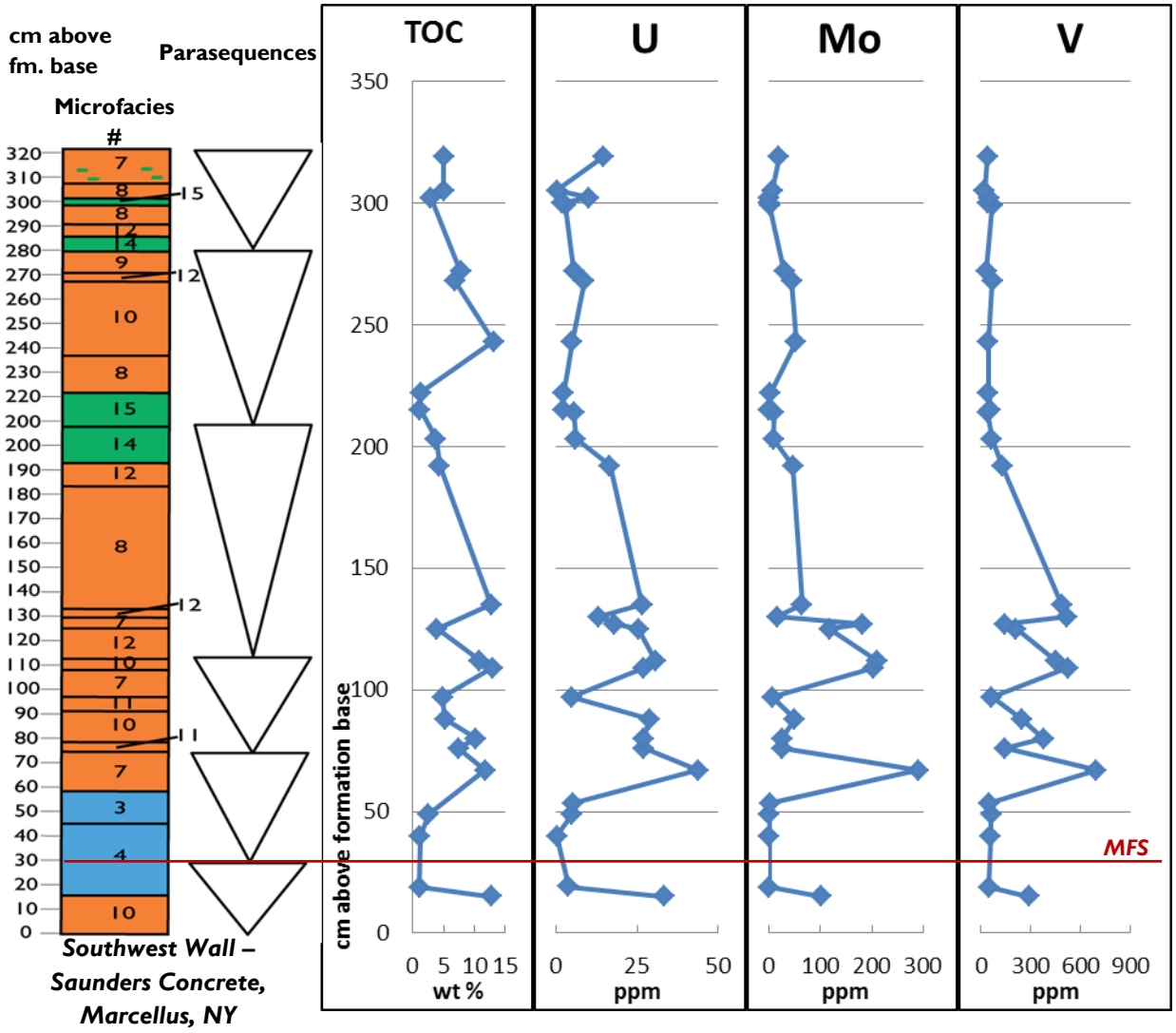

Figure 16: Measured Union Springs stratigraphic section at Saunders Concrete in Marcellus, NY, with parasequences and microfacies identifications (see Appendix A and Chapter 1). Within microfacies column, blue corresponds to Limestone, orange to Carbonaceous Mudstone, and green to Calcareous Concretion. Oriented abundances are given for total organic carbon and the redox sensitive trace metals uranium, molybdenum, and vanadium.

Using those criteria, the maximum flooding surface is placed at the top of the uppermost packstone unit at each location. Using those criteria, slight increases in both TOC and uranium content occur near the maximum flooding surface at both locations. Evidence that this chosen horizon corresponds to the maximum transgression exists in the vertical trends above this level: The immediately overlying parasequence transitions upward into beds with

significantly enriched organic carbon and redox-sensitive trace elements. Additionally, this overlying interval hosts strata with elevated Si and Al contents suggestive of an increase in clastic input (Figures 5, 15). We interpret this to represent the beginning of progradation during the highstand systems tract, even given the euxinic depositional setting. Although one might argue that the maximum flooding surface ought to coincide with the most organic-rich and anoxic conditions, the proxies for anoxic to euxinic conditions (high organic carbon, molybdenum and vanadium) recur at a minimum of four higher positions within the Union Springs. That repetition indicates that anoxic to euxinic bottom water conditions remained possible well into the regressive systems tracts and have no strong relationship to the maximum flooding surface (Figures 6, 16).

An alternative explanation is that the differing flooding surface chemical signals reflect spatial variability of the constituents deposited simultaneously in different parts of the Marcellus-age Acadian foreland epicontinental sea. Detrital clastic sediment supply to the basin was asymmetric, with maximum volumes delivered to the southeastern margin of the basin where subsidence was also a maximum. All the locations used by Kohl et al. (2014) to calibrate their facies interpretations of gamma log data are on the proximal flank of the seaway, where there was a significant clastic influx delivered by river systems. That sediment supply actively shaped the bathymetric profile as well as supplying sand, silt and clay. Lash and Blood's (2014) study highlights a location approximately along the axis of the basin. In contrast, this study looks at a location on the distal basin flank, not reached by siliciclastic detritus from the proximal delta systems. Even though eustatic sea level change and crustal tilting that contributed to the organization of the Pennsylvania sections into parasequences probably also

impacted the northern Finger Lakes sites at the same times, the materials recording the basin-wide events were not the same.

During the regressive systems tracts, a number of petrographic signals were utilized to delineate parasequences (e.g., Chapter 1); similarly there are multiple chemical signals that are interpreted to indicate parasequence boundaries (flooding surfaces). In principle siliciclastic-rich sedimentary basin parasequences are identified by upward shoaling facies that are capped by facies indicative of a shift to deeper water facies, which commonly means decreased rate of sediment supply (Posamentier et al., 1988). Therefore the two strategies for identifying parasequences in the distal and highly condensed sections of north central New York are vertical trends in depositional facies indicative of relative sea level change and horizons indicative of sediment starvation. Karaca (2012) found the latter strategy to be most applicable, using concretionary horizons that mark horizons of extended sediment starvation as parasequence boundaries in a Union Springs section located about 60 m from the *Seneca North* section. These calcareous concretions (Table 2; Chapter 1; Karaca, 2012) have chemical signals that permit identification in chemostratigraphic columns (Figures 5, 6, 15, 16): high calcium abundance, low aluminum and silica content, general lack of redox-sensitive trace element enrichment, and lower TOC than the mudstones around them. Concretionary abundances of Ti and Zr, elements associated with continentally-derived heavy minerals, are moderate and generally lower than abundances within the Carbonaceous Mudstone facies group. The concretions, formed as a result of reactions mediated by sulfate-reducing bacteria (Raiswell & Fisher, 2000), contain significantly more pyrite, and thus Fe, than the limestones found at the base of the formation (Table 2).

In some cases facies changes also reveal parasequences. An example is found within the third parasequence above the base of the formation (Figure 15). Here, Carbonaceous Mudstones show gradually increasing percentages of Al and Si moving upwards from the shell-rich storm-associated Microfacies XI (Interbedded Dacryoconarid-Rich Calcareous Mudstone) before these terrigenous proxy elements dip slightly at a flooding surface represented by Microfacies XII (Clay and Calcareous-Cement Bearing Carbonaceous Mudstone) (Figure 15). Uranium, molybdenum, and vanadium enrichments indicate anoxic bottom waters at this flooding surface (Figure 16; Table 3).

Nevertheless, the use of chemical trends to identify facies trends in these distal columns is not straightforward. For example, overall the aluminum abundances are highly variable throughout the section and most of the petrographically defined parasequences do not align with patterns of Al variation. Consequently, lithologic criteria including compositional variation, grain size trends, and continuous concretionary horizons serve as more reliable markers of flooding surfaces in many cases. Despite the progradation of clastic facies into the Acadian foreland basin as Union Springs deposition progressed, sediment supply was insufficient across the distal study area to cause large facies changes such as those occurring in more proximal areas of the basin, where the deposition of the coarser-grained Stony Hollow Member is expressed in New York (Ver Straeten, 2007), and the Mahantango delta in Pennsylvania (Kohl et al., 2014).

Potential Effects of Depositional Steadiness on Paleo-oceanographic Interpretation

Because this study is executed in the distal region of the basin, the thickness of the Union Springs Formation at the study site is significantly condensed when compared to more proximal areas which have been the focus of a number of aforementioned geochemical studies. Comparing and interpreting trends in data collected across facies transitions and with significantly less rock may be problematic; particularly if condensation in the distal region is associated with a marked increase in depositional unsteadiness. In this section, the relative degree of depositional time represented by the strata of the distal Union Springs Formation is discussed in order to establish whether or not the data collected in this region is comparable to studies in more proximal locales.

Deposition of the Union Springs Formation began following the emplacement of the Tioga F K-Bentonite (Ver Straeten, 2004) and ended prior to the beginning of the Givetian stage identified within the overlying Oatka Creek Formation (Over et al., 2011). If the Union Springs Formation constitutes 2-3 million years elapsed time, a bulk rate of sediment accumulation of the Union Springs Formation in the northern Finger Lakes region is ~2-3 mm/1000 years. Within this study, instrument specifications dictated that handheld XRF analyses probe rock composition in 3-mm-thick intervals of Union Springs Formation. Thus, it is plausible that the content of the compositional data can be documented for time steps on the order of ~1000 years. However, it is now generally understood that active sediment deposition occurs as quantum packages (Ager, 1981) and it has been demonstrated that time is very unequally represented in the East Berne Member of the Oatka Creek Formation (Bartholomew and

Schramm, 2013). Whereas unsteady pelagic deposition in the Union Springs would contrast with well-documented steady accumulation in some pelagic environments (Anders et al., 1987), this difference may be anticipated because the Union Springs Formation formed in an epicontinental setting near an active mountain belt, very unlike the deep ocean realm studied by Anders et al. (1987). Specific to the Union Springs Formation and its record of paleo-oceanographic fluctuations, we do not know *a priori* if every year contributed 3 microns of sediment (thickness after compaction), or whether a small fraction of that time span experienced moderately high accumulation rates that were offset by stasis all the rest of the time. Laminations in the black mudstone facies in two studied quarries are 10 micron to 1 mm thick, and many are event beds (Chapter 1; Karaca, 2012). If we assume a mean lamination thickness of 100 microns, then the full ~3.8 m thickness could represent 38,000 depositional events. We do not know whether those all occurred in a single 11,000 years span, or were well distributed over the entire available ~2-3 Myr.

While this postulation may initially suggest a bleak reality, examination of the compositional data indicates that Union Springs time is relatively well-represented and well-distributed. Data from 101 sampled horizons across 3 Union Springs columns which measure 3.22-3.87 meters in thickness record responses to dynamic basin conditions recorded by strata in more proximal locations, although sedimentologic expressions may differ. Basin subsidence, sediment starvation, the effect of parasequence-level base level fluctuations on terrigenous sediment supply are largely recorded by pelagic limestone deposition, bone beds, grain size trends, and the formation of calcareous concretions. This sedimentologic evidence, along with the lack of any major facies discontinuities, points to Union Springs depositional time being

sufficiently well-represented and well-distributed throughout the studied strata to allow for paleo-oceanographic conclusions to be drawn and for comparison to high-resolution physical and chemical analyses of Union Springs sections elsewhere in the basin, including those of Kohl et al. (2014), Lash and Blood (2014), Zapata (2014), Bruner et al. 2015, Wendt et al. (2015), and others.

Conclusion

X-ray fluorescence and TOC analysis of three lithologically-characterized Union Springs sections allowed the placement of compositional variability within a geologic context. When studying the covariation of two compositional parameters, the use of petrographic information proved to be very helpful in elucidating the controls on covariation of pairs of chemical parameters. The principal controls on elemental variability were found to include the competition between terrigenous sediment supply against carbonate deposition, and euxinia against some degree of bottom water oxygenation. For the pairs Ca/TOC, Al/Si, and U/Mo, the controls proved to include bioturbation, sediment supply, and the impact on the depositional substrate of seafloor currents.

Despite the strong control of anoxia/euxinia on variability, and evidence of anoxic conditions throughout significant volumes of each studied section, the presence of periodically-occurring laminations within “anoxic” microfacies containing fossil evidence of inhabitance by brachiopods or bivalves indicates that anoxia was not an environmentally-permanent feature. Here, paleontologic examination serves as an interpretative aid and check on geochemical data,

which samples several laminations with each measurement made in rocks which often possess laminations just hundreds of microns thick.

Some of the elemental abundance trends are related to the distribution of diagenetic features, such as calcite cementation or exotic sulfide precipitation, rather than environmental attributes. Identification of the chemical controls exerted by diagenesis is important to enable exclusion of those signals from the set used for the interpretation of depositional conditions.

Within the significantly condensed study area, terrigenous deposition rates were never high enough over sustained periods of time to dilute the organic carbon. As a result, throughout the north-central New York study area organic carbon enrichment is significant on average, but unevenly vertically distributed. This is relevant to the resource characterization of the Union Springs Formation for its implications for the distribution of recoverable hydrocarbons within the formation as well as variations in mechanical behavior within and between stratigraphic horizons (Chapter 3).

The organic carbon enrichment is greatest in the highstand to falling stage systems tracts. The highest organic carbon values occur above the maximum flooding surface and are accompanied by a jump in aluminum abundance as well as by intense redox-sensitive trace element enrichment. High values of TOC repeat in multiple horizons of all the parasequences above the maximum flooding surface. In contrast, redox-sensitive trace element abundances are elevated in the lower three parasequences (two at Marcellus Saunders quarry) above the maximum flooding surface and then within the fourth parasequence (third at Marcellus Saunders quarry) begins a long-lived decrease toward the top of the formation, indicating less

intense oxygen restriction. This pair of trends suggests that a highly productive water column continued to deliver large quantities of biomass to the depositional substrate during the time of regression even though the overall oxygenation of the bottom waters increased.

Appendix A: Microfacies Identified Across Study Area

Facies Name	Facies Number	Lithofacies Group
Dacryoconarid Wackestone	**1**	Limestone
Dacryoconarid Packstone	**2**	Limestone
Benthic Wackestone	**3**	Limestone
Benthic Packstone	**4**	Limestone
Quartz and Dolomite- Bearing Carbonaceous Mudstone	**5**	Carbonaceous Mudstone
Clay-Rich Carbonaceous Mudstone	**6**	Carbonaceous Mudstone
Clay-Rich Quartz Silt-Bearing Carbonaceous Mudstone	**7**	Carbonaceous Mudstone
Clay-Rich Calcite-Silt Bearing Carbonaceous Mudstone	**8**	Carbonaceous Mudstone
Fossil-Bearing Clay-Rich Carbonaceous Mudstone	**9**	Carbonaceous Mudstone
Interbedded Dacryoconarid-Bearing Calcareous Mudstone	**10**	Carbonaceous Mudstone
Interbedded Dacryoconarid-Rich Calcareous Mudstone	**11**	Carbonaceous Mudstone
Clay and Calcareous-Cement Bearing Carbonaceous Mudstone	**12**	Carbonaceous Mudstone
Algae-Bearing Calcareous Concretion	**13**	Calcareous Concretion
Algae- and Dacryoconarid-Bearing Calcareous Concretion	**14**	Calcareous Concretion
Algae- and Dacryoconarid-Bearing Zoned Calcareous Concretion	**15**	Calcareous Concretion

Appendix B: Principal Component Analysis

Analyzed parameters include total organic carbon, total inorganic carbon, bioturbation, Mg, Al, Si, S, K, Ca, Ti, V, Cr, Mn, Fe, Co, Ni, As, Pb, Th, Rb, U, Sr, Y, Zr, Nb, Sb, and Mo.

For each analysis, closed data set was subjected to additive log-ratio transformation after Aitchison (1986). Analysis completed using PAST software. Data transformations completed using CoDaPak software.

A. Results – Full Data Set Analysis (Seneca Falls, NY and Marcellus, NY)

i. Coordinates

Sample positions give the precise coordinates of each analyzed sample with respect to the three principle components as determined by the analysis.

	PC 1	PC 2	PC 3
JSS25	-2.5887	1.5679	-1.321
JSS47	-3.5912	1.3553	-2.0549
JSS66	-2.4635	1.5684	-1.0782
JSS33	-4.5672	-0.58858	-1.9648
JSS59	-5.685	-0.42801	-2.2562
JSS78	-1.8198	2.8768	-0.66685
JMS49	-2.8655	1.8451	-2.134
JMS19	-5.272	0.4466	-2.4282
JMS40	-5.3274	-1.2157	-1.6212
JSS14	5.5572	7.0386	0.30511
JSS160	3.9989	1.9979	0.13045
JSS117	6.9396	-2.655	-0.24013
JSS119	5.2483	-0.66833	0.21587
JMS67	7.3878	-3.6427	-1.0555
JMS109	5.8213	-2.9342	-0.38805
JMS319	3.3678	3.3587	-0.14953
JSS130	5.771	-3.1765	-0.14643
JSS171	6.5775	-1.9547	0.28636
JSS211	4.9967	-1.4848	0.046692
JSS219	5.7894	-1.1575	0.48
JSS326	-0.04232	1.0223	0.66245
JMS135	5.0319	0.98593	-0.19317
JMS305	2.1597	2.6483	1.2383

JSS288	2.6056	-0.01571	0.1633
JMS272	2.7777	1.0212	0.441
JSS235	4.4018	-3.0649	0.63242
JSS245	2.8075	-1.0549	0.42086
JMS15	2.8886	-0.64041	-1.2374
JMS76	0.089482	0.083193	-0.74087
JMS80	2.0939	-0.23908	-1.3241
JMS88	0.89336	0.064808	-0.5066
JMS112	4.982	-1.3816	-0.09279
JMS243	-4.9605	-7.0713	-3.1344
JSS108	0.73268	0.85277	-0.01292
JMS97	-2.7302	-1.5067	0.93261
JSS99	-3.2106	-0.30337	-1.0912
JMS125	2.9631	-0.86693	-0.80351
JMS192	1.5532	0.5266	-0.45763
JSS139	-0.79893	2.0905	0.075538
JSS149	0.79783	2.439	0.61662
JSS190	-1.4708	1.6732	-0.15813
JSS199	-1.314	2.8093	-1.2104
JSS223	-0.41574	-0.16788	0.056264
JSS272	0.79995	3.9912	0.005187
JSN266	-3.3866	0.005006	1.3456
JSS213	-3.0546	0.44329	2.2423
JSS256	-3.7019	-1.766	1.6924
JMS203	-0.87023	0.064045	0.9003
JSN164	-3.8173	0.44225	0.79016
JSN234	-3.7538	0.87213	1.8154
JSN241	-0.96492	1.3145	0.18738
JSS233	-2.4716	0.66277	1.0891
JSS370	-3.8858	0.091623	2.0537
JMS215	-1.0791	0.29406	0.1682
JMS222	-4.5895	-1.6506	0.58057
JMS302	-0.06298	2.7175	0.25151
JSN171	-3.4703	-0.91847	0.67764
JSN337	-3.1737	0.099295	1.4947
JSN347	-4.351	-2.8693	2.4751
JSN357	-4.1646	-4.8672	2.374
JSS336	-3.1125	-0.97995	1.6209

ii). Principal Component Loadings

Component loadings represent the coefficients for each variable in the linear combination forming each principal component. Loadings are used to show the correlation between each variable with the calculated components.

	PC 1	**PC 2**	**PC 3**
Bioturbation	-0.06452	0.12893	-0.59614
IOC	-0.1908	0.24097	0.16333
TOC	0.20352	0.039799	0.017412
Mg	-0.05636	0.27648	0.11491
Al	0.22641	0.10453	-0.02927
Si	0.23556	0.15256	-0.11383
S	0.21339	-0.04939	0.33883
K	0.23949	0.1358	-0.13681
Ca	-0.2026	0.26652	0.11032
Ti	0.24246	0.12211	-0.02349
V	0.20611	-0.0819	-0.07104
Cr	0.19572	0.10092	-0.04334
Mn	-0.13063	0.37316	0.068218
Fe	0.21444	-0.04313	0.32579
Co	0.22857	-0.01291	0.22563
Ni	0.25437	0.024378	-0.00384
As	0.20971	-0.12287	-0.04076
Pb	0.21599	0.059481	0.2289
Th	0.19098	0.26974	0.040633
Rb	0.24262	0.11257	-0.08426
U	0.15461	0.049012	-0.38893
Sr	-0.0817	0.36194	-0.12059
Y	-0.11156	0.35767	0.19477
Zr	0.23595	0.15464	-0.01855
Nb	0.089428	0.38903	-0.01901
Mo	0.22784	-0.08268	-0.09202

iii). Mapped Principal Components

The following charts show the positions of each sample in the sample set with respect to the three most significant principal components.

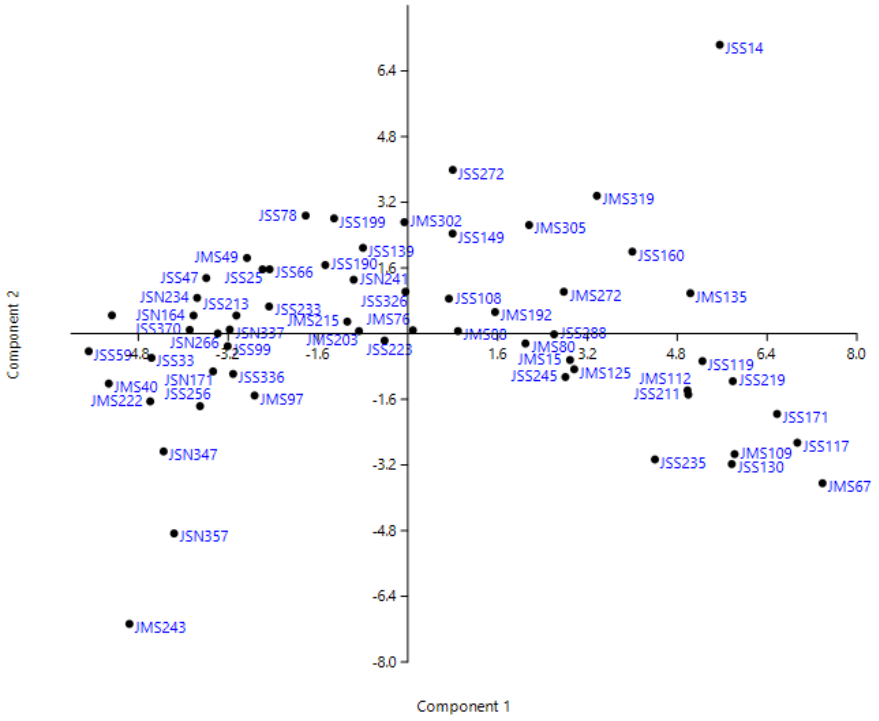

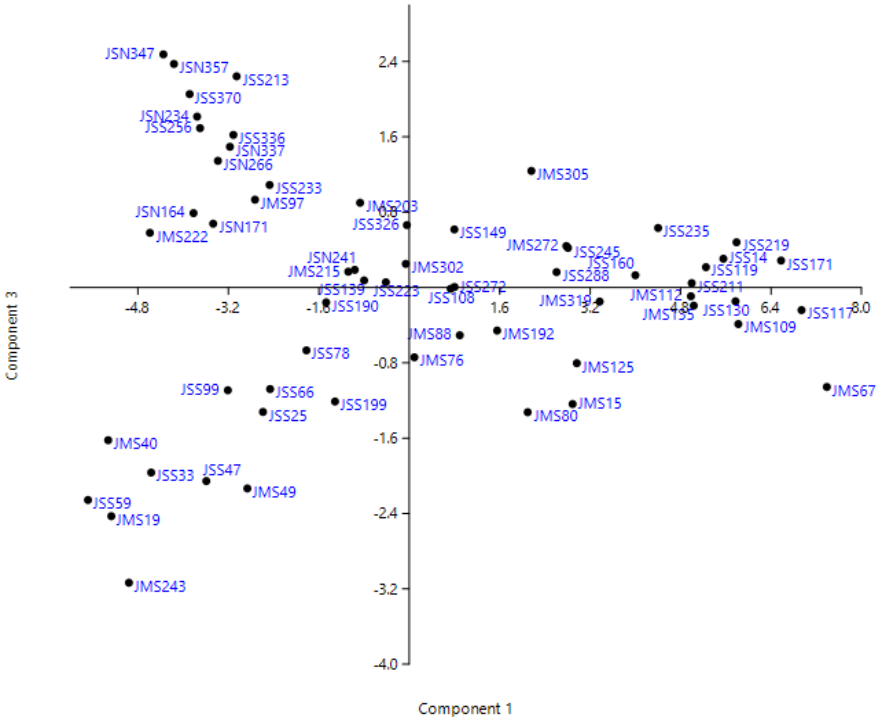

B. Seneca Falls, NY Analysis

i. Coordinates

	PC 1	PC 2	PC 3
JSS59	-5.3256	-0.50116	-2.8514
JSS33	-4.1984	-0.67917	-2.836
JSN347	-3.7469	-3.6913	1.4793
JSN164	-3.5878	0.098607	0.39942
JSS370	-3.5404	-0.55247	1.5709
JSN234	-3.4579	0.26841	1.49
JSN357	-3.4553	-5.8925	0.71963
JSS47	-3.3271	1.5053	-2.1573
JSS256	-3.2291	-2.2635	1.3281
JSN171	-3.0629	-1.3464	0.096397
JSN266	-3.0505	-0.58072	0.77419
JSS99	-2.9853	-0.2605	-1.852
JSN337	-2.7885	-0.48967	1.1271
JSS213	-2.7504	-0.13325	2.1344
JSS336	-2.7478	-1.4522	1.0246
JSS25	-2.2904	1.5175	-1.6301
JSS66	-2.2142	1.5218	-1.3935
JSS233	-2.1852	0.34322	0.92282
JSS78	-1.7146	2.9813	-0.33949
JSS190	-1.2116	1.4848	-0.06889
JSS199	-1.1682	2.913	-0.99406
JSN241	-0.7088	1.1588	0.25134
JSS139	-0.6094	2.0566	0.2299
JSS223	-0.0613	-0.31736	-0.29812
JSS326	0.276	0.69907	1.377
JSS272	0.90106	4.0319	0.44521
JSS108	0.96154	0.8357	-0.60663
JSS149	1.0212	2.3713	0.69924
JSS288	2.9966	-0.20497	-0.42651
JSS245	3.301	-1.1942	0.033197
JSS160	4.2552	2.1074	0.3587
JSS235	5.0488	-3.0862	-0.42515
JSS14	5.4815	7.4295	1.5346
JSS211	5.5961	-1.4956	-0.16679

JSS119	5.7896	-0.64862	-0.1452
JSS219	6.3816	-1.1449	0.13903
JSS130	6.5196	-3.0988	-0.88862
JSS171	7.2125	-1.8203	-0.14253
JSS117	7.6755	-2.4702	-0.91264

ii. Loadings

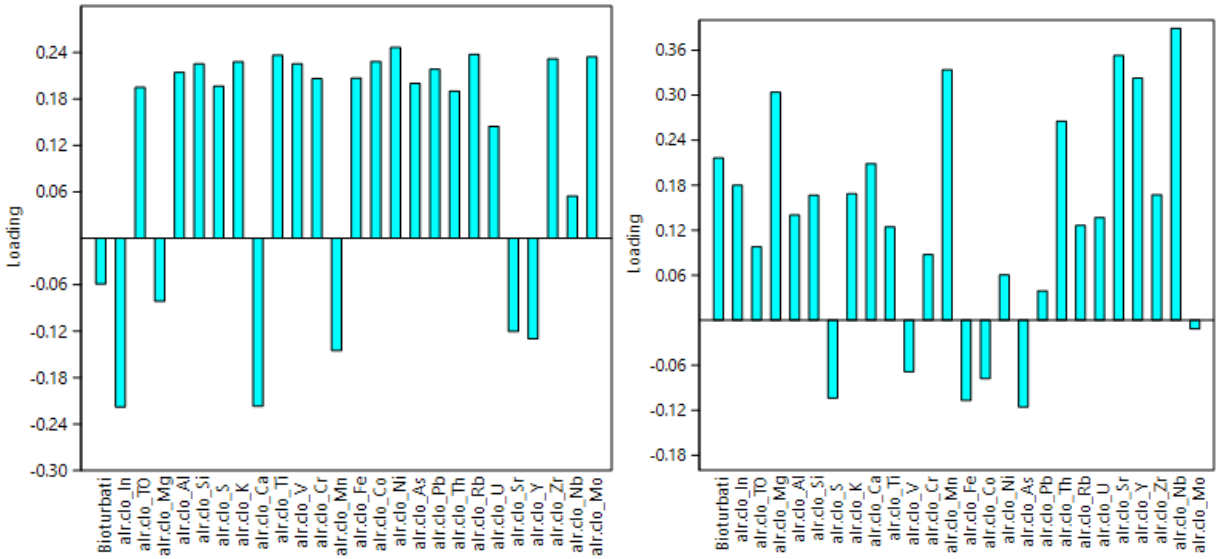

iii. Mapped Components

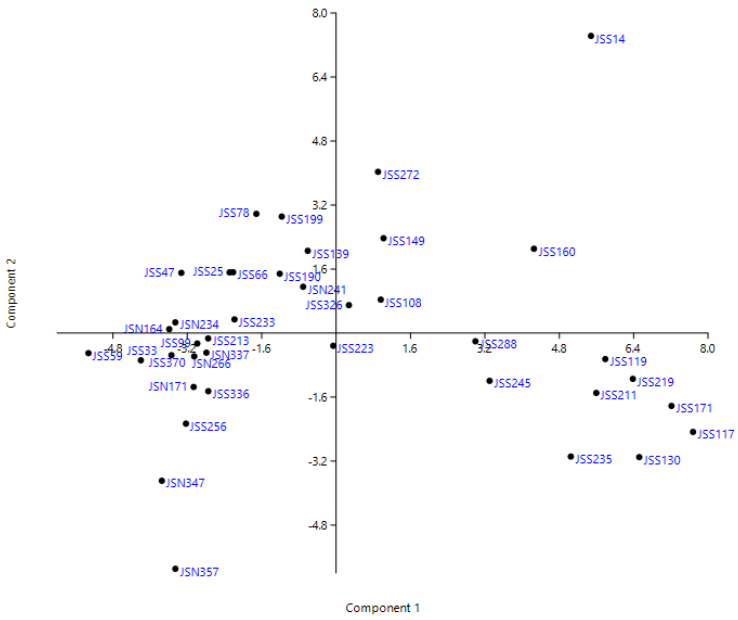

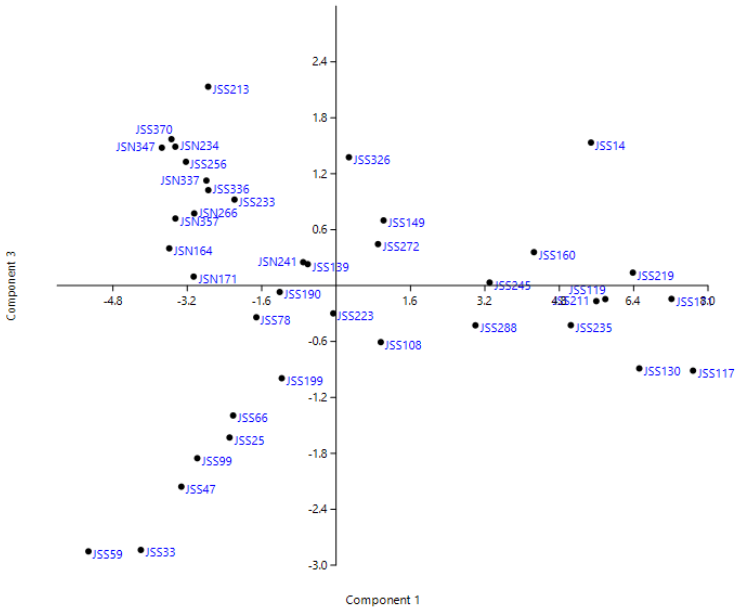

C. Marcellus, NY

i. Sample Positions

	PC 1	PC 2	PC 3
JMS49	-3.4191	2.1971	1.9204
JMS19	-5.9605	1.2376	2.2779
JMS40	-6.2336	0.032519	2.3827
JMS67	6.2108	-3.9029	2.2988
JMS109	4.7184	-2.9039	0.40092
JMS319	3.0835	3.1343	-0.4892
JMS135	4.4091	0.61569	-0.16422
JMS305	1.7751	3.1257	-0.85325
JMS272	2.2627	1.2512	-1.5005
JMS15	2.1424	-0.86609	-0.23239
JMS76	-0.35551	0.24978	-0.59677
JMS80	1.4846	-0.22925	-1.0816
JMS88	0.38	0.21506	-0.10988
JMS112	4.1521	-1.3711	0.17128
JMS243	-6.2533	-6.4198	-1.7573
JMS97	-3.2087	-0.49868	-2.4105
JMS125	2.2114	-0.657	1.3719
JMS192	1.0265	0.71532	0.72372
JMS203	-1.3566	0.68815	- 0.42568
JMS215	-1.566	0.93261	-0.5036
JMS222	-5.1228	-0.52115	-0.58695
JMS302	-0.38048	2.9748	-0.83567

ii. Loadings

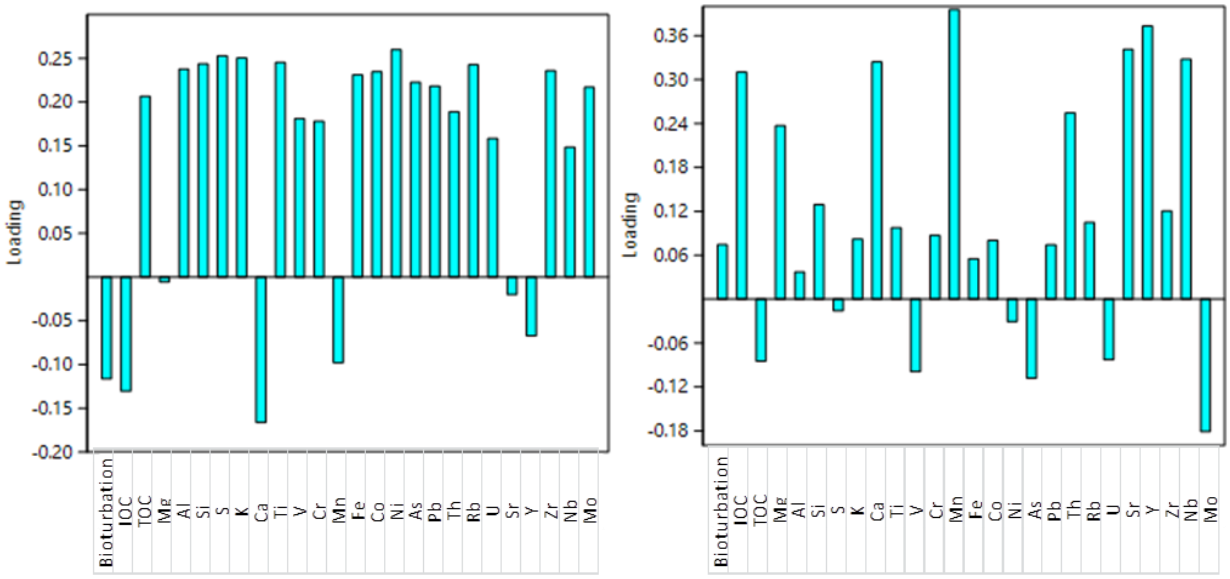

iii. Mapped Components

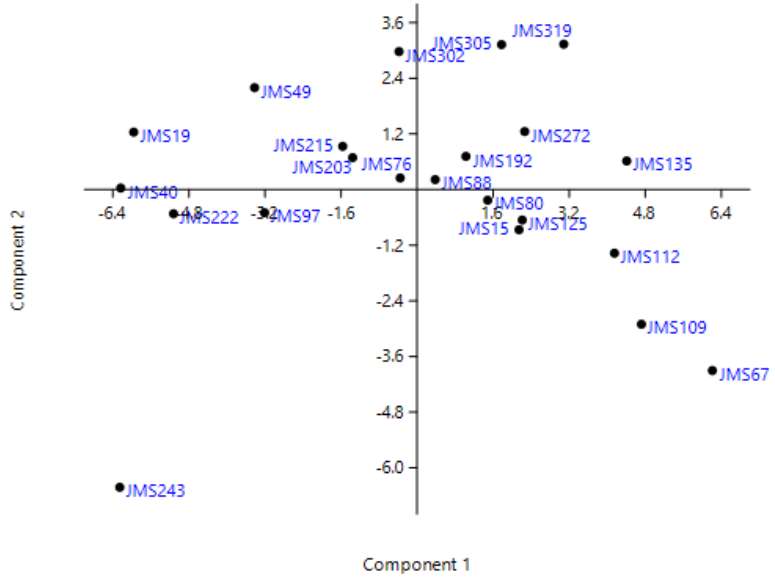

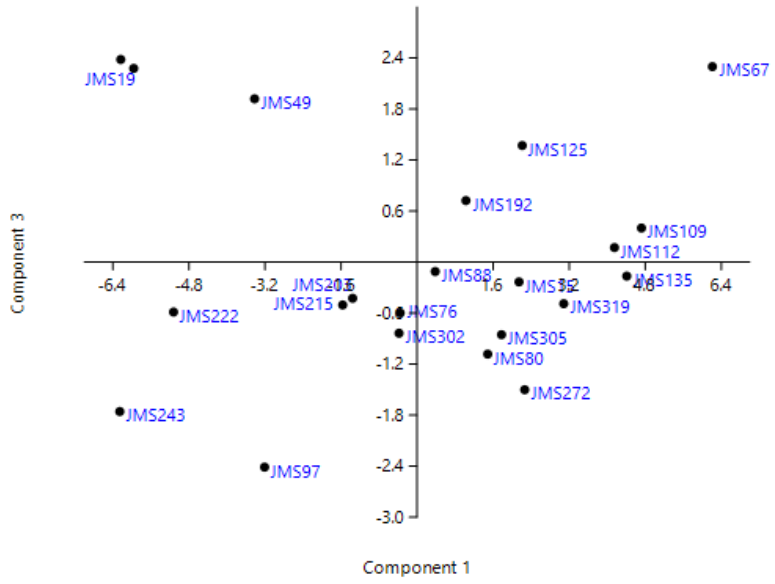
JMS19
JMS49
JMS67
JMS125
JMS192
JMS109
JMS112
JMS88
JMS135
JMS319
JMS222
JMS215
JMS76
JMS302
JMS305
JMS80
JMS272
JMS243
JMS97
2.4
1.8
1.2
0.6
-1.2
-1.8
-2.4
-3.0
-6.4
-4.8
-3.2
6.4
Component 3
Component 1

Appendix C: Geochemical Data Set

Obtained at University of Kentucky Stratigraphy Lab using Bruker Tracer IV X-Ray Fluorescence Spectrometer.

JSS = Seneca Stone Quarry, Seneca Falls, NY – South Wall

JSN = Seneca Stone Quarry, Seneca Falls, NY – North Wall

JMS = Saunders Quarry, Marcellus, NY – Southwest

Sample Position = Height above base of formation, in centimeters

Repeated sample positions indicate multiple resolvable characteristics were scanned within a sample. (e.g. zoned concretion).

Values below detection limit are placed at .1 ppm for trace elements; major elements at .01%.

i. Bioturbation & Major Element Abundances

Column	Sample Position	Microfacies #	Bioturbation Index (1-5)	Inorg. Carb wt%	TOC wt%	Mg wt%	Al wt%	Si wt%	S wt%	K wt%	Ca wt%	Ti wt %	Fe wt%
JSN	30	1	x	10.12	1.19	0.99	0.50	4.29	0.22	0.41	35.11	0.05	0.36
JSN	52	1	x	10.67	1.37	0.76	0.30	3.75	0.19	0.41	34.97	0.05	0.37
JSS	25	1	4	9.90	1.31	0.84	0.63	5.70	0.23	0.44	34.47	0.05	0.84
JSS	47	1	5	9.33	1.86	1.16	0.50	4.26	0.26	0.38	35.15	0.04	0.33
JSS	66	1	3	10.16	1.46	0.81	0.75	4.47	0.32	0.54	32.33	0.05	0.47
JSN	43	2	x	8.90	4.20	0.94	0.55	3.78	0.26	0.44	35.97	0.04	0.42
JSN	48.5	2	x	8.76	4.81	0.74	0.18	3.42	0.20	0.32	35.89	0.03	0.38
JSN	61	2	x	8.77	2.32	0.88	0.43	3.81	0.29	0.38	36.09	0.03	0.37
JSS	33	2	4	9.58	1.60	0.65	0.33	3.59	0.18	0.38	35.80	0.03	0.42
JSS	59	2	4	10.51	0.88	0.84	0.04	3.56	0.31	0.21	36.45	0.03	0.34
JSS	78	2	2	9.50	2.59	1.37	1.04	4.71	0.48	0.70	34.52	0.07	0.45
JMS	49	3	5	5.54	2.50	0.87	0.32	3.87	0.35	0.35	37.62	0.03	0.37
JMS	53.5	3	5	x	x	0.78	0.01	3.37	0.00	0.25	33.10	0.02	0.47

Column	Sample Position	Microfacies #	Bioturbation Index (1-5)	Inorg. Carb wt%	TOC wt%	Mg wt%	Al wt%	Si wt%	S wt%	K wt%	Ca wt%	Ti wt %	Fe wt%
JMS	19	4	5	7.76	1.01	0.81	0.02	3.06	0.11	0.21	37.35	0.02	0.28
JMS	40	4	5	9.90	1.11	0.78	0.13	3.74	0.16	0.25	37.74	0.03	0.64
JSS	14	5	3	3.62	4.84	1.35	5.49	14.55	1.03	3.89	17.20	0.18	1.44
JSS	160	5	2	3.32	12.77	0.74	3.22	11.12	2.18	1.52	21.58	0.16	2.17
JSN	139	6	x	4.50	11.03	0.54	6.05	16.83	2.81	3.16	11.72	0.27	3.02
JSS	117	6	1	1.48	12.73	0.78	5.46	16.74	3.81	2.89	9.22	0.27	4.59
JSS	119	6	1	3.36	11.23	0.64	4.21	12.87	3.40	2.29	16.29	0.22	3.21
JMS	67	7	2	1.79	11.71	1.07	5.18	18.91	6.99	2.63	4.05	0.25	5.04
JMS	109	7	1	1.72	12.93	0.43	4.65	15.30	2.94	2.48	9.92	0.21	3.79
JMS	319	7	2	5.37	5.00	0.54	4.41	11.74	1.90	1.82	20.68	0.17	1.36
JMS	130	7	3	x	x	0.89	5.34	18.67	5.34	2.95	8.23	0.30	4.43
JSN	91.5	7		1.43	11.74	0.78	4.80	14.51	3.45	2.52	14.91	0.26	3.61
JSN	183	7	x	6.51	7.89	0.39	2.84	9.16	1.64	1.54	19.61	0.15	5.48
JSN	309	7	x	5.13	9.70	0.84	5.97	16.31	5.03	2.38	10.31	0.24	2.31
JSS	130	7	1	2.49	12.55	0.65	5.29	16.83	4.28	2.58	8.39	0.24	4.10
JSS	171	7	1	1.49	13.29	0.90	5.09	17.68	4.94	2.48	8.81	0.24	4.76
JSS	211	7	1	2.53	13.73	0.58	5.06	16.63	3.35	2.51	11.72	0.28	3.15
JSS	219	7	1	2.28	14.06	0.57	4.77	15.55	3.87	2.32	10.87	0.22	3.60
JSS	326	7	1	4.91	7.91	0.49	3.95	12.07	2.89	1.73	17.09	0.17	0.37
JMS	135	8	1	2.24	12.69	0.65	4.58	13.58	2.59	2.62	15.63	0.25	1.89
JMS	305	8	2	5.60	4.95	0.40	3.46	9.52	0.88	1.44	22.88	0.14	2.25
JSN	296	8	x	x	x	0.44	3.82	11.99	2.20	1.96	16.93	0.20	2.51
JSS	205	8	1	x	x	0.68	3.82	11.52	1.85	1.78	22.77	0.20	2.12
JSS	288	8	2	7.44	6.06	0.51	3.24	10.98	1.63	1.54	21.76	0.18	2.51
JMS	272	8	2	6.18	7.76	0.22	2.70	8.81	1.71	1.25	17.71	0.11	2.37
JSN	219	9	x	4.99	9.91	0.65	2.68	8.85	2.10	1.29	24.38	0.15	2.01
JSS	235	9	2	7.75	5.93	1.26	3.95	12.01	7.85	2.01	13.44	0.23	4.47
JSS	245	9	1	5.12	9.14	0.61	3.15	9.98	2.75	1.45	20.94	0.14	2.31

Column	Sample Position	Microfacies #	Bioturbation Index (1-5)	Inorg. Carb wt%	TOC wt%	Mg wt%	Al wt%	Si wt%	S wt%	K wt%	Ca wt%	Ti wt %	Fe wt%
JMS	15	10	2	1.92	12.66	0.52	2.53	8.91	1.81	1.32	24.82	0.14	1.72
JMS	76	10	2	5.62	7.34	0.66	1.11	5.19	1.20	0.60	31.17	0.08	1.36
JMS	80	10	2	4.54	10.26	0.27	3.06	11.53	2.21	1.81	17.67	0.19	1.36
JMS	80	10	2	x	x	0.47	2.25	7.92	1.59	1.10	25.54	0.11	1.62
JMS	88	10	2	8.15	5.24	0.74	2.25	7.71	1.76	1.09	27.88	0.11	1.42
JMS	112	10	1	5.08	10.79	0.51	4.21	13.49	3.15	2.27	14.43	0.20	3.13
JMS	112	10	1	x	x	0.47	1.57	5.69	1.07	0.77	28.11	0.06	1.08
JMS	243	10	2	4.18	13.05	0.31	0.98	4.68	0.60	0.60	27.90	0.06	0.49
JSN	72	10	x	x	x	0.56	0.61	3.58	0.57	0.29	33.25	0.03	0.49
JSN	72	10	x	4.92	8.18	0.40	2.49	8.20	2.20	1.28	22.81	0.14	2.67
JSN	87	10	x	8.43	4.65	0.83	1.34	5.35	1.09	0.63	33.09	0.08	0.91
JSS	85	10	x	8.43	2.83	1.39	2.38	6.91	11.26	1.01	15.45	0.13	2.63
JSS	108	10	2	7.78	4.97	0.91	1.02	5.26	1.40	0.57	32.66	0.06	1.19
JMS	97	11	1	9.20	4.78	0.27	0.43	3.31	0.56	0.22	27.25	0.02	1.89
JSS	99	11	2	6.47	6.85	0.69	0.29	3.18	0.39	0.24	36.47	0.03	0.37
JMS	125	12	1	x	x	0.88	0.46	3.49	1.11	0.31	37.02	0.04	1.01
JMS	122	12	3	9.73	3.93	0.79	3.01	10.22	2.38	1.56	21.23	0.15	2.40
JMS	130	12	2	x	x	0.76	2.92	9.63	1.70	1.48	26.23	0.16	1.10
JMS	192	12	3	8.61	4.32	0.89	2.47	7.73	1.56	1.21	29.27	0.11	2.14
JMS	268	12	2	6.77	6.81	0.48	3.23	9.88	2.23	1.59	19.61	0.16	2.05
JSN	128	12	x	8.94	6.34	0.83	1.01	4.78	0.90	0.63	32.17	0.07	0.70
JSN	199	12	x	9.05	3.62	0.86	0.89	4.44	0.69	0.48	35.42	0.06	0.71
JSN	212	12	x	6.79	7.20	0.64	1.99	6.89	1.18	0.98	29.49	0.11	1.14
JSN	337	12	x	x	x	0.48	2.29	6.95	0.14	0.92	30.70	0.11	0.71
JSN	357	12	x	x	x	0.48	2.78	7.89	0.20	1.14	27.80	0.13	1.33
JSS	139	12	2	8.96	4.47	1.00	0.75	4.51	0.70	0.46	36.30	0.06	0.60
JSS	149	12	2	8.35	5.10	0.74	1.18	5.15	1.31	0.67	32.43	0.07	0.99
JSS	190	12	3	9.27	3.08	0.80	1.02	5.17	1.01	0.55	33.43	0.08	0.60

Column	Sample Position	Microfacies #	Bioturbation Index (1-5)	Inorg. Carb wt%	TOC wt%	Mg wt%	Al wt%	Si wt%	S wt%	K wt%	Ca wt%	Ti wt %	Fe wt%
JSS	199	12	4	7.97	3.97	0.91	0.97	5.46	0.53	0.54	34.26	0.07	0.54
JSS	223	12	2	8.65	4.09	0.95	1.35	6.24	1.21	0.75	31.94	0.09	1.21
JSS	268	12	x	8.62	3.79	0.84	4.92	14.54	2.63	2.05	17.28	0.26	2.90
JSS	272	12	3	9.19	3.28	0.92	1.67	6.02	0.77	0.84	32.91	0.10	0.97
JSS	361	12	2	x	x	0.58	3.43	9.76	0.76	1.47	25.64	0.17	1.52
JSN	200	13	1	x	x	0.88	1.21	4.69	0.56	0.51	35.20	0.06	0.59
JSN	207	13	1	x	x	0.73	0.17	2.56	0.67	0.20	36.87	0.03	0.66
JSN	266	13	1	11.19	1.05	0.78	0.22	2.63	1.05	0.21	37.57	0.04	1.05
JSS	213	13	1	8.06	5.02	0.93	0.24	2.65	0.85	0.21	38.09	0.03	0.90
JSS	256	13	1	8.86	2.65	0.99	0.22	2.40	2.27	0.17	36.16	0.03	0.55
JMS	203	14	1	9.33	3.69	0.81	0.83	4.21	1.19	0.48	35.13	0.05	1.33
JSN	164	14	1	9.17	3.62	0.68	0.20	2.58	0.64	0.20	37.78	0.03	0.45
JSN	234	14	1	10.95	1.70	0.70	0.19	2.54	0.47	0.19	38.18	0.03	0.60
JSN	241	14	1	9.79	3.15	0.80	1.29	4.98	0.77	0.62	34.10	0.08	0.72
JSS	233	14	1	7.48	6.08	0.75	0.35	2.71	0.79	0.23	37.50	0.03	0.71
JSS	295	14	1	x	x	0.87	0.16	2.35	0.53	0.17	37.47	0.03	0.57
JSS	370	14	1	10.97	1.37	0.84	0.21	2.55	0.93	0.19	38.00	0.03	0.63
JMS	215	15	1	10.55	1.12	0.54	1.45	5.26	0.73	0.70	30.52	0.07	0.76
JMS	215	15	1	x	x	0.66	0.34	2.72	0.82	0.21	34.88	0.04	0.97
JMS	222	15	1	10.82	1.25	0.70	0.21	2.48	0.55	0.19	36.79	0.02	0.65
JMS	302	15	1	8.22	2.95	0.54	2.19	6.80	0.49	0.97	30.86	0.10	0.68
JMS	302	15	1	x	x	0.97	0.24	2.44	0.81	0.16	38.12	0.04	0.97
JMS	302	15	1	x	x	0.71	0.49	3.04	0.58	0.26	36.94	0.04	0.87
JSN	171	15	1	x	x	1.12	1.65	7.45	2.27	0.77	29.29	0.12	0.99
JSN	171	15	1	8.55	3.65	0.68	0.28	2.84	0.60	0.22	36.17	0.04	0.76
JSN	337	15	1	8.86	2.30	0.68	0.69	3.76	0.27	0.29	36.13	0.05	1.29
JSN	347	15	1	9.11	2.11	0.96	0.01	2.18	1.45	0.12	37.25	0.03	1.60
JSN	357	15	1	8.46	0.88	0.72	0.64	3.25	1.83	0.18	31.82	0.04	3.55

Column	Sample Position	Microfacies #	Bioturbation Index (1-5)	Inorg. Carb wt%	TOC wt%	Mg wt%	Al wt%	Si wt%	S wt%	K wt%	Ca wt%	Ti wt %	Fe wt%
JSS	336	15	1	7.48	5.08	0.90	0.19	2.29	1.62	0.13	35.23	0.02	1.48
JSS	336	15	1	10.12	x	1.05	0.01	1.83	2.21	0.06	36.27	0.02	0.59
JSS	351	15	1	10.67	x	1.01	0.21	2.48	1.39	0.16	37.55	0.03	1.49
JSS	351	15	1	9.90	x	0.71	1.66	5.89	0.69	0.77	31.55	0.09	0.74

ii. Trace Element Abundances

Column	Real Sample Position	MF #	V (ppm)	Cr (ppm)	Mn (ppm)	Co (ppm)	Ni (ppm)	As (ppm)	Pb (ppm)	Th (ppm)	Rb (ppm)	U (ppm)	Sr (ppm)	Y (ppm)	Zr (ppm)	N (ppm)	Mo (ppm)
JSN	30	1	53.82	7.60	205.97	2.73	31.08	1.27	5.94	2.77	8.18	0.10	369.81	28.67	21.71	4.58	0.10
JSN	52	1	55.81	13.51	204.80	1.86	25.05	1.41	6.53	2.73	14.77	8.40	443.66	23.08	16.99	4.59	0.10
JSS	25	1	53.24	19.00	212.17	2.75	26.70	1.23	11.54	2.93	18.67	6.17	390.49	26.91	22.61	4.68	0.10
JSS	47	1	58.12	12.07	207.55	1.80	26.70	1.53	7.85	2.87	15.61	1.38	375.54	23.81	18.79	4.18	0.10
JSS	66	1	42.64	6.38	206.33	2.42	31.11	1.33	11.00	3.08	17.38	9.40	372.25	24.31	28.86	5.23	0.24
JSN	43	2	45.68	6.71	205.95	2.33	38.98	1.65	7.30	2.96	15.09	5.13	406.80	25.49	20.35	4.99	0.10
JSN	48.5	2	54.24	2.78	203.73	2.05	30.08	1.26	6.28	2.70	13.39	9.87	538.64	23.34	19.53	4.80	0.10
JSN	61	2	64.34	8.62	204.56	2.14	32.19	1.80	10.51	2.98	16.06	13.01	553.92	25.99	15.29	5.78	0.10
JSS	33	2	43.28	2.86	203.71	2.40	30.99	1.82	10.61	2.65	14.29	3.63	387.50	26.90	19.82	4.49	0.10
JSS	59	2	57.89	5.73	202.86	1.51	24.60	1.22	5.47	2.58	10.64	6.84	434.70	26.29	14.57	4.85	0.10
JSS	78	2	54.58	16.58	205.54	2.75	49.32	0.99	6.54	3.34	20.76	14.07	491.83	29.37	24.91	6.63	0.10
JMS	49	3	63.42	13.34	213.55	2.43	21.22	0.81	4.84	3.03	11.22	4.79	299.02	18.19	20.30	4.34	0.10
JMS	53.5	3	52.21	0.46	217.37	2.41	22.92	0.83	8.22	2.84	12.18	5.32	263.14	21.68	15.86	4.38	1.72
JMS	19	4	47.82	5.83	205.83	1.94	15.00	1.35	7.79	2.76	9.42	3.75	307.66	22.87	15.55	4.53	0.10
JMS	40	4	58.32	15.11	211.04	1.59	22.53	1.31	7.77	2.29	7.06	0.10	288.37	18.20	10.68	2.74	0.10
JSS	14	5	41.77	53.45	204.66	7.12	109.12	1.50	11.17	7.44	79.53	8.55	241.58	20.13	110.57	8.02	8.45
JSS	160	5	136.61	37.53	180.53	9.79	228.74	6.45	16.10	5.85	64.84	15.87	343.31	35.24	102.31	8.61	82.65
JSN	139	6	542.95	87.29	168.24	13.44	423.53	5.84	18.78	7.04	91.98	17.10	285.30	31.01	107.44	8.47	120.16
JSS	117	6	925.09	70.18	101.05	26.83	478.63	65.25	29.85	6.95	101.62	38.95	219.18	14.46	125.79	6.80	257.93
JSS	119	6	427.33	70.11	145.16	15.10	340.56	37.24	24.22	6.63	82.86	26.65	280.67	23.99	96.74	7.74	110.10

Column	Real Sample Position	MF #	V (ppm)	Cr (ppm)	Mn (ppm)	Co (ppm)	Ni (ppm)	As (ppm)	Pb (ppm)	Th (ppm)	Rb (ppm)	U (ppm)	Sr (ppm)	Y (ppm)	Zr (ppm)	N (ppm)	Mo (ppm)
JMS	67	7	698.69	53.11	59.95	24.70	414.60	108.39	37.20	7.18	94.50	43.83	164.59	10.49	99.67	7.08	291.13
JMS	109	7	525.21	37.73	142.48	17.48	336.78	56.10	28.98	6.74	92.54	27.06	216.68	14.46	106.29	5.79	204.26
JMS	319	7	39.17	47.73	199.57	7.79	116.15	1.72	9.35	7.68	90.34	14.71	325.48	24.32	78.24	8.93	19.32
JMS	130	7	520.14	76.32	129.86	19.51	385.87	48.98	29.94	6.69	86.93	18.07	170.14	17.82	112.76	5.71	181.93
JSN	91.5	7	797.89	56.16	153.47	17.35	406.07	33.58	21.87	6.70	90.13	32.07	219.70	17.23	135.24	7.10	330.26
JSN	183	7	173.76	50.69	184.48	27.35	525.10	46.16	29.92	7.32	92.43	8.61	122.94	19.78	118.36	5.86	227.72
JSN	309	7	251.15	93.72	92.56	12.04	208.31	6.39	18.63	6.29	79.65	11.29	296.87	29.62	77.27	7.18	54.79
JSS	130	7	634.79	61.86	132.69	16.49	379.45	60.27	29.02	7.11	98.75	24.81	167.98	18.69	104.06	6.37	201.97
JSS	171	7	595.32	65.53	125.15	21.15	420.45	36.65	24.91	6.90	88.97	20.41	182.25	18.44	146.97	6.44	203.95
JSS	211	7	264.74	69.55	170.83	15.12	298.58	12.25	19.34	7.14	87.27	11.37	191.60	23.05	128.33	7.17	106.16
JSS	219	7	333.87	61.46	142.88	16.69	342.17	23.78	26.82	6.78	89.71	14.66	202.31	24.23	112.01	6.56	128.02
JSS	326	7	63.32	48.22	160.97	1.66	30.74	1.07	10.01	2.90	14.48	0.14	382.39	28.58	21.37	4.74	0.10
JMS	135	8	488.01	63.89	161.96	8.23	200.50	9.42	17.06	6.13	77.01	26.51	337.20	28.19	95.53	8.30	63.80
JMS	305	8	22.05	27.46	209.20	9.14	92.94	3.25	11.48	6.20	67.72	0.10	331.90	27.54	64.05	6.58	6.19
JSN	296	8	195.07	59.42	173.02	10.38	183.03	26.44	16.59	6.19	74.55	11.55	296.78	31.01	91.43	7.44	71.08
JSS	205	8	109.58	56.41	186.07	11.32	145.15	6.34	17.53	6.12	69.65	9.93	313.63	29.61	91.58	7.44	31.55
JSS	288	8	65.62	41.97	193.17	9.34	132.44	30.39	26.11	5.04	60.10	9.70	322.32	31.96	64.02	5.86	39.12
JMS	272	8	31.09	22.34	172.32	9.17	120.46	5.21	18.59	5.92	61.97	5.50	328.10	27.94	60.14	7.01	29.45
JSN	219	9	199.44	39.96	174.44	8.71	211.65	4.71	17.91	5.08	54.52	14.92	347.94	30.42	75.62	7.31	79.62
JSS	235	9	288.39	85.79	101.19	18.77	521.65	77.87	36.29	6.13	84.44	8.22	199.22	24.41	101.14	4.42	74.14
JSS	245	9	202.88	40.40	162.91	10.50	203.72	8.32	19.02	4.51	53.54	13.20	267.45	29.87	60.52	5.89	73.58
JMS	15	10	289.94	27.31	177.89	5.28	182.73	9.48	17.38	4.87	49.00	33.24	415.35	20.61	62.48	7.66	101.94
JMS	76	10	146.08	13.32	178.81	5.60	87.27	12.25	12.46	3.19	26.02	26.93	740.39	28.98	27.37	6.99	25.32
JMS	80	10	378.63	33.17	167.36	5.60	87.27	12.25	12.46	3.19	26.02	26.93	740.39	28.98	27.37	6.99	25.32
JMS	80	10	236.69	14.37	179.64	7.69	188.37	5.86	14.78	4.57	41.58	24.14	450.56	24.56	59.35	7.35	93.29
JMS	88	10	243.94	24.37	184.26	5.22	100.79	4.36	16.03	2.99	28.40	28.63	438.20	29.06	31.12	6.52	50.34
JMS	112	10	450.40	48.51	151.34	12.47	331.89	24.67	24.21	6.17	80.72	30.62	266.78	16.82	95.83	6.69	210.43
JMS	112	10	142.81	5.72	187.39	4.62	132.24	2.11	13.08	3.62	35.44	28.85	591.55	32.78	36.01	7.82	47.51
JMS	243	10	43.37	17.15	205.22	1.73	56.26	1.17	8.86	2.96	24.32	4.79	284.55	33.31	25.28	5.28	51.77
JSN	72	10	77.08	-3.95	196.62	3.36	53.32	11.98	10.74	3.07	7.38	19.38	569.76	34.63	16.71	8.20	3.40
JSN	72	10	249.71	25.98	161.66	10.56	278.55	10.08	18.37	4.69	58.71	41.75	357.69	16.07	58.52	6.83	212.38
JSN	87	10	177.31	12.23	194.90	6.79	112.87	149.26	10.14	3.28	28.94	31.12	435.78	31.55	30.26	7.69	46.41
JSS	85	10	116.52	55.47	165.41	17.68	304.13	5.94	16.69	2.79	28.41	37.52	657.45	166.06	15.60	24.87	51.57
JSS	108	10	145.34	20.86	193.76	7.22	103.55	141.64	13.99	3.26	21.33	21.60	468.45	36.28	25.78	7.80	38.55

Column	Real Sample Position	MF #	V (ppm)	Cr (ppm)	Mn (ppm)	Co (ppm)	Ni (ppm)	As (ppm)	Pb (ppm)	Th (ppm)	Rb (ppm)	U (ppm)	Sr (ppm)	Y (ppm)	Zr (ppm)	N (ppm)	Mo (ppm)
JMS	97	11	65.32	-13.84	186.81	7.04	65.73	4.07	13.93	2.77	8.99	4.72	503.87	34.43	13.11	5.85	5.32
JSS	99	11	83.03	0.53	203.53	2.42	44.37	12.88	7.08	2.46	12.37	16.13	394.81	32.17	15.95	6.20	3.95
JMS	125	12	109.01	22.74	197.58	3.29	61.98	1.71	12.18	2.70	13.53	14.22	330.37	31.95	19.82	6.16	24.37
JMS	122	12	211.04	35.91	163.65	10.94	239.12	22.88	22.68	5.34	64.40	25.34	287.83	18.05	75.74	5.96	117.24
JMS	130	12	146.55	37.59	187.04	4.48	101.02	2.20	13.28	3.96	33.42	13.09	414.45	30.70	51.94	6.70	15.24
JMS	192	12	128.46	36.18	189.95	6.91	139.19	11.76	16.82	4.09	42.63	16.50	324.48	30.31	45.45	6.18	45.98
JMS	268	12	67.94	51.02	189.85	7.69	117.11	6.60	19.24	5.18	60.32	8.59	345.94	31.00	53.80	6.50	43.49
JSN	128	12	68.75	20.21	196.68	3.46	52.57	0.70	8.11	3.06	22.39	10.92	332.88	30.21	27.86	5.66	2.16
JSN	199	12	59.93	18.18	200.62	3.40	51.43	1.00	11.83	3.12	23.69	8.45	387.23	28.99	35.73	5.30	0.10
JSN	212	12	74.58	27.68	193.91	4.57	91.92	2.57	13.46	4.13	36.64	5.03	389.63	33.07	50.37	6.24	18.22
JSN	337	12	38.95	26.73	208.12	2.46	41.57	1.69	7.63	3.98	26.18	0.10	387.67	35.84	38.53	6.85	0.10
JSN	357	12	29.97	37.76	195.70	4.72	65.97	2.63	14.84	4.61	49.92	3.07	308.67	31.10	48.73	5.79	9.39
JSS	139	12	97.62	17.19	203.86	3.34	76.66	1.11	12.56	3.05	16.73	8.12	366.09	34.54	28.89	6.33	13.90
JSS	149	12	97.68	18.14	194.91	3.54	100.33	3.16	17.87	3.76	26.87	6.25	385.64	33.30	37.53	6.39	8.62
JSS	190	12	61.40	20.00	197.02	3.23	57.84	1.06	10.49	3.58	22.53	1.10	376.23	30.54	35.73	5.72	0.10
JSS	199	12	49.54	17.60	207.07	2.98	44.42	1.86	8.51	3.39	20.57	6.65	387.46	32.90	41.11	6.49	0.10
JSS	223	12	65.70	27.80	202.16	4.73	87.33	5.87	16.23	3.71	25.93	3.26	365.00	29.26	47.43	5.40	7.03
JSS	268	12	52.11	63.73	170.92	12.91	233.26	10.09	19.87	6.55	79.76	0.85	265.54	24.95	89.38	5.90	31.28
JSS	272	12	49.02	23.35	198.07	3.72	84.88	1.22	9.52	4.91	40.83	2.41	376.11	29.28	58.12	6.75	4.79
JSS	361	12	57.65	46.99	204.40	6.50	93.99	4.00	16.76	5.63	58.72	5.44	368.25	29.57	60.53	6.97	11.82
JSN	200	13	60.85	20.82	199.34	2.75	45.65	1.34	10.74	3.18	21.44	5.95	384.24	32.55	30.11	5.85	0.10
JSN	207	13	60.74	6.59	190.64	2.29	37.34	1.71	8.43	2.86	4.40	0.10	262.90	29.83	18.95	5.45	0.10
JSN	266	13	55.52	8.37	191.53	3.77	29.26	0.82	7.55	2.52	13.12	3.57	224.34	32.95	20.21	5.03	0.10
JSS	213	13	55.83	8.00	191.83	2.87	31.32	1.01	11.27	2.76	5.15	0.10	274.85	26.20	18.30	4.51	0.10
JSS	256	13	64.38	12.10	168.18	2.47	31.87	1.47	9.81	2.53	10.85	0.10	216.63	27.76	15.44	4.17	2.30
JMS	203	14	66.30	23.23	189.49	5.17	61.93	1.72	13.10	3.25	26.06	5.96	324.94	27.90	22.67	4.84	8.25
JSN	164	14	46.66	1.18	199.39	1.71	32.10	1.66	6.45	2.54	8.92	1.86	265.86	28.69	16.27	4.74	0.10
JSN	234	14	56.47	4.45	198.80	2.20	31.70	1.08	8.78	2.59	6.57	0.10	262.76	28.44	17.15	4.57	0.10
JSN	241	14	55.61	21.56	197.61	2.65	50.43	1.11	10.96	3.59	26.94	6.82	376.88	27.97	33.25	5.62	4.84
JSS	233	14	60.57	6.02	189.67	3.09	45.02	0.92	9.30	2.55	10.92	5.32	254.92	30.58	18.24	5.09	0.10
JSS	295	14	58.14	0.76	193.95	1.97	38.62	1.48	12.80	2.59	9.23	3.47	250.75	31.35	17.12	5.18	0.10
JSS	370	14	58.28	3.23	194.91	2.65	29.80	0.96	10.24	2.66	7.64	0.10	246.13	27.69	16.21	4.42	0.10
JMS	215	15	57.08	13.38	195.41	3.11	56.52	1.30	13.50	3.41	31.83	5.34	324.57	26.22	33.19	4.55	8.89
JMS	215	15	39.51	-0.04	184.26	3.56	31.63	1.11	10.77	2.90	7.84	2.06	211.53	26.49	19.75	5.08	0.10

Column	Real Sample Position	MF #	V (ppm)	Cr (ppm)	Mn (ppm)	Co (ppm)	Ni (ppm)	As (ppm)	Pb (ppm)	Th (ppm)	Rb (ppm)	U (ppm)	Sr (ppm)	Y (ppm)	Zr (ppm)	N (ppm)	Mo (ppm)
JMS	222	15	42.88	0.41	189.84	1.96	22.54	1.24	9.45	2.66	10.67	2.30	228.07	22.35	22.18	3.96	1.86
JMS	302	15	47.99	24.61	230.25	2.42	45.15	1.62	13.66	4.84	39.29	2.79	386.77	33.23	46.39	7.45	1.37
JMS	302	15	68.57	-0.19	201.29	4.07	14.99	2.02	9.40	2.47	11.48	1.81	255.20	22.43	15.61	3.59	0.10
JMS	302	15	42.35	8.47	198.12	3.13	24.02	1.17	6.73	2.40	14.38	10.18	207.14	22.61	20.92	4.07	0.10
JSN	171	15	51.16	32.21	181.62	3.77	52.24	1.23	10.84	3.86	29.29	2.94	371.05	32.29	48.52	6.06	0.32
JSN	171	15	47.44	6.90	195.35	3.27	20.94	1.72	11.68	2.54	7.67	5.48	270.62	26.24	21.27	4.83	0.10
JSN	337	15	48.73	14.90	198.27	2.89	22.38	1.77	10.38	3.06	8.58	0.10	267.68	31.00	17.91	4.69	0.10
JSN	347	15	59.71	9.15	178.07	4.52	26.09	1.91	13.61	2.42	11.88	0.10	207.68	22.50	14.30	2.84	0.10
JSN	357	15	43.35	9.72	152.25	14.53	13.66	3.00	11.37	1.94	10.34	0.10	216.34	22.45	10.11	2.25	0.10
JSS	336	15	52.79	5.55	177.93	4.90	34.74	1.74	8.03	2.43	8.93	4.88	254.74	26.74	14.30	4.53	0.10
JSS	336	15	50.23	7.90	166.11	2.33	20.98	2.20	9.51	2.38	3.34	0.10	407.99	24.79	9.95	3.83	0.10
JSS	351	15	68.07	6.08	180.51	5.32	19.64	1.58	12.43	2.70	7.76	2.57	238.72	23.13	17.54	4.37	0.10
JSS	351	15	52.39	21.75	205.12	3.10	42.88	1.24	11.98	4.52	27.24	0.10	383.80	34.04	46.37	6.84	2.00

References

Ager, D. V. (1981). Major marine cycles in the Mesozoic. *Journal of the Geological Society*, *138*(2), 159-166.

Aitchison, J. (1986). The statistical analysis of compositional data.

Algeo, T. J., & Maynard, J. B. (2004). Trace-element behavior and redox facies in core shales of Upper Pennsylvanian Kansas-type cyclothems. *Chemical geology*, *206*(3), 289-318.

Algeo, T. J., & Lyons, T. W. (2006). Mo–total organic carbon covariation in modern anoxic marine environments: Implications for analysis of paleoredox and paleohydrographic conditions. *Paleoceanography*, *21*(1).

Algeo, T. J., & Tribovillard, N. (2009). Environmental analysis of paleoceanographic systems based on molybdenum–uranium covariation. *Chemical Geology*, *268*(3), 211-225.

Aller, R. C. (1982). The effects of macrobenthos on chemical properties of marine sediment and overlying water. In *Animal-sediment relations* (pp. 53-102). Springer US.

Anders, M.H., Krueger, S.W., and Sadler, P.M., 1987, A new look at sedimentation rates and the completeness of the stratigraphic record: Journal of Geology, v. 95, p. 1-14.

Arthur, M. A., Dean, W. E., Pollastro, R., Scholle, P. A., & Claypool, G. E. (1985). A comparative geochemical study of two transgressive pelagic limestone units, Cretaceous Western Interior basin, US. *Fine-Grained Deposits and Biofacies of the Cretaceous Western Interior Seaway: Evidence of Cyclic Sedimentary Processes: SEPM, Field Trip Guidebook*, (4), 16-27.

Bartholomew, A. J., & Schramm, T. J. (2013). The nature and timing of the Middle Devonian Kačák bioevents in the Marcellus Subgroup of the Appalachian Basin. *Palaios*, *28*(11), 825-836.

Bohacs, K. M., Grabowski, G. J., Carroll, A. R., Mankiewicz, P. J., Miskell-Gerhardt, K.

J., Schwalbach, J. R., Wegner, M. B., and Simo, J. A. 2005, Production, destruction, and dilution – the many paths to source-rock development: *SEPM Special Publication 82*, p. 61-101.

Boyer, D. L., & Droser, M. L. (2009). Palaeoecological patterns within the dysaerobic biofacies: Examples from Devonian black shales of New York state. *Palaeogeography, Palaeoclimatology, Palaeoecology*, *276*(1), 206-216.

Boyer, D. L., Owens, J. D., Lyons, T. W., & Droser, M. L. (2011). Joining forces: Combined biological and geochemical proxies reveal a complex but refined high-resolution palaeo-oxygen history in Devonian epeiric seas. *Palaeogeography, Palaeoclimatology, Palaeoecology*, *306*(3), 134-146.

Breit, G. N., & Wanty, R. B. (1991). Vanadium accumulation in carbonaceous rocks: a review of geochemical controls during deposition and diagenesis. Chemical Geology, 91(2), 83-97.

Brett, C. E., & Baird, G. C. (1996). Middle Devonian sedimentary cycles and sequences in the northern Appalachian Basin. *SPECIAL PAPERS-GEOLOGICAL SOCIETY OF AMERICA*, 213-242.

Brett, C. E., Ivany, L. C., Bartholomew, A. J., DeSantis, M. K., & Baird, G. C. (2009). Devonian ecological-evolutionary subunits in the Appalachian Basin: a revision and a test of persistence and discreteness. *Geological Society, London, Special Publications*, *314*(1), 7-36.

Brett, C. E., Baird, G. C., Bartholomew, A. J., DeSantis, M. K., & Ver Straeten, C. A. (2011). Sequence stratigraphy and a revised sea-level curve for the Middle Devonian of eastern North America. *Palaeogeography, Palaeoclimatology, Palaeoecology*, *304*(1), 21-53.

Bruner, K. R., Walker-Milani, M., & Smosna, R. (2015). Lithofacies of the Devonian Marcellus Shale in the Eastern Appalachian Basin, USA. *Journal of Sedimentary Research*, *85*(8), 937-954.

Calvert, S. E., & Pedersen, T. F. (2007). Elemental proxies for palaeoclimatic and palaeoceanographic variability in marine sediments: interpretation and application. *in* Hillaire-Marcel, C., & De Vernal, A., *Proxies in Late Cenozoic Paleoceanography — Developments in Marine Geology*, *1*, 567-644.

Comas-Cufí, M., Thió-Henestrosa, S., (2011). CoDaPack 2.0: a stand-alone, multi-platform compositional software. In: Egozcue JJ, Tolosana-Delgado R, Ortego MI, eds. *CoDaWork'11: 4th International Workshop on Compositional Data Analysis*. Sant Feliu de Guíxols; 2011.

Condie, K. C. (1993). Chemical composition and evolution of the upper continental crust: contrasting results from surface samples and shales. *Chemical geology*, *104*(1), 1-37.

Cross, T. A., Baker, M. R., Chapin, M. A., Clark, M. S., Gardner, M. H., Hanson, M. S., Lessenger, M.A., Little, L.D., McDonough, K.J., Sonnenfeld, M.D., & Valasek, D. W. (1993). Applications of high-resolution sequence stratigraphy to reservoir analysis. *Collection Colloques et Seminaires-Institut Francais Du Petrole*, 51, 11-11.

Dean, W. E., & Arthur, M. A., (1998). Geochemical expressions of cyclicity in Cretaceous pelagic limestone sequences: Niobrara Formation, Western Interior Seaway.

DeSantis, M. K., & Brett, C. E. (2011). Late Eifelian (Middle Devonian) biocrises: timing and signature of the pre-Kačák Bakoven and Stony Hollow events in eastern North America. *Palaeogeography, Palaeoclimatology, Palaeoecology*, *304*(1), 113-135.

Droser, M. L., & Bottjer, D. J. (1986). A semiquantitative field classification of ichnofabric: Research method paper. *Journal of Sedimentary Research*, *56*(4).

Droser, M. L., & Bottjer, D. J. (1993). Trends and patterns of Phanerozoic ichnofabrics. *Annual Review of Earth and Planetary Sciences*, *21*, 205-225.

Ettensohn, F. R. (1985). The Catskill delta complex and the Acadian orogeny: A model. *Geological Society of America Special Papers*, *201*, 39-50.

Ettensohn, F. R. (2008). The Appalachian foreland basin in eastern United States. *Sedimentary basins of the world*, *5*, 105-179.

Fabricius, I. L., Fazladic, L. D., Steinholm, A., & Korsbech, U. (2003). The use of spectral natural gamma-ray analysis in reservoir evaluation of siliciclastic sediments: a case study from the Middle Jurassic of the Harald Field, Danish Central Graben. *Geological Survey of Denmark and Greenland Bulletin*, *1*, 349-366.

Hammer, Ø., Harper, D.A.T., Ryan, P.D. (2001). PAST: Paleontological statistics software package for education and data analysis. Palaeontologia Electronica 4(1): 9pp. http://palaeo-electronica.org/2001_1/past/issue1_01.htm

Haq, B. U., Hardenbol, J., & Vail, P. R. (1987). Chronology of fluctuating sea levels since the Triassic. Science, 235(4793), 1156-1167.

Huc, A. Y. (1980). Origin and formation of organic matter in recent sediments and its relation to kerogen. Kerogen: insoluble organic matter from sedimentary rocks. Paris: Editions Technip, 445-74.

Karaca, C. (2012). Characterization of the Union Springs Formation, Finger Lakes Region, NY: An Integrated High Resolution Facies, Geochemical And Sequence Stratigraphical Approach. Cornell University. Thesis.

Kesler, S. E. (1996). Appalachian Mississippi Valley-type deposits: Paleoaquifers and brine provinces. Society of Economic Geologists Special Publication, 4, 29-57.

Klinkhammer, G. P., & Palmer, M. R. (1991). Uranium in the oceans: where it goes and why. *Geochimica et Cosmochimica Acta*, *55*(7), 1799-1806.

Kohl, D., Slingerland, R., Arthur, M., Bracht, R., & Engelder, T. (2014). Sequence stratigraphy and depositional environments of the Shamokin (Union Springs) Member, Marcellus Formation, and associated strata in the middle Appalachian Basin. *AAPG bulletin*, *98*(3), 483-513.

Lash, G. G., & Blood, D. R. (2014). Organic matter accumulation, redox, and diagenetic history of the Marcellus Formation, southwestern Pennsylvania, Appalachian basin. *Marine and Petroleum Geology*, *57*, 244-263.

Leeder, M. R. (1982). *Sedimentology: Process and Product*. London, UK: George Allen and Unwin.

McHargue, T. R., & Price, R. C. (1982). Dolomite from clay in argillaceous or shale-associated marine carbonates. *Journal of Sedimentary Research*, *52*(3).

Murphy, A. E., Sageman, B. B., Hollander, D. J., Lyons, T. W., & Brett, C. E. (2000). Black shale deposition and faunal overturn in the Devonian Appalachian basin: Clastic starvation, seasonal water-column mixing, and efficient biolimiting nutrient recycling. *Paleoceanography*, *15*(3), 280-291.

Over, D.J., Rabideau, S., Travis, M., Grady, B., & Ver Straeten, C.E., *in* Ver Straeten, C.E., BAIRD, G., BRETT, C., LASH, G., OVER, J., KARACA, C., JORDAN, T. and BLOOD, R. (2011). The Marcellus subgroup in its type area, Finger Lakes area of New York, and beyond. *Guidebook—New York State Geological Association, 83(2011),* pp. 67-69.

Posamentier, H.W., Jervey, M.T., Vail, P.R. (1988), Eustatic Controls On Clastic Deposition. I. Conceptual Framework. In: Wilgus, C.K., Hastings, B.S., Kendall, C.G.St.C., Posamentier, H.W., Ross, C.A., Van Wagoner, J.C. (Eds.), Sea Level Changes—An Integrated Approach, vol. 42. SEPM Special Publication, pp. 110– 124.

Raiswell, R., & Fisher, Q. J. (2000). Mudrock-hosted carbonate concretions: a review of growth mechanisms and their influence on chemical and isotopic composition. *Journal of the Geological Society*, *157*(1), 239-251.

Ring, E., (1989). The preparation and certification of fourteen South African silicate rocks for use as reference materials. Mintek Report M393.

Rowe, H., Hughes, N., & Robinson, K. (2012). The quantification and application of handheld energy-dispersive x-ray fluorescence (ED-XRF) in mudrock chemostratigraphy and geochemistry. Chemical Geology, 324, 122-131.

Sageman, B. B., Murphy, A. E., Werne, J. P., Ver Straeten, C. A., Hollander, D. J., & Lyons, T. W. (2003). A tale of shales: the relative roles of production, decomposition, and dilution in the accumulation of organic-rich strata, Middle–Upper Devonian, Appalachian basin. *Chemical Geology*, *195*(1), 229-273.

Sageman, B. B., Lyons, T.W., (2004). Geochemistry of fine-grained sediments and sedimentary rocks *in* MacKenzie, F., ed., *Treatise on Geochemistry*, 7: Elsevier Publishing, pp. 115–158.

Savrda, C. E., & Bottjer, D. J. (1986). Trace-fossil model for reconstruction of paleo-oxygenation in bottom waters. *Geology*, *14*(1), 3-6.

Savrda, C. E., & Bottjer, D. J. (1991). Oxygen-related biofacies in marine strata: an overview and update. *Geological Society, London, Special Publications*, *58*(1), 201-219.

Schieber, J. (2009). Discovery of agglutinated benthic foraminifera in Devonian black shales and their relevance for the redox state of ancient seas. Palaeogeography, Palaeoclimatology, Palaeoecology, 271(3), 292-300.

Schieber, J., Krinsley, D., & Riciputi, L. (2000). Diagenetic origin of quartz silt in mudstones and implications for silica cycling. *Nature*, *406*(6799), 981-985.

Scotese, C. R., & McKerrow, W. S. (1990). Revised world maps and introduction. Geological Society, London, Memoirs, 12(1), 1-21.

Selleck, B. (2014). GEOCHEMISTRY AND SULFIDE MINERAL PARAGENESIS IN MARCELLUS SUBGROUP AND UTICA FORMATION GAS SHALE INTERVALS. In Geological Society of America Abstracts with Programs (Vol. 46, No. 2, p. 98). Presentation.

Tribovillard, N., Ramdani, A., & Trentesaux, A., (2005). Controls on organic accumulation in Upper Jurassic shales of northwestern Europe as inferred from trace-metal geochemistry.

Tribovillard, N., Algeo, T. J., Lyons, T., & Riboulleau, A. (2006). Trace metals as paleoredox and paleoproductivity proxies: an update. *Chemical geology*,*232*(1), 12-32.

Van Wagoner, J. C., Posamentier, H., Mitchum, R., Vail, P., Sarg, J., Loutit, T., & Hardenbol, J. (1988). An overview of the fundamentals of sequence stratigraphy and key definitions.

Van Wagoner, J. C., Mitchum, R. M., Campion, K. M., & Rahmanian, V. D. (1990). Siliciclastic sequence stratigraphy in well logs, cores, and outcrops: concepts for high-resolution correlation of time and facies.

Ver Straeten, C. A. (2004). K-bentonites, volcanic ash preservation, and implications for Early to Middle Devonian volcanism in the Acadian orogen, eastern North America. *Geological Society of America Bulletin*, *116*(3-4), 474-489.

Ver Straeten, C. A. (2007). Basinwide stratigraphic synthesis and sequence stratigraphy, upper Pragian, Emsian and Eifelian stages (Lower to Middle Devonian), Appalachian Basin. *Geological Society, London, Special Publications*, *278*(1), 39-81.

Ver Straeten, C. A. (2010). Lessons from the foreland basin: Northern Appalachian basin perspectives on the Acadian orogeny. *Geological Society of America Memoirs*, *206*, 251-282.

Ver Straeten, C. A., Griffing, D. H., & Brett, C. E. (1994). The lower part of the Middle Devonian Marcellus “Shale,” central to western New York State; stratigraphy and depositional history. *Guidebook—New York State Geological Association*, *66*(1994), 271-323.

Ver Straeten, C. A., & Brett, C. E. (2006). Pragian to Eifelian strata (middle Lower to lower Middle Devonian), northern Appalachian Basin-stratigraphic nomenclatural changes. *Northeastern Geology and Environmental Sciences*,*28*(1), 80.

Ver Straeten, C. A., Brett, C. E., & Sageman, B. B. (2011). Mudrock sequence stratigraphy: a multi-proxy (sedimentological, paleobiological and geochemical) approach, Devonian Appalachian Basin. *Palaeogeography, Palaeoclimatology, Palaeoecology*, *304*(1), 54-73.

Ver Straeten, C.E., BAIRD, G., BRETT, C., LASH, G., OVER, J., KARACA, C., JORDAN, T. and BLOOD, R. (2011b). The Marcellus subgroup in its type area, Finger Lakes area of New York, and beyond. *Guidebook—New York State Geological Association, 83(2011), 1-64*.

Wedepohl, K. H. (1995). The composition of the continental crust. *Geochimica et Cosmochimica Acta*, 59(7), 1217-1232.

Wendt, A. K., Arthur, M. A., Slingerland, R., Kohl, D., Bracht, R., & Engelder, T. (2015). Geochemistry and depositional history of the Union Springs Member, Marcellus Formation in central Pennsylvania. *Interpretation*, *3*(3), SV17-SV33.

Werne, J. P., Sageman, B. B., Lyons, T. W., & Hollander, D. J. (2002). An integrated assessment of a “type euxinic” deposit: evidence for multiple controls on black shale deposition in the Middle Devonian Oatka Creek Formation. *American Journal of Science*, *302*(2), 110-143.

Wignall, P. B., & Myers, K. J. (1988). Interpreting benthic oxygen levels in mudrocks: a new approach. *Geology*, *16*(5), 452-455.

Young, G. M., & Nesbitt, H. W. (1998). Processes controlling the distribution of Ti and Al in weathering profiles, siliciclastic sediments and sedimentary rocks.*Journal of Sedimentary Research*, *68*(3).

Zapata, A. (2014). Geological Characterization of the Union Springs Formation, Lower Marcellus Shale in the Appalachian Basin, Central New York. Brooklyn College. Thesis.

Zheng, Y., Anderson, R. F., van Geen, A., & Fleisher, M. Q. (2002). Preservation of particulate non-lithogenic uranium in marine sediments.*Geochimica et Cosmochimica Acta*, *66*(17), 3085-3092.

CHAPTER THREE

Micro-mechanical Characterization of the Marcellus Shale: Testing mechanical properties across lithofacies and the efficacy of experimental indentation methods in mudstone characterization

Introduction

Mudstone formations can be highly heterogeneous in both an interformational and an intraformational sense across a wide range of length scales (Chapter 2; Chapter 3; Ulm et al., 2006). Also, changes in primary rock properties can affect the hydrocarbon production potential of shale reservoirs over relatively short length scales (Passey et al. 2010). While it is certainly not the only control, spatial heterogeneity of primary rock properties is an important factor in evaluating the resource potential of a mudstone formation in a given location (King 2010). Here, the effect of geologic variability on grain-scale mechanical properties is examined, and best practices are established for nanoindentation on mudstones of variable total organic carbon content.

Although intentionally induced hydraulic fractures may extend for hundreds of meters within a shale formation (Maxwell, 2012), bedding commonly occurs on the millimeter-scale, naturally-occurring fractures may have apertures on the order of 50 µm (Gale et al., 2007), and the target hydrocarbon is often sequestered in pore spaces which are less than a micrometer along their longest axis (Loucks et al., 2009). According to the definition of MacQuaker & Adams (2003), mudstones have greater than 50% of their volume comprised of particles 63 µm or less

in diameter. Thus, while resource extraction procedures create percolated crack networks on the scale of tens to hundreds of meters in length, the processes that determine local crack behavior are determined by the behavior of the rock at the micrometer scale. Whether resource-containing pores are bypassed or included in the network also depends on micrometer scale properties.

The organic-rich mudstones which host these hydrocarbons are composite materials: they are comprised of any number of mechanically continuous and discontinuous mineral and organic phases, including hydrated minerals, as well as organic matter in a liquid, solid, or gas state (Berthelot, 1999). A wide range of constituents with disparate mechanical properties are combined into one material with its own mechanical characteristics. This study probes these system-scale characteristics, in addition to the characteristics of the individual components, utilizing indentation techniques.

Nanoindentation is a depth-sensing method which extracts mechanical parameters through continuous measurements of load and tip displacement. This technique is one of few used to characterize grain scale properties in mudstones, which present a challenge in terms of constituent characterization as a result of their typical grain size. Nanoindentation utilizes extremely small displacements and can probe micron-scale features with precision. Given the small average grain size, nanoindentation is a natural method for high-resolution characterization of material properties of mudstones at the individual constituent scale. Nanoindentation is capable of characterizing single material constituents utilizing precisely

located indentations within single material constituents which are larger than the indentations (Oliver & Pharr, 2004). Methodology developed by Oliver & Pharr (2004) allows for the determination of hardness and indentation modulus of the region of material being examined through the analysis of the unloading segment of the continuously-generated load-displacement curve at each indentation site. Currently, nanoindentation can be used in the mudstone realm as a means of characterizing mechanical properties trends within compositionally diverse unconventional reservoirs and in the characterization of relationships between microstructure and mechanical heterogeneity (Kumar et al., 2012a; Kumar et al., 2015; Abedi et al., 2016). Testing hardness of mudstone samples at a scale larger than that of their individual constituents was accomplished via Vickers micro-hardness indentation testing. This technique returns hardness data and can provide a valuable point of comparison, allowing interested parties to view the mechanical properties of complex composites at the nanometer through centimeter scale.

In order to begin to understand how natural mudstone microstructure controls bulk mechanical behavior in such a complex multi-scale system, three geologically-characterized samples of Marcellus shale were investigated using indentation methods. The tested rocks were selected to represent a wide range of total organic carbon contents, from 0.6 – 11.9% (Karaca, 2012). This parameter was selected as the primary variable in this study because changes in total organic carbon content have been observed to significantly correlate with mudstone brittle deformation behavior relevant to resource recovery operations at reservoir depths (Jarvie et al., 2007; Sondergeld et al., 2010; Rickman et al., 2008). Other rock properties

(*e.g.* texture) or mineral phases (*e.g.* clay type) certainly have an effect on deformation and reservoir quality, but this study focuses on the role of varying total organic carbon.

Microindentation was used to obtain bulk composite mechanical properties (Vickers hardness), and to induce cracks (cube-corner indenter) on the 100 micrometer scale. Nanoindentation was used to determine the mechanical properties (hardness and elastic modulus) of the individual constituents of these rocks on the micrometer and sub-micrometer scale. The properties, and variability of those properties on the micrometer-scale, were then correlated with the average properties and the details of local crack propagation paths. Scanning electron microscopy was used to image the surfaces and to identify the individual constituents.

Instrumented indentation experiments have been carried out on mudrocks previously, and mechanical properties data have been gathered for these rocks at a variety of orientations, mineralogies, and organic matter abundances (Zeszotarski et al., 2004; Ulm et al., 2006; Ulm et al., 2007; Kumar et al, 2012a; Abedi et al., 2016; Bennett et al., 2015). Previous work has also investigated the spatial distribution of mineral phases on indented shale surfaces (Deirieh et al., 2012). This study builds upon this body of work by providing mineralogy data for large arrays of nanoindentation measurements at the individual constituent scale, for rocks that represent a wide range of total organic carbon content. Additionally, it is shown that nanoindentation and micro-fracture experiments have potential to provide detailed information about the spatial variation of the mechanical properties in these rocks at the scale of the fundamental

constituents, although such experiments can be significantly affected by experimental conditions.

Materials and Methods

Three samples collected from the Union Springs Formation (Marcellus Subgroup) were selected for analysis. These samples, taken from a roughly 4 meter thick section of the Union Springs Formation near the northern margin of the Appalachian Basin (see Figure 1), were characterized and assigned into a microfacies framework by Karaca (2012).

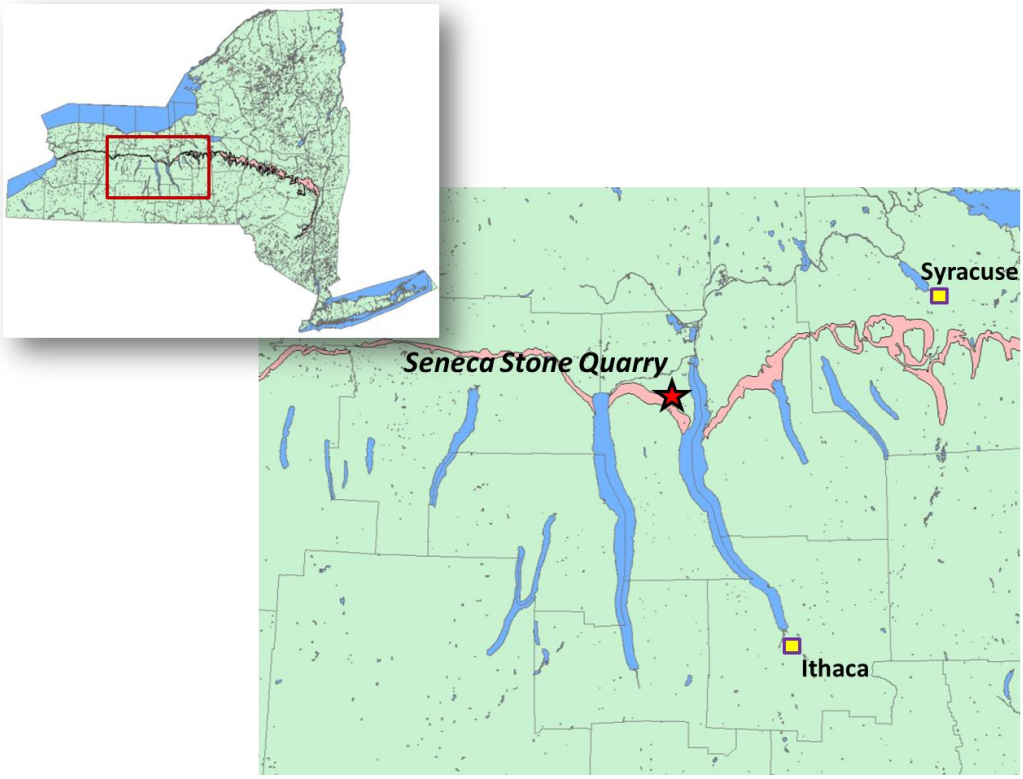

Figure 1: Map showing the sample collection area in Seneca Falls, NY, near the northern margin of the Appalachian Basin.

Similar to those described in previous chapters (Chapter 2), Karaca (2012) defined three broad lithofacies groups which are comprised of several higher-order microfacies. Lithofacies

and microfacies reflect primary sedimentary characteristics, such as mineralogy, texture, and organic matter abundance. Karaca's (2012) lithofacies groups share some common traits with those described in Chapter 1, and roughly align with the Limestone, Carbonaceous Mudstone, and Calcareous Concretion facies described therein.

Hailing from three separate lithofacies groups, the three samples selected for this study represent a relatively wide compositional and textural range (Table 1). To preserve simplicity here, samples are distinguished by the name of their respective lithofacies group (Limestone, Concretionary Mudstone, and Organic Rich Mudstone), as opposed to the microfacies they represent. The Limestone sample (MF II – Chapter 1) is a packstone dominated by fossil debris and micrite. Organic carbon is scarce and the original bedding texture has been destroyed by bioturbation. The Concretionary Mudstone (MF XIII – Chapter 1) is comprised primarily of silt-sized calcite spar, and contains organic carbon in the form of the uncompacted remains of *Tasmanites* algal cysts. The Organic Rich Mudstone (MF VII – Chapter 1) is a finely-laminated sample with 11.9% organic carbon. Clay and organic matter are its most volumetrically abundant constituents, followed by quartz silt, pyrite, and calcite. TOC values within the tested samples range between 1.3-11.9% by weight (Karaca, 2012). Thermal maturity has been estimated to be 1.0-1.5 % R_o for all samples (Repetski et al., 2006).

Table 1: Sample roster, including compositional and textural data that may be relevant to mechanical properties. Sample numbers and microfacies descriptions from Chapter 1 and Karaca (2012). "Dac" within bioclast column is shorthand for "Dacryoconarid," an extinct order of planktonic organisms common in the middle Devonian.

Sample ID	Lithofacies	Microfacies Name (Chapter 1)	Microfacies Name (Karaca, 2012)	Lamination	TOC (%)	Pyrite Type	Bioclast Components	
							Type	%
SQ7	Limestone	Dacryoconarid Packstone	Styliolinid Packstone	Disturbed	1.3	Fine pyrite cubes in insoluble seam	Dac	40
SQS	Concretionary Mudstone	Algae Bearing Calcareous Concretion	Algae Bearing Calcareous Concretion	None	5.7	NA	NA	1
SQ11	Organic Rich Mudstone	Clay-Rich Quartz Silt-Bearing Carbonaceous Mudstone	Clay and Organic Rich Laminated Mudstone	Parallel	11.9	Framboids (5-10 µm)	Dac	5

To produce a flat and smooth surface suitable for indentation, samples were cut and then mechanically polished parallel to the direction of bedding. Nanoindentation measurements depend on continuous contact area between the tip and the indented material, and the technique requires that the surface roughness be much smaller than the depth of the indentations. The extreme heterogeneity of these rocks limits the efficacy of mechanical polishing (Loucks et al., 2009), particularly in those with the greatest abundance of clay minerals and organic matter. To create a surface that allows for shallow indentations that probe the individual constituents of the rock, the surfaces were further polished using a broad-beam argon ion mill. The milling process was conducted at an accelerating voltage of no higher than 1025 V, and a current of 70-80 nA. The sample was continuously rotated at 1 rpm, with a beam angle of incidence ranging from 60-80˚ from the sample normal. A typical surface roughness of less than 100 nm RMS was achieved by the ion milling.

In order to probe the bulk composite response of each lithofacies, 10 microindentations were emplaced on each sample. The measured Vickers hardness numbers were converted to Meyer hardnesses (force/projected residual indentation area) that can be compared with the hardness data gathered via nanoindentation. The Vickers hardness was calculated by indenting at a maximum load of 2.94 N with a dwell time of 15 seconds. These tests leave residual indentations with diameters between 70 and 150 μm, significantly larger than the average constituent sizes in these rocks (Figure 2). In all cases, indentations were performed in areas containing multiple mineral grains, and within regions that appear to be representative of the facies as described by Karaca (2012). During cube-corner microindentation, the maximum applied force was 19.6 N and the dwell time was 15 seconds. Deformation morphology and crack propagation behavior were analyzed using scanning electron microscopy.

Nanoindentation was performed (TriboIndenter TI-900, Hysitron Inc.) within areas representative of the identified rock facies. To aid in finding the tested location for further analysis, the corners of an approximately 1 mm square grid were marked by etching with a laser in each sample (Figure 3). Arrays of 400 nanoindentation tests were performed within the grids on each sample. The indents had an even spacing of 50 μm, and were arranged in 20 rows and 20 columns. For each indentation (e.g., Figure 2b), the load was ramped up to 10 mN in 5 s, held at that load for 5 s, and then ramped back down to zero in 5 s. Since each indentation was performed to the same maximum load, the resultant depth of the indentations varied depending on the hardness of the tested material.

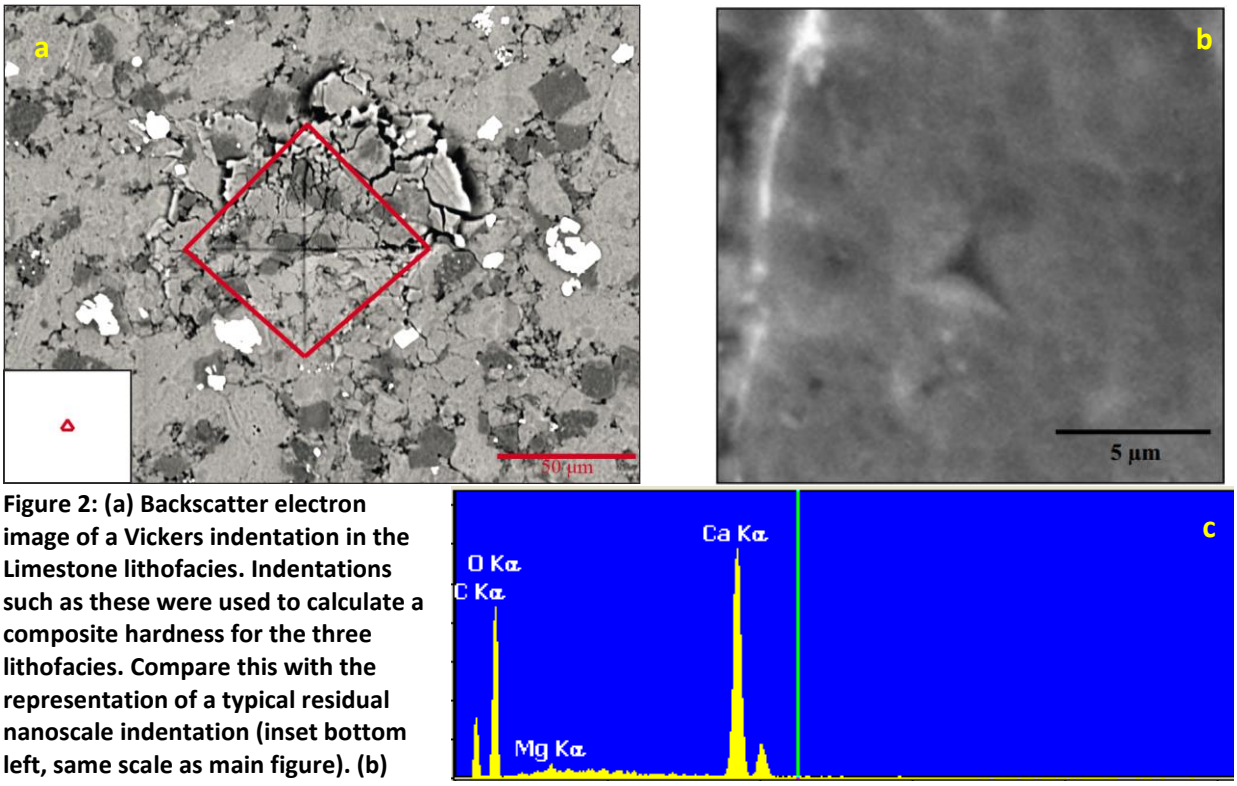

Figure 2: (a) Backscatter electron image of a Vickers indentation in the Limestone lithofacies. Indentations such as these were used to calculate a composite hardness for the three lithofacies. Compare this with the representation of a typical residual nanoscale indentation (inset bottom left, same scale as main figure). (b) Typical residual nanoindentation in a calcite grain. Vickers indentations sampled average behavior, while nanoindentations sampled individual constituents. (c) A typical energy dispersive x-ray spectroscopy spectrum obtained from an indented grain. Along with morphology, peaks for calcium, carbon, and oxygen in this spectrum identify the grain as calcite.

After indentation, samples were examined using a scanning electron microscope (SEM). Each indentation was imaged, and the mineralogy of the material under each indentation was identified. Mineralogy was determined using morphology revealed by SEM, backscatter electron intensity, and x-ray dispersive spectrometry (EDS). If the residual indentation was wholly within a single grain of a constituent mineral, then it was assigned to one of six mineral categories (Calcite, Dolomite, Quartz, Feldspar, Pyrite, or Apatite).

Because of their unique grain morphology, individual grains of clay minerals were often too small to host an indentation. However, clay grains often occurred as floccules or within

segregated clay-rich regions which allowed for the emplacement of a nanoindentation. It is also recognized that some amount of organic matter is associated with the clay phases in the studied rocks, exhibiting nanometer-scale intercalation which cannot be resolved via nanoindentation (Kennedy et al., 2014; Abedi et al., 2016). Indentations within regions such as this represent the response of multiple clay grains, and/or include a response from associated organic matter. Although the organic phase does not form true mineral "grains," segregated regions of organic matter as preserved *Tasmanites* algal cysts, disseminated within the mineral matrix, or within secondary veins are common (Chapter 1). If an indentation landed wholly within a clay grain, floccule, or an organic maceral, it was categorized as such (Clay, or Organic). Indentations that contacted boundaries of any other mineral category (grain boundaries or boundaries between constituents) were separated into a final category (Boundary). Indentations which probed clay in association with any other mineral phase or segregated organic maceral (e.g. a flattened algal cyst) were included in this boundary category as well.

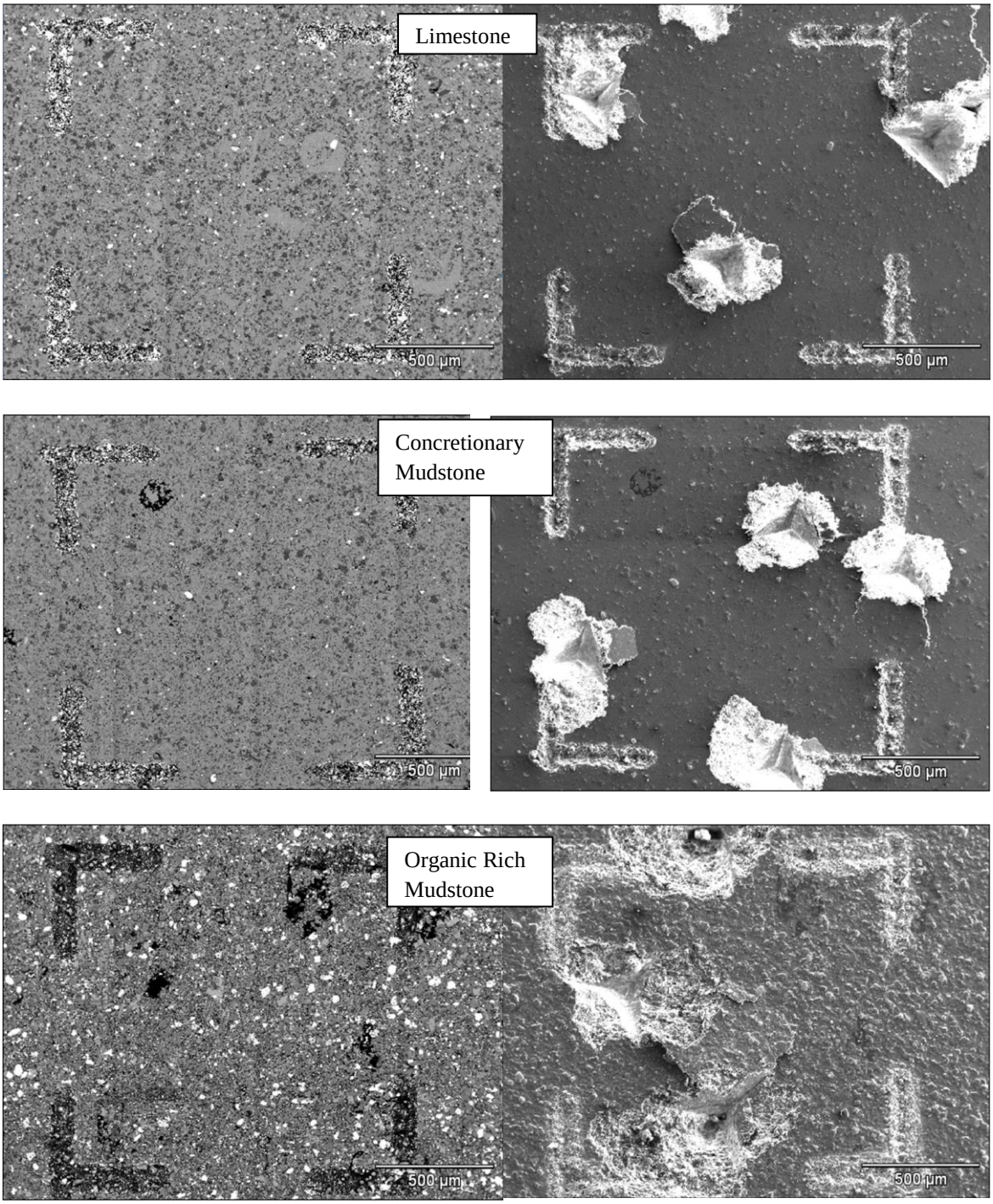

Figure 3: Backscatter and secondary electron images of ion-milled indented areas in Limestone (top row), Organic Rich Mudstone (middle row), and Concretionary Mudstone (bottom row) lithofacies. Note the apparent textural differences between samples. Grid areas were marked (right angle-corners) with a laser, and arrays of 400 nanoindentation tests were performed within each grid area (left column). Following nanoindentation, cube-corner microindentation was performed to investigate the fracture behavior of the bulk composite within the characterized area (right column). Grey scale variations between images in the left column are representative of compositional differences between lithofacies. Scale bars are 500 µm.

Results

Microindentation

Vickers hardness data for the 10 microindentations in each sample, and the corresponding Meyer hardness values, are shown in Table 2. The average diagonal span of these indentations (~70–150 μm) is much greater than the characteristic size of the constituents, and these measurements are expected to reflect the response of the bulk composite, based on the criteria identified by Ulm et al. (2006). The limestone lithofacies returned the highest mean hardness value, while the Organic Rich Mudstone recorded the lowest, significantly removed from the other two tested categories (Table 2). Deformation morphologies around the Vickers indentations were relatively constant between lithofacies, and were characterized by moderate cracking in the immediate vicinity of many indentations (see Figure 2a).

Table 2: Experimentally determined Vickers hardness numbers (HV) and Meyer hardnesses, with standard deviations, for each facies. Meyer hardness is force/projected indentation area and is comparable with nanoindentation results.

Lithofacies Group	Vickers Hardness (HV)	Meyer Hardness (Gpa)
Limestone	110 ± 5.4	1.61 ± 0.06
Concretionary Mudstone	93 ± 3.1	0.99 ± 0.03
Organic Rich Mudstone	45 ± 4.9	0.48 ± 0.05

Nanoindentation

The residual impressions of the indentations ranged in size from approximately 1 to 10 μm in diameter, corresponding with contact depths between 100 and 2000 nm. Within the indentation grid on each sample, the fraction of indentations that fell into each category is

shown in Figure 4. Because the indentations were evenly spaced, but otherwise randomly positioned, the distribution of indented constituents should be representative of the lithofacies composition. Of the 1200 indentations, images and mineral identifications show that **58.5%** of the indentations are located entirely within one of the material constituent areas, and **41.5**% are located on boundaries between two or more constituents. Within the Limestone and Concretionary Mudstone lithofacies, calcite is the most abundant constituent mineral probed by single nanoindentations (Fig. 4). Clay is the only constituent type that is of importance (>5% of indents) across all three lithofacies groups. In the Organic-Rich mudstone, organic matter was the most abundant constituent tested by an indentation (**27**%).

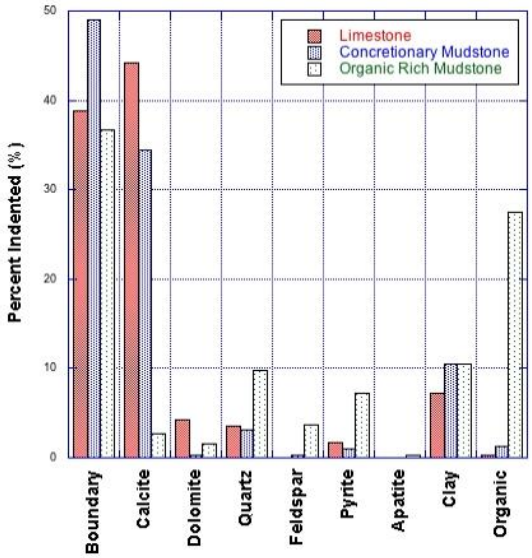

Figure 4: Percent of each material category indented, identified by lithofacies. For each sample, many indentations occurred on boundaries. The distribution of indentations in the other constituent categories should be representative of the lithofacies.

For each nanoindentation located within a material category rather than at a boundary, the indentation modulus and hardness of the material directly beneath the indentation was

calculated from the load-displacement data. For each lithofacies, the averages of the measured indentation modulus and hardness of the indentations that occurred within areas of each material category and the standard deviations are shown in Figure 5. Figure 5 also shows the average modulus and hardness of the total set of measurements of all the indentations, excluding those made in boundaries (Figure 4) but combining all other material category.

The indentations at boundaries are excluded in Figure 5 and in later analysis. They are excluded because, as regions typified by increased surface roughness, they are not suitable for indentation analysis, given that surface roughness leads to errors in the determination of the contact area between the indenter and specimen (Fischer-Cripps, 2011). Additionally, nanoindentations on boundaries return data which reflect the configuration of each probed grain at a unique configuration and orientation. Boundary indentations also may introduce additional deformation mechanisms, such as intergranular sliding, not observed in grain-centered indentations. For these reasons, the measured properties from indentations touching boundaries are segregated from boundaries fully within mineral grains.

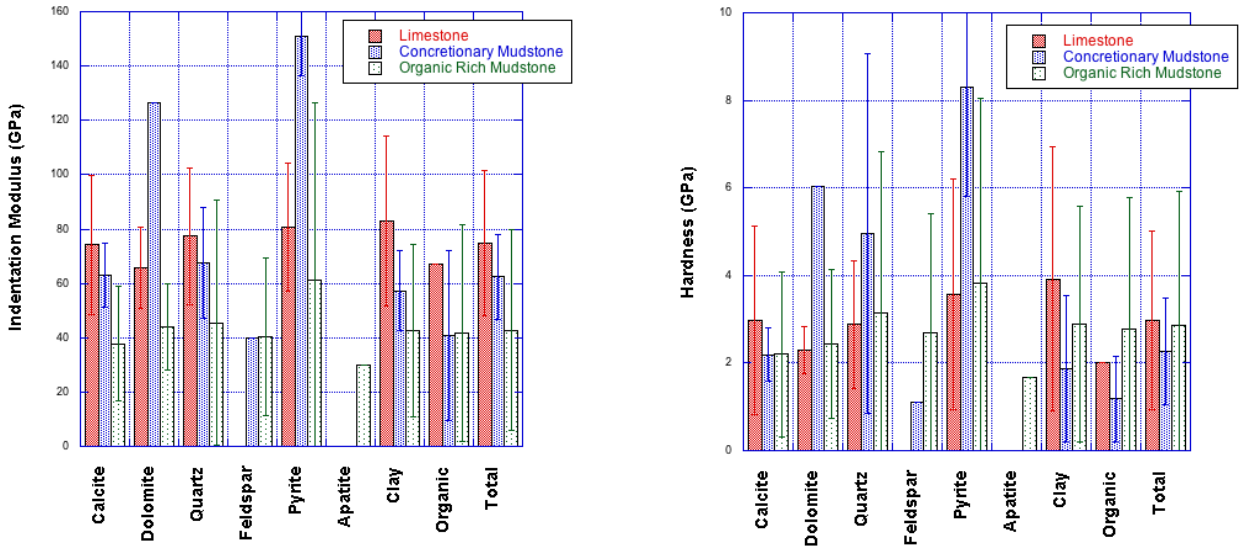

Figure 5: Average modulus and hardness of each material category by sample, as determined by nanoindentation. A number of constituent categories return a higher average measured modulus in the Limestone lithofacies than in the Organic Rich Mudstone. Hardness values vary less systematically.

The scheme for classifying indentation properties by material category did not account for the types of neighbors, or the distances of those neighbors from the edges of the residual indentations. Furthermore, it is not possible to tell what is below the surface of an indented grain. Thus, despite the categorization into material types, it is likely that the results in each category include some effect of the surrounding constituents. This effect appears to be expressed in the hardness and modulus of the organic matter (Figure 5), where the mean indentation moduli for Limestone, Concretionary Mudstone and Organic Rich Mudstone are approximately 67 Gpa, 41 Gpa, and 42 Gpa respectively. These data erroneously suggest that the organic phase has nearly the hardness and modulus of the mineral constituents. Based on previous studies, the hardness and modulus of the organic solids should be much lower than for the minerals; on the order of 10 Gpa (Kumar et al., 2012b).

To explore the effect of the surrounding material on the measurement of a constituent, the indentations in organic solid were further sub-divided into indents that occurred in the centers of especially large organic inclusions (~30 µm from any grain boundary), and those near boundaries or within small patches of organic matter. Five indentations were identified to have occurred within a large organic solid and at a distance exceeding 50 microns from the visible boundaries. The average measured modulus and hardness of these 5 indentations is 14.0 ± 4.64 Gpa and 0.49 ± 0.08 Gpa, respectively. These values are consistent with measurements in the literature (Kumar et al., 2012b; Zeszotarski et al., 2004).

For calcite, the apparent indentation modulus varies widely among the three lithofacies (i.e., 74 Gpa, 63 Gpa, and 38 Gpa) (Figure 5). Expected modulus values for calcite range between approximately 70 and 90 Gpa (Carloni & Baker, unpublished work). To explore this anomalous finding, the load-displacement curves for indentations in the centers of large grains from the Limestone lithofacies were compared with indentations in a large single crystal of calcite (Iceland Spar, Carloni and Baker, unpublished work). Example load-displacement data for the two cases are plotted in Figure 6. The curves are nearly identical, and the measured modulus is the same (72.0 Gpa). This suggests that it is the measurements for calcite in the other, more organic rich lithofacies that are anomalous, and it is assumed that the same is true for the other mineral constituents, which more closely match accepted values when measured in the Limestone lithofacies (Bass, 1995).

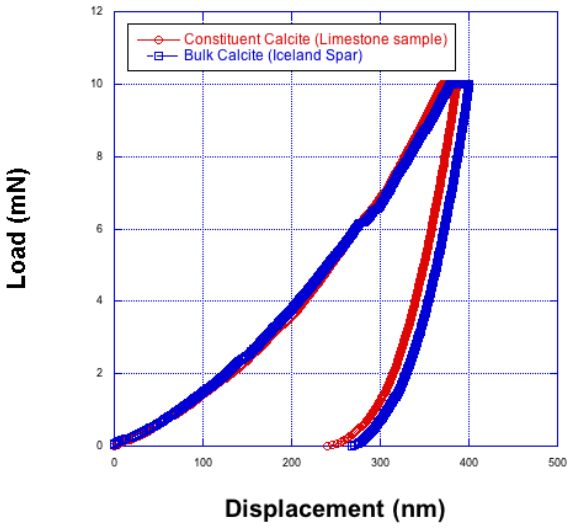

Figure 6: Example load-displacement data indentations in bulk calcite (Iceland Spar) and in a microscopic calcite constituent in the limestone lithofacies. Note the close agreement.

Crack Propagation

Cube-corner microindentation produced surface cracks through mechanically characterized areas. The extent of fracture induced by these indentations varied significantly between samples, becoming more extensive with increasing organic carbon content. In all cases, subsurface lateral cracks formed near the edges of the indentations, and in many cases large chunks of material were delaminated as a result and were found some distance away from the corresponding indentation after unloading. This phenomena resembles the formation of lateral vent cracks described by Lawn & Swain (1975), and caused damage zones which were often much larger than the direct residual impressions in the tip-surface contact area.

Preliminary crack path analysis on an approximately 200 µm fracture network within the Limestone lithofacies indicated that cube-corner induced cracks cross-cut grains for 42% of their total length, and followed grain boundaries 58% of their length.

Discussion

Based on the relative size of the Vickers microindentations, these measurements (Table 2) were expected to represent the composite behavior of the rock (Ulm et al., 2006). Comparing the measurements by micro- and nanoindentation (Table 3), the average measured hardnesses, expressed by Meyer hardness and nanoindentation hardness, differ in magnitude based on the scale of measurement. Additionally, the lithofacies exhibit differing trends in hardness values (e.g., Meyer hardness decreases from concretionary mudstone to organic-rich mudstone, whereas apparent nanoindentation hardness increases).

Table 3: Measured hardness and modulus from micro-hardness testing (left) and nanoindentation (right)

Lithofacies Group	Vickers Hardness (HV)	Meyer Hardness (Gpa)	Nanoindentation modulus mean of all materials (Gpa)	Nanoindentation hardness mean of all materials (Gpa)
Limestone	110 ± 5.4	1.61 ± 0.06	74.68 ± 26.78	2.97 ± 2.15
Concretionary Mudstone	93 ± 3.1	0.99 ± 0.03	62.46 ± 15.69	2.26 ± 1.21
Organic Rich Mudstone	45 ± 4.9	0.48 ± 0.05	42.80 ± 36.85	2.85 ± 3.07

For most of the constituent categories and across the lithofacies, the average hardness by nanoindentation is above 2 Gpa, but the average Meyer hardness measured by Vickers microindentation for each lithofacies is well below 2 Gpa (Figure 5; Table 2). If the Vickers indents are truly measuring the bulk response of the composite rock, and the nanoindentations are truly measuring the individual properties of the constituents that make up this composite, then for the case of randomly distributed nanoindentations over a representative area of the lithofacies, a simple rule of mixtures suggests that the averaged hardness at either length scale should match (Kim, 2000). However, a significant percentage of nanoindentations in this study

incorporated boundaries (Figure 4) for which a corresponding mechanical property has not been calculated. Boundaries, not analyzed by the nanoindentation analysis in this study, can provide additional deformation mechanisms (e.g. sliding) which may lead to a less hard, more compliant response during the measurement of the composite material (Marshall & Oliver, 1987). Additionally, the Vickers indentations were accompanied by significant cracking at the surface (see Figure 2a), which was not observed at the constituent scale. This would also reduce the hardness of the Vickers indentations relative to the nanoindentations (Armstrong & Elban, 2010).

The elastic measurements obtained through nanoindentation of volumes of individual materials also do not follow the expected response. Wide error bars can make interpretation difficult, and comparison of Figures 4 and 5 reveals that this is particularly the case for those mineral categories for which there are few measurements. This is an artifact of the large grid indentation method. Because of grain size and shape biases amongst mineral categories, some constituents are more likely than others to fall into the boundary category when indentations are not deliberately placed within individual constituents.

Elastic modulus is an intrinsic material property and should be constant for materials of identical crystallographic structure, orientation, and composition, regardless of the lithofacies in which it occurs (Hosford, 2010). However, a consistent trend is observed here across most constituent types of decreasing modulus with increasing organic content in the lithofacies (Figure 7, Figure 5a). This study has experimentally verified that the average measured modulus

for calcite in the low-organic lithofacies (Limestone) matches the expected value, and the measured modulus of some of the other mineral constituents (e.g. quartz, pyrite) in this lithofacies fell within the range of previously reported values (Bass, 1995). Hence, the relatively low modulus measurements for mineral constituents in the more organic-rich lithofacies are anomalous. I hypothesize that this is a result of the presence of compliant organic material distributed throughout the rock matrix. As such, this indicates that absent a correction, the ability to accurately measure grain scale properties within the sample set decreases as rock texture and composition changes from calcite-dominated, highly bioturbated limestones to finely laminated, clay-rich carbonaceous mudstones. This implies that nanoindentation measurements of the Union Springs Formation and other mudstones will vary in accuracy depending on the facies being characterized. Thus, uncorrected nanoindentation of Union Springs samples from more clay-dominated depositional regimes (e.g. central Pennsylvania) returns less accurate results overall than measurements from areas where clay is less abundant.

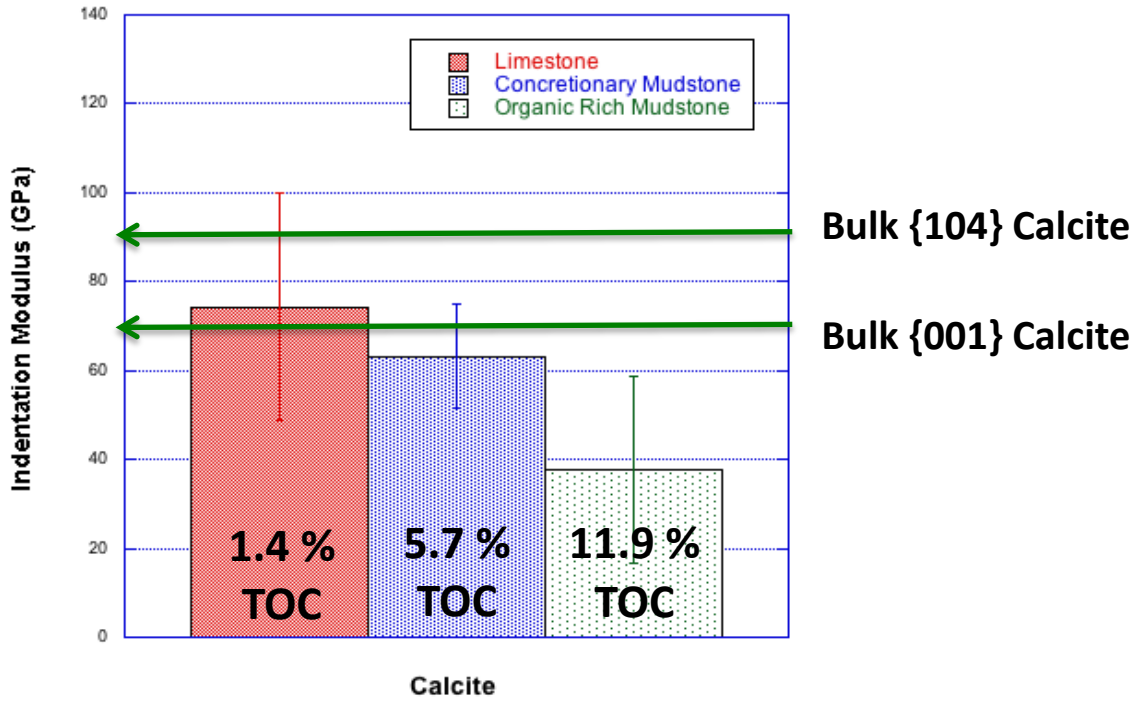

Figure 7: Modulus measurements for calcite determined by nanoindentation within each Marcellus lithofacies. Note the decrease in values as indentations are placed within increasingly organic rich lithofacies. This effect, a result of indenting stiff particles embedded in a compliant matrix, can be subtracted utilizing the correction developed by Carloni & Baker (2017). Experimentally-determined modulus values of bulk crystalline calcite at differing orientations are shown in green.

If organic matter is sufficiently well-distributed throughout the region hosting a single indentation, then the measurement of an individual mineral grain is equivalent to the measurement of a stiff particle in a compliant matrix. This matrix provides additional compliance that is not accounted for in the analysis model of Oliver & Pharr (2004) and thus artificially decreases the calculated modulus and hardness of the stiff particle (Saha & Nix, 2002). This effect can be overcome with sufficiently small indentation size, however it must be noted that minimum indentation size is limited by the achievable surface roughness. Independent of this study, Carloni & Baker (2017) have developed a technique to isolate the effect of a compliant matrix on the indentation measurement of a stiff particle. The technique involves the application of a dynamic load function that samples the response of the material at

multiple contact depths over the course of a single indentation (Carloni & Baker, 2017). Preliminary data from this work indicate that this technique successfully subtracts the effect of excess matrix compliance in organic-rich mudstones. With the correction, single concretionary calcite grains (D = 10's of μm) in direct contact with large (D = 100's of μm) organic macerals return mechanical properties similar to those measured in calcite grains from the same sample which are distant (many indentation widths) from organic macerals.

Other studies have aimed to describe the bulk behavior of shale through statistical nanoindentation techniques such as the work described here (Ulm et al., 2006). However, the results of this study indicate that indentation at this scale is susceptible to experimental artifacts. The random distribution of indentations, employed in this study as well as by Ulm et al. (2006), yields many indentations which occur at boundaries, and so the data returned are not representative of any particular depositional or diagenetic constituent (Figure 4). Grids of indentations should be analyzed at the individual indentation scale (e.g. Bennett et al., 2015; Abedi et al., 2016), and a more targeted method of placing indentations wholly within single grains, floccules, or organic macerals could prove to be a more efficient means of probing grain-scale features in mudstones (e.g. scanning electron microscopy with a nanoindentation apparatus).

More targeted means of indentation placement can also aid in returning a suite of indentation data more reflective of facies composition for a given rock. Differing compositional grain size and shape distributions may lead to a compositional bias with respect to the amount

of useful (non-boundary) data from each mineral category. Small grains, such as clay minerals dispersed throughout the rock matrix (not within relatively large clay floccules), which have a higher perimeter to area ratio than do large diameter grains, are more likely to be underrepresented, due to the fact that only indentations fully contained within one grain, floccule, or organic maceral are acceptable for measuring the properties of a given mineral phase.

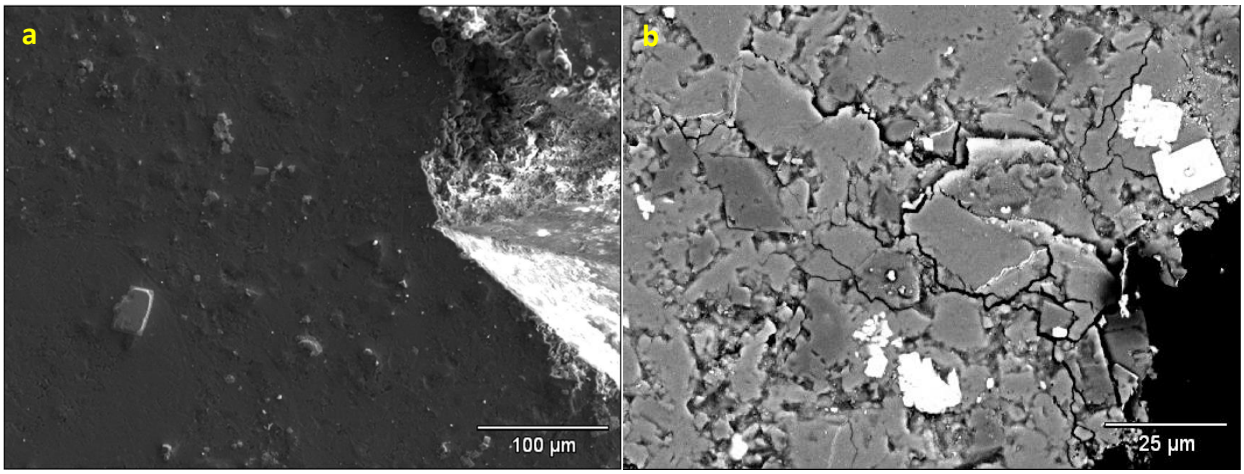

Figure 8: A) Secondary electron image showing the corner of a cube-corner indentation with the absence of radial crack propagation in the Limestone lithofacies. Lateral shear cracking was the most commonly observed fracture mode, and can be observed in Figure 3. B) Backscatter electron image of a cube-corner indentation with small cracks emanating from the indentation corner in the calcite-rich Limestone lithofacies. 25 µm scale bar.

The intent of cube-corner micro-fracture experiments was to examine crack propagation at the scale characterized by nanoindentation. Results were mixed, with tests in the Organic-Rich Mudstone lithofacies failing to produce sufficient stable cracks, and the other two lithofacies experience only minor amounts of suitable cracking (Figure 3, Figure 8). The experiment was designed to propagate continuous radial cracks from indenter corners and to track their progress with respect to rock texture and composition across the same bedding-

parallel surfaces characterized via nanoindentation. Such cracks were generally small (Figure 8) and were completely absent in the Organic Rich Mudstone lithofacies. Instead, subsurface lateral cracks led to spallation of large volumes of rock (relative to the grain size) to come loose and be ejected from the system. This eliminated any chance of providing a comprehensive analysis of the crack paths. It is hypothesized that these spallation patterns result from the linkage of multiple lateral cracks surrounding the zone of plastic deformation underneath the indentation (Figure 9). This linkage would allow lateral cracks to branch upwards toward the indented surface, possibly influenced by bedding planes or clay alignment in the finely-laminated rock. This would indicate that bedding surfaces and/or the alignment of clay minerals significantly influence fracture behavior at this scale, further suggesting that similar fracture path analysis work at different orientations would likely yield different results. Anisotropy within shales has been well-documented (Ulm et al., 2006; Sondergeld et al., 2010; and others). Therefore, it might be useful to investigate the effect of anisotropy on small-scale crack behavior across a broad range of mineralogies. If radial cracks of sufficient length can be induced, there may exist the potential to conduct robust crack path analysis on a region whose spatial distribution of mechanical properties is known from nanoindentation.

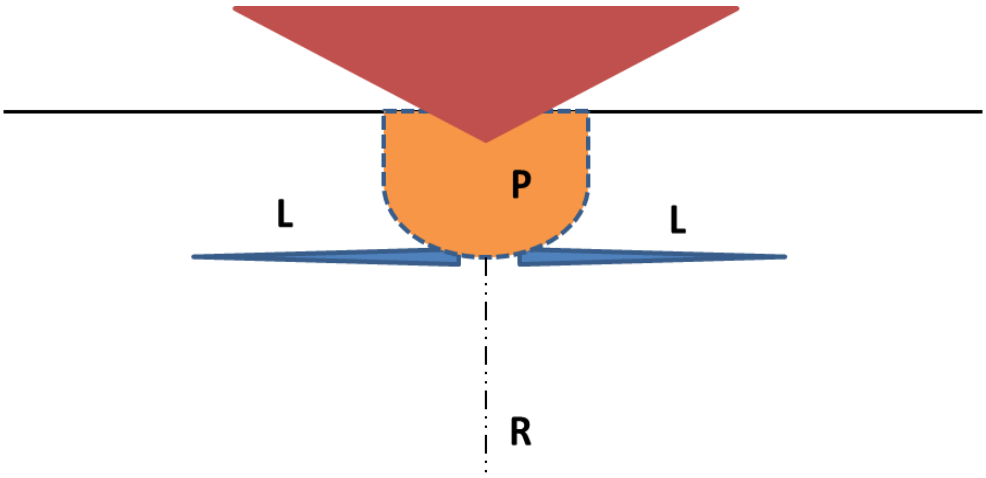

Figure 9: Schematic showing the initiation of lateral cracking (L) underneath the zone of plastic deformation (P) during the process of indentation. I represents radial cracking. After Marshall et al. (1982).

Conclusions

Work presented here documents significant modulus and hardness variability within each studied lithofacies. A comparison of sub-millimeter mechanical properties of three different mudstone lithofacies reveals that the composite hardness decreases with increasing organic solid content. Yet a grid-based method of gathering a large number of elastic modulus and hardness data for the constituents of the mudstone reveals systematic problems with the nanoindentation experimental approach. Although data from the less organic-rich lithofacies more closely matched predicted values, modulus data within organic-rich lithofacies display a negative bias as a result of excessive substrate compliance which occurs in the presence of high materials properties contrasts.

In grid-indentation experiments such as those performed here, placing a large array of nanoindentations should yield results in which the distribution of constituents measured is consistent with the composition of the lithofacies. In theory, this is true, and the 1200

nanoindentations sampled an aggregate of points representative of each lithofacies. In practice, the nature of a method which places indentations randomly with respect to rock fabric renders significant percentages of the data returned useless for measuring mechanical properties of individual constituents. The effects of boundary indentations must be fully accounted for. Even when the boundary results are excluded (Figure 5), the properties of the constituents, as measured by nanoindentation, cannot simply be averaged to approximate the bulk response of the rock (Table 3). This difference across scales occurs due to multiple factors. For one, the deformation mechanism varies between length scales. Vickers indentations are accompanied by significant cracking that is not observed for nanoindentation. Also, the behavior at boundaries is likely to have a strong effect on the composite response, and this behavior cannot be captured by straightforward nanoindentation experiments. Finally, it is shown that neighboring material affects the measured response of individual constituents during nanoindentation. This results in artificially high elastic modulus and hardness in compliant organics surrounded by stiff minerals, and artificially low elastic modulus and hardness in stiff minerals surrounded by compliant organics. Note that this discrepancy was only uncovered through careful mineralogical identification of the indented regions, and this phenomenon is likely to affect any experiments in which nanoindentation results are analyzed in a statistical way without sufficient screening of the data, particularly in composite materials in which significant percentages of constituents measure only tens of microns in length. A nanoindentation strategy has been developed (Carloni and Baker, 2017) that can isolate the effect of a compliant matrix. Use of this method produces elastic modulus and hardness data

that more accurately measure the stiff constituents, particularly within clay- and organic-rich lithofacies.

If the properties of individual mudstone constituents can be accurately measured, then the spatial variation in property recorded by nanoindentation could be especially useful for analyzing the propagation of cracks through characterized regions. From the nanoindentation results of this study, the variation of mechanical properties across the indented area is known at numerous discrete points within each microfacies, and recent studies (Eliyahu, 2014; Zargari, 2015) have demonstrated more continuous means of characterizing mechanical properties measurements in mudstone utilizing atomic force microscopy and dynamic nanoindentation. Coupling high-resolution mechanical properties data including nanoindentation analyses with the characteristic fracture response of the rock at the micron to millimeter scale should prove useful in understanding the overall mechanical behavior of the rock at a large scale. Performing micro-fracture experiments in regions with well-characterized mechanical properties could prove especially useful, particularly if anisotropy as well as bedding orientation and spacing are taken into account in order to better detail the significance of rock texture with respect to constituent mineral interfaces and orientations in the fracture propagation process. An accurate understanding of the fundamental response of the rock at this scale can be beneficial for mechanical modelling applications, as well as the prediction of the bulk material response at a larger scale without requiring more complicated or destructive experiments.

Acknowledgments

This work is a result of a collaborative pilot study sponsored by the Atkinson Center for a Sustainable Future. Content presented is adapted from: Mason, J., Carloni, J., Zehnder, A., Baker, S. P., & Jordan, T. (2014). Dependence of Micro-Mechanical Properties on Lithofacies: Indentation Experiments on Marcellus Shale. In SPE/AAPG/SEG Unconventional Resources Technology Conference. Society of Petroleum Engineers.

This work was supported in part by Cornell University's David R. Atkinson Center for a Sustainable Future (ACSF). Thanks to the Cornell Center for Materials Research Shared Facilities and NSF award DMR-1120296. This work was performed in part at the Cornell NanoScale Facility, a member of the National Nanotechnology Coordinated Infrastructure (NNCI). I acknowledge the donors of the American Chemical Society Petroleum Research Fund, PRF grant-in-aid #52282-ND8, for funding support, and the National Science Foundation award DMR-1210304 for support of participant Carloni.

References

Abedi, S., Slim, M., Hofmann, R., Bryndzia, T., & Ulm, F. J., 2016, Nanochemo-mechanical signature of organic-rich shales: a coupled indentation—EDX analysis: Acta Geotechnica, v. 11, p. 559-572

Armstrong, R. W., & Elban, W. L. (2010). Macro-to nano-indentation hardness stress–strain aspects of crystal elastic/plastic/cracking behaviors. *Experimental mechanics*, *50*(4), 545-552.

Bennett, K. C., Berla, L. A., Nix, W. D., & Borja, R. I. (2015). Instrumented nanoindentation and 3D mechanistic modeling of a shale at multiple scales. *Acta Geotechnica*, *10*(1), 1-14.

Berthelot, J. M. (1999). Dynamics of composite materials and structures. *Institute for Advanced Materials and Mechanics, Springer, New York*.

Carloni, J., Baker, S. P., (2017, in preparation). Measuring the elastic modulus and hardness of particles within a dissimilar matrix using instrumented indentation.

Deirieh, A., Ortega, J. A., Ulm, F. J., & Abousleiman, Y. (2012). Nanochemomechanical assessment of shale: a coupled WDS-indentation analysis. *Acta Geotechnica*, *7*(4), 271-295.

Eliyahu, M., Emmanuel, S., Day-Stirrat, R. J., & Macaulay, C. I. (2015). Mechanical properties of organic matter in shales mapped at the nanometer scale. *Marine and Petroleum Geology*, *59*, 294-304.

Fischer-Cripps, A. C. (2011). Nanoindentation. Third edition. New York, NY: Springer.

Gale, J. F., Reed, R. M., & Holder, J. (2007). Natural fractures in the Barnett Shale and their importance for hydraulic fracture treatments. *AAPG bulletin*,*91*(4), 603-622.

Hosford, W. F. (2010). *Solid mechanics*. Cambridge University Press.

Jarvie, D. M., Hill, R. J., Ruble, T. E., & Pollastro, R. M. Unconventional shale-gas systems: The Mississippian Barnett Shale of north-central Texas as one model for thermogenic shale-gas assessment. *AAPG Bulletin*, *91*, 475-499.

Karaca, C. (2012). Characterization Of The Union Springs Formation, Finger Lakes Region, Ny: An Integrated High Resolution Facies, Geochemical And Sequence Stratigraphical Approach. Cornell University, 92 p.

Kennedy, M. J., Löhr, S. C., Fraser, S. A., & Baruch, E. T. (2014). Direct evidence for organic carbon preservation as clay-organic nanocomposites in a Devonian black shale; from deposition to diagenesis. *Earth and Planetary Science Letters*, *388*, 59-70.

Kim, H. S. (2000). On the rule of mixtures for the hardness of particle reinforced composites. *Materials Science and Engineering: A*, *289*(1), 30-33.

King, G. E. (2010, January). Thirty years of gas shale fracturing: what have we learned?. In *SPE Annual Technical Conference and Exhibition*. Society of Petroleum Engineers.

Kumar, V., Sondergeld, C. H., & Rai, C. S. (2012a). Nano to macro mechanical characterization of shale. In *SPE Annual Technical Conference and Exhibition*. Society of Petroleum Engineers.

Kumar, V., Curtis, M. E., Gupta, N., Sondergeld, C. H., & Rai, C. S. (2012b). Estimation of Elastic Properties of Organic Matter in Woodford Shale Through Nanoindentation Measurements. In *SPE Canadian Unconventional Resources Conference*. Society of Petroleum Engineers.

Kumar, V., Sondergeld, C., & Rai, C. S. (2015). Effect of mineralogy and organic matter on mechanical properties of shale. *Interpretation*, *3*(3), SV9-SV15.

Lawn, B. R., & Swain, M. V. (1975). Microfracture beneath point indentations in brittle solids. *Journal of Materials Science*, *10*(1), 113-122.

Loucks, R. G., Reed, R. M., Ruppel, S. C., & Jarvie, D. M. (2009). Morphology, genesis, and distribution of nanometer-scale pores in siliceous mudstones of the Mississippian Barnett Shale. *Journal of Sedimentary Research*, *79*(12), 848-861.

Macquaker, J. H., & Adams, A. E. (2003). Maximizing information from fine-grained sedimentary rocks: an inclusive nomenclature for mudstones. *Journal of Sedimentary Research*, *73*(5), 735-744.

Makee, D., Goulas, J., (2016). Micromechanical Characterization of Marcellus Shale. Cornell University. Master of Engineering Project Report.

Marshall, D. B., Lawn, B. R., & Evans, A. G. (1982). Elastic/plastic indentation damage in ceramics: the lateral crack system. *Journal of the American Ceramic Society*, *65*(11), 561-566.

Marshall, D. B., & Oliver, W. C. (1987). Measurement of Interfacial Mechanical Properties in Fiber-Reinforced Ceramic Composites. *Journal of the American Ceramic Society*, *70*(8), 542-548.

Mason, J., & Jordan, T. (2014). Geologic Variability Within the Marcellus Shale and Its Relationship With Natural Fractures. *American Association of Petroleum Geologists Annual Conference*, *Poster*.

Mason, J., & Jordan, T. (2015). *High-Resolution Facies Variability in the Union Springs Formation of the Northern Appalachian Basin*. Geological Society of America Annual Meeting, Poster.

Maxwell, S. C. (2012, January 1). Comparative Microseismic Interpretation of Hydraulic Fractures. Society of Petroleum Engineers. Doi:10.2118/162782-MS

Oliver, W. C., & Pharr, G. M. (2004). Measurement of hardness and elastic modulus by instrumented indentation: Advances in understanding and refinements to methodology. *JOURNAL OF MATERIALS RESEARCH-PITTSBURGH THEN WARRENDALE-*, *19*(1), 3-20.

Passey, Q. R., Bohacs, K. M., Esch, W. L., Klimentidis, R., & Sinha, S. (2010). From oil-prone source rock to gas-producing shale reservoir–geologic and petrophysical characterization of unconventional shale-gas reservoirs. *Beijing, China, June*, *8*.

Repetski, J.E., Ryder, R.T., Weary, D.J., Harris, A.G., and Trippi, M.H. (2008). Thermal maturity patterns (CAI and $\%R_o$) in Upper Ordovician and Devonian rocks of the Appalachian basin: A major revision of USGS Map I–917–E using new subsurface collections: U.S. Geological Survey Scientific Investigations Map 3006.

Rickman, R., Mullen, M. J., Petre, J. E., Grieser, W. V., & Kundert, D. (2008, January). A practical use of shale petrophysics for stimulation design optimization: All shale plays are not clones of the Barnett Shale. In *SPE Annual Technical Conference and Exhibition*. Society of Petroleum Engineers.

Saha, R., & Nix, W. D. (2002). Effects of the substrate on the determination of thin film mechanical properties by nanoindentation. *Acta Materialia*, *50*(1), 23-38.

Sondergeld, C. H., Ambrose, R. J., Rai, C. S., & Moncrieff, J. (2010, January). Micro-structural studies of gas shales. In *SPE Unconventional Gas Conference*. Society of Petroleum Engineers.

Sondergeld, C. H., Newsham, K. E., Comisky, J. T., Rice, M. C., & Rai, C. S. (2010, January). Petrophysical considerations in evaluating and producing shale gas resources. In *SPE Unconventional Gas Conference*. Society of Petroleum Engineers.

Ulm, F. J., & Abousleiman, Y. (2006). The nanogranular nature of shale. *Acta Geotechnica*, *1*(2), 77-88.

Ulm, F. J., Vandamme, M., Bobko, C., Alberto Ortega, J., Tai, K., & Ortiz, C. (2007). Statistical indentation techniques for hydrated nanocomposites: concrete, bone, and shale. *Journal of the American Ceramic Society*, *90*(9), 2677-2692.

Zargari, S. (2015). *Effect of thermal maturity on nanomechanical properties and porosity in organic rich shales (a Bakken shale case study)* (Doctoral dissertation, Colorado School of Mines).

Zeszotarski, J. C., Chromik, R. R., Vinci, R. P., Messmer, M. C., Michels, R., & Larsen, J. W. (2004). Imaging and mechanical property measurements of kerogen via nanoindentation. *Geochimica et cosmochimica acta*, *68*(20), 4113-4119.

EPILOGUE

The Union Springs Formation, the lower formation of the Marcellus subgroup, is a widespread mudstone unit in the eastern United States currently being exploited as a natural gas resource in a number of states. With an aim to serve as a resource to all interested parties, this document describes the physical and chemical variability of the Union Springs in the northern Appalachian Basin, and explores the relationship between this variability and grain-scale mechanical properties.

The foundation of this research is the description and interpretation of the physical properties of the Union Springs Formation (Chapter 1). Physical variability captures important details of the geologic past, and dictates a number of parameters of human interest, including hydrocarbon resource potential. Three complete Union Springs sections in central New York, irregularly spaced and oriented roughly along strike, are described in detail. The studied sections are separated by 600 m and 38.6 km in order to facilitate the examination of near and far field variability. By grouping together rocks with similar physical properties, a high-resolution microfacies framework is established. Fifteen microfacies are identified across the study area, and can be broadly classified within three lithofacies groups: Limestone, Carbonaceous Mudstone, and Calcareous Concretion. The arrangement of these facies is connected to understanding the paleo-oceanographic and tectonic factors which controlled deposition basin-wide. Variability of depositional properties is described both within and between facies. Low sediment supply, high primary productivity, and an oxygen-stressed seafloor are established as general characteristics of the depositional system, and variation of these characteristics is shown to impact bulk mineralogy, bedding character, and organic

carbon enrichment. To facilitate additional far-field comparison, the studied sections were placed into a sequence stratigraphic framework. Using facies changes to delineate sequence and parasequence boundaries, parasequences were defined and correlated in the near-field, while some limited potential was shown for precise correlation in the far-field.

The addition of whole-rock compositional data (Chapter 2) to the large petrographic data set of Chapter 1 permits the study of chemical variability within petrographically-defined categories, and further characterizes the controls on organic carbon enrichment and paleoenvironmental conditions in the Union Springs. Elemental abundance data gathered via handheld XRF are becoming increasingly common as a means of characterizing resource potential, the potential for environmental risk, and the variability of ancient depositional environments. Within the study area, Limestones and Calcareous Concretions may appear similar compositionally, but are generated within distinct depositional settings. Rocks of the Carbonaceous Mudstone lithofacies group exhibit the most compositional variability, but some microfacies are more tightly compositionally constrained than others. The calcareous cement-bearing microfacies is particularly variable due to highly inconsistent degrees of cementation. The Carbonaceous Mudstone group is rich in total organic carbon (TOC) on average, but factors such as bioturbation, paleoredox state, and diagenetic alteration are shown to significantly impact individual samples. TOC and redox-sensitive trace element abundances indicate temporally and spatially variable paleo-oxygenation of the seafloor in a sediment starved environment. Principal components analysis confirmed that major controls on compositional variability include terrigenous sediment supply and an occasionally euxinic water column. The distinction between calcium abundance (associated with calcite) and the abundance of

siliciclastic-associated elements (Si, Al, Ti), proved especially powerful for its influence on compositional variability, as well as its implications for the depositional environment, organic richness, and mechanical properties variation.

Modern mechanical rock properties in the Union Springs Formation can be conceptualized in part as a result of the composition, bedding character, depositional energy, and burial history of the sediments that were deposited into the ancient basin. High-resolution knowledge of these properties developed in Chapters 1 and 2 is used in Chapter 3 to guide the development of a method by which mechanical properties of mudstones can be tested at the grain scale across a range of compositions. This chapter works at the smallest scale of the three chapters in this work in order to characterize rocks at the scale at which fractures propagate. A method is developed for utilizing nanoindentation to accurately measure properties of individual grains in organic-poor, calcite-dominated rocks as well as organic-rich rocks with abundant clay minerals and minimal calcite abundance. When comparing results of nanoindentation with Vickers and cube-corner microindentation tests, differences emerge between the grain scale and the bulk mechanical behavior. For example, hardness disparities are explained via the incorporation of additional deformation mechanisms under the greater load and more extensive area being probed within the micro-scale test. High-resolution characterization of organic-rich mudstone mechanical properties has a promising future as a non-destructive testing method with potential to expand its prevalence in industrial and mechanical modelling applications.